

A slip of the tongue

Tribology of soft surfaces and complex lubricants



Raisa E. D. Rudge

Propositions

1. The complex frictional dynamics behind soft tribology can simply be described by the gap size.
(this thesis)
2. Friction coefficients measured using tribometers with different surface motions cannot be compared with one another.
(this thesis)
3. More funding does not equal better science.
(Fortin & Currie, PLOS ONE, 2013)
4. Healthy and sustainable diets do not emerge from producing and marketing new food products as suggested by Munday and Bagley (Munday & Bagley, Nutrition bulletin, 2017)
5. Adopting the local tongue is essential to integration and acceptance into a community.
(Bleakly & Chin, The Review of Economics and Statistics, 2014)
6. Transforming vegetables into “meat” is an insult both to plants and to animals.
7. Comparing live Disc Jockeying (DJ'ing) to a prepared playlist is like comparing a home-cooked meal to fast food.
8. The most astringent propositions are often diluted to avoid societal or institutional friction.

Propositions belonging to the thesis, entitled

A slip of the tongue: Tribology of soft surfaces and complex lubricants

Raisa E. D. Rudge

Wageningen, 27 May 2021

A slip of the tongue

Tribology of soft surfaces and complex lubricants

Raisa E. D. Rudge

Thesis committee

Promotor

Dr. Elke Scholten

Associate professor

Physics and Physical Chemistry of Foods

Wageningen University & Research

Co-promotor

Dr. J. A. Dijksman

Assistant professor

Physical Chemistry and Soft matter

Wageningen University & Research

Other members

Prof. Dr. M.A. Stieger, Wageningen University & Research, The Netherlands

Prof. Dr. M.M.G. Kamperman, University of Groningen, The Netherlands

Prof. Dr. A. Pitenis, University of California, USA

Prof. Dr. J. Chen, Zhejiang Gongshang University, China

This research was conducted under the auspices of
the Graduate School VLAG (Advanced studies in
Food Technology, Agrobiotechnology, Nutrition and Health Sciences)

A slip of the tongue

Tribology of soft surfaces and complex lubricants

Raisa E. D. Rudge

Thesis

Submitted in fulfillment of the requirements for the degree of doctor
at Wageningen University,

by the authority of the Rector Magnificus,

Prof. Dr. A.P.J. Mol,

in the presence of the

Thesis Committee appointed by the Academic Board,

to be defended in public

on Thursday May 27th 2021

at 11:00 a.m. in the Aula.

Raisa E. D. Rudge

A slip of the tongue — Tribology of soft surfaces and complex lubricants

282 pages

PhD thesis, Wageningen University, Wageningen, The Netherlands (2021)
with references, with summaries in English and Dutch.

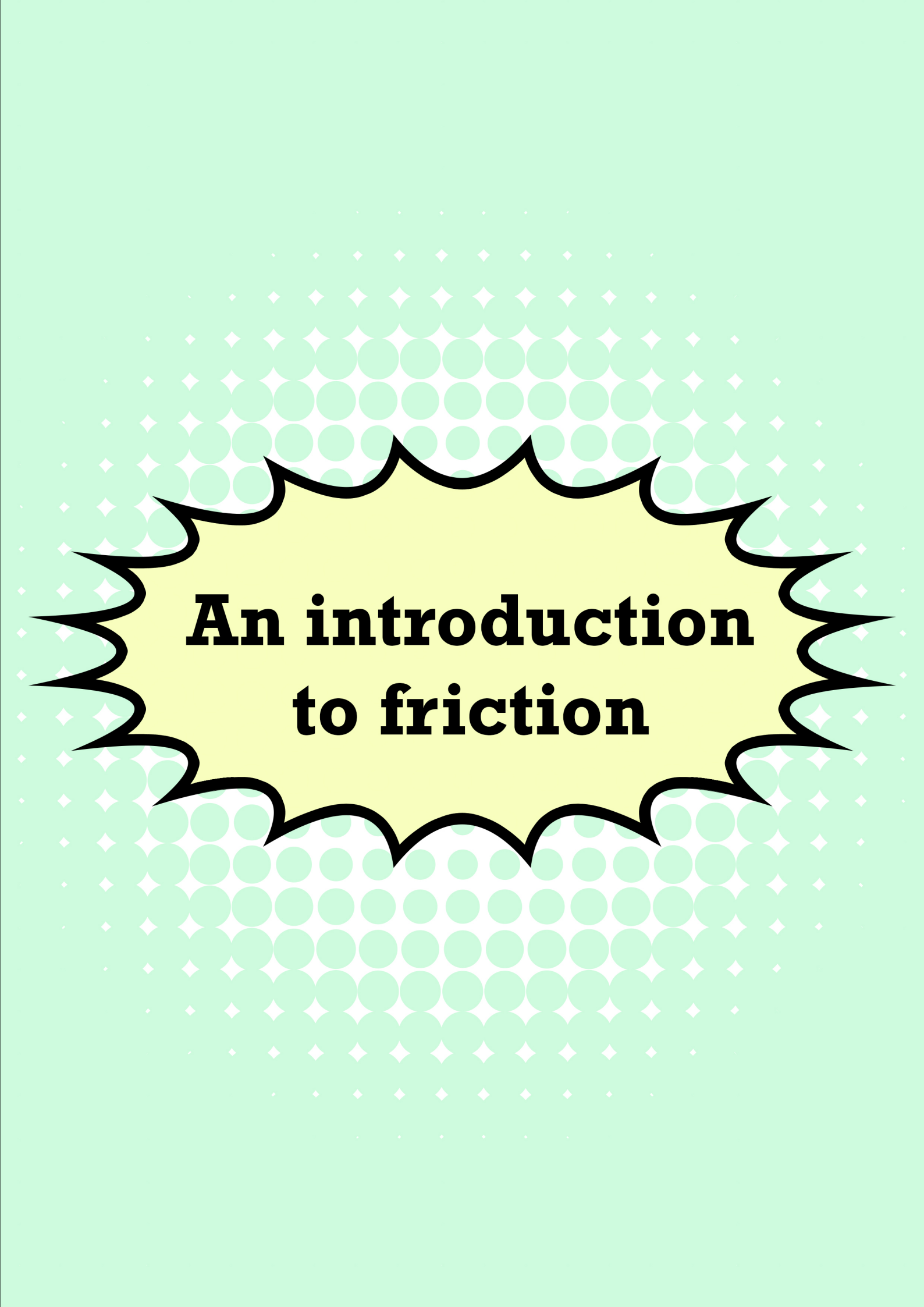
ISBN: 978-94-6395-787-8

DOI: <https://doi.org/10.18174/545753>

Chikito y simpel mi por ta, pero si respeta.

Table of contents

1	An introduction to friction	1
I	Hydrogel - hydrogel friction	21
2	Soft surface roughness determines frictional regimes in hydrogel pairs	23
3	Is there a pattern? Frictional properties of micro-patterned hydrogels	51
II	Particle lubrication	75
4	Uncovering friction dynamics using hydrogel particles as soft ball bearings	77
5	Rolling and sliding friction of hard particles lubricating soft surfaces	111
6	Lubrication properties of hard particle suspensions between soft surfaces	131
III	Tribological applications	157
7	A tribological approach to astringency perception and astringency prevention	159
8	Fluid and suspension lubrication using four different tribometers	189
9	General Discussion	225
	Summary/Samenvatting	249
	Appendix	259
	List of publications	260
	Acknowledgements	263
	About the author	269
	Overview of completed training activities	270



An introduction to friction

Nothing starts and nothing stops without friction. Friction is the resistance force between two surfaces sliding alongside one another. From the day we are born (or perhaps, even before that) we are constantly confronted with friction and wherever there are materials in contact, friction exists. Opening our eyes in the morning, brushing our teeth, drinking coffee, and driving to work: these actions all rely on having the right degree of friction. The concept of friction is far older than mankind. The initial formation of stars and galaxies after the Big Bang could not have taken place without friction between the clouds of primary elements (e.g. hydrogen, helium). [1, 2] Using friction, the early inhabitants of our planet created fire and they invented the wheel thousands of years ago. [3, 4] Similarly, ancient construction works, such as the pyramids, could not have been built without the assistance of friction. [5] Nowadays, friction is still a large part of our daily lives. Examples of sliding systems where the degree of friction greatly impacts the performance and can lead to economic, medical or other societal benefits include modern day machinery (e.g. cars, planes) with rotating gears, computer components such as hard drives, and contact lenses. As was shown in Walt Disney's Uncle Scrooge's comic, a "frictionless" world would result in objects (including gold coins) flowing uncontrollably into unwanted directions, including into the hands of bank robbers (Figure 1.1). [6]



Figure 1.1: Panel from Walt Disney's Uncle Scrooge's comic series. The story includes a device that renders objects frictionless. Due to the low friction, Uncle Scrooge's money readily flows into the hands of his nemeses, the Beagle boys. The image used here originates from the "Cash flow" comic from the Uncle Scrooge series. [6]

Early frictional studies

Although friction is all around us, the study of friction is relatively young. Leonardo Da Vinci (1452-1519) was the first person to systematically study friction. [7] In the 1700s, Guillaume Amontons and Charles Coulomb established the first frictional theories. They defined the friction coefficient (μ) as the ratio between the friction force (F_F) and the normal force (F_N) and stated that $\mu = F_F/F_N$. [8, 9] A schematic representation of sliding surfaces and the respective forces are shown in Figure 1.2. In general, low friction coefficients are found when surfaces easily slide alongside one another as is the case with an ice skate on ice. [10, 11] The friction of a rubber bicycle tire on concrete is at the high end of the friction coefficient spectrum. [12, 13]

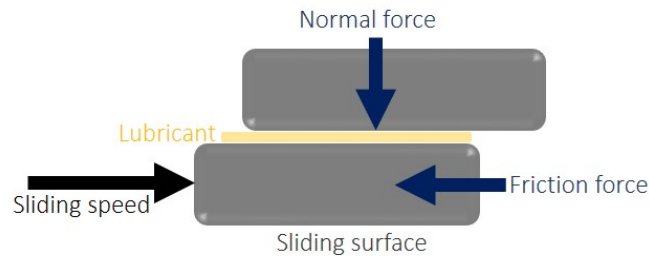


Figure 1.2: A diagram of two sliding surfaces subjected to a normal force, a push force attempting to move the surface and a friction force restricting the motion. The blue arrows indicate the forces that are used to calculate the friction coefficient, μ .

The term friction here refers to kinetic friction; the friction generated by two moving surfaces. This kinetic friction can be decreased by the presence of a lubricant (Figure 1.2) that separates the surfaces from one another to provide lubrication and reduce friction. For solid surfaces lubricated by Newtonian fluids, the Stribeck curve (Figure 1.3) shows that the friction coefficient depends on the Hersey (or Sommerfeld) number: $\frac{\text{viscosity} \cdot \text{velocity}}{\text{load}}$. [14–17] This results in three sliding regimes; a boundary or contact regime at low Hershey numbers, followed by a mixed regime where partial contact exists and a hydrodynamic regime where the hydrodynamic pressure of the fluid generates lift forces that push the sliding surfaces apart, often at high viscosities and/or velocities. The Stribeck curve is a useful tool to assess the lubrication behavior of a wide range of solid materials paired with Newtonian lubricants and is, therefore, used extensively in the field of tribology. [15, 16, 18, 19]

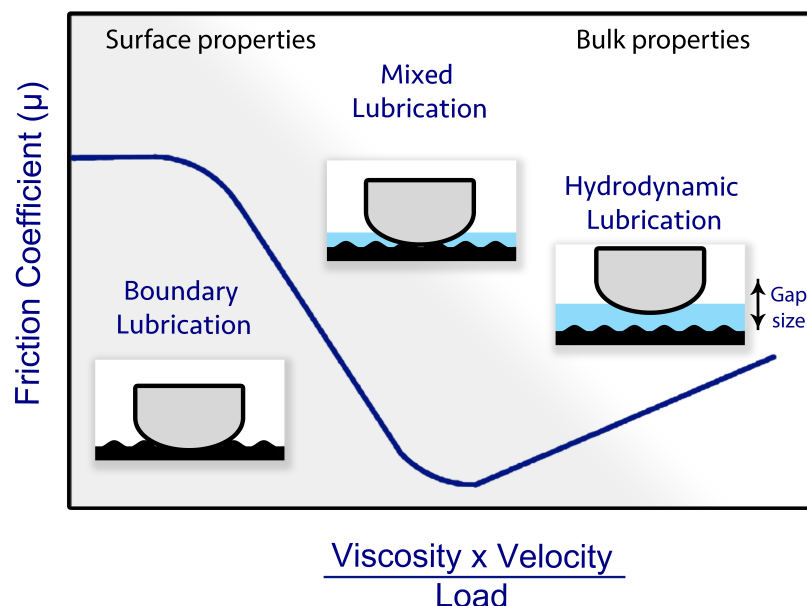


Figure 1.3: A traditional Stribeck curve showing the relation between the friction coefficient and the viscosity, velocity and load parameter. The boundary, mixed and hydrodynamic regimes are indicated in the figure.

The majority of modern day materials and lubricants show frictional behavior beyond the laws established in the last centuries. [18, 20] These materials include semi-solid, deformable surfaces such as soft hydrogels [21, 22] or rubber-like elastomers.[23] Soft surfaces are of interest in food sciences [24], biomedical sciences [25], pharmaceutical sciences [26], and different areas of material science and engineering. The lubricants commonly used nowadays often contain nanoparticles [26], microparticles [27], or polymers [28] dispersed in a continuous phase. These lubricants often generate more complex frictional behavior than simple, Newtonian fluids. For particulate lubricants, the interactions between the particles, fluids and surfaces all need to be considered.

There is currently a lack of frictional laws that cover the behavior of deformable surfaces, especially when paired with non-Newtonian lubricants. What makes matters even more complicated, is that the above-mentioned parameters depend on the roughness and geometry of the surfaces, as well as the motion of the tribometer that measures the friction coefficients. In this thesis, we therefore study the frictional behavior of such soft surfaces and complex lubricants. A better understanding of soft friction and lubrication or soft tribology contributes to constructing widely applicable frictional laws that describe such soft materials. This can lead to a better interpretation of the frictional behavior of soft materials

and complex lubricants and to the design of materials with controlled friction or lubrication properties.

We first discuss the most important applications of soft tribology. Then, we describe the deviating Stribeck frictional behavior of soft materials. Lastly, we explain how we investigate soft materials in this thesis, by introducing the outline of the thesis as well as the aim.

Applications of soft tribology

Soft tribology, in this work, refers to the friction and lubrication properties of soft materials and/or semi-solid lubricants. Soft, in this context, refers to low stiffness. Our soft materials have elastic moduli between the kilopascal (kPa) and the lower megapascal (MPa) range. These surfaces are used to measure the frictional properties when combined with a wide range of lubricants. The results obtained can be used to better understand friction in a large number of real-life applications.

Soft surfaces

As surfaces in our tribological studies, we use polydimethylsiloxane (PDMS). Elastomers are viscoelastic polymer-based materials. PDMS is the material of choice in various applications including microfluidic channels, [29, 30] and medical devices [31] as the material is transparent, biocompatible [32] and available at low costs (around US\$ 100 per kilo). In frictional studies, PDMS is used to mimic biological tissue such as skin, cartilage, or the tongue.[18, 33] The advantage of using PDMS for these tribological measurements is that the stiffness or deformability can be tailored to those of the aforementioned body parts. Additionally, PDMS is easily molded to the shape or surface roughness of the biological material mimicked by the elastomer. PDMS surfaces have been used to assess the frictional properties of a great number of materials we encounter in daily life including foods [18, 24, 34], beverages [35, 36] and personal care products such as skin creams. [37] An advantage of using elastomers is that the surfaces are soft and measurements can be carried out under dry conditions without the surface dehydrating.

Besides elastomers, we also use hydrogels as soft materials in the work presented here. Hydrogels in contact show extremely low friction coefficients both when submerged in water and even when measurements are carried out in air. [22, 38, 39] A limited understanding of the exact frictional mechanism behind the low

friction of hydrogels currently exists. Hydrogels are composed of a chemically or physically cross-linked polymer network, that is able to hold large amounts of water. As a result, hydrogels have properties of both a solid and a liquid. Measurements involving hydrogels need to be carried out in a wet or humid environment as the material may dehydrate. Hydrogels have recently been the subject of various soft tribological studies. Hydrogel components can be of biological origins such as gelatin (animal skin or bone), agar (algae), or whey (cow milk). It is also possible to synthetically produce polymers that can form a network resulting in a hydrogel. Hydrogels find applications as food components [40, 41], pharmaceuticals systems [42, 43], and medical implants. [44, 45] Many of these applications require a specific degree of friction. For example, the processing of food in the mouth and the motion of artificial joints; in both of these cases the surfaces need to move frequently with limited resistance. As the food and biomedical industries are both billion dollar industries that heavily impact our daily lives, the frictional mechanisms behind hydrogel friction is currently of interest.

Solid surfaces

In our frictional studies, we often pair soft surfaces with solid surfaces. This represents situations where the soft surface is in contact with a harder surface such as the soft tongue and the relatively hard palate. Here, we use glass and stainless steel as solid surfaces. Combining solid surfaces with soft surfaces allows us to study a situation where one surface deforms while the other surface remains in its original form. Solid surfaces are, however, more difficult to mold and less representative of the biological surfaces often represented in this thesis. By combining soft and solid surfaces the work presented here is intended to generate new insights into the frictional behaviour when surface of particle deformation plays a role.

Complex lubricants

As previously mentioned, the frictional behavior of Newtonian fluids is generally well captured by traditional frictional laws. For these fluids, mainly the viscosity and the wettability drive the fluid entrainment and ultimately the friction coefficient. Newtonian lubrication thus mostly depends on the fluid – surface interactions. Better fluid – surface interactions in terms of wettability cause a decrease in the friction coefficients and a thick, viscous layer separating the surfaces has a positive effect on the friction coefficient as well. The lubricants we study in this thesis, often deviate from Newtonian fluids in many ways. We use particulate systems with dry particles or particles suspended in a fluid. For these systems, we vary the size, stiffness, number of particles and the properties of the fluid matrix. Particulate

lubricants are often found in foods (e.g. cocoa particles in chocolate, [46] oil droplets in mayonnaise [47]) personal care products such as skin creams, [48] and in drug delivery systems. [49] While fluids are often easily entrained, particle entrainment may require a degree of surface or particle deformation due to the limited size of the gap. Once entrained, particles can separate the surfaces and roll to facilitate sliding. This is often referred to as the ball-bearing mechanism. [50, 51] An additional lubricant type we consider are polymers. These polymers can be present in solution as a lubricant or they can be anchored on a (hydrogel) surface where they often form a brush-like lubricating layer. [39, 52] Polymers are efficient lubricants owing to their ability to hold large amounts of water and polymers can slide alongside one another with limited resistance. [22] This often leads to extremely low friction coefficients. [21, 38, 53] The complex particle and polymer lubricants we use here are expected to show different regimes than the traditional Stribeck regimes for Newtonian fluids, especially when combined with soft surfaces. The surface and lubricant materials we investigate here, are important to science, industry, and society. A thorough mechanistic understanding of their frictional behavior is thus essential. In the following sections, we will discuss how we measure the lubrication curves of elastomer and hydrogel materials paired with complex lubricants.

Tribological devices

In many areas where tribology is used, different type of tribometers are used. Probing the friction of an ice skate on ice [5] naturally requires different materials and surface motions than studying materials for hip replacements. [54] As different applications require different measuring methodologies, various tribological devices have been designed in the past century. The way in which the friction coefficient is measured (e.g. rolling surfaces or sliding surfaces) greatly impacts the friction coefficient and the underlying mechanisms. [18, 55] We acknowledge this complexity and, therefore, include results obtained on different tribological devices in this thesis. The tribometers we use differ in their sliding/rolling motion, as well as the available speed range. The four tribometers are the Anton Paar Tribocell (APT), the Bruker Universal Mechanical Tester TriboLab (BTL), the PCS Mini Traction Machine (MTM), and a custom-made 3D-printed tribotool (CTT). The tribological devices are displayed in Figure 1.4 and they will be described more extensively in the relevant chapters.

Anton Paar Tribocell

The APT is a tribology measuring cell mounted on an Anton Paar modular compact rheometer (MCR). This ball-on-three-pins tribometer (Figure 1.4a) consists of a holder for a spherical probe attached to the rheometer axle. The surfaces (commercially) available for this tribometer are made of glass, steel, and PDMS.

Bruker TriboLab

The BTL (Figure 1.4b) tribometer operates using a sliding reciprocating linear drive. In the BTL the probe remains in one place, while the substrate slides in an oscillating manner. The surfaces used in this tribometer are primarily glass and PDMS surfaces.

PCS Instruments MTM

The MTM (located at the University of Queensland, Australia), is known as a rolling/sliding tribometer. This device has a rotating spherical probe and a rotating disk-shaped substrate (Figure 1.4c). These surfaces can rotate simultaneously in the same or opposite directions. Alternatively, one of the surfaces can be fixed in one position while the opposing surface rotates. The ratio between the motion of the surfaces with respect to the average speed is called the slide-to-roll ratio (SRR). On this tribometer, we use PDMS, glass, and steel surfaces.

Custom-made Tribotool

The CTT is a 3D-printed set-up that was designed and fabricated in house. The tribometer consists of an arm that can hold a probe and a container, in which a substrate can be placed (Figure 1.4d). We attach the arm to a rheometer axle and make use of the force sensors and rotational and vertical moving parts of the (Anton Paar MCR) rheometer. This tribometer was especially designed to measure hydrogel surfaces but we also use the tribometer to measure the friction coefficients of PDMS and glass surfaces.

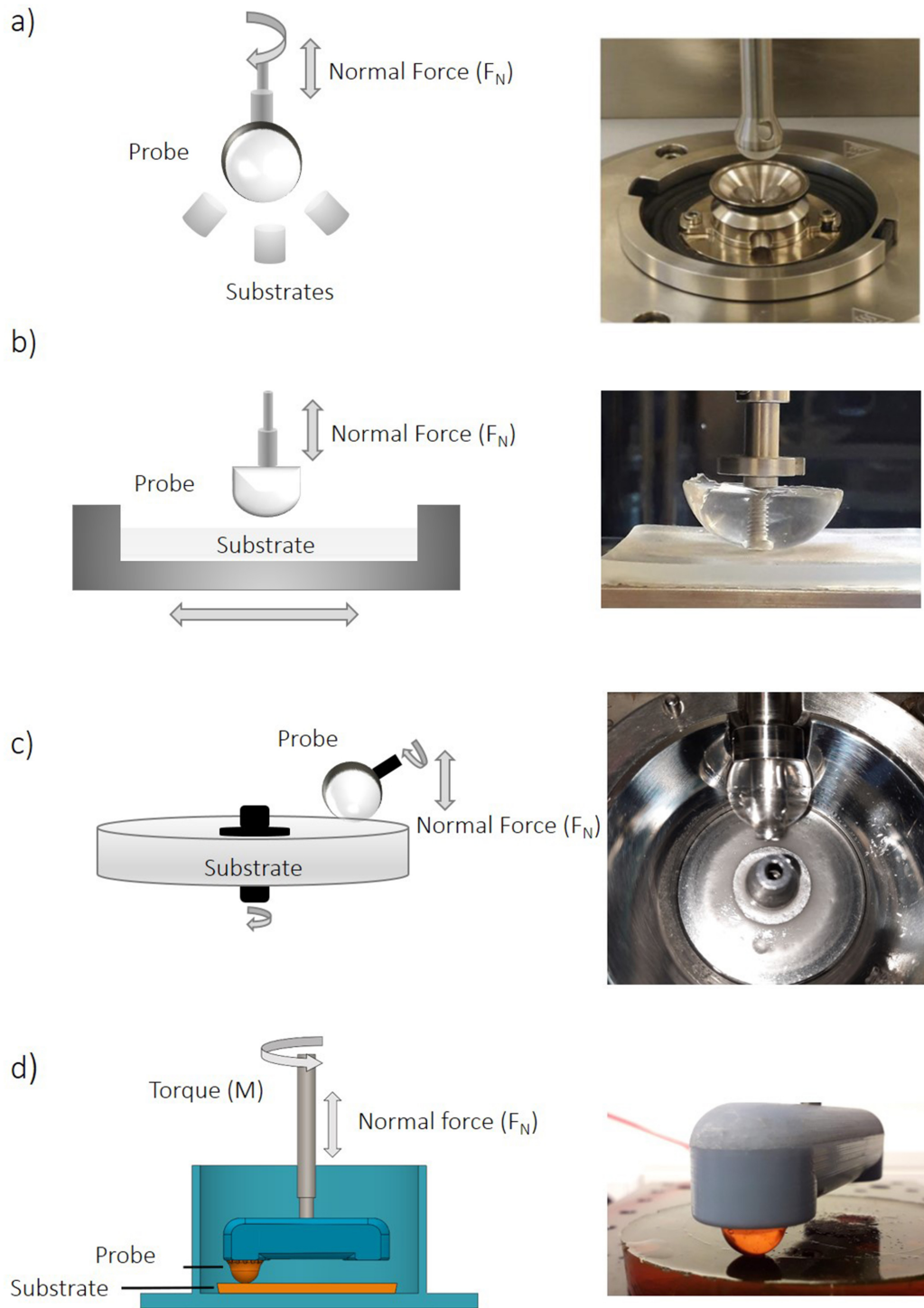


Figure 1.4: Schematic representations and photographs of the tribometers used in this thesis. a) Anton Paar Tribocell (APT), b) Bruker UMT TriboLab (BTL), c) PCS instruments Mini Traction Machine (MTM), d) Custom-made 3D-printed Tribotool (CTT).

Ahead of the Stribeck Curve

Now that we have introduced the concept of tribology in a soft material context, we proceed to have a more in-depth look at the frictional behavior of soft materials compared to that of solid materials. Lubrication behavior is often assessed through the Stribeck curve. As previously mentioned, a Stribeck curve for Newtonian fluids shows three regimes: boundary regime, mixed regime, and (elasto)hydrodynamic regime (Figure 1.5).

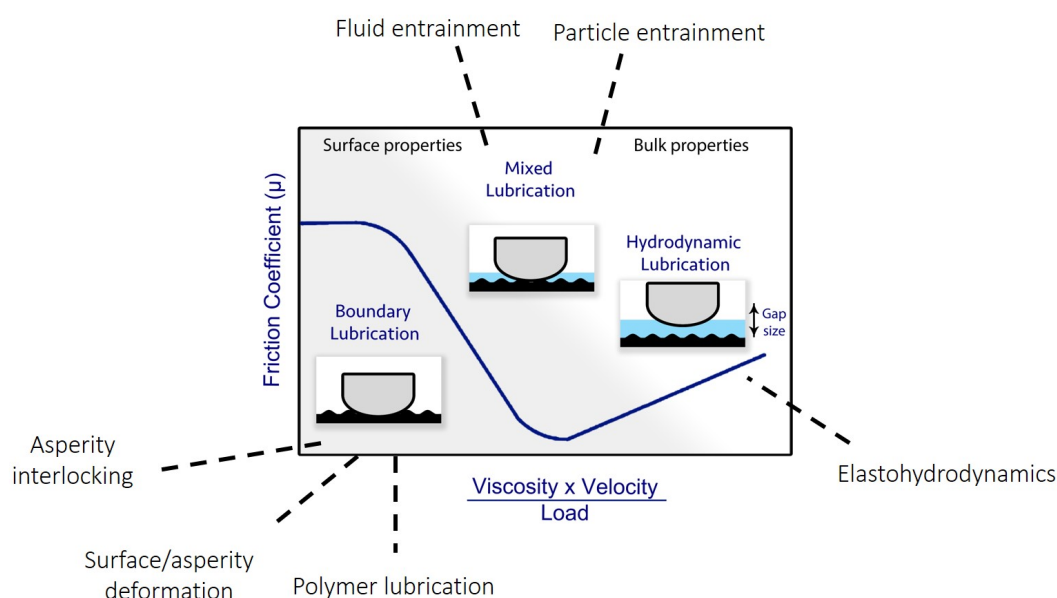


Figure 1.5: A Stribeck curve with the potential mechanisms for soft surfaces and complex lubricants. These mechanisms are shown in the most relevant Stribeck regimes. The different parameters indicate which factors can influence the frictional behavior to deviate from the traditional Stribeck curve.

Soft surfaces and non-Newtonian lubricants show complex frictional behavior that differs strongly from classical frictional laws. It is therefore challenging to predict and interpret the behavior of these materials. The soft surfaces deform once in sliding contact. These deformations change the contact area and the indentation depth as described by classical contact mechanical theories. [56] If surfaces are rough, the deformation of the asperities can contribute to the overall friction coefficient as well. Additionally, asperities of similar sizes on opposing surfaces may become interlocked with one another, restricting the forward motion of the probe. [23, 57, 58]

The friction coefficient is also influenced by semi-solid and fluid lubricant components entering the gap at different sliding velocities. [59] Once the lubricant is entrained, a lubricating layer is formed. When soft surfaces are used, in the hydrodynamic regime, the thick fluid film can cause the soft surface to elastically

deform. This is why the hydrodynamic regime for soft surfaces is often called the elastohydrodynamic or EHL regime. [60] When polymeric surfaces or lubricants are used, a polymer layer may also contribute to the overall friction coefficient. [18, 20, 21]

The Stribeck curve is thus of limited use when soft surfaces and complex lubricants are investigated. A need, therefore, exists for new frictional theories that relate surface deformation, polymer fluctuations, particle entrainment, and other mechanisms behind soft tribology. In Figure 1.5, several soft tribological mechanisms are shown and we relate this to boundary contact, mixed contact and (elasto)hydrodynamic surface separation.

Aim and Outline

In this thesis, the friction coefficients of soft substrates combined with various types of lubricants are measured on different tribometers. This contributes to the overall aim of this thesis: to uncover the key frictional mechanisms behind tribosystems with soft surfaces and complex lubricants. We measure the friction coefficient of surfaces that differ in stiffness (Young's modulus), surface roughness, and material type. The lubricants range from Newtonian fluids to (soft) particle suspensions and biopolymer solutions. We also investigate the relation between the friction coefficient and the tribometer motion by using four tribometers that have a rotating or linear sliding motion. To obtain a broad overview of soft lubrication, we thus measure parameters across various length scales.

The results are presented in eight experimental chapters which are divided into three sections. These sections are related to the surface or lubricant materials used and the most important frictional mechanisms observed. The sections of this thesis are:

- (I) Hydrogel - hydrogel friction
- (II) Particle lubrication
- (III) Tribological applications

After presenting the experimental chapters, we discuss our main findings, conclusions, and our outlook in the general discussion. We will proceed to briefly introduce the relevance, content, and approach of each section.

(I) Hydrogel - hydrogel friction

As hydrogel surfaces easily deform, the elastic deformation and interlocking of asperities are anticipated to contribute to the friction coefficient. In this section, we investigate the effect of the polymer network, hydrogel deformability, and hydrogel surface roughness to better understand the interplay between the different length scales (e.g. polymer interactions, nm scale) and surface deformations (μm scale) on hydrogel friction.

In **Chapter 2**, we use hydrogels composed of different polymeric constituents. This will allow us to gain insight into how the surface roughness and the material stiffness influence the friction coefficient. Hydrogel surfaces are easily molded, as they are initially fluid and solidify at specific conditions (temperature, pH, cross-linking density, etc). We take advantage of this molding ability and cast hydrogels in molds with different degrees of roughness. Using these artificially rough surfaces, we aim to gain knowledge on hydrogel friction by considering both polymer interactions as well as asperity interactions. We also use molded hydrogels in **Chapter 3** and vary the asperity geometry (height, diameter, distance between the pillars) while keeping the same type of polymer network. This allows us to focus on the effect of μm -mm sized asperities.

(II) Particle lubrication

We assess the lubrication behavior of particulate lubricants in section II. Rolling, load-bearing particles decrease the friction coefficient by means of a ball-bearing mechanism. In **Chapter 4** we use hydrogel microparticles. The size, hardness, and volume fraction of the particles are varied. As the particles are soft while the surfaces are relatively hard, this will cause particle deformation and deformed particles are less able to roll or separate the surfaces. We investigate these effects on the frictional behavior of soft particles present between hard surfaces.

In **Chapter 5**, we consider the inversed case: hard microparticles between soft surfaces. In this case, the particles remain spherical while the elastomeric surfaces deform around the particles. This surface deformation leads to enhanced contact between the surfaces and between the particles. We manipulate the distance between the surfaces by changing particle properties including particle size, number of particles, and the normal force during measurement. When we use microparticles suspended in a fluid matrix, the interactions between the fluid and the particles and the particles and the fluid need to be considered as well.

We study the effects of these aspects in **Chapter 6** by varying the properties of the fluid matrix and the properties of the particles. The specific conditions under which the different components of the lubricant enter the gap and what mechanisms are behind this entrainment are discussed in this chapter.

(III) Tribological applications

In section III, we put the scientific knowledge on soft tribology in an applied context. In **Chapter 7**, we study frictional events between human saliva and food components. The most important molecules involved in food consumption are the salivary proteins mucins and proline-rich proteins (PRPs). These salivary proteins provide a good lubricating layer on the oral surfaces. [61, 62] These salivary proteins are combined with with astringent solutions. This emulates what happens in the mouth, for example when drinking wine and tea or when eating nuts or plant leaves. This can lead to an astringent mouthfeel. We use the frictional behavior to gain insights into whether these mouthfeel characteristics are purely receptor-response based [63] or also frictional response based. [64, 65]

Many tribological studies are designed to mimic realistic situations such as sliding joints or the tongue moving against the palate. This often requires specific tribological sliding or rotating motions. We display the effect of different sliding motions on the friction coefficient in **Chapter 8**. In this chapter, we use Newtonian fluids and particle suspensions as lubricants and we vary different aspects of the tribometer set-up. The variables in this study are the sliding surfaces which are smooth or rough. We also use four different tribometers to investigate the impact of tribometer motion on the lubrication behavior, even when the same surfaces and lubricants are used. We thus study tribological mechanisms on different length scales using various lubricants, surfaces, and tribometers. A schematic overview of the sections and chapters presented in this thesis is shown in Figure 1.6 on the following page.

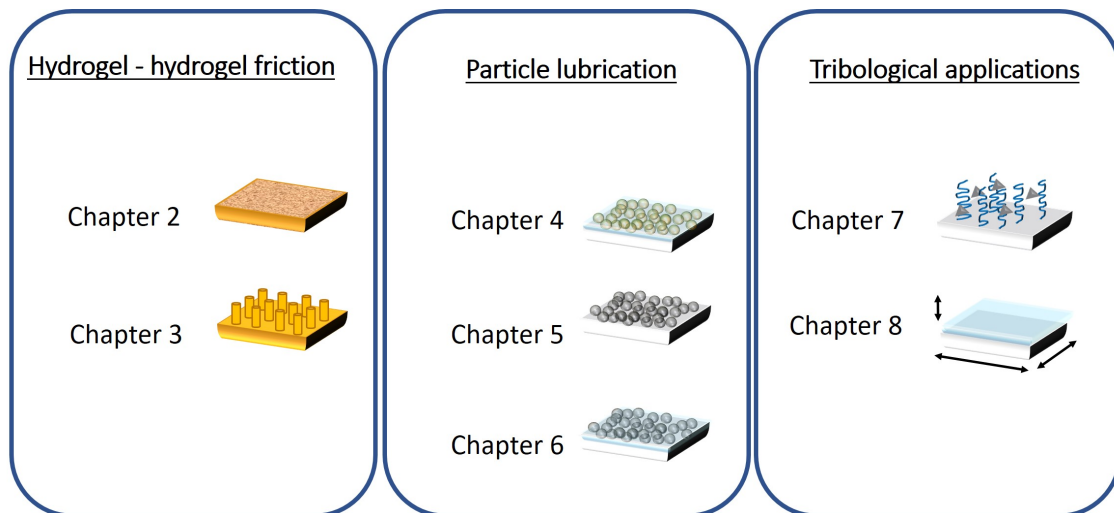


Figure 1.6: An overview of the chapters in this thesis as subdivided into three sections: Hydrogel - hydrogel friction, particle lubrication and tribological applications.

References

1. Hawking, S. *A brief history of time: from big bang to black holes* (2009).
2. Longair, M. S. Unveiling the distant universe. *Astronomy & Geophysics* vol. 39, 2–10 (1998).
3. Krim, J. Friction at the atomic scale. *Scientific American* vol. 275, 74–80 (1996).
4. Sorensen, A. C., Claud, E. & Soressi, M. Neandertal fire-making technology inferred from microwear analysis. *Scientific reports* vol. 8, 1–16 (2018).
5. Liefferink, R., Weber, B. & Bonn, D. Ploughing friction on wet and dry sand. *Physical Review E* vol. 98, 052903 (2018).
6. Rosa, D. Cash Flow. *Uncle Scrooge* vol. 224 (1987).
7. Pitenis, A. A., Dowson, D. & Sawyer, W. G. Leonardo da Vinci's friction experiments: An old story acknowledged and repeated. *Tribology Letters* vol. 56, 509–515 (2014).
8. Popova, E. & Popov, V. L. The research works of Coulomb and Amontons and generalized laws of friction. *Friction* vol. 3, 183–190 (2015).
9. Desplanques, Y. Amontons-coulomb friction laws, A review of the original manuscript. *SAE International Journal of Materials and Manufacturing* vol. 8, 98–103 (2015).
10. Kietzig, A.-M., Hatzikiriakos, S. G. & Englezos, P. Physics of ice friction. *Journal of Applied Physics* vol. 107, 4 (2010).
11. Canale, L. *et al.* Nanorheology of interfacial water during ice gliding. *Physical Review X* vol. 9, 041025 (2019).
12. Persson, B. N. On the theory of rubber friction. *Surface science* vol. 401, 445–454 (1998).
13. Persson, B. Rubber friction and tire dynamics. *Journal of Physics: Condensed Matter* vol. 23, 015003 (2010).
14. Lu, X., Khonsari, M. & Gelinck, E. The Stribeck curve: experimental results and theoretical prediction (2006).
15. Bongaerts, J., Fourtouni, K. & Stokes, J. Soft-tribology: lubrication in a compliant PDMS–PDMS contact. *Tribology International* vol. 40, 1531–1542 (2007).
16. Jacobson, B. The Stribeck memorial lecture. *Tribology International* vol. 36, 781–789 (2003).
17. Stribeck, R. Die wesentlichen eigenschaften der gleit-und rollenlager. *Zeitschrift des Vereines Deutscher Ingenieure* vol. 46, 1341–1348 (1902).
18. Rudge, R. E. D., Scholten, E. & Dijkman, J. A. Advances and challenges in soft tribology with applications to foods. *Current Opinion in Food Science* vol. 27, 90–97 (2019).
19. Khonsari, M. M. & Booser, E. R. On the Stribeck curve. *Recent Developments in Wear Prevention, Friction and Lubrication*, 263–278 (2010).
20. Nguyen, P. T., Kravchuk, O., Bhandari, B. & Prakash, S. Effect of different hydrocolloids on texture, rheology, tribology and sensory perception of texture and mouthfeel of low-fat pot-set yoghurt. *Food Hydrocolloids* vol. 72, 90–104 (2017).
21. Pitenis, A. *et al.* Polymer fluctuation lubrication in hydrogel gemini interfaces. *Soft Matter* vol. 10, 8955–8962 (2014).
22. Gong, J. P. Friction and lubrication of hydrogels—its richness and complexity. *Soft Matter* vol. 2, 544–552 (2006).

23. Yu, J. *et al.* Friction and adhesion of gecko-inspired PDMS flaps on rough surfaces. *Langmuir* vol. 28, 11527–11534 (2012).
24. Shewan, H. M., Pradal, C. & Stokes, J. R. Tribology and its growing use toward the study of food oral processing and sensory perception. *Journal of Texture Studies* vol. 51, 7–22 (2020).
25. Walker, P. & Gold, B. The tribology (friction, lubrication and wear) of all-metal artificial hip joints. *Wear* vol. 17, 285–299 (1971).
26. Bolzinger, M.-A., Briancon, S. & Chevalier, Y. Nanoparticles through the skin: managing conflicting results of inorganic and organic particles in cosmetics and pharmaceuticals. *Wiley Interdisciplinary Reviews: Nanomedicine and Nanobiotechnology* vol. 3, 463–478 (2011).
27. Shewan, H. M. *et al.* Interpreting Rheological Behaviour of Sugar-Fat Mixtures as a Function of Solids Phase Volume. *Journal of Food Engineering* vol. 297, 110474 (2021).
28. Authimoolam, S. P. & Dziubla, T. D. Biopolymeric mucin and synthetic polymer analogs: their structure, function and role in biomedical applications. *Polymers* vol. 8, 71 (2016).
29. Workamp, M., Saggiomo, V. & Dijkman, J. A. A simple low pressure drop suspension-based microfluidic mixer. *Journal of Micromechanics and Microengineering* vol. 25, 094003 (2015).
30. Skurtys, O. & Aguilera, J. Applications of microfluidic devices in food engineering. *Food Biophysics* vol. 3, 1–15 (2008).
31. Yabuta, T. *et al.* Synthesis of PDMS-based porous materials for biomedical applications. *Journal of Sol-gel Science and Technology* vol. 26, 1219–1222 (2003).
32. Mata, A., Fleischman, A. J. & Roy, S. Characterization of polydimethylsiloxane (PDMS) properties for biomedical micro/nanosystems. *Biomedical Microdevices* vol. 7, 281–293 (2005).
33. Morales-Hurtado, M., Zeng, X., Gonzalez-Rodriguez, P., Ten Elshof, J. E. & van der Heide, E. A new water absorbable mechanical Epidermal skin equivalent: The combination of hydrophobic PDMS and hydrophilic PVA hydrogel. *Journal of the mechanical behavior of biomedical materials* vol. 46, 305–317 (2015).
34. Fuhrmann, P. L., Aguayo-Mendoza, M., Jansen, B., Stieger, M. & Scholten, E. Characterisation of friction behaviour of intact soft solid foods and food boli. *Food Hydrocolloids* vol. 100, 105441 (2020).
35. Wang, S., Mantilla, S. M. O., Smith, P. A., Stokes, J. R. & Smyth, H. E. Astringency sub-qualities drying and pucker are driven by tannin and pH—Insights from sensory and tribology of a model wine system. *Food Hydrocolloids* vol. 109, 106109 (2020).
36. Laguna, L., Farrell, G., Bryant, M., Morina, A. & Sarkar, A. Relating rheology and tribology of commercial dairy colloids to sensory perception. *Food & function* vol. 8, 563–573 (2017).
37. Timm, K., Myant, C., Nuguid, H., Spikes, H. & Grunze, M. Investigation of friction and perceived skin feel after application of suspensions of various cosmetic powders. *International journal of cosmetic science* vol. 34, 458–465 (2012).
38. Urueña, J. M. *et al.* Mesh size control of polymer fluctuation lubrication in gemini hydrogels. *Biotribology* vol. 1, 24–29 (2015).
39. Simič, R., Yetkin, M., Zhang, K. & Spencer, N. D. Importance of hydration and surface structure for friction of acrylamide hydrogels. *Tribology Letters* vol. 68, 64 (2020).

40. Shewan, H. M. & Stokes, J. R. Review of techniques to manufacture micro-hydrogel particles for the food industry and their applications. *Journal of Food Engineering* vol. 119, 781–792 (2013).
41. Wu, B.-C. & McClements, D. J. in *Microencapsulation and Microspheres for Food Applications* 131–149 (Elsevier, 2015).
42. Li, J. & Mooney, D. J. Designing hydrogels for controlled drug delivery. *Nature Reviews Materials* vol. 1, 16071 (2016).
43. Hoare, T. R. & Kohane, D. S. Hydrogels in drug delivery: Progress and challenges. *Polymer* vol. 49, 1993–2007 (2008).
44. Seliktar, D. Designing cell-compatible hydrogels for biomedical applications. *Science* vol. 336, 1124–1128 (2012).
45. Hafezi, M., Qin, L., Mahmoodi, P., Yang, H. & Dong, G. Releasable agarose-hyaluronan hydrogel with anti-friction performance and enhanced stability for artificial joint applications. *Tribology International* vol. 153, 106622 (2021).
46. Masen, M. & Cann, P. Friction measurements with molten chocolate. *Tribology Letters* vol. 66, 24 (2018).
47. De Wijk, R. A. & Prinz, J. F. Fatty versus creamy sensations for custard desserts, white sauces, and mayonnaises. *Food Quality and Preference* vol. 18, 641–650 (2007).
48. Singh, P. & Nanda, A. Enhanced sun protection of nano-sized metal oxide particles over conventional metal oxide particles: An in vitro comparative study. *International journal of cosmetic science* vol. 36, 273–283 (2014).
49. Popova, T. *et al.* Mesoporous silica MCM-41 and HMS as advanced drug delivery carriers for bicalutamide. *Journal of Drug Delivery Science and Technology*, 102340.
50. Liu, K., Tian, Y., Stieger, M., van der Linden, E. & van de Velde, F. Evidence for ball-bearing mechanism of microparticulated whey protein as fat replacer in liquid and semi-solid multi-component model foods. *Food Hydrocolloids* vol. 52, 403–414 (2016).
51. Jones, A. Ball motion and sliding friction in ball bearings. *Journal of Basic Engineering* vol. 81, 1–12 (1959).
52. Meier, Y. A., Zhang, K., Spencer, N. D. & Simic, R. Linking Friction and Surface Properties of Hydrogels Molded Against Materials of Different Surface Energies. *Langmuir* vol. 35, 15805–15812 (2019).
53. Gong, J. P. *et al.* Synthesis of hydrogels with extremely low surface friction. *Journal of the American Chemical Society* vol. 123, 5582–5583 (2001).
54. Nečas, D. *et al.* Running-in friction of hip joint replacements can be significantly reduced: The effect of surface-textured acetabular cup. *Friction*, 1–16 (2020).
55. Campbell, C. L., Foegeding, E. A. & van de Velde, F. A Comparison of the lubrication behavior of whey protein model foods using tribology in linear and elliptical movement. *Journal of texture studies* vol. 48, 335–341 (2017).
56. Urueña, J. M. *et al.* Normal load scaling of friction in gemini hydrogels. *Biotribology* vol. 13, 30–35 (2018).
57. Archard, J. Surface topography and tribology. *Tribology* vol. 7, 213–220 (1974).

58. Bhushan, B. Contact mechanics of rough surfaces in tribology: multiple asperity contact. *Tribology letters* vol. 4, 1–35 (1998).
59. Yakubov, G., Branfield, T., Bongaerts, J. & Stokes, J. Tribology of particle suspensions in rolling-sliding soft contacts. *Biotribology* vol. 3, 1–10 (2015).
60. Johnson, K. Regimes of elastohydrodynamic lubrication. *Journal of Mechanical Engineering Science* vol. 12, 9–16 (1970).
61. Bongaerts, J., Rossetti, D. & Stokes, J. The lubricating properties of human whole saliva. *Tribology Letters* vol. 27, 277–287 (2007).
62. Mystkowska, J. *et al.* Artificial mucin-based saliva preparations—Physicochemical and tribological properties. *Oral Health Prev. Dent* vol. 16, 183–193 (2018).
63. Schöbel, N. *et al.* Astringency is a trigeminal sensation that involves the activation of G protein–coupled signaling by phenolic compounds. *Chemical Senses* vol. 39, 471–487 (2014).
64. Upadhyay, R., Brossard, N. & Chen, J. Mechanisms underlying astringency: introduction to an oral tribology approach. *Journal of Physics D: Applied Physics* vol. 49, 104003 (2016).
65. Ma, S., Lee, H., Liang, Y. & Zhou, F. Astringent mouthfeel as a consequence of lubrication failure. *Angewandte Chemie* vol. 128, 5887–5891 (2016).

PART I

Hydrogel - hydrogel friction



2

**Soft surface roughness
determines frictional
regimes in hydrogel pairs**

Abstract

Hydrogels display extremely complex frictional behavior with surprisingly slippery surfaces. We measured the sliding behavior of hydrogels submerged in water using a custom-made tribotool. Samples with a degree of surface roughness, gave two distinct frictional regimes. Friction coefficients in the first regime change with asperity sizes and Young's moduli. Under increased normal force, a second frictional regime emerges likely due to smoothening of asperities. Friction coefficients in the second regime remain constant across length scales of roughness and appear to be material specific. The hydrogel polymer network also directly influences the surface topography, and with that, the frictional behavior of hydrogels. We highlight the tribological importance of surface roughness at different length scales, which provides the potential to engineer functional frictional behavior.

This chapter was published as:

Rudge, R.E.D., Scholten, E., and Dijkman, J. A. (2019). Natural and induced roughness determine frictional regimes in hydrogel pairs. *Tribology International* vol. 141, 105903.

Introduction

Hydrogels are chemically or physically cross-linked water-absorbing networks of polymers. The material can be easily modified and thus applied in many contexts such as bio-inspired applications [1–4] and novel food systems [5–7], as their network formation is sensitive to easily accessible tuning parameters such as polymer type, polymer concentration, pH, and temperature. The large range of tunable material properties including porosity, hardness, and water holding ability make hydrogels a material of choice for many applications. One significant feature of hydrogels is that they can be very slippery [8–10]. Despite this promise, there is a general lack of fundamental understanding of the interfacial dynamics during sliding, specifically of hydrogels and soft materials in general [11–13], even against ideally flat substrates [14–16]. The variety of potential applications makes understanding the emergence of friction between two hydrogel surfaces of pressing interest. More broadly, to illuminate the origin of the complex frictional behavior displayed by soft and porous solids, hydrogels are very suitable candidates to test various tribological hypotheses. This is thanks to their material properties, including strength, porosity, elasticity, and surface roughness which can be easily monitored and adapted.

Simple dry sliding friction between two non-porous solid materials is usually well described by Amontons-Coulombs' laws of friction. [17] The implied proportionality of the friction force, F_F and the load, W does not always hold and appears not sufficient to capture the frictional behavior of more complex systems, including lubricated friction between two soft solids. Mechanisms observed in hydrogel friction include attraction and repulsion between interacting surfaces, non-uniform fluid film formations, and normal force dependencies. [12, 18, 19] Using hydrogels and glass substrates with varying degrees of roughness, clear differences in frictional behavior have been found for smooth and rough solid surfaces as smooth surfaces gave lower friction coefficients. [20] Previous work has also shown that material friction depends also on the Young's modulus of the material. [21] Friction between soft materials is thus dependent on (bulk) contact mechanics at the hydrogel interface but also depends on direct interactions between the two surfaces. [22, 23] It is not intuitive how to apply or modify the framework used to describe dry solids to hydrogels: first, the materials are porous deformable solids that consist mainly of water, a lubricating fluid that could be expelled under applied loads. Second, hydrogels are soft solids and under high normal loads will thus deform substantially. [24, 25] This, in turn, affects the shape of the contacting surfaces and with that, the contact area and pressure. [14, 19]

Additional dissipation mechanisms such as water release or even hydrogel network rearrangements or breakdown may then arise, which can add to the effective friction coefficient. In light of all the possible dissipation mechanisms that can occur, the robustness of low frictional sliding of hydrogels may seem especially surprising. Nevertheless, the slipperiness of hydrogels has been observed when paired with different materials from glass to textile. [20, 26–28] The low friction dynamics remain when friction between two hydrogels in so-called “Gemini” contacts are studied. [18, 19, 29] One may naively think that Gemini contacts are relatively simple systems, yet also here friction depends on bulk and interface characteristics. For example, increasing the hydrogel mesh size by increasing the polymer concentrations [29] leads to lower friction. With this same Gemini system, normal force dependence was observed: a decrease in friction coefficient was found with an increasing normal force, which scaled with $\mu \propto F_N^{-1/3}$. [19] In a different study with two cellulose hydrogel disks in contact, it was found that a fluid trap is created in the center of the hydrogel-hydrogel contact. As such, the lubricating fluids present strongly influenced the contact area and the frictional behavior of the hydrogels in contact. [18]

Among the complexity in the frictional dynamics in soft hydrogel contacts, we find that roughness is a surprisingly simple, yet dominant contributor to friction on soft hydrogel substrates across length scales. We measure friction dynamics between two fully submerged, water-lubricated hydrogels in a custom-3D-printed tribology set-up. The ability to tune surface roughness enables us to show that surface roughness is responsible for a normal force dependence of μ . Specifically, the creation of two distinct frictional regimes and their respective friction coefficients are associated with rougher substrates, even with two highly elastic surfaces. We use molding techniques and a variety of polymer properties to create hydrogels with different roughness, ranging from extremely smooth to randomly rough. We use the natural surface structure of seemingly “flat” substrates to extend the range of surface structures we can probe to length-scales ranging from micrometers to millimeters. Via 3D-printed patterned molds, we create regular surface patterns, and we exploit the tunability of hydrogels to investigate the role of the Young’s modulus. For all substrates explored, we find that surface roughness enhances friction but only up to a certain level of normal forces, which we hypothesize to indicate the maximum load needed for asperity flattening. Consistent with this picture is that for samples that naturally have no micro-asperities, we find the typical ultra-low friction dynamics and no normal force dependence. Our results indicate that surface roughness can be relevant for materials that may appear to be flat and provides a route towards the rational control over frictional dynamics.

Experimental section

Samples of 10, 15, and 20 wt% gelatin were made by slowly adding gelatin powder (gelatin from porcine skin, Type A, Sigma-Aldrich) to water at room temperature. The mixture was stirred vigorously, heated to 60° C, and left to stir for at least 30 minutes until a clear solution was obtained. Agar powder (Agar-Agar, Caldic ingredients) and water were mixed at room temperature and subsequently microwaved for approximately 30 seconds to obtain a clear 3 wt% agar solution. Polyacrylamide (PAAm) polymer solutions were made by mixing 20 wt% of acrylamide (Sigma-Aldrich) with 1 wt% N,N'-methylenebis(acrylamide) (Sigma-Aldrich), in water and slowly heating the mixture while stirring, allowing the powders to fully dissolve. The polyacrylamide mixture was then cooled down to room temperature, after which 0.05 wt% of the initiator, ammonium persulfate (Bio-Rad) was added. Then, 0.05 wt% of cross-linker N,N,N',N'-tetramethylethylenediamine (TEMED, Sigma-Aldrich) was added to the aqueous mixture for chemical cross-links to form upon gelation. The gelatin, agar, and PAAm hydrogel solutions were then used to prepare hydrogel probes and substrates used as tribopairs.

Hydrogel tribopair preparation

The (bio)polymer solutions were poured into a Petri dish with an inner diameter of 86 mm to obtain flat hydrogel substrates. Sample height was approximately 1.5 mm, similar to that of the Petri dish. For the hemispherical probe, a custom-made silicone rubber mold was used (Moldstar TM 20 T, Smooth-On, Inc). After the molds were filled with the hydrogel solutions, samples were left overnight to allow the gelation process to complete. The samples remained on a level tabletop at room temperature during the first stages of hardening to ensure a smooth and evenly flat surface. To chemically cross-link gelatin hydrogels, hardened samples were submerged in a 5 wt% glutaraldehyde solution (Sigma Aldrich). The cross-linking process was assumed to be completed when the near-colorless sample changed into a uniformly brownish-orange hydrogel. Residual glutaraldehyde was removed by first rinsing the hydrogels with water and then immersing the samples overnight in a container with a large amount of water which was placed on a mechanical shaker. Coated abrasives were used to create irregularities on the surface of the hydrogel disks. Grit labels of the sandpapers used were P2500 (Starcke USA), P400, P180, P120, and P80 (3M), representing an average particle diameter of 8.4, 35, 82, 125, and 201 μm respectively. The particles on a sandpaper surface can however vary greatly in diameter, height, shape, and distribution on the surface. Negative molds of the sandpaper were made using Moldstar TM 20 T (Smooth-On, Inc). The gelatin

solution was poured onto the molds and gel formation was allowed. The hydrogels were subsequently cross-linked with glutaraldehyde as described previously. After solidification, the substrate and probe were inserted in the homemade tribotool geometry.

Stiffness of Hydrogels

The Young's modulus (E) of all hydrogels was measured using samples made in a Petri dish with a diameter of 35 mm with a height of around 7 mm. These compression tests are non-destructive, allowing the materials to elastically return to their original shape. Elastic behavior is also expected during our frictional measurements relatively low normal forces (below 1 N). Samples were compressed using a 75 mm diameter cone-plate with a 1° angle indenter on a rheometer (MCR 501, Anton Paar) at a compression rate of $50 \mu\text{m/s}$. During compression the force was measured as a function of deformation. Using the sample area and height, this was transformed into a stress-strain curve. This stress-strain curve typically displays non-linear behavior at small deformation for hydrogels in part due to natural sample height variation. [2] At a strain of approximately 5%, the obtained stress-strain curve becomes linear and the corresponding slope was used to calculate the Young's moduli of all hydrogels.

Cryogenic temperature Scanning Electron Microscopy (cryo-SEM)

The hydrogel surfaces were visualized using cryo-SEM (FEI Magellan 400). The samples were frozen by plunge freezing using liquid nitrogen to keep them in their natural *hydrated* state. Due to rapid freezing, water forms amorphous ice that does not damage the material structure like crystalline ice would. The frozen samples were fractured by striking the sample with a metal rod similar to the method reported by Kim & co-workers. [30] This allows for viewing of not only the surface but also exposes parts of the internal (bulk) structures. Distinctly different internal and surface characteristics could be distinguished for each chemically distinct sample using this technique.

X-Ray tomography (XRT)

For 3D imaging, XRT, a non-invasive imaging technique, was used to image surfaces with asperities from 50 to $400 \mu\text{m}$. A Phoenix v[tome]x m (General Electric, Germany) tomographer was used for this purpose. Hydrogel samples were cut into pieces of several mm and inserted into an Eppendorf tube. The tube was

kept closed to avoid dehydration of the hydrogel samples during measurements. Hydrogel samples were scanned over 360 ° and analyzed using Avizo software for image reconstruction and visualization post-processing.

Frictional measurements

The gel-on-gel tribotool used in our measurements (Figure 2.1) was made using a 3D printer (Stratasys Objet30, Scholar, RGD240 plastic) and is also described more extensively elsewhere. [31] The upper part of our custom-made tribotool consists of an arm (3 cm) with a cavity, for insertion of the hemispherical hydrogel probe. This component was installed on a rheometer (MCR 501, Anton Paar, Austria). The rheometer can rotate the arm and move the arm vertically. The lower component of the tribotool is a cylindrical holder for a flat, disk-shaped hydrogel substrate. The hydrogel disk was fastened in the container using a ring-shaped clamp to avoid movement of the hydrogel substrate during measurements. This container was filled with water covering both the substrate and the upper part of the arm. The hydrogel probe attached to the arm was rotated at preset angular velocities between 0.005 and 0.1 rotations per second (rps) corresponding to sliding velocities of 1 to 20 mm/s. Measurements started after the value of the normal force was reset to zero on the rheometer and the zero-gap was set as a reference distance between the probe and the substrate. The initial point of contact between the hydrogels was determined by constructing a force-distance curve. The slightest increase in normal force was taken as the first contact point. From the torque (M) measured by the rheometer we calculate the friction force as $F_F = M/R$ ($R=0.03$ m).

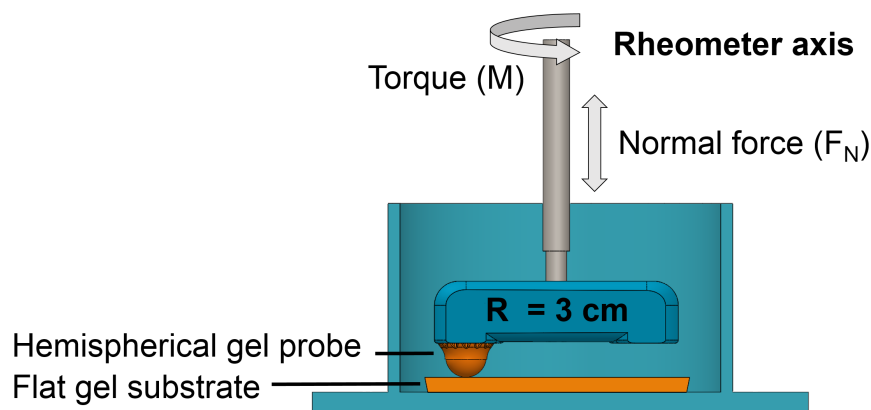


Figure 2.1: Cross-sectional illustration of the gel-on-gel tribotool. The hemispherical probe is inserted into the holder and is moved alongside the hydrogel substrate using the rheometer axis. The distance between the rheometer shaft and the center of the probe is 3 cm. The diameter of the hemispherical probe is 2 cm.

Frictional measurements were performed with alternating “rotational” and “indenting” intervals. The first measurement interval consists of the rotation of

the probe without the probe and substrate being in contact, while the probe is completely submerged in water. This measurement provides the background signal to correct for the torque needed to move the arm at a given angular velocity in the fluid inside the measuring cup. After this step, the probe is brought into contact with the substrate during the first indentation interval. During subsequent rotational intervals, the probe is rotated over the substrate at a fixed mean vertical indentation depth, leading to friction between the probe and the substrate. During rotation, a small range of normal force variations was measured at every mean indentation position, due to the naturally occurring height variation of the surface of the hydrogel substrate. After each rotational interval, the vertical position was increased and the mean normal force increased to measure friction coefficients at normal forces well below 1 N. All measurements are highly reproducible from day to day and from probe to probe. Also, no signs of wear were observed even after repeated use of hemispherical probes and substrates. These alternating rotating and indenting intervals give us a large data set of coupled normal force (F_N) and torque (M) values at a constant preset angular velocity. With these values the dimensionless friction coefficient (μ) is determined. We verify that our custom tribometer gives the expected behavior for two dry sliding contacts ($F_F = \mu F_N$). The friction between a rough glass marble (Intertoys, The Netherlands) as a probe against both a commercial-grade laser-cut acrylic glass disk and a polystyrene foam surface as substrates was measured to validate our method (Figure 2.2). For these dry solids, the friction force scales linearly with the normal force as is expected from Amontons-Coulomb frictional laws.

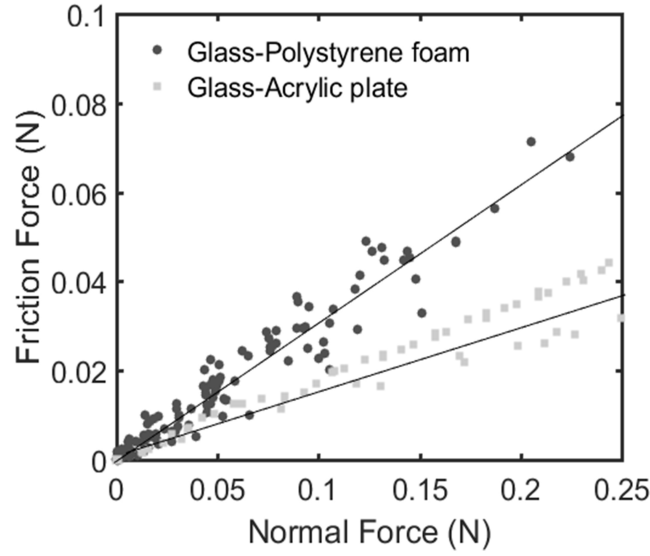


Figure 2.2: Friction force – normal force curve of friction between a glass probe and polystyrene foam and between a glass probe and acrylic glass as measured with our custom-made tribotool. We observe the expected Amontons-Coulombic behavior in this context (solid lines).

Results

We measure friction using probes and substrates made of physically cross-linked gelatin (uGel) and chemically treated irreversibly cross-linked gelatin (xGel) as shown in Figure 2.3. Chemically cross-linking the gelatin samples gives a five-fold increase of the Young's Modulus from about 0.1 MPa to 0.5 MPa. To study the effect of normal force on the friction coefficient of gelatin hydrogels we measure the friction force at increasing vertical displacements leading to normal forces up to at least 0.3 N for each sample as measured by the rheometer.

The exact indentation depth corresponding to a specific range of normal forces depending on the mechanical properties of the materials in contact. Even though substrate and probe vary in shape and thickness, them having the same modulus suggests that we can make the approximation that the deformation is equally shared among substrate and the smooth hemispherical probe (radius $r_p = 2$ cm). The deformation, δ_p , of both the substrate and the probe is then 300 μm . Hertzian contact analysis then gives the contact radius $r_c = \sqrt{r_p \delta_p}$ to be approximately 1.7 mm and thus a contact area of 9 mm^2 . We observe a decreasing slope with increasing normal force in our hydrogels submerged in water. The change in slope in Figure 2.3 indicates a drop in friction coefficient with increasing normal forces, leading to the emergence of two distinct frictional regimes. Each of the regimes has a defined friction coefficient. This behavior is not in accordance with classical

Soft surface roughness determines frictional regimes in hydrogel pairs

frictional laws as friction in dry solid materials is expected to be normal force independent. [17]

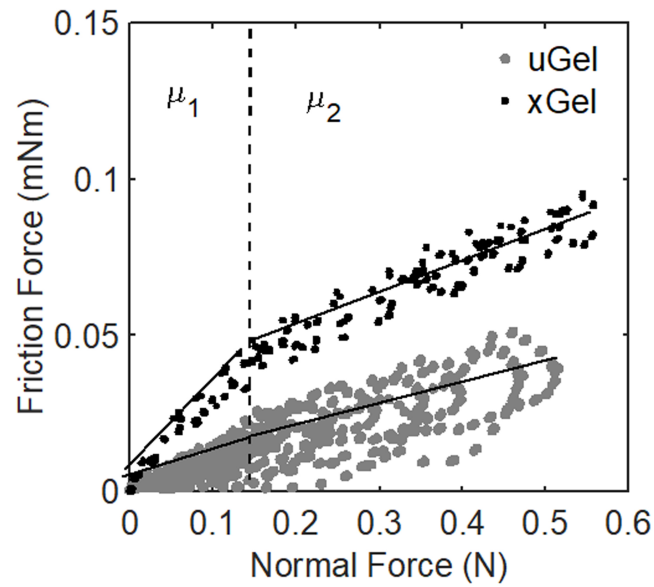


Figure 2.3: Raw friction data of untreated, physically cross-linked gelatin (uGel), chemically cross-linked gelatin (xGel) at 0.1 rps. Surfaces are patterned using sandpaper (grit size $8.4 \mu\text{m}$). The dashed line indicates the beginning of the second frictional regime.

Changes in friction coefficient with increasing loads have however been reported for soft materials including gellan, polyvinyl alcohol (PVA) and poly(2-acrylamido-2-methylpropanesulfonic acid) (PAMPS) hydrogels on glass surfaces. [8, 22, 32] More recently this has also been found for hydrogel-hydrogel contacts. [19] The uniqueness of the results is found in the clear transition from one regime to another and in the differences between the regimes. The first regime (μ_1) in Figure 2.3 predominately contains relatively low normal forces from 0 up to 0.15 N as caused by the applied indentations. The second regime (μ_2), after the kink, contains intervals with deeper indentations and as a result larger asperity deformations due to higher normal forces. The slope of the lines that represents the friction coefficient is only moderately affected by changes in the selected starting and ending point of each regime. Selecting several different transition points in close proximity to the kink resulted in a maximum error in friction coefficient around 10%.

The expression of the two regimes can be attributed to the deformable nature of the hydrogels. Applying a normal load on soft surfaces leads to deformation or even flattening of the elastic surface asperities, as was already conjectured long ago. [33, 34] More recently, this deformation was also shown for two hydrogels in contact. [19] We confirm this picture through a systematic variation of the stiffness and the surface roughness of the hydrogels.

Friction on substrates with an imposed random surface roughness

To study the influence of material stiffness on the sudden decrease in friction coefficient found, we use surfaces made of both chemically and physically cross-linked hydrogels ranging from 10% to 20% of xGel and uGel. Young's moduli ranged from 0.1 to 0.8 MPa. We systematically vary the roughness of the hydrogels using sandpaper with different average particle sizes or grit sizes. The asperities on the sandpaper used to make negative molds range from very fine, densely packed grains with a grit size (or average particle size) of 8.4 μm (P2500) to coarse grains with a grit size of 201 μm with large spaces between the grains and larger size distribution of the particles (P80). The hydrogel disks were cast on negative molds of the sandpaper to obtain surfaces with the same roughness as the sandpaper as shown in Figure 2.4.

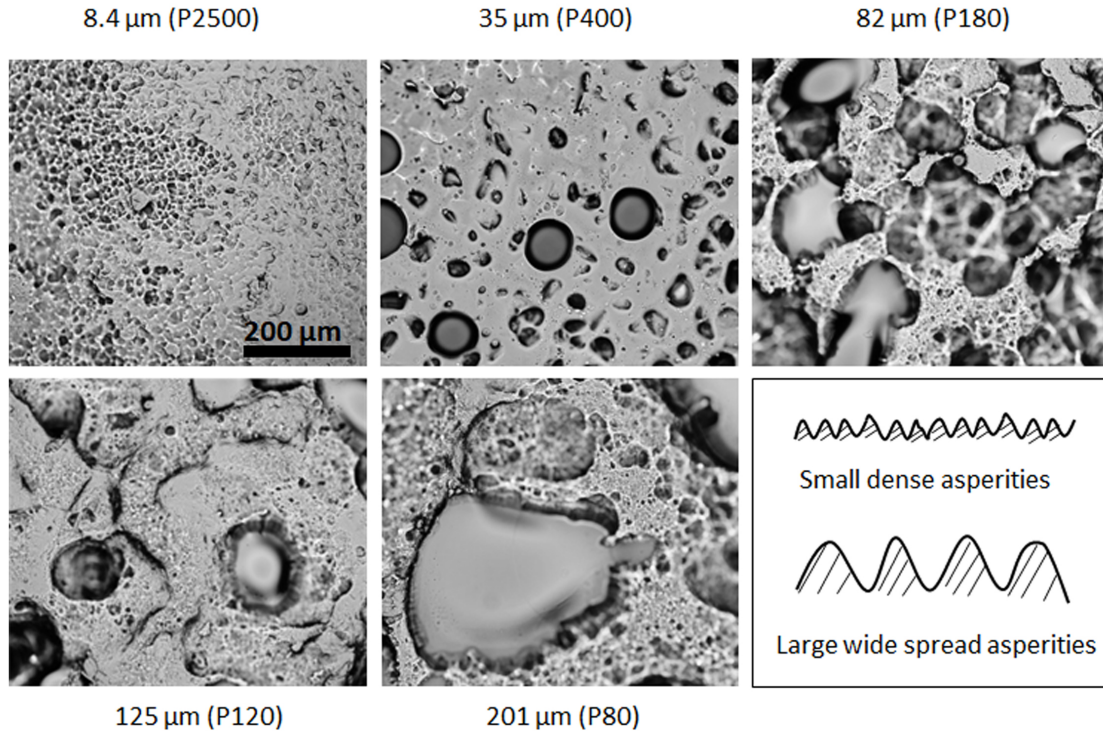


Figure 2.4: Microscopy images of gelatin hydrogel surfaces patterned using sandpaper together with the ISO/FEPA grit size label of the sandpaper used for molding the hydrogels. The small asperities are more closely packed and have a more uniform particle size than the large asperities.

In addition, we then studied the effect of stiffness and mesh size of the hydrogel, as well as surface topography on the friction coefficient for samples with the same polymeric constituents. With the expanded range of surface roughnesses and hydrogel moduli, we confirm the same picture: the friction coefficient is reduced with increasing normal force. The slopes in the friction force – normal force curves are used to calculate the dimensionless friction coefficient (μ) using $\mu = F_F / F_N$. The frictional values found for our artificially rough gelatin samples range from $\mu = 0.05$ to 0.45 . These values are much lower than friction coefficients typically found for dry solids [35, 36] while the upper limit, $\mu = 0.45$ is rather high compared to values typically reported for hydrogel-hydrogel friction using polyacrylamide or poly(2-acrylamido-2-methyl-1-propane sulfonic acid) (PAMPS). [12, 19] For gelatin substrates paired with glass, friction coefficients between 0.08 and 0.25 have been reported [37] however, the high friction coefficients in our samples are found in the first regime and are likely caused by the imposed roughness on our hydrogel surfaces. The friction coefficient in the first regime (μ_1) and the second regime (μ_2) for the different asperity sizes and gelatin concentrations have been summarized in Figure 2.5.

Soft surface roughness determines frictional regimes in hydrogel pairs

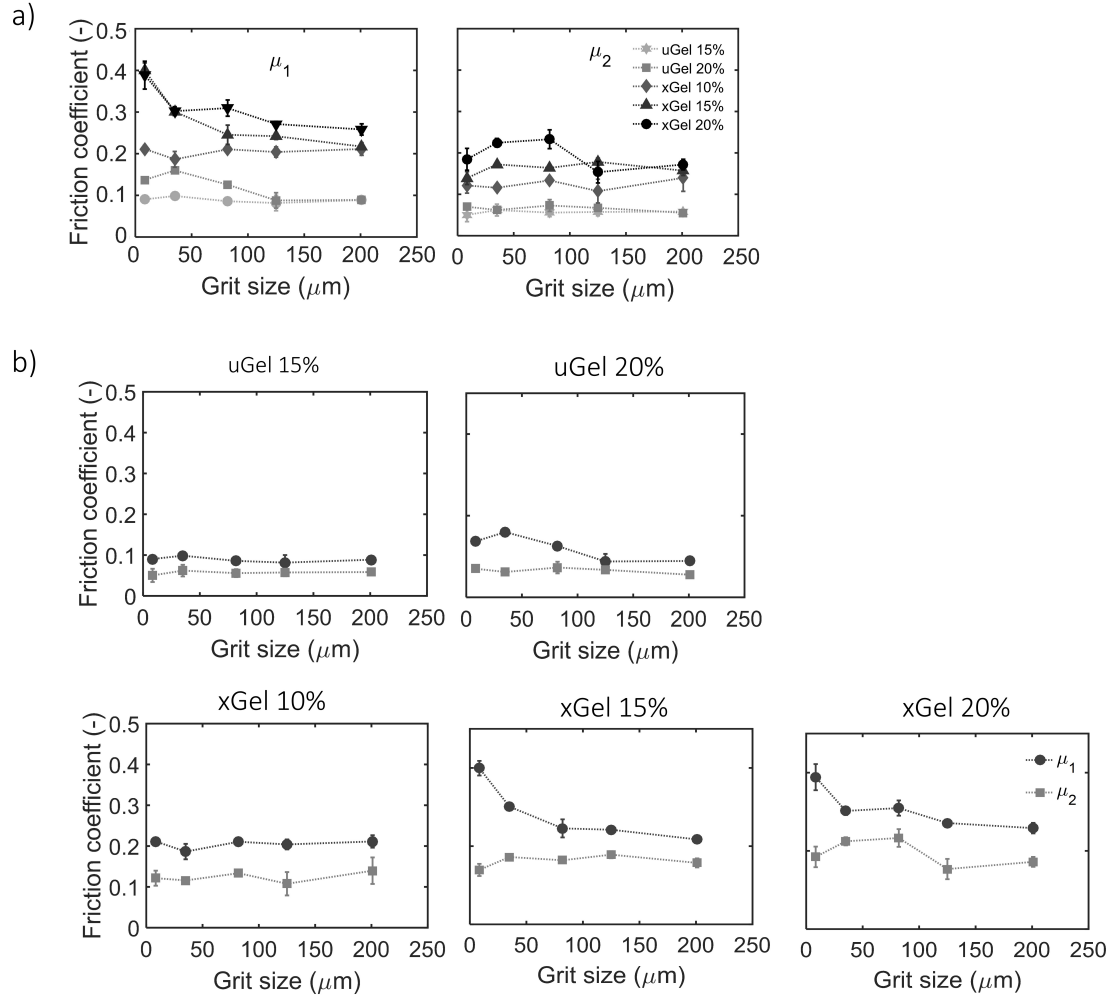


Figure 2.5: Friction coefficients for a) 10%, 15% and 20% chemically cross-linked gelatin and 15% and b) 20% physically cross-linked gelatin with different degrees of roughness patterned using sandpaper. The grit size refers to the average size of the grains on the sandpaper as stated by the manufacturer. The friction coefficient in the low load regime (μ_1) is shown on the left and the friction coefficient in the second regime (μ_2) on the right for both hydrogels. Measurements were performed at 0.1 rps = 20 mm/s.

We observe that the gelatin concentration has a systematic role: gelatin tribopairs made using lower concentrations of gelatin give lower frictional values for both xGel and uGel (Figure 2.6). The Young's moduli measured for uGel were 0.1 and 0.13 MPa for the 15% and 20% gelatin respectively. The Young's moduli for xGel with 10% gelatin was 0.35 MPa while 15% xGel has a modulus of 0.5 MPa and the highest modulus was found for 20% xGel with 0.8 MPa. The friction coefficients in both regimes show a logarithmic increase with the Young's modulus in both regimes. This increase is found for the smallest, most concentrated asperities (grit size 8.4 μm) up to the largest, more scattered asperities (201 μm). This difference in friction coefficient can be caused by the size of the asperities (contact area) as well as the distribution of the asperities on the surface (interlocking events).

Soft surface roughness determines frictional regimes in hydrogel pairs

The friction coefficient in the second regime appears independent of the grit size and depends mainly on material stiffness. This second regime seems to be a lower limit for the friction coefficient attainable with these physically and chemically cross-linked gelatin hydrogels.

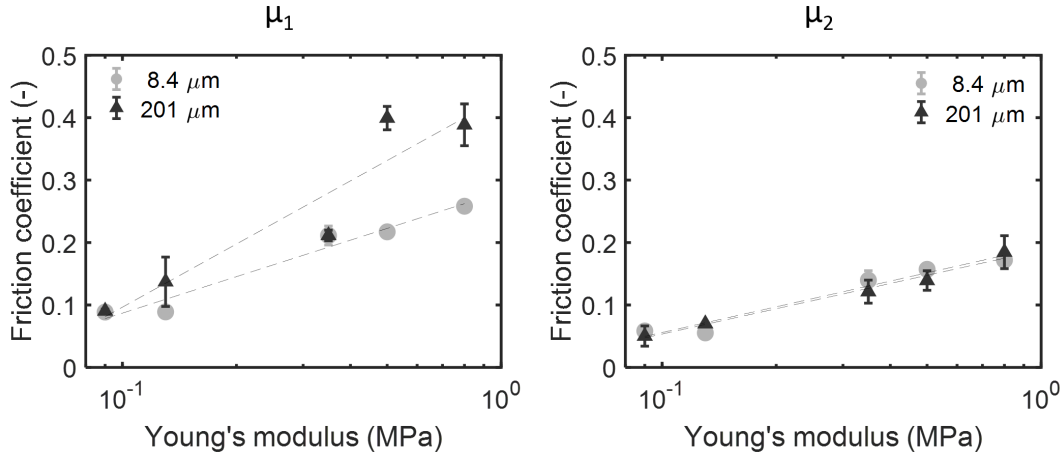


Figure 2.6: The increase of the friction coefficients μ_1 and μ_2 as a function of Young's modulus for grit sizes 8.4 and 201 μm . Hydrogels used here are 10%, 15% and 20% chemically cross-linked gelatin and 15% and 20% physically cross-linked gelatin at sliding velocities of 0.1 rps = 20 mm/s.

Across different polymer concentrations and Young's moduli, we find a recurring trend as a function of grit size: surfaces with fine, closely packed asperities display higher friction coefficients than large asperities that are widely distributed. The stiff samples appear to be more sensitive to changes in roughness, especially below grit sizes of 100 μm . This thus tells us that the friction coefficient in the first regime is a result of both the asperity size and/or distribution and the Young's modulus of the material.

At low normal forces, the asperities on a rough soft surface can act as obstacles, requiring more force to move the surfaces along one another. Small asperities are expected to have more contact points and perhaps even a larger contact area than larger asperities which would explain the higher friction coefficients. As we will see below, the hemispherical probe also has a natural roughness scale on the order of a couple of μm . If asperities of materials in contact are within the same size range, interlocking may occur. This in turn increases the friction between the materials. [38] As the Young's modulus of the samples increases (from left to right in Figure 2.5b) the overall decrease in friction coefficient from μ_1 to μ_2 ($\Delta\mu$) becomes larger. Reducing the polymer concentration decreases the stiffness of the material which makes it easier to deform asperities leading to lower friction coefficients in the second regime (Figure 2.5 and 2.7). As the deformability decreases, the stiff asperities play an increasingly large role in hindering the

probe from moving forward, resulting in high friction coefficients. Alternatively, in the low normal force regime, the asperity flattening is incomplete and probably fluctuating in time, adding a dissipation that disappears at higher normal load, where flattening effects are stronger. This effect is most pronounced at high asperity densities and small grit sizes (e.g. $8.4 \mu\text{m}$) and may be related to the number of asperities per unit surface area.

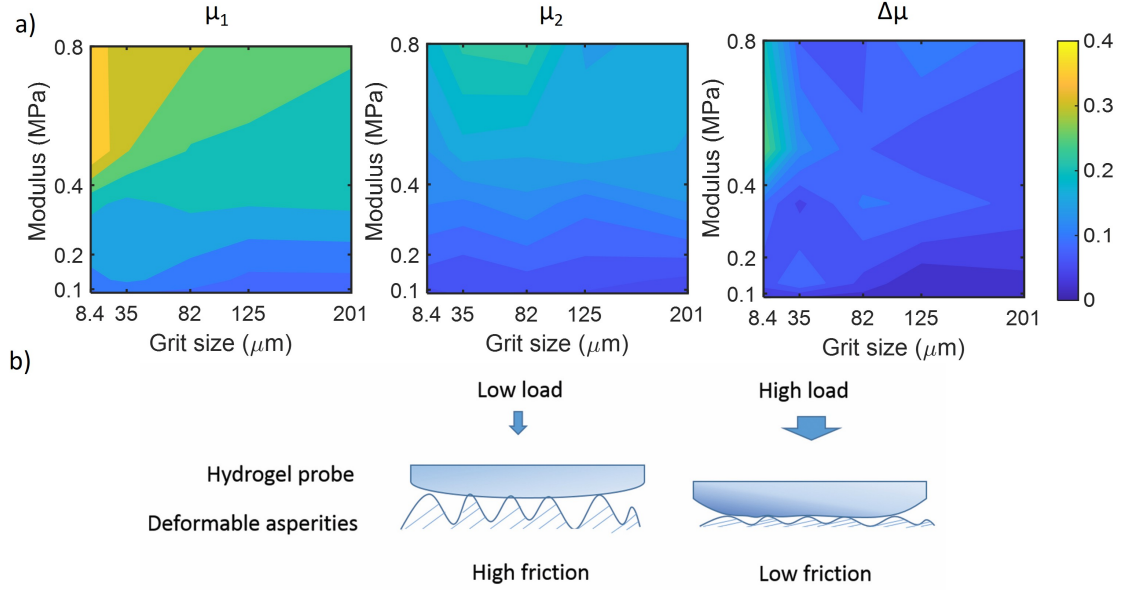


Figure 2.7: a) Frictional values as a function of the Young's modulus and grit size for all experiments; data extracted from Figure 2.3. The color bar indicates values for the friction coefficients. μ_1 , μ_2 and $\Delta\mu$. The y axis shows the Young's moduli of the materials used and the x-axis shows the used grit sizes. b) Schematic representation of asperities elastically deformed as a result of an increased applied load.

Above $100 \mu\text{m}$ interlocking events vanish as the asperities are likely too large to interlock with the surface of the hemispherical probe. In the second regime, we see that the friction coefficient approaches the same value for each sample regardless of the roughness. This indicates that the friction coefficient in the second regime is a material property. In this low friction regime, the asperities are likely permanently flattened by the applied load (Figure 2.7b) and only other dissipative dynamics (bonding/debonding, polymer entanglement, etc) remain.

To summarize the effects of asperity size and substrate modulus, we show how the frictions coefficient and the decrease thereof depend on these factors in Figure 2.7. Friction is highest for small asperities and high moduli. μ_2 is much less dependent on these mechanical features; in this regime, flattening has already occurred and remaining dissipation is due to other mechanisms. We schematically show the envisioned mechanism in Figure 2.7b.

Friction on substrates with a systematic surface roughness

As the sandpaper surfaces are patterned randomly, the asperities vary not only in size but also in location and distribution on the surface. To evaluate our suggested asperity-flattening mechanism, we compare regularly patterned uGel and xGel surfaces at 15% gelatin content. We specifically designed and 3D printed molds with desired asperity sizes. The distance and height of the asperities are kept constant while the diameter of the asperities is varied. The surface pillars were designed to have a height of $200\ \mu\text{m}$ and a distance of $500\ \mu\text{m}$ between the centers, so both surfaces were decorated with 4 pillars per mm^2 . We designed molds with two different asperities diameters; $50\ \mu\text{m}$ and $400\ \mu\text{m}$. (Figure 2.8).

Gel type	Pillar diameter	μ_1	μ_2	$\Delta\mu$
xGel	$50\ \mu\text{m}$	0.26	0.18	0.08
xGel	$400\ \mu\text{m}$	0.32	0.19	0.13
uGel	$50\ \mu\text{m}$	0.11	0.05	0.06
uGel	$400\ \mu\text{m}$	0.22	0.17	0.05

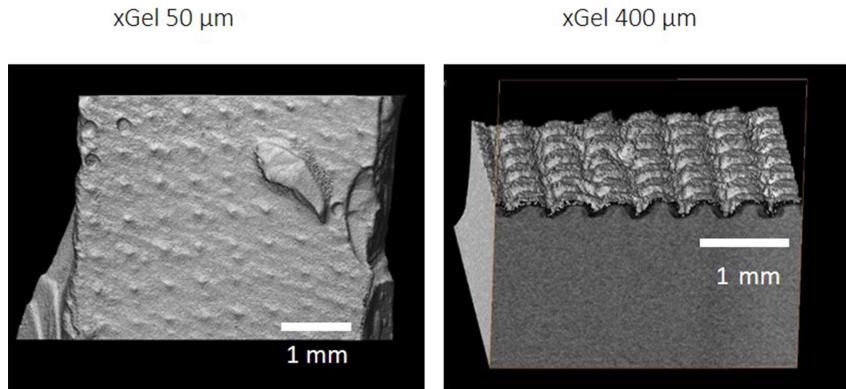


Figure 2.8: Friction coefficients for patterned xGel and uGel surfaces (top). X-ray tomography (XRT) images of xGel with asperities of $50\ \mu\text{m}$ (left) and asperities of $400\ \mu\text{m}$ (right) in diameter (bottom). The asperity height and distance was kept constant at $200\ \mu\text{m}$ and $500\ \mu\text{m}$ respectively.

For 15% uGel and xGel with regularly patterned surfaces again we find a second frictional regime. For xGel samples we find higher friction than for uGel samples (Figure 2.8).

Soft surface roughness determines frictional regimes in hydrogel pairs

Asperities with a diameter of 50 μm give $\mu_1 = 0.26$ and $\mu_1 = 0.11$ for xGel and uGel respectively, well within the range of the randomly patterned surfaces. Values in the second regime, μ_2 , approach values found for both the natural and the sandpaper patterned surfaces; 0.16 (xGel) and 0.07 (uGel) (see previous sections), which is yet more evidence for the friction coefficient in the second regime to be a material-specific constant. However, for the uGel samples with larger 400 μm pillars μ_2 is found to be 0.17, larger than previously found for uGel ($\mu_2 \approx 0.1$). For the sandpaper samples, we also found the decrease in friction to be smaller for hydrogels with low moduli. This relatively small decrease in friction is likely related to the deformability of the probe and the soft pillars. Within this limit of material stiffness and asperity size, the force applied is most likely not enough to deform the relatively large 400 μm pillars. As the dimensions of each asperity are now known, the compression ΔL of each pillar can be approximated by means of the simple relationship $\Delta L = F_N L / AE$, where ΔL is the deformation calculated from the normal force F_N , the initial length L , the area of the asperity A , and the Young's modulus E , respectively.

The deformation for the pillars of 400 μm diameter is about 60 times smaller compared to the 50 μm pillars due to the difference in aspect ratio. While the 50 μm pillar can be flattened to large extent, the 400 micron wide pillars experience limited compression. It appears that the regularity of the surface patterning plays an important role: irregularly patterned surfaces have a wide distribution of asperity heights. This leads to the normal force applied being distributed over the few asperities sticking out at every compression level. In contrast, the regular pillar height of the patterned rough substrate imposes that at all times, the normal force applied will be distributed over many pillars. By creating large and evenly sized pillars, the ability to flatten the asperities has been restrained, leading to a limited decrease in friction. Patterning the hydrogels in a controlled manner is thus an efficient way to tune the friction coefficient and its sensitivity to changes in normal force.

Friction on substrates with a natural surface roughness

In what way does friction of samples with an imposed surface roughness resemble the behavior of hydrogel surfaces generated in smooth molds? Hydrogels including gellan, polyvinyl alcohol (PVA), and poly(2-acrylamido-2-methylpropanesulfonic acid) (PAMPS) cast on smooth surfaces all show different frictional behavior when sliding against glass substrates. [8, 22, 32] This is commonly evaluated in terms of molecular interactions between the hydrogel-glass interface. However, in previous

sections, we have seen how important the role of surface roughness is. This makes it interesting to wonder whether roughness could have played a role and thus it is important to know how the chemical composition of a hydrogel affects its surface structure.

We use four hydrogels with varying network structures: physically cross-linked gelatin (uGel), chemically cross-linked gelatin (xGel), agar, and polyacrylamide (PAAm). Gelatin is known to form a triple helical structure while agar forms double helices. [39, 40] PAAm, a synthetic polymer, forms short and rigid cross-links due to the presence of bisacrylamide chains that cross-link the longer polymer strands. [41] Due to the differences in network formation and polymer concentration, we obtain gels with different moduli. Physically cross-linked gelatin provides the lowest modulus (0.1 MPa), followed by agar (0.2 MPa) and PAAm (0.5 MPa) and chemically cross-linked gelatin (0.5 MPa). It appears that the chemical structure of the gel affects not only the bulk properties of the hydrogels, but also their surface properties. To differentiate between the different degrees of naturally occurring surface roughness, we performed cryo-SEM imaging on the hydrogel surfaces (Figure 2.9). The top surfaces of the hydrogels, on which we also perform tribological tests (see below), are seen above the dashed lines; the internal gel structures are visible below the line. In addition, we show the schematic network structure that is typically expected for these hydrogels.

The PAAm hydrogel (Figure 2.9a) with short and linear chemical cross-links has the smoothest surface according to our cryo-SEM results. The lack of structure in the assembling molecules gives the gel a tightly bound structure resulting in a flat surface. Agar and gelatin hydrogels show a rougher surface (Figure 2.9b, c, and d). This relatively rough surface may be caused by coil-like helical structures that build up the hydrogels [39, 40]. The covalent chemical cross-links formed by glutaraldehyde transform the wavy gelatin surface (Figure 2.9c) into a rather bumpy landscape (Figure 2.9 d). The chemical cross-linker irreversibly brings polymer chains closer together leading to a stiffer network with a higher degree of roughness. By varying the polymer constituents and the interactions between them, we have obtained four hydrogels with distinct bulk and surface properties. Figure 2.10 shows the results of the lubricated friction between physically cross-linked or untreated gelatin (uGel), chemically cross-linked gelatin (xGel), agar, and polyacrylamide (PAAm) tribopairs in water. The values of the friction coefficients in both frictional regimes (μ_1 and μ_2) and the difference between the two regimes ($\Delta\mu$) together with the Young's moduli of the hydrogels are also shown here.

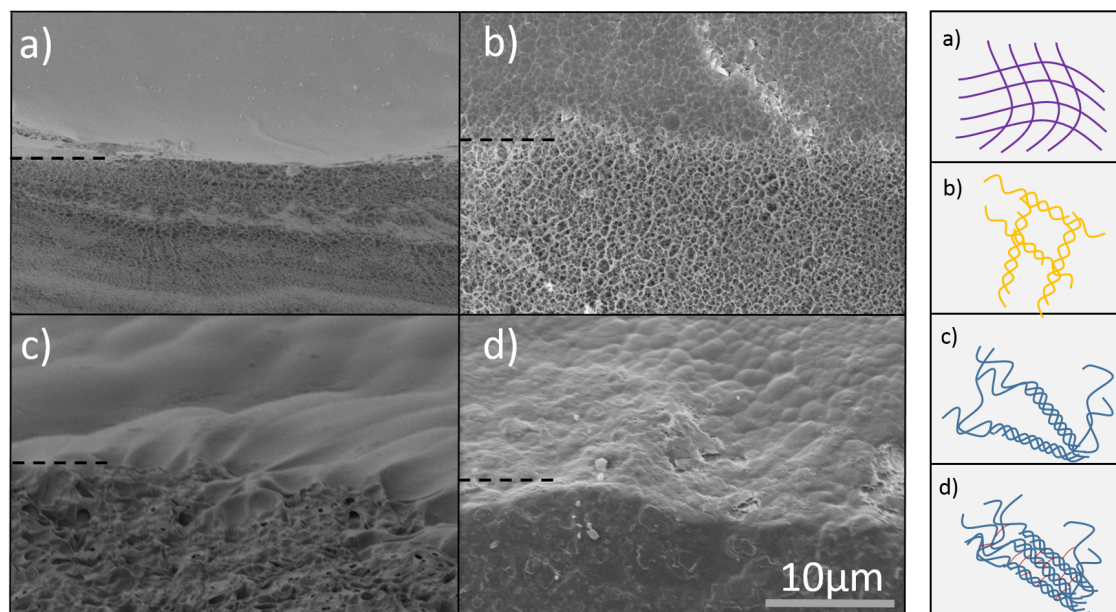


Figure 2.9: Cryo-SEM images of the surface and internal structures of a) PAAm, b) agar, c) uGel, and d) xGel on the left with the proposed schematic polymer network structure shown on the right. Microscope images were obtained using scanning electron microscopy with a magnification of 8000 times at cryogenic temperatures. North of the dashed line represents the surface. Below the dashed line the internal structure of the hydrogels can be seen.

Each hydrogel has a distinct friction coefficient that can be related to the degrees of roughness observed in the cryo-SEM images (Figure 2.9). The frictional behavior of these diverse samples further demonstrates that the normal force dependency is a robust property of hydrogel friction. Interestingly, the decrease in friction is absent in dry, solid friction experiments and extremely low for lubricated PAAm friction. This is likely because the asperities in dry solids are too stiff to be deformed at the normal forces used here. The PAAm surface is smoother than that of the remaining hydrogels, with no irregularities to be deformed in a second regime. The hydrogels submerged in water give low friction coefficients in a range from 0.008 to 0.31. In the second regime, xGel shows the highest friction coefficient followed by uGel and agar. PAAm has the lowest friction coefficient in this regime. Samples made of xGel and PAAm have similar Young's moduli (0.5 MPa), yet we see large differences in the friction coefficients of these two hydrogels (Figure 2.10). The low friction coefficient found for PAAm in the first regime can be related to the smooth surface as observed by cryo-SEM (Figure 2.9): there are no asperities to flatten and the molecular structure of PAAm does not give rise to other dissipative mechanisms, producing a dissipation during sliding that is only borderline detectable in our setup. The hydrogels with a more pronounced surface roughness all show two regimes of friction and higher friction coefficients than PAAm. Hydrogel-hydrogel friction thus depends on a combined effect of bulk and surface properties.

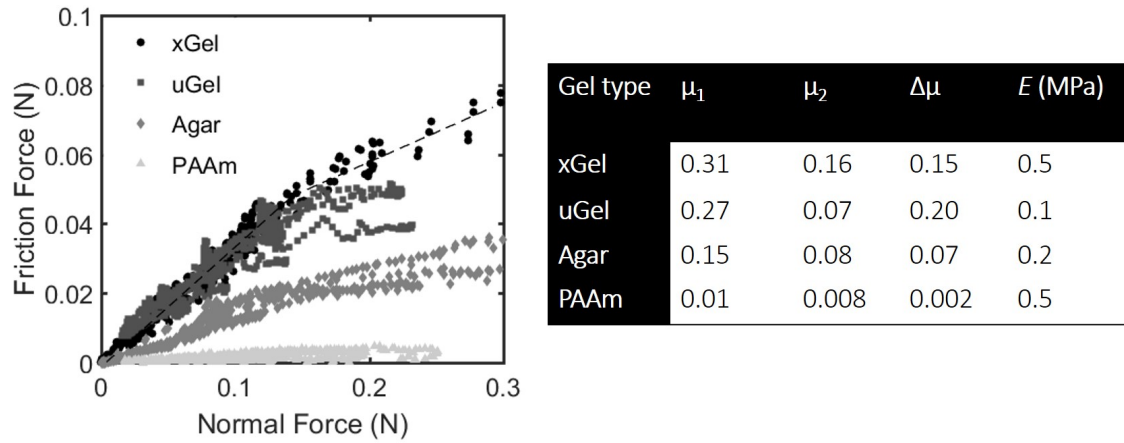


Figure 2.10: Friction curves of untreated, physically cross-linked gelatin (uGel), chemically cross-linked gelatin (xGel), agar and polyacrylamide (PAAm) tribopairs at 0.1 rps. We find two normal force dependent friction coefficients (μ_1 and μ_2) for all hydrogels. The calculated friction coefficients and the Young's modulus of each sample are shown in the table on the right.

The role of polymeric lubrication

Physical mechanisms that are commonly discussed in hydrogel friction include the presence of a fluid layer [20], gel relaxation [10, 29] poroelastic effects [18, 42] and surface adhesion. [27] These mechanisms are potentially also involved in the decrease of friction we find in our hydrogels. As our measurements are carried out in water, we do not expect adhesion between the hydrogels to be of large influence. A thin film of water being squeezed out of the hydrogel is not expected to significantly further decrease the friction, as measurements are carried out in large amounts of water and a fluid layer is already present. [8] In addition, the asperities of rough gels would expel more water than flat gels under an applied load as the asperities undergo a large compression. [20] This would lead to a larger decrease in friction for rough gels, which we do not observe in our measurements. We look further into the drop in friction coefficient by performing measurements with longer duration and lower sliding velocities, to determine whether time or velocity-dependent effects are at play in hydrogel-hydrogel friction. For this purpose we selected xGel, as this chemically cross-linked material is stable over a long period with respect to swelling. Since the cross-linking is performed in a water-bath with glutaraldehyde and the gel is then immediately submerged and stored in water, maximum swelling is already attained. The results in Table 2.1 show that the friction between two cross-linked gelatin hydrogels is time and velocity independent within the available velocity range of our equipment. Friction coefficients μ_1 and μ_2 for xGel remained constant within the measuring range of 0.005 to 0.1 rps. The rate and time independence found for xGel indicates that the decrease in friction is indeed not caused by adhesion or fluid film formations at

the interface as these are rate-dependent phenomena. We also do not observe any significant wear effects in these soft materials. Frictional measurements performed on the same substrate and probe pairs consistently yielded reproducible results over several weeks. Time-dependent effects such as fluid migrating to the interface, relaxation phenomena, or serum release, do not seem to be the main driving forces behind the normal force dependence found for hydrogels. Another effect leading to a decrease in friction in hydrogels might be the loosening or dissolving of polymers within the hydrogel network. [8, 32] A viscous layer could be formed on the hydrogel interface which promotes a decrease in friction. In chemically cross-linked substrates this effect would be less profound as the polymers are covalently bound. However, we do find a large drop in friction coefficient in our chemically cross-linked xGel, eliminating the loosening of polymer layers as the main cause for the normal force dependence. Repeating a full cycle of measurements with the same samples yields highly reproducible results. Loosening or permanently dissolving polymer chains are thus an unlikely source of the reduced friction in the second regime.

Table 2.1: Friction coefficients for xGel at 0.1, 0.05, 0.001 and 0.005 rps in the low-load (μ_1) and the high-load (μ_2) regime. The measurements at different velocities were carried out with the same hydrogel probe and substrate.

Angular velocity (rps)	μ_1	μ_2
0.1	0.31	0.16
0.05	0.33	0.16
0.01	0.28	0.14
0.005	0.28	0.15

Discussion

With the combined results of the imposed regular, irregular, and naturally rough surfaces it is clear that elastic deformation of the surface asperities plays a key role in the observed drop in friction coefficient. This is concretely observed by making direct comparisons: we find that for materials with the same stiffness (xGel and PAAm) the difference in their surface roughness leads to a large difference in friction coefficients in both regimes. When comparing two relatively rough materials (xGel and uGel), our results demonstrate that stiffness plays an increasingly large role. The appearance of a second frictional regime at high normal forces

thus appears to be a function of the stiffness and surface roughness (imposed or induced by the polymeric nature of the hydrogel) regardless of the length scale of the asperities. Further parameters contributing to the friction coefficients of hydrogels include the difference in chemical make-up along with the mesh sizes and network structures for each of the samples.

We can further elucidate the flattening hypothesis by estimating the asperity deformation at a normal force F_N of 0.2 N and maximum probe displacement of 400 μm . The contact area is then approximately 6 mm^2 as estimated using Hertz theory. The hardest gel surface (xGel) has asperities with a radius of roughly $r_a = 1.5 \mu\text{m}$ as estimated from Figure 2.9. The number of asperities with which the probe is in contact is then approximately 2×10^6 if we assume all asperities are hemispherical and completely cover the surface. Every asperity thus experiences a contact force of $\approx 1 \times 10^{-7}$ N. To estimate the deformation of a single naturally occurring asperity, we assume that every single substrate asperity equally exerts 1×10^{-7} N on the probe, which due to the separation of length scales can be considered a flat plane. We would like to again highlight that this is an underestimation: due to the irregularity of the surface, the applied normal load is most likely not evenly distributed over all contacts, but instead focused on only a few asperities. We then estimate the deformation of an asperity under such load again with Hertz theory, $F_a = \frac{4}{3}Er_a^{1/2}\delta_a^{3/2}$ to be $\delta_a/r_a \sim 0.1$: in this limit, the deformation predicted by Hertz' theory is already ten percent of the asperity radius. This is in fact independent of r_a : the relative deformation of an asperity is $\delta_a/r_a = \frac{3F_N}{4E\delta_p r_p}$.

This supports our hypothesis that the deformation of asperities plays a significant role, even for the stiffest gels used. The less stiff gels are easier to deform or flatten and therefore give an even larger drop in the friction coefficient in the second regime. This estimation gives a clear suggestion of the physical mechanisms behind the asperity flattening. However, it does not include the height of the asperities which can not be estimated from the cryo-SEM images. The spatial variability of the pressure in the Hertz solution, a possible deviation from incompressibility, and deformation coupling between asperities have been omitted from the estimation for simplicity. Recently, it was found in “Gemini” hydrogel pairs, that an increase in normal force leads to a decrease in friction in the speed independent regime [19]. Hertzian contact mechanical behavior was observed for these hydrogels and the contact area, friction coefficient, and normal force were found to be directly related to one another ($\mu \propto F_N^{-1/3}$). As we have shown here, Hertzian behavior alone would not suffice to accurately describe the two distinct regimes observed in hydrogel friction with our rough substrates.

Conclusions

Friction on soft substrates is influenced by many factors including material surface properties such as roughness, and bulk properties such as the elasticity of the surfaces. We measure friction on a range of patterned hydrogels with different chemical composition using a home built tribotool. The frictional dynamics observed are strongly normal-force dependent in our soft lubricated contacts. When increasing the normal force, a drop in friction coefficient is found, defining two distinct frictional regimes. The first frictional regime is sensitive to the nature and the length scale of the asperities (synthetic or naturally occurring) on the hydrogel surface. The friction coefficient in the second regime appears to be a material property. For samples made of the same polymeric materials, we find that lower Young's moduli lead to lower friction in both regimes regardless of the surface roughness. The decrease in friction coefficient is likely to be induced by the deformation of the soft surface asperities leading to a smoother surface. In the second regime, dissipative dynamics are determined by other bulk or surface properties. The experimental tribology we have introduced in this chapter, enables tribologists to explore the complexity behind lubricated hydrogel-hydrogel friction over a wide range of material types, surface characteristics, and lubricants.

References

1. Milner, P. E. *et al.* A low friction, biphasic and boundary lubricating hydrogel for cartilage replacement. *Acta Biomaterialia* vol. 65, 102–111 (2018).
2. Karimi, A. & Navidbakhsh, M. Material properties in unconfined compression of gelatin hydrogel for skin tissue engineering applications. *Biomedical Engineering/Biomedizinische Technik* vol. 59, 479–486 (2014).
3. Ma, J. *et al.* Highly stretchable and notch-insensitive hydrogel based on polyacrylamide and milk protein. *ACS applied materials & interfaces* vol. 8, 29220–29226 (2016).
4. Hofman, A. H., van Hees, I. A., Yang, J. & Kamperman, M. Bioinspired underwater adhesives by using the supramolecular toolbox. *Advanced Materials* vol. 30, 1704640 (2018).
5. Shewan, H. M. & Stokes, J. R. Review of techniques to manufacture micro-hydrogel particles for the food industry and their applications. *Journal of Food Engineering* vol. 119, 781–792 (2013).
6. Gomez-Guillen, M. C., Gimenez, B., Lopez-Caballero, M. E. & Montero, M. P. Functional and bioactive properties of collagen and gelatin from alternative sources: A review. *Food Hydrocolloids* vol. 25, 1813–1827 (2011).
7. Torres, O., Andablo-Reyes, E., Murray, B. S. & Sarkar, A. Emulsion microgel particles as high-performance bio-lubricants. *ACS applied materials & interfaces* vol. 10, 26893–26905 (2018).
8. Gong, J. P., Iwasaki, Y. & Osada, Y. Friction of gels. 5. Negative load dependence of polysaccharide gels. *Journal of Physical Chemistry B* vol. 104, 3423–3428 (2000).
9. Liu, G. *et al.* Hairy polyelectrolyte brushes-grafted thermosensitive microgels as artificial synovial fluid for simultaneous biomimetic lubrication and arthritis treatment. *ACS applied materials & interfaces* vol. 6, 20452–20463 (2014).
10. Pitenis, A. *et al.* Polymer fluctuation lubrication in hydrogel gemini interfaces. *Soft Matter* vol. 10, 8955–8962 (2014).
11. Tominaga, T. *et al.* Effect of substrate adhesion and hydrophobicity on hydrogel friction. *Soft Matter* vol. 4, 1033–1040 (2008).
12. Gong, J. P. & Osada, Y. Surface friction of polymer gels. *Progress in Polymer Science* vol. 27, 3–38 (2002).
13. Rudge, R. E. D., Scholten, E. & Dijkman, J. A. Advances and challenges in soft tribology with applications to foods. *Current Opinion in Food Science* vol. 27, 90–97 (2019).
14. Skotheim, J. & Mahadevan, L. Soft lubrication. *Physical Review Letters* vol. 92, 245509 (2004).
15. Leroy, S. *et al.* Hydrodynamic interaction between a spherical particle and an elastic surface: a gentle probe for soft thin films. *Physical Review Letters* vol. 108, 264501 (2012).
16. Sekimoto, K. & Leibler, L. A mechanism for shear thickening of polymer-bearing surfaces: elasto-hydrodynamic coupling. *EPL (Europhysics Letters)* vol. 23, 113 (1993).
17. Amontons, G. *Remarques et experiences phisiques sur la construction d'une nouvelle clepsidre, sur les barometres, termometres, & higrometres* (chez Jean Jombert, Paris, 1695).

18. Dolan, G. K., Yakubov, G. E., Bonilla, M. R., Lopez-Sanchez, P. & Stokes, J. R. Friction, lubrication, and in situ mechanics of poroelastic cellulose hydrogels. *Soft Matter* vol. 13, 3592–3601 (2017).
19. Urueña, J. M. *et al.* Normal load scaling of friction in gemini hydrogels. *Biotribology* vol. 13, 30–35 (2018).
20. Yashima, S., Takase, N., Kurokawa, T. & Gong, J. P. Friction of hydrogels with controlled surface roughness on solid flat substrates. *Soft Matter* vol. 10, 3192–3199 (2014).
21. Riedo, E. & Brune, H. Young modulus dependence of nanoscopic friction coefficient in hard coatings. *Applied Physics Letters* vol. 83, 1986–1988 (2003).
22. Gong, J. P. Friction and lubrication of hydrogels—its richness and complexity. *Soft Matter* vol. 2, 544–552 (2006).
23. Dunn, A. C., Sawyer, W. G. & Angelini, T. E. Gemini Interfaces in Aqueous Lubrication with Hydrogels. *Tribology Letters* vol. 54, 59–66 (2014).
24. Drozdov, A., Sanporean, C.-G. & Christiansen, J. d. C. Mechanical response of HEMA gel under cyclic deformation: Viscoplasticity and swelling-induced recovery. *International Journal of Solids and Structures* vol. 52, 220–234 (2015).
25. Zhao, X. Multi-scale multi-mechanism design of tough hydrogels: building dissipation into stretchy networks. *Soft Matter* vol. 10, 672–687 (2014).
26. Gong, J. P., Kagata, G., Iwasaki, Y. & Osada, Y. Surface dynamic friction of polymer gels. *Chinese Journal of Polymer Science* vol. 18, 271–275 (2000).
27. Gong, J., Iwasaki, Y., Osada, Y., Kurihara, K. & Hamai, Y. Friction of gels. 3. Friction on solid surfaces. *The Journal of Physical Chemistry B* vol. 103, 6001–6006 (1999).
28. Dąbrowska, A. *et al.* A water-responsive, gelatine-based human skin model. *Tribology International* vol. 113, 316–322 (2017).
29. Urueña, J. M. *et al.* Mesh size control of polymer fluctuation lubrication in gemini hydrogels. *Biotribology* vol. 1, 24–29 (2015).
30. Kim, J.-Y., Song, J.-Y., Lee, E.-J. & Park, S.-K. Rheological properties and microstructures of Carbopol gel network system. *Colloid and Polymer Science* vol. 281, 614–623 (2003).
31. Workamp, M. & Dijkman, J. A. Contact tribology also affects the slow flow behavior of granular emulsions. *Journal of Rheology* vol. 63, 275–283 (2019).
32. Kim, S. H., Opdahl, A., Marmo, C. & Somorjai, G. A. AFM and SFG studies of pHEMA-based hydrogel contact lens surfaces in saline solution: adhesion, friction, and the presence of non-crosslinked polymer chains at the surface. *Biomaterials* vol. 23, 1657–1666 (2002).
33. Denny, D. The influence of load and surface roughness on the friction of rubber-like materials. *Proceedings of the Physical Society. Section B* vol. 66, 721 (1953).
34. Schallamach, A. Friction and abrasion of rubber. *Rubber Chemistry and Technology* vol. 31, 982–1014 (1958).
35. Blau, P. J. The significance and use of the friction coefficient. *Tribology International* vol. 34, 585–591 (2001).
36. Lorenz, B., Oh, Y., Nam, S., Jeon, S. & Persson, B. Rubber friction on road surfaces: Experiment and theory for low sliding speeds. *The Journal of Chemical Physics* vol. 142, 194701 (2015).

37. Baumberger, T., Caroli, C. & Ronsin, O. Self-healing slip pulses and the friction of gelatin gels. *The European Physical Journal E* vol. 11, 85–93 (2003).
38. Müser, M. H., Wenning, L. & Robbins, M. O. Simple microscopic theory of Amontons's laws for static friction. *Physical Review Letters* vol. 86, 1295 (2001).
39. Duconseille, A., Andueza, D., Picard, F., Santé-Lhoutellier, V. & Astruc, T. Molecular changes in gelatin aging observed by NIR and fluorescence spectroscopy. *Food Hydrocolloids* vol. 61, 496–503 (2016).
40. Taylor, M. J., Tomlins, P. & Sahota, T. S. Thermoresponsive Gels. *Gels* vol. 3, 4 (2017).
41. Baek, K. *et al.* In situ assembly of the collagen–polyacrylamide interpenetrating network hydrogel: Enabling decoupled control of stiffness and degree of swelling. *European Polymer Journal* vol. 72, 413–422 (2015).
42. Reale, E. R. & Dunn, A. C. Poroelasticity-driven lubrication in hydrogel interfaces. *Soft Matter* vol. 13, 428–435 (2017).



3

Is there a pattern?
Frictional properties of
micro-patterned hydrogels

Abstract

Soft and slippery surfaces such as hydrogel surfaces are known for their low friction coefficients, especially in the presence of aqueous lubricants. Hydrogels can also be easily modified to have a particular surface roughness, changing their frictional properties. In the previous chapter, we showed that the surface roughness has a strong influence on the friction coefficient of hydrogel surfaces. Here, we show how several roughness parameters (height, diameter, distance between pillars) can be used to alter the friction coefficient in hydrogel-hydrogel friction. While a smooth (unpatterned) hydrogel surface gives friction coefficients around 0.31, using different patterned surfaces we were able to generate friction coefficients that are 50% lower or higher. We show that each surface roughness parameter has a specific contribution to the friction coefficient. Slender pillars conjure a higher friction coefficient, which we attribute to their bending and hence larger contact area. In contrast, we measure low friction coefficients when the sparse presence of pillars reduces the effective contact area. Our findings thus provide a clear path towards optimization of frictional properties of patterned surfaces. Hydrogels with tunable roughness and friction coefficients can find applications in soft solids where friction plays an important role.

This chapter was submitted as:

Rudge, R.E.D., Scholten, E., and Dijkstra, J. A. Is there a pattern? Frictional properties of micro-patterned hydrogels.

Introduction

The frictional properties of two sliding surfaces are often influenced by the specific properties of the surface, including the material type and the surface roughness. The impact of surface properties on friction, lubrication and wear, also known as tribology, has been the focus of various studies. [1–8] Surface roughness can be used as a tool to control the friction coefficient of a specific tribosystem. This approach has been used successfully to control the frictional and adhesive properties of various soft surfaces such as elastomers [9, 10] and hydrogels. [7, 8, 11] Controlling the frictional properties is of importance for many materials in contact. Low friction is often required for biomimetic applications such as skin replacements, [12] artificial joints [13–15] or oral lubrication during food consumption. [9, 16] Systems that require high friction for optimal performance include car brakes, or tires. [17, 18] Controlling the frictional properties of materials by manipulating the surface roughness can thus lead towards the optimization of various processes where contacting surfaces are involved.

Even surfaces that are visually smooth may have micro or even nano-scale asperities that affect their contact mechanics and frictional behavior as also seen in Chapter 2. These asperities play a role in the contact mechanics and deformation of the surface, leading to variations in friction and wear. [6, 8, 19] When asperities are present on the surface, the *real* contact area between opposing surfaces is often far smaller than the *apparent* area of contact. It is commonly thought that a larger degree of surface roughness leads to a smaller contact area and with that less adhesion and lower friction coefficients. [20, 21] Paradoxically, also high friction coefficients have been found for rough surfaces [22], for example due to asperity interlocking events occurring between asperities. Such an increase in friction coefficient was found for patterned polydimethylsiloxane (PDMS) surfaces paired with rough surfaces [23] and for polyurethane surfaces decorated with nano-scaled asperities, sliding against smooth mica surfaces. [6] Our findings in **Chapter 2** also confirmed the importance of roughness, as we showed that hydrogels with a larger number of surface asperities give higher friction coefficients than apparent smooth surfaces. Our optically smooth hydrogel surfaces displayed low friction and surfaces with a degree of micro-scale roughness gave higher friction coefficients. [8]

Existing work in the field of soft, rough substrates thus shows that the effect of surface roughness on the frictional behavior of a tribosystem is still not completely understood. For most surfaces used in tribological studies, the roughness is not well defined as surfaces are randomly rough. This makes it difficult to relate

Is there a pattern? Frictional properties of micro-patterned hydrogels

friction to specific roughness parameters and identify which parameters play the most important role in defining frictional behavior. To understand which asperity characteristics are important regarding the frictional behavior, the roughness parameters (asperity height, distance, diameter) need to be changed independently from each other to obtain proper control over the surface roughness spectrum. [24]

In this chapter, we therefore designed hydrogel surfaces with controlled properties: we cover the surface with asperities that have a variable height, radius and spatial distribution. Hydrogels are of interest to researchers in different fields thanks to their biocompatibility and their ability to hold large amounts of water and form a soft material with solid like properties.[25, 26] By systematically varying the surface topography of the soft materials, we aim to unveil the effect of each of the individual roughness parameters on the friction coefficient. This systematic exploration on the relationship between the type of surface roughness and the friction coefficient will provide us with new methods to effectively design surfaces with desired frictional properties by simply varying the surface characteristics of the contacting surfaces.

Experimental section

Hydrogel tribopair preparation

Hydrogel probes and substrates were made using 15 wt% porcine skin gelatin (Sigma-Aldrich) according to a method presented in **Chapter 2**. [8] In short, we used 3D-printed molds to make negative rubber molds (Moldstar 20T, Smooth On). The gelatin solution was poured into negative rubber molds to obtain hydrogel surfaces with similar surface asperities as the 3D-printed samples. The method used is shown schematically in Figure 3.1.

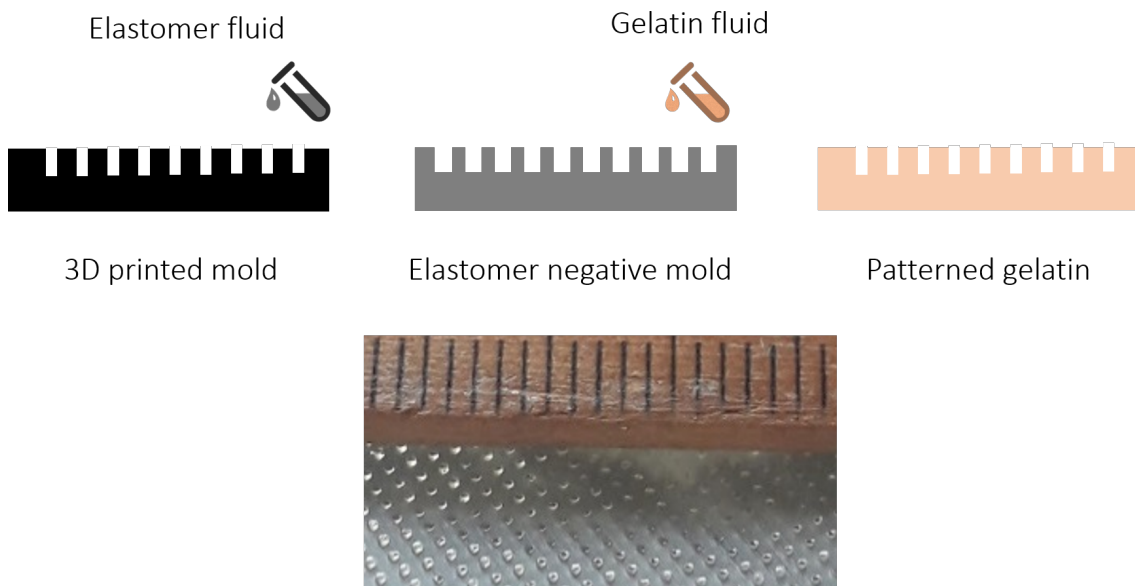


Figure 3.1: Method used to obtain patterned gelatin surfaces with a 3D-printed mold by first making elastomeric negative molds and subsequently pouring the gelatin solution into the negative mold to obtain the desired surface pattern. A result of this type of patterning is shown in the figure on the bottom as an example, with a ruler to indicate the size of the pillars. The distance between two black lines is 1 mm.

After samples were stiffened by cooling the gels down at 4 °C and removed from the mold, we obtained hydrogels with varying surface structures. The surface structures include pillars varying in height, diameter, spacing and pattern type. Solidified samples were chemically cross-linked using a 10 times diluted solution of glutaraldehyde (50% in water, Sigma-Aldrich) as a cross-linking agent. The disk-shaped samples were 86 mm in diameter and 10 mm in height. The hemi-spherical hydrogel probe was 20 mm in diameter.

Frictional measurements using a gel-on-gel tribometer

To measure the friction coefficient, a customized rheo-tribometer (Figure 3.2) was used. Technical details on this device were described in **Chapter 2**. [8] The hemi-spherical probe is inserted into the 30 mm long arm, attached to a rheometer (Anton Paar MCR 501) which we used to measure hydrogel-hydrogel friction in a gap-controlled manner. Measurements were carried out at normal forces from 0 up to 0.2 N and at speeds of 0.005 revolutions per second (rps), which corresponds to 1 mm/s. The average values and corresponding error bars we report, are based on two measurements using two different sets of hydrogel tribopairs with two rotations performed at each gap size. We use five different gap sizes to obtain a range of normal forces. We calculate the total friction coefficient by averaging over all the friction coefficients measured while the probe is travelling over the substrate, as long as these friction coefficients are measured at small normal forces (≤ 0.2 N). This cut-off normal force is determined by the normal force at which the asperities are expected to not be flattened by the probe. Such flattening would lead to an undesired transition into another frictional regime, which was shown and discussed in **Chapter 2**. [8]

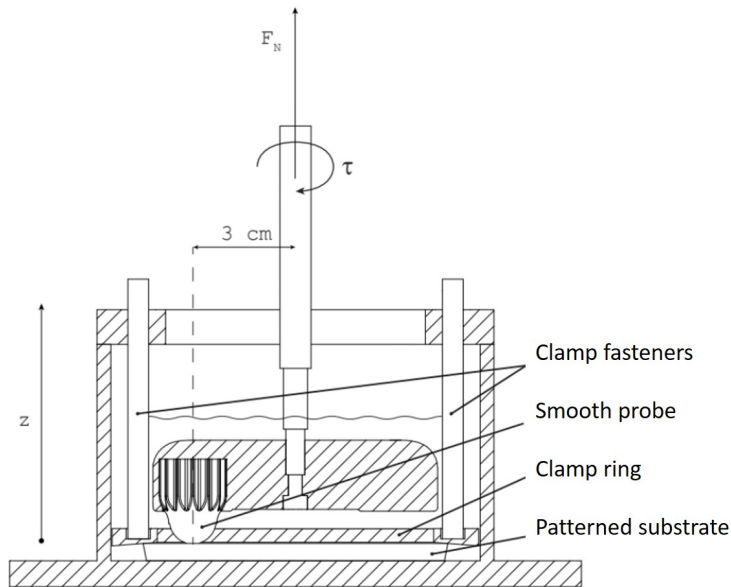


Figure 3.2: Side view of the gel-on-gel tribometer used in this study. The gel probe attached to a rheometer is rotated over our patterned surfaces with an arm length of 3 cm. Probe diameter is 2 cm while substrate disks have a diameter of 86 cm. The rheometer records the normal force (F_N) and the torque (τ). The measuring container has a height (z) of 10 cm. Measurements are performed under fully submerged conditions.

Results and discussion

We measured the friction coefficient for a smooth hemi-spherical hydrogel probe sliding against a hydrogel substrate. The hydrogel substrate was designed to have cylindrical pillars on the surface to alter the surface roughness. During measurements, we obtained the torque and normal forces using a rheometer (Figure 3.3a). We previously estimated the contact area diameter of the same hydrogel probe against the (unpatterned) substrate to be 1.7 mm using Hertzian contact mechanics. [8]

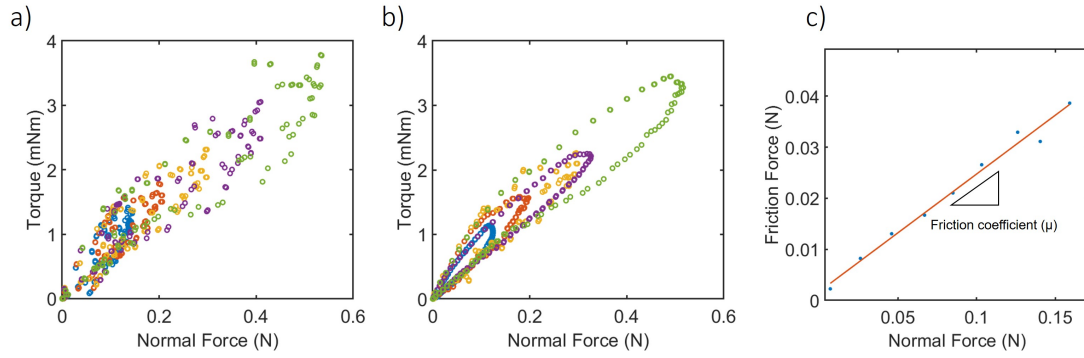


Figure 3.3: a) Raw torque and normal force signals measured during rotation. The different colors show different intervals. b) The same torque and normal force values as shown in (a) after smoothing the data. c) Friction force against normal force, from which the friction coefficient is determined.

Due to the irregular surface of the hydrogels, the obtained data has a strong angular displacement (location on the gel) dependence. Therefore, we group the data into 50 sections (bins) to obtain a better overview of the various measuring intervals. The normal force and torque values were used to calculate friction coefficients as $\mu = F_F / F_N$ and $F_F = \tau / R$ with F_F the friction force and τ the torque and R , the arm length, of 3 cm. The friction coefficient was calculated from the slope of the linear F_F vs F_N plots (Figure 3.3c). As indicated, smoothing the raw data gave only minor changes in the friction coefficient (Figure 3.3b). We use this 3D-printed tribotool to measure the friction coefficient of patterned hydrogels with different asperity sizes. The ranges in height, diameter (width) and distance used, are shown in Table 3.1.

Is there a pattern? Frictional properties of micro-patterned hydrogels

Table 3.1: An overview of the different asperity parameters for the patterned substrates used in this study. We describe the patterned surfaces in terms of asperity height, diameter (width) and distance.

	Height (μm)	Diameter (μm)	Distance (μm)
Height Series	250	500	1000
	500	500	1000
	1000	500	1000
	1500	500	1000
Diameter Series	500	250	1000
	500	500	1000
	500	1000	1000
	500	1500	1000
Distance Series	500	500	555
	500	500	600
	500	500	750
	500	500	1000
	500	500	1500
Radial pattern	500	500	1700
	500	500	3500
	500	500	16000
	500	500	310000

Asperity height: flexible beams as barriers

To investigate the effect that asperities on a substrate surface have on the frictional behavior, we use micron-sized pillars with controlled height (H), diameter (D) and distance or spacing (S). The cylindrical surface pillars have a flat top and are ordered on a square lattice. The pillars are designed to have a centre-to-centre spacing of $1000\ \mu\text{m}$ between the pillars and the pillars have a diameter of $500\ \mu\text{m}$. Using a custom-made tribotool [8], we find that the presence of short pillars ($250\ \mu\text{m}$) on the hydrogel surface leads to similar friction coefficients as found for a smooth, unpatterned (u) gelatin surface ($\mu_u = 0.31$, $\mu_{H250} = 0.32$).

With taller pillars (500 , 1000 and $1500\ \mu\text{m}$ in height) present on the surface, we find an increase in friction coefficient, which reaches a maximum of almost 0.5 for pillars that are $1500\ \mu\text{m}$ in height as shown in Figure 3.4. As the top surface area of the pillars is the same for all pillar heights, the increase in friction coefficients is likely due to other factors than the actual surface area. An increase in friction coefficient with pillar height was also found using soft polymer surfaces with nano-patterned asperities [27] and micro-patterned asperities. [10]

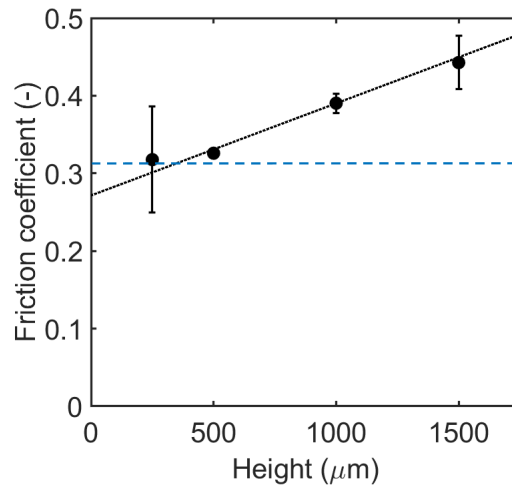


Figure 3.4: Friction coefficients of hydrogel-hydrogel friction with patterned substrates at $1\ \text{mm/s}$. Pillars on the surface were varied in height ranging from $250\ \mu\text{m}$ to $1500\ \mu\text{m}$. A blue dashed line was added to represent the average friction coefficient of an unpatterned gelatin hydrogel.

In a soft substrate tribology experiment, it is in general not easy to disentangle the role of asperity or substrate deformation on the ratio of shear and normal stresses. This is the case because one cannot independently control (or even measure) the relevant variables such as probe and substrate deformation and effective gap size. We can, however, hypothesize a mechanism for the enhancement of friction for taller pillars. The relatively high friction forces for tall pillars may be due to the bending of the pillars. The bending ability of the pillars depends on the height and

the aspect ratio of the pillars. As the width of the pillars is the same ($500 \mu\text{m}$), short pillars thus bend less than tall pillars under the same shear force. The extent to which the pillars can bend by the sliding or friction force (F_F) of the probe can be estimated by beam bending theories, which describe how the height (H), diameter (D) and second moment of area (I) of a beam influence the maximum deflection (δ): $\delta = F_F H^3 / 3EI$ with E the Young's modulus and $I = \pi D^4 / 4$ (schematically shown in Figure 3.5). [28–30] The absolute values for δ we find, are in the order of $20 \mu\text{m}$ for the H_{500} pillars. Pillars that are three times larger in height (e.g. H_{1500} compared to H_{500}) will show a 30-fold increase in deflection δ at the same applied force. The much larger deflection of the tallest pillars makes that the side of the pillars also comes in direct contact with the probe, and the increased contact area may also increase the friction coefficient. Qualitatively consistent, we find an increase in the friction coefficient of H_{1500} compared to that of H_{500} of about a factor 1.3.

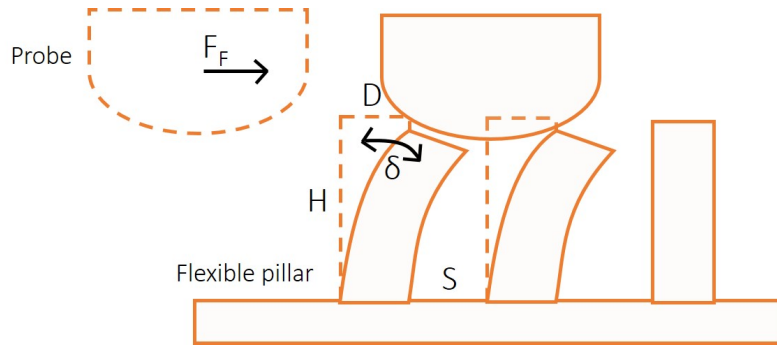


Figure 3.5: A schematic depiction of the pillar bending mechanism as caused by the contacting probe. The parameters used to estimate the deflection angle δ of the pillar are indicated in this Figure.

Asperity diameter: The effect of contact area

In the previous section it appeared that the observed high friction coefficients are due to the fact that tall pillars are more easily bent due to their high aspect ratio. The bending can increase the contact area, as also the pillars' sides are in contact with the probe when the pillars are bent. To test whether indeed this change in contact area can explain the changes in friction coefficient, we changed the contact area of the pillars by varying the D from $500 \mu\text{m}$ to a lower value of $250 \mu\text{m}$ and higher values of 1000 and $1500 \mu\text{m}$. By varying the pillar diameter while keeping S constant, we investigate both the effect of deformation (due to differences in aspect ratio) and the effect of contact area. In these experiments we keep the height and interpillar distance constant at $500 \mu\text{m}$ and $1000 \mu\text{m}$, respectively.

Is there a pattern? Frictional properties of micro-patterned hydrogels

As shown in Figure 3.6, we find that increasing the D increases the friction coefficient. However, the range of friction coefficients obtained by increasing the diameter is relatively small and the friction coefficient does not reach values over 0.35. The values obtained here are all higher than values obtained for a unpatterned, flat gelatin substrate ($\mu_u = 0.31$).

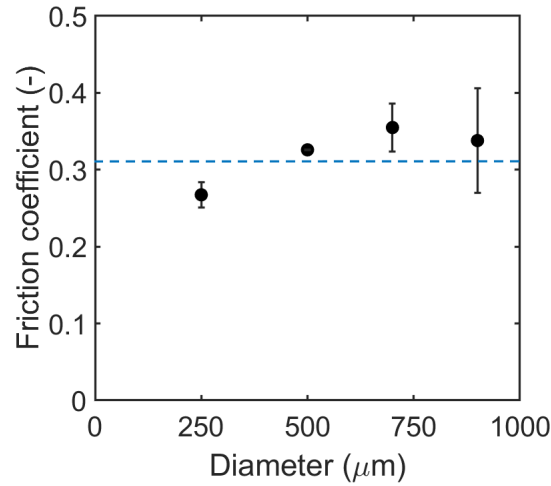


Figure 3.6: Friction coefficients of patterned surfaces with surface pillars varying in diameter from 250 μm to 900 μm . The blue line represents the friction coefficient of an unpatterned gelatin surface.

The values for the diameter series are lower than the ones observed in Figure 3.4 where we studied the effect of pillar height. This indicates that effective contact area alone is not the reason for the relatively high friction coefficients observed when increasing the pillar height. The increase in friction coefficient when we increase the pillar diameter, is likely caused by the increased contact area from 0.05 mm^2 for the narrower pillars to 0.64 mm^2 for the widest pillars. A 13-fold increase in contact area thus gives an increase in friction coefficient from $\mu = 0.27$ to 0.36. Such an increase with contact area is similar to trends seen for dry, solid surfaces [31] and for soft surfaces. [25]

When we increase the pillar diameter, we also strongly decrease the ability of a pillar to bend, as δ scales with D^4 . The maximum degree of deflection of a pillar with a diameter of 250 μm is then 16 times larger than that of a pillar with a diameter of 500 μm . While varying D , we find that the asperities with the larger deflection give lower friction, as opposed to the trend observed with the H variation. The much slender bending pillars apparently do not contribute as much to an increase in contact area: their smaller radius results in a smaller contact area, even when strongly bent. We suggest that pillar bending changes friction, and that the bending-related effect is radius dependent: wider pillars enhance the contact

Is there a pattern? Frictional properties of micro-patterned hydrogels

area and give an increase in friction as observed in Figure 3.4, while slender bent pillars are too narrow to create extra surface area and reduce friction.

Pillar density: Contact area and number of physical barriers

We can also change the contact area by changing the pillar-to-pillar distance S at constant D and H values. We do so by placing the pillars further away from one another while keeping the same contact area per pillar, decreasing the pillar density. The space between the centers of the pillars ranged from 555 to 2000 μm . The smallest size used here gives a distance of 55 μm between the edges of the pillars. This small distance is close to the smallest size our printer can provide, which means the distance may be larger or the pillars may actually be fully in contact. This is why we also use a surface with 600 μm distance between the pillars as a more reliable sample. The largest distance used here is similar to the estimated diameter of the contact area between the probe and a (flat) substrate (1.7 mm). Pillar height and width were both kept constant at 500 μm . The number of pillars ranged from 0.2 pillars/ mm^2 for the pillars with the largest distance between the pillars to 3.25 pillars/ mm^2 for the patterned surfaces with the smallest distance between the pillars. We find that larger spacing of the pillars (lower contact area) gives lower friction coefficients (Figure 3.7).

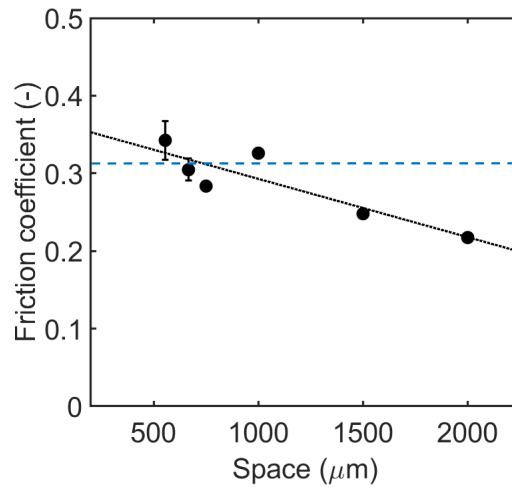


Figure 3.7: Friction coefficients of patterned surfaces varying in center-to-center distance between the pillars from 555 μm to 2000 μm . The blue dashed line indicates the friction coefficient for unpatterned gelatin.

In the case of smaller interpillar distance and thus high pillar densities and large contact areas, high friction coefficients are found, in agreement with the results shown in Figure 3.6. As already discussed, samples with high pillar density and thus larger contact areas, give similar friction coefficients as the native gelatin

Is there a pattern? Frictional properties of micro-patterned hydrogels

surfaces without pillars with values around 0.31, which is likely due to similarities in the total contact area.

It has to be noted that due to the lower number of pillars, also the shear load distribution per pillar changes. The pillars on the surfaces with a low pillar density will have to sustain a higher load per pillar which increases the likelihood of pillar bending. This bending could have an additional effect on the friction coefficient, as bending would lead to more probe resistance and higher friction forces due to contact area enhancement, as described above. The results indicate that even for higher loads per pillar (easier bending) in the case of larger pillar distance, friction coefficients are still lower than for lower loads per pillar. This confirms that in this case, changes in contact area influence the friction coefficient more than bending events.

Friction coefficient and contact area

The previous results suggest that the frictional behavior of soft patterned hydrogels is mostly determined by their net contact area. To test whether contact area is indeed the main source of dissipation, we compare the previously discussed data on samples with the same contact area, but with a different number of pillars per mm^2 . These samples are a combination of the pillars varying in diameter, D , (blue squares) and varying in space between the pillars, S , (black circles). The results are displayed in Figure 3.8.

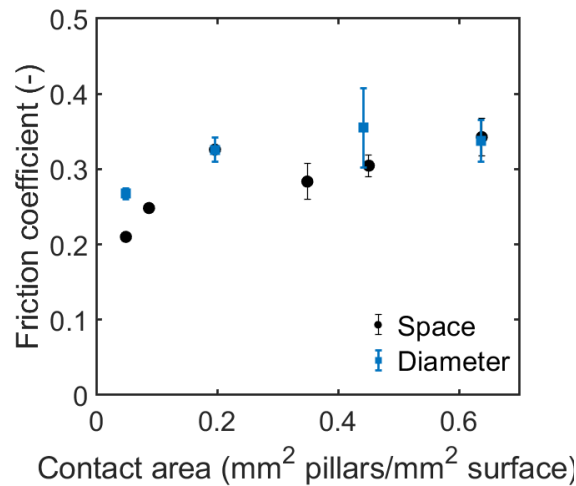


Figure 3.8: Friction coefficients of hydrogel-hydrogel friction with patterned substrates as function of the contact area of the surface asperities. Substrates are decorated with pillars either differing in pillar diameter, D , or in space, S , between the pillars.

Is there a pattern? Frictional properties of micro-patterned hydrogels

In general, we observe that the friction coefficient increases with contact area for both series. However, the data from the D variation experiment show lower friction coefficients. Friction coefficients are therefore not only determined by contact area. The absolute number of barriers appears to be relevant as well: reducing the total surface area by decreasing S is more effective in reducing μ . Thus far, we have identified the following potential parameters to contribute to the friction coefficient in our patterned hydrogels: (I) the total contact area, (II) the number of physical barriers to overcome, (III) pillar bending, which affects the net contact area.

Star patterned substrates: effect of pillar positioning

The reduction of μ with larger spacing cannot go on monotonically with increasing S : at some point the pillars are spaced so far apart that the contact area of the hemi-spherical probe at given normal force is small enough to fit in between two pillars entirely. To test this limit and create a better understanding of the friction mechanisms of patterned hydrogel surfaces, we designed patterned surfaces, for which the probe travels over a smaller number of pillars, and even over one row of pillars at a time. With individual pillar-probe interaction becoming relevant, we need to guarantee that the probe approaches all the pillars from the same angle. To achieve this, we designed surfaces with a radial, star-like pattern instead of a square-like pattern. This star pattern ensures that the probe will slide over the symmetrically placed pillars periodically. An image of the 3D designs used to print the molds for the stars-shaped pattern is shown in Figure 3.9.

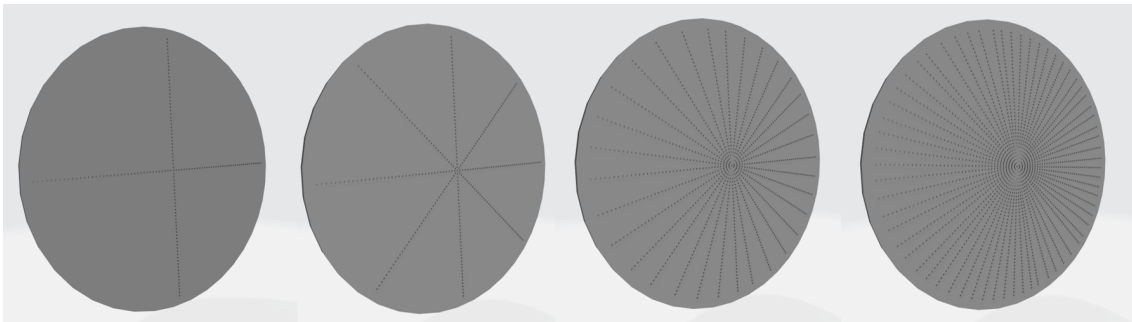


Figure 3.9: 3D designs of the star-shaped patterns. Samples were made with 4, 8, 36 and 72 rows of pillars on the surface with distances of 31, 16, 3.5 and 1.7 mm, respectively. The distance between the pillars within the rows remained constant at 1 mm.

The pillars are placed in lines that originate in the centre of the substrate, with specific (angular) distances between each line. The distance between each line at the contact region (3 cm from the center of the probe) is 1.7, 3.5, 16 or 31 mm, which corresponds to 72, 36, 8 and 4 lines of pillars, respectively. We keep both

Is there a pattern? Frictional properties of micro-patterned hydrogels

the diameter and the height of the pillars constant at $500\ \mu\text{m}$. Also here, the top of the pillar is flat. The radial distance between the pillars placed on one line is $1000\ \mu\text{m}$ (1 mm). At the normal forces used here, we previously estimated the diameter of the contact between the probe and the substrate gel to be around 1.7 mm using Hertzian deformation laws for soft surfaces in contact.[8] At a contact diameter of 1.7 mm, the probe is thus expected to constantly be in contact with pillars for the most dense star pattern as the spacing for the 72 lines pattern is also 1.7 mm. The probe is then not able to touch the base between the pillars.

For larger distances, we expect the probe to be able to contact the base between the pillars. At larger distances, the probe slides across the base, and has to overcome just one row of pillars at a time. This allows us to gain information on the effect of one separate physical barrier on the friction coefficient. The probe contact area is large enough compared to the radial pillar distance to always require the interaction with at least one pillar, at most two. Using the star patterns, we observe a strong decrease in friction coefficient as a function of the number of pillar rows (Figure 3.10).

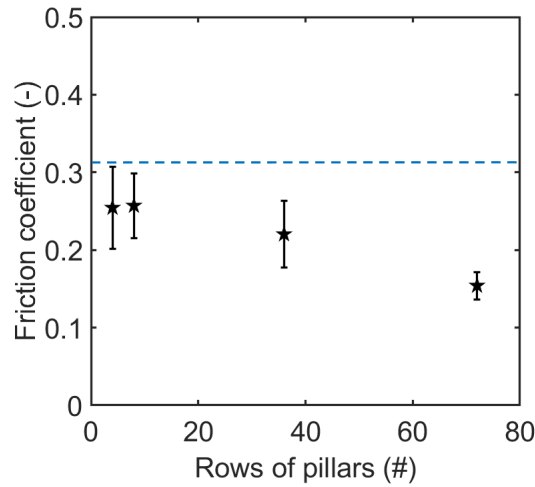


Figure 3.10: Frictional behavior of hydrogel substrates patterned with a radial pattern as a function of the number of rows of pillars. Dashed line indicates the frictional value for unpatterned gelatin-gelatin friction.

At a distance of 1.7 mm (72 rows), the friction coefficient is lower than for a larger distance of 3.5 mm (36 rows). We thus find that the friction coefficient decreases with the number of pillars, so a decrease of friction with increasing pillar-probe contact area. This is a striking opposite to what we have seen in the previous section, where we saw an increase in friction coefficient with an increasing contact area for the square patterned surfaces (Figure 3.7).

Is there a pattern? Frictional properties of micro-patterned hydrogels

We should note the relevance of the hemi-spherical probe contact area here, which is of the order of 1-2 mm. For larger number of rows, the pillar spacing is 1.7 mm and hence the probe remains in contact with pillars while essentially sliding directly from pillar to pillar without touching the base. This explains the low frictional values measured for densely packed pillars compared to pillars with larger distances between them. At larger distances between pillars of the star pattern, when there are fewer rows of pillars, the probe starts to contact the substrate base more frequently than it touches pillars, and more probe-base contact is obtained. In addition, the probe also needs to “climb” over the height of an entire pillar. Due to the increased probe-base contact area, the friction coefficient approaches that of an unpatterned gelatin substrate ($\mu = 0.31$). Similarly, if we were to design a denser radial pillar pattern, we would expect an increase of the friction coefficient, as in that limit the probe would also start to interact with a virtually continuous gel surface. The nature of the substrate making process makes it however challenging to obtain denser radial patterns.

The friction coefficients we measured for these star patterned surfaces are all somewhat lower than for the unpatterned hydrogel (blue dashed line in Figure 3.10). We have no clear explanation for this, but perhaps there is always a systematic reduced contact between the probe and the substrate due to the presence of pillars. Additionally, we would like to highlight that the substrate pattern is organized such that the hemi-spherical probe always moves orthogonal over a row of pillars. For the square pillar pattern, the pillar-probe interaction is much more path-specific. The effective reduction of friction of already four radial lines of pillars may point towards the relevance of this “angle of attack” on the friction coefficient.

Is there a pattern?

So far, we have seen low friction coefficients when the distance between substrate pillar shaped asperities is large and the contact area between the pillars and the probe is low, providing that the probe does not touch the hydrogel base. We find high friction coefficients when the number of pillars is too high leading to high contact areas (Figure 3.7). When the number of pillars is too low, probe-base contact occurs, which increases friction as we observed for the star-shaped pattern with 4 rows of pillars in Figure 3.10. We summarize these findings in Figure 3.11 where we have combined the results of Figure 3.7 and Figure 3.10. In this figure, we see that an optimum (low) friction coefficient exists when the pillars are at sufficient distance to create moderate contact areas while avoiding base contact. Additionally, low friction coefficients are expected when the effective pillar height is

Is there a pattern? Frictional properties of micro-patterned hydrogels

low enough to keep the influence of bending events limited, and when the number of physical barriers is relatively small. These results demonstrate the impact of the different roughness parameters (height, distance, and diameter) on the frictional properties of soft materials. Limited contact between the probe and substrate, and a low number of pillars acting as physical barriers as well as limited insertion of the probe between the asperities seem crucial to obtaining low friction coefficients.

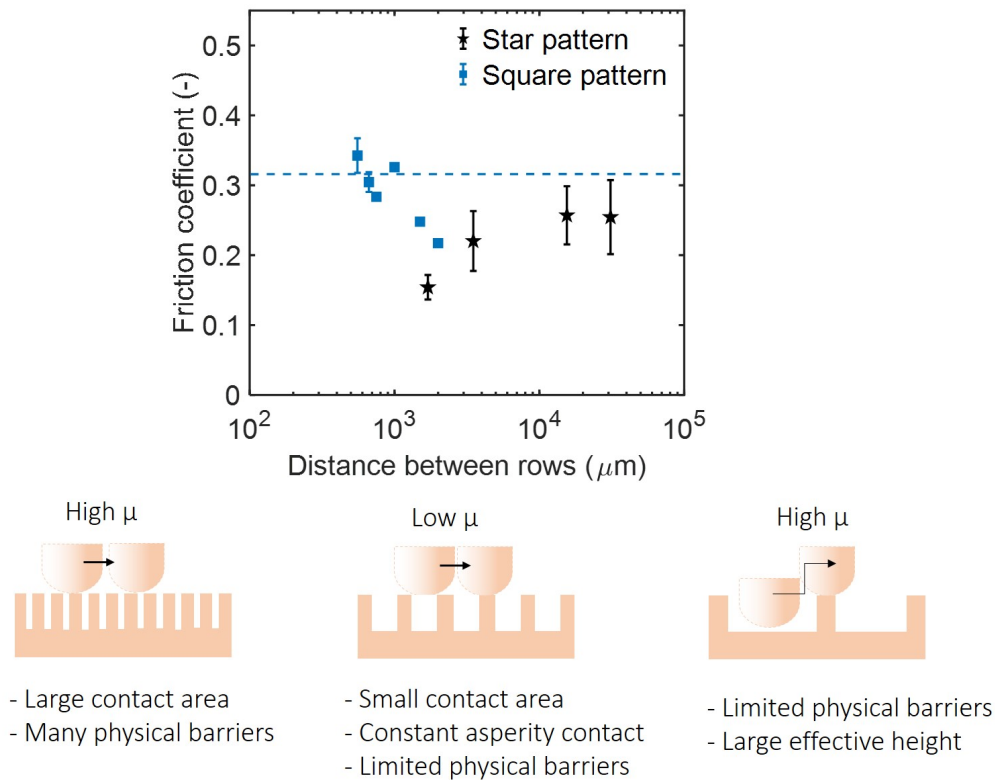


Figure 3.11: Results of the hydrogel patterns varying in space for the square pattern and star pattern combined together with a schematic view of the proposed frictional mechanism. The data shown here originate from Figures 3.7 and 3.10. We show the friction coefficient of an unpatterned gelatin gel by means of a blue dashed line.

Single pillar friction coefficient

For our patterned surfaces we find that the larger effective height of a pillar (e.g. from the base over an entire pillar rather than sliding from pillar top to pillar top), the higher overall friction coefficient is measured. We observed this using both the tall pillars and short pillars where tall pillars gave higher friction coefficients than short pillars and the star pattern discussed in the previous section. The friction coefficient is calculated from the normal force and torque values measured by the rheometer during rotation. A closer look at the deflection angle(θ)-dependent signal of both F_N and F_F reveals that pillars indeed obstruct the motion of the probe and temporarily lead to higher frictional values. While the probe is sliding over the base or over the pillars, we measure friction events at different locations on the hydrogel surface. If we look at the torque signals for our four different patterns (4, 8, 36 and 72 rows of pillars), we can see exactly when the probe collides with a pillar by the distinct peaks seen in the torque signal (Figure 3.12). This peak pattern shows an increasing number of sharp peaks as the number of rows increases. For the 72-row substrate, the sampling of the torque and normal force signal by the rheometer becomes too slow to distinguish individual peaks. The torque signal also increases with increasing indentation depth or smaller gap size, shown here in a darker shade of blue. Also, as our measurements are gap controlled, the probe is not always in contact with the surface due to natural height variations on the hydrogel surface. We see this in Figure 3.12 as the torque occasionally drops to values of zero, indicating little or no contact between the probe and the substrate.

Using the torque values and the normal values, we can calculate the friction coefficient separately for each peak for the pattern with 4 rows and 72 rows. The friction coefficient based on the three tallest peaks of the 4 line pattern (at the beginning, halfway and at three quarters of a rotation), provides values of 0.35, 0.63 and 0.20. On the 72 line pattern, the friction coefficients for peaks at around the same deflection angle used for the 4 line pattern give values of 0.29, 0.14 and 0.17.

Is there a pattern? Frictional properties of micro-patterned hydrogels

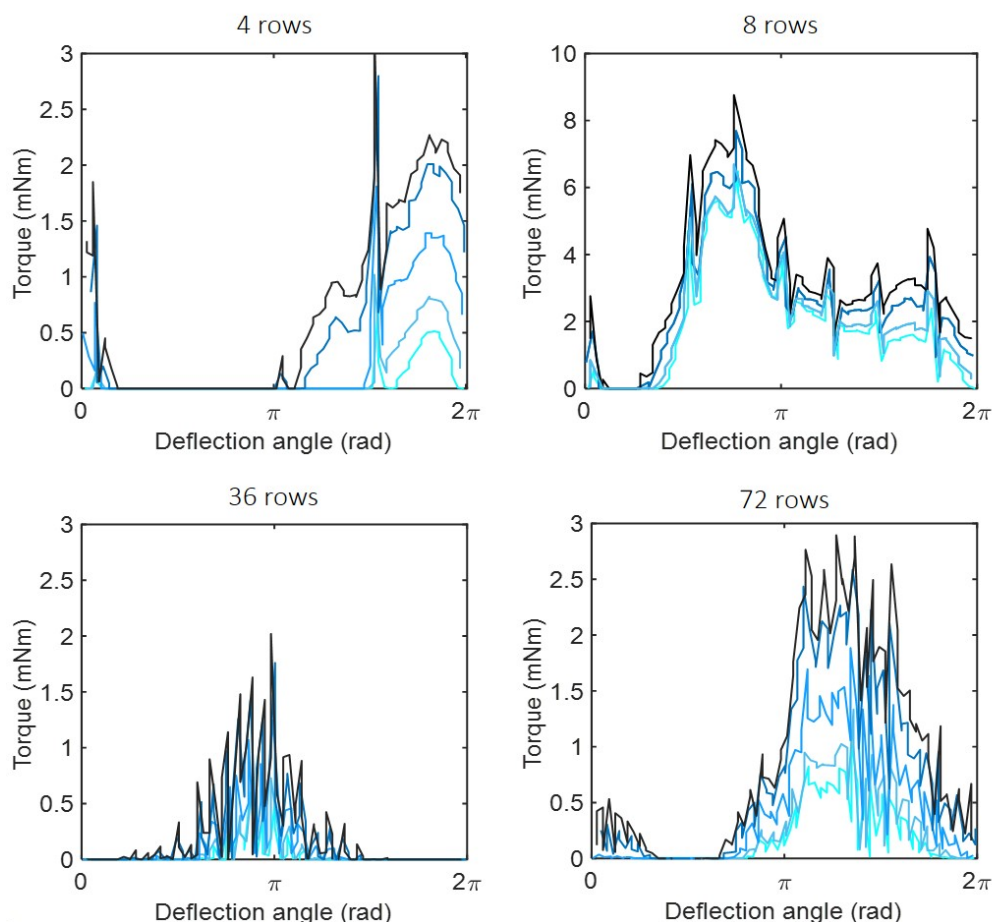


Figure 3.12: Torque signals as function of deflection angle for the star-pattern with 4, 8, 36 and 72 lines of pillars during one full rotation of the probe alongside the substrate. Darker blue colors indicate larger indentation depths. Sharp peaks suggest probe-pillar contact.

The friction coefficients of these peaks are lower than the peaks of the 4-row pattern. This shows how the friction coefficient of individual pillars contribute to the total friction coefficient. Our observations strongly suggests that the high values measured for 4 lines of pillars are due to a larger net height of the physical barrier, i.e from the base to the top of the pillar, that the probe needs to overcome when sliding over the row of pillars. A study by Zhang and co-workers using atomic force microscopy and a colloidal probe indeed showed that such “collision” events between the probe and the surface pillars are responsible for the high friction and, as also seen here, while contact with few pillars at the same time led to low friction. [32]

Is there a pattern? Frictional properties of micro-patterned hydrogels

Based on the systematic study presented here we can thus differentiate between three ways in which asperities influence the friction coefficient. (I) An optimum (low friction coefficient) is found when the number of pillars (contact area) is low, while still maintaining constant contact between the probe and the pillar thus preventing probe-base contact. (II) The friction coefficient increases when the contact area is high. This is either due to a large pillar diameter, small interpillar distance or due to enhanced contact with the side of the pillar, caused by bending of the pillars. (III) The friction coefficient also increases when the distance between the pillars is too large and the probe is able to enter the space between the pillars. The probe may then contact the base and has to climb over the entire pillar, leading to a large effective asperity height as was previously shown in Figure 3.11. To obtain the interpretation presented here, we neglect any pillar-pillar interactions that may occur. [33, 34]

Conclusions

We used 3D-printing as an affordable and accurate method of micro-patterning pillar shaped asperities to provide hydrogel surfaces of different friction coefficients. We studied the impact of individual roughness parameters such as asperity height, diameter and interpillar distance on hydrogel-hydrogel friction. Using this method, we demonstrated that the friction coefficient of these patterned hydrogels increases with contact area and effective pillar height. The pillar height causes an increase in the friction coefficient as the probe is essentially held back by these physical pillars. Additionally, tall pillars may bend, leading to an increase in the contact area. By studying the frictional behavior of individual pillars, we observed that the friction coefficient is lowest when probe insertion between the pillars is limited and the probe can slide directly from one asperity to another without touching the hydrogel base between the pillars. We measure high friction coefficients when the probe touches the base and needs to overcome a large physical barrier by climbing over a pillar while colliding with the side or top of the pillar. We thus identified contact area, effective pillar height and probe-base contact as the main contributors to high friction coefficients in soft patterned hydrogels. The findings presented here can be used to design pillared soft surfaces with controlled frictional behavior that have applications in medical implants, biomimetic robots and food materials.

References

1. Denny, D. The influence of load and surface roughness on the friction of rubber-like materials. *Proceedings of the Physical Society. Section B* vol. 66, 721 (1953).
2. Porgess, P. & Wilman, H. The dependence of friction on surface roughness. *Proceedings of the Royal Society of London. Series A. Mathematical and Physical Sciences* vol. 252, 35–44 (1959).
3. Briggs, G. & Briscoe, B. Effect of surface roughness on rolling friction and adhesion between elastic solids. *Nature* vol. 260, 313–315 (1976).
4. Kusy, R. P. & Whitley, J. Q. Effects of surface roughness on the coefficients of friction in model orthodontic systems. *Journal of Biomechanics* vol. 23, 913–925 (1990).
5. Bhushan, B. Contact mechanics of rough surfaces in tribology: multiple asperity contact. *Tribology letters* vol. 4, 1–35 (1998).
6. Zappone, B., Rosenberg, K. J. & Israelachvili, J. Role of nanometer roughness on the adhesion and friction of a rough polymer surface and a molecularly smooth mica surface. *Tribology Letters* vol. 26, 191 (2007).
7. Yashima, S., Takase, N., Kurokawa, T. & Gong, J. P. Friction of hydrogels with controlled surface roughness on solid flat substrates. *Soft Matter* vol. 10, 3192–3199 (2014).
8. Rudge, R. E. D., Scholten, E. & Dijkman, J. A. Natural and induced surface roughness determine frictional regimes in hydrogel pairs. *Tribology International* vol. 141, 105903 (2019).
9. Selway, N. & Stokes, J. R. Insights into the dynamics of oral lubrication and mouthfeel using soft tribology: Differentiating semi-fluid foods with similar rheology. *Food research international* vol. 54, 423–431 (2013).
10. Ranc, H., Servais, C., Chauvy, P.-F., Debaud, S. & Mischler, S. Effect of surface structure on frictional behaviour of a tongue/palate tribological system. *Tribology International* vol. 39, 1518–1526 (2006).
11. Kamperman, M., Kroner, E., del Campo, A., McMeeking, R. M. & Arzt, E. Functional adhesive surfaces with “gecko” effect: The concept of contact splitting. *Advanced Engineering Materials* vol. 12, 335–348 (2010).
12. Bhushan, B. & Tang, W. Surface, tribological, and mechanical characterization of synthetic skins for tribological applications in cosmetic science. *Journal of Applied Polymer Science* vol. 120, 2881–2890 (2011).
13. Walker, P. & Gold, B. The tribology (friction, lubrication and wear) of all-metal artificial hip joints. *Wear* vol. 17, 285–299 (1971).
14. Damm, P., Bender, A., Duda, G. & Bergmann, G. In vivo measured joint friction in hip implants during walking after a short rest. *Plos one* vol. 12, e0174788 (2017).
15. Nečas, D. *et al.* Observation of lubrication mechanisms in knee replacement: A pilot study. *Biotribology* vol. 17, 1–7 (2019).
16. Prinz, J., De Wijk, R. & Huntjens, L. Load dependency of the coefficient of friction of oral mucosa. *Food Hydrocolloids* vol. 21, 402–408 (2007).
17. Chan, D. & Stachowiak, G. Review of automotive brake friction materials. *Proceedings of the Institution of Mechanical Engineers, Part D: Journal of Automobile Engineering* vol. 218, 953–966 (2004).

18. Stinson, K. *et al.* *Coefficient of friction between tires and road surfaces* in *Highway Research Board Proceedings* (1934).
19. Persson, B. N. *Sliding friction: physical principles and applications* (Springer Science & Business Media, 2013).
20. Hendriks, C. & Franklin, S. Influence of surface roughness, material and climate conditions on the friction of human skin. *Tribology Letters* vol. 37, 361–373 (2010).
21. Derler, S., Gerhardt, L.-C., Lenz, A., Bertaux, E. & Hadad, M. Friction of human skin against smooth and rough glass as a function of the contact pressure. *Tribology International* vol. 42, 1565–1574 (2009).
22. Svahn, F., Kassman-Rudolphi, Å. & Wallén, E. The influence of surface roughness on friction and wear of machine element coatings. *Wear* vol. 254, 1092–1098 (2003).
23. Yu, J. *et al.* Friction and adhesion of gecko-inspired PDMS flaps on rough surfaces. *Langmuir* vol. 28, 11527–11534 (2012).
24. Persson, B. N. J. Relation between Interfacial Separation and Load: A General Theory of Contact Mechanics. *Phys. Rev. Lett.* vol. 99, 125502 (12 2007).
25. He, B., Chen, W. & Wang, Q. J. Surface texture effect on friction of a microtextured poly (dimethylsiloxane) (PDMS). *Tribology Letters* vol. 31, 187 (2008).
26. Hoare, T. R. & Kohane, D. S. Hydrogels in drug delivery: Progress and challenges. *Polymer* vol. 49, 1993–2007 (2008).
27. Yoon, E.-S. *et al.* Tribological properties of bio-mimetic nano-patterned polymeric surfaces on silicon wafer. *Tribology Letters* vol. 21, 31–37 (2006).
28. Kings, T. “Advanced mechanics of materials” 5th edition, AP Boresi, RJ Schmidt and OM Sidebottom. *Strain* vol. 29, 141–142 (1993).
29. Gere, J. & Timoshenko, S. *Mechanics of materials*, 1997. *PWS-KENT Publishing Company* vol. 534, 4 (1997).
30. Alvarado, J., Comtet, J., de Langre, E. & Hosoi, A. Nonlinear flow response of soft hair beds. *Nature Physics* vol. 13, 1014–1019 (2017).
31. Johnson, K. Regimes of elastohydrodynamic lubrication. *Journal of Mechanical Engineering Science* vol. 12, 9–16 (1970).
32. Zhang, X., Wang, X., Kong, W., Yi, G. & Jia, J. Tribological behavior of micro/nano-patterned surfaces in contact with AFM colloidal probe. *Applied surface science* vol. 258, 113–119 (2011).
33. Al-Bender, F., Lampaert, V. & Swevers, J. A novel generic model at asperity level for dry friction force dynamics. *Tribology Letters* vol. 16, 81–93 (2004).
34. Dies, L., Restagno, F., Weil, R., Léger, L. & Poulard, C. Role of adhesion between asperities in the formation of elastic solid/solid contacts. *The European Physical Journal E* vol. 38, 130 (2015).

PART II

Particle lubrication



4

**Uncovering friction dynamics
using hydrogel particles as
soft ball bearings**

Abstract

Rolling ball bearings are widely known and applied to decrease friction between two surfaces. More recently, hydrogel-hydrogel tribopairs have also revealed good but rather complex lubrication properties. Here, we combine both mechanisms to elucidate the way soft spherical particles have nontrivial rate-dependent lubrication behavior. Unlike Newtonian lubrication or dry solid friction, hydrogel particles in suspension transition through four frictional regimes as function of sliding velocity. We relate the different regimes to the deformation of the particles at different gap sizes, which changes the effective contact area between the sliding surfaces. By systematically varying the particle characteristics and the surface properties of the sliding surfaces we assign potential mechanisms for each of the different lubricating regimes as function of velocity: (I) relatively high friction due to particle flattening and direct contact between interacting bodies, (II) decrease of friction owing to the presence of rolling particles, (III) large inflow of particles in a confined space leading to compressed particles, and (IV) the formation of a thick lubricating layer. Using these suspensions with soft, deformable particles as a ball-bearing system, we provide new insights into soft material friction with applications in emulsions, powders, microgels or other granular materials.

This chapter was published as:

Rudge, R.E.D., Van De Sande, J. P., Dijksman, J. A., and Scholten, E. (2020). Uncovering friction dynamics using hydrogel particles as soft ball bearings. *Soft Matter* vol. 16, no. 15, 3821–3831.

Introduction

Friction is of importance for the functionality of many different mechanical systems such as car tires, steel bearings, biomedical implants, and even human joints. There are numerous mechanisms known to influence friction between two surfaces. In general, μ can depend on velocity, normal force, adhesion, roughness as shown in the previous chapters. A simple strategy to obtain lubrication is to keep sliding surfaces from physically touching each other. It should be noted that low friction can also be obtained when surfaces are in contact with one another. In the case of hydrogels, it has been shown that a decrease in friction can be obtained with increased contact areas. [1, 2] To decrease the high frictional values caused by increased contact, the contact area between surfaces in motion can be minimized in many ways. The simple presence of a thin lubricating fluid layer or polymer coating can already decrease the friction coefficient by orders of magnitude by preventing the surfaces to come into close contact. [3, 4] Additionally, solid spheres are able to decrease friction (Figure 4.1a).

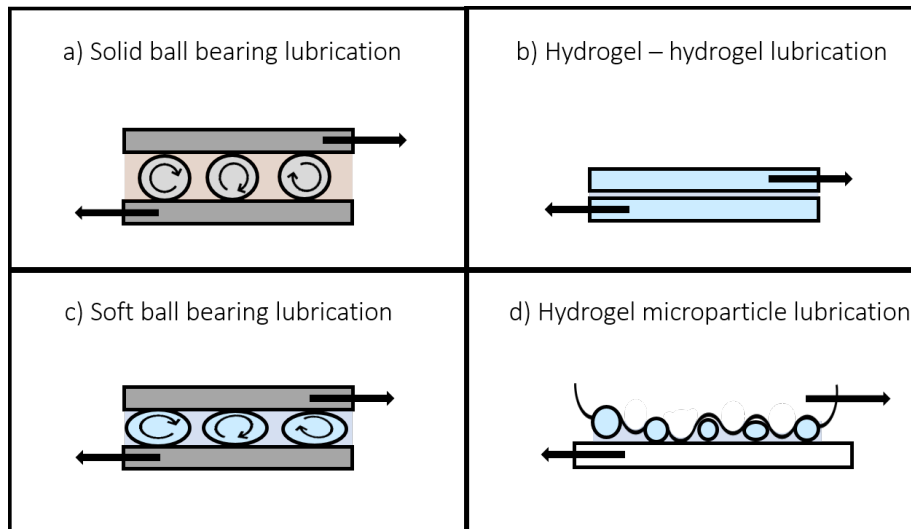


Figure 4.1: Examples of frictional mechanisms for different combinations of surfaces and lubricants. a) The traditional solid ball bearing lubrication involves rolling spheres between hard surfaces, sometimes grease-lubricated. b) Hydrogel-hydrogel friction with two hydrogels sliding directly against one another. There is commonly a thin layer of water present between the soft surfaces. c) Hydrogel spheres as soft ball bearings. Here deformability strongly influences the friction coefficient. d) Hydrogel particles in contact with a hard/soft rough surface.

Solid spheres between two sliding surfaces can decrease friction by separating the sliding surfaces. Although the spheres themselves are in direct contact with both surfaces, their ability to roll provides a lubrication mechanism. This is known as the ball-bearing mechanism [5–7] or third body friction [8] and this mechanism plays an important role in most machinery with rotating parts and can be found in applications from kitchen appliances [9] to space crafts. [10] Due to the

Uncovering friction dynamics using hydrogel particles as soft ball bearings

smoothness of the sphere's surface, the presence of rolling bearings can reduce the friction coefficient, much more compared to sliding surfaces in direct contact. [11] By using ball bearings that are by themselves of very low (rate-dependent) friction, one can ask how the bearing contact friction affects the ball-bearing mechanism. Second, ball bearing or substrate deformation is often not considered in ball-bearing mechanisms, as ball bearings are typically stressed much below their internal strength. Deformation of ball bearings might significantly affect the lubrication behavior of ball bearings. For soft, slippery ball bearings we can thus expect nontrivial lubrication behavior. To explore this potentially nontrivial lubrication behavior, we consider hydrogels. Hydrogels have become immensely popular in the past decades and these materials have, more recently, been the subject of a broad range of frictional studies. [1, 12–15] Hydrogels exhibit unique frictional behavior and friction coefficients as low as 0.01 have been reported for hydrogel-on-hydrogel friction (Figure 4.1b) as we have already discussed in **Chapters 2 and 3**. [2, 16] This is similar to friction coefficients in synovial joints. The exact mechanism by which these low friction coefficients in hydrogels come about is still under debate with many proposed mechanisms including the presence of hydrated polymeric brushes on the surfaces. [13, 17–20]

Here, we present a hybrid lubricant that combines the rolling ability of spherical particles with the slipperiness of hydrogels (Figure 4.1c) and show that using soft hydrogel particles as ball bearings indeed induces unique lubricating properties. To achieve this, we use a suspension containing custom-made gelatin microparticles as a lubricant. These gelatin microparticles allow us to tune the frictional behavior by varying the particle properties, such as particle deformability and size. We show that when combined with real-life rough surfaces, soft slippery ball bearings indeed bring an additional lubrication effect. (Figure 4.1d) By systematically exploring the role of different particle characteristics, we elucidate the microscopic mechanism behind the lubricating behavior of soft hydrogel suspensions.

Particle suspensions have been studied before for their lubricating efficiency. Previous studies have addressed the effect of the polymer content of the lubricating particles [21], particle volume fraction in suspension [22], along with changes in the continuous phase [23, 24] and the tribopairs used. [25] From these studies it becomes evident that hydrogel particles enhance the lubrication behavior over a range of velocities and past authors have proposed several different mechanisms to interpret their findings. While it was suggested that the particles are not yet present between the surfaces at low velocities [21, 26], this interpretation contradicts the findings of other authors. [27] The different results obtained by various

authors may be in part due to the use of different tribometers and different types of particles. As a tribological measurement strongly depends on the properties of the entire system (measuring device, lubricant type, velocity, etc.), [28, 29] comparing results of different studies is often difficult. In the present work, we present a systematic study highlighting the rate-dependent dynamics of hydrogel ball-bearing lubrication. We vary the volume fraction of the particles in suspension, the deformability of the hydrogel particles, and the particle size, and ensure that all measurements were carried out under the same conditions. In addition, we show the importance of the surface roughness of the interacting surfaces on the frictional behavior over a range of velocities. Our soft particles show frictional behavior that deviates from fluid lubricated systems as commonly described by means of a Stribeck curve which predicts a boundary, mixed and hydrodynamic regime. [11] In the case of particle suspensions, four or even more frictional regimes can be observed. [21, 28] The exact mechanisms behind the frictional behavior of soft particle suspensions are however not fully understood. [26, 28, 30]

To contribute to a better general understanding of soft particle lubrication, we introduce gelatin microparticles as soft ball-bearing spheres. The deformability of the particles introduces the four rate-dependent regimes for rolling lubricating particles. We discuss possible underlying mechanisms for the different regimes. Overall, our soft sphere suspensions show that limited contact between the sliding surfaces gives rise to easy sliding and low friction coefficients. This is the case for high volume fraction suspensions, hard particles, and large particles, as these samples are well able to separate the sliding surfaces. The suspension of soft spherical particles we introduced can function as a model system to thoroughly understand the frictional behavior of powders, pastes, and suspensions commonly used in agriculture, pharmaceuticals, and foods.

Experimental section

Gelatin Microparticle Preparation

We use gelatin microparticles (Figure 4.2) as our soft hydrogel particles. To obtain the gelatin microparticles, we first make gelatin solutions of the relevant weight percentages (w/w%). This is done by adding gelatin powder (Type A, Sigma-Aldrich) to Milli-Q water. The mixture was shaken and left at room temperature to allow the gelatin powder to hydrate before the mixture was heated to 60 °C to dissolve the gelatin. The gelatin solution was then added in a 1:4 ratio to a mixture of sunflower oil and 2.5 wt% emulsifier polyglycerol polyricinoleate (PGPR) at 60 °C. A gelatin solution-in-oil emulsion was created by premixing the gelatin solution with the oil-PGPR mixture for 15 minutes using a magnetic stirring bar. The premixed emulsion was further homogenized using rotor-stator homogenization (IKA Ultra Turrax) after which the emulsion was immediately cooled down in an ice bath to induce gelation of the gelatin and create the hydrogel particles. Mixing time and mixing speed was varied to alter the droplet size. A complete overview of the mixing times and speeds used for each sample can be found in Table 4.1. To collect the gelatin hydrogel particles, the bulk amount of oil was removed by centrifugation for one cycle of 30 minutes at 16000 rpm and 4 °C. The residual oil was removed by dispersing the gelatin microparticles in acetone overnight.

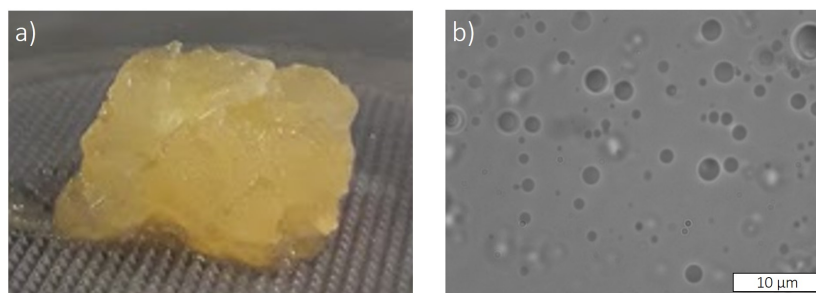


Figure 4.2: a) Densely packed (“100%”) gelatin microparticle suspension made with 15 wt% gelatin placed on a 50 mm serrated rheometer plate. b) Microscopic image of diluted gelatin microparticle suspension in water.

Acetone with the dissolved oil was removed by filtration, and further drying by air resulted in a dry powder. To prepare the hydrogel particle suspensions, dried particle powder was added in an excess of water to rehydrate the particles. The rehydration returns the particles to their original spherical form and can be done repeatedly. To avoid agglomeration of the hydrogel particles, we homogenized the suspension for 1 minute using an IKA Ultra Turrax and then for four cycles (one cycle at 40 bar followed by three cycles at 80 bar) using a LAB Homogeniser (Delta Instruments). To confirm the particles remained spherical after treatment, we

imaged the particles using brightfield microscopy (Figure 4.2b). To further increase the hardness of certain microgel particles, we chemically cross-linked gelatin using the treatment described in **Chapters 2 and 3**. [2] After filtration, we obtained a densely packed hydrogel particle suspension, which was used for rheological and tribological measurements. We refer to this densely-packed suspension as “100%”, which refers here to maximum packing. The actual volume fraction of particles is much lower, as the maximum packing of spherical, monodisperse particles is theoretically between 64 and 74%. [31] In reality, due to the polydisperse and deformable nature of the particles, the volume fraction may be slightly higher; we hence refrain from making claims about the specific value of the packing fraction and label it as “100%”. This densely packed 100% suspension is diluted with Milli-Q water to obtain 50%, 25%, and 10% of the maximum packing by weight.

Young’s moduli

The stiffness of the microparticles was estimated by measuring the elastic modulus of macroscopic gels, assuming that the properties of the gels at the two different length scales are comparable. Gelatin gels with the same ingredients as used for the particles were cut into disks of 26 mm in diameter with a height of 20 mm. A uniaxial compression was performed using a TA.XT Plus Texture analyzer (Stable Micro Systems Ltd) loaded with a 50 kg load cell and equipped with a disk-shaped acrylic indenter of 100 mm diameter moving at a speed of 1.0 mm/s. We determined the stress-strain ratio in the linear regime to obtain the Young’s modulus for samples of 5, 10, 15, 20, and 25% (w/w) of gelatin.

Particle Size

The size distribution and polydispersity of the gelatin hydrogel microparticles were investigated using static light scattering (Malvern Mastersizer 2000 (Malvern Instruments Ltd.)). The average particle size was determined by the volume-weighted mean which is referred to as the $D[4,3]$ value. Additionally, particle shape and size were examined using bright-field optical microscopy (Zeiss Axioskop 50 + AxioCam HRc) with a 63x objective oil lens. To obtain clear and informative microscopy images, the samples were diluted with MilliQ water with a dilution ratio of 1:9 as displayed in Figure 4.2b.

Rheological Properties

The rheological properties of the densely packed hydrogel particle suspensions were determined using an Anton Paar MCR 502 Rheometer equipped with a plate-plate

Uncovering friction dynamics using hydrogel particles as soft ball bearings

Table 4.1: An overview of the preparation methods used to obtain gelatin microparticles of different volume fractions, particle deformability (Young’s modulus, (YM)) and particle size.

Sample	Gelatin concentration (wt%)	Young’s Modulus (kPa)	Mixing time and speed
Microparticle content			
“100%”	15	150	10 min, 6000 rpm
“50%”	15	150	10 min, 6000 rpm
“25%”	15	150	10 min, 6000 rpm
“10%”	15	150	10 min, 6000 rpm
Microparticle deformability			
YM50	10	50	10 min, 6000 rpm
YM90	15	90	10 min, 6000 rpm
YM150	20	150	10 min, 6000 rpm
YM500	15	500	10 min, 6000 rpm
Microparticle size			
Size	15	150	15 min, 20000 rpm
Medium	15	150	10 min, 6000 rpm
Large	15	150	5 min, 500 rpm

geometry (measuring plate PP50/P2 profiled 1x0.5 and Inset 50 mm profiled plate) at 20 °C. Serrated plates were used to reduce the influence of wall slip. The sample was placed on the serrated plate and the viscosity was measured as a function of decreasing shear rate of 100-0.1 s⁻¹ (logarithmic ramp) during 468 seconds.

Tribological Properties

The tribological properties of densely packed gelatin hydrogel particle suspensions were investigated using an Anton Paar MCR 302 rheometer with a tribocell setup (measuring shaft BC 12.7 with a spherical glass probe (diameter: 12.7 mm) and three cylindrical polydimethylsiloxane (PDMS) substrates (diameter: 6 mm height: 6 mm) as schematically displayed in Figure 4.3. The rough surface of the glass probe has asperities of sizes ranging between 10 and 100 μm as visualized using a light microscope (section Surface-particle interactions). From atomic force microscopy (AFM) measurements, we estimate the surface asperities of the PDMS substrate to be well below 1 μm. Our measurements were performed at a fixed normal load of 1 N and a temperature of 20 °C. Using these settings we ensure that the hydrogel particles do not melt or fracture. At this normal force, the diameter of the contact area is estimated to be 2.2 mm using Hertzian contact mechanics for a spherical object with a modulus of 50 GPa and a flat plane with a modulus of 3 MPa. The corresponding contact pressure is then around 0.4 MPa.

Each measurement consisted of four measuring intervals, in which the rotation speed was logarithmically increased from 0.1 to 1000 rpm (approximately 0.05 to 500 mm/s) in the first and third interval and decreased from 1000 to 0.1 rpm in the second and fourth interval, respectively. The duration of one interval was 300 s, a complete measurement lasted 1200 s. The friction coefficient (μ) is determined using the frictional force (F_F) and the normal force (F_N) as shown in equation 4.1.

$$\mu = F_F / F_N \quad (4.1)$$

The results of the first interval consistently deviated from those from subsequent intervals. This is likely because the sample was not fully entrained between the surfaces or because the system had simply not arrived at an equilibrium state. The results of the first interval were therefore discarded, and only results from the second, third and fourth interval were used for data analysis as these intervals were highly reproducible. The samples were measured in triplicate. Results of particle suspensions presented in the same data set are measured with the same PDMS and glass probe pairs to minimize the effect of small differences in the (surface) properties of the probe and the substrates.

Uncovering friction dynamics using hydrogel particles as soft ball bearings

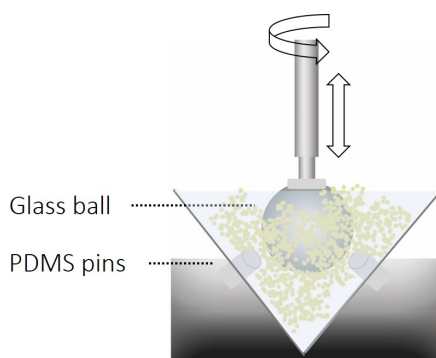


Figure 4.3: Anton Paar tribocell equipped with a rough glass ball rotating against flat PDMS pins. The sample is placed in the cup and the velocity and normal force is controlled and monitored. The friction coefficient is obtained from the ratio between the friction force and the normal force as described in equation 4.1.

Results

To explore the lubrication properties of soft particles between relatively hard surfaces, we use hydrogel microparticle suspensions. We measure the friction coefficients using a tribometer equipped with a glass ball and polydimethylsiloxane (PDMS) pins. We first show friction curves for our suspensions at maximum packing fraction, here referred to as 100% (Figure 4.4). The particles in the suspension contained 15% gelatin and had an average particle size of $8\text{ }\mu\text{m}$. We compare our gelatin particle suspension to a gelatin solution containing the same total gelatin concentration. Both the gelatin solution and the gelatin particle suspension give much lower friction coefficients than water. Gelatin can, both in the form of a biopolymer solution and as a solid particle suspension, reduce the friction coefficient efficiently. This is not surprising, as biopolymers are known to give low friction coefficients. [2, 13, 32–34] As can be seen, the friction coefficients for both gelatin samples are both similarly low, although the shape of the curves is rather different.

Differences in friction coefficient are often driven by the viscosity. [24, 35–38] These hydrogel particle suspension, in general, has a rate-dependent viscosity; at a shear rate of 1 s^{-1} it is $12.5\text{ Pa}\cdot\text{s}$, and the gelatin solution has a viscosity of $12\text{ mPa}\cdot\text{s}$ at the same shear rate. Although the viscosities of both gelatin samples are very different, the samples show similar friction coefficients. Similarly, although the viscosity of the gelatin solution ($12\text{ mPa}\cdot\text{s}$) is relatively close to that of water ($1\text{ mPa}\cdot\text{s}$ [39]) the friction coefficients are very different. For such complex lubricants, the friction coefficient is not simply driven by the lubricant viscosity.

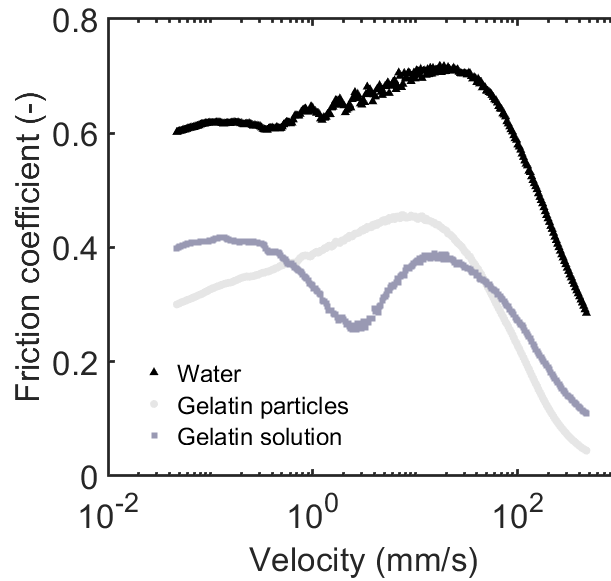


Figure 4.4: Lubrication properties of water (black), a suspension containing hydrogel particles (dark grey) and a gelatin solution with the same dry gelatin content as the particle suspension (light grey). Frictional measurements were performed between a glass probe and PDMS substrates at increasing velocity.

Comparing fluid lubrication to suspension lubrication

The gelatin solution presumably lowers friction simply by forming a thin, hydrated lubricating layer that can keep the surfaces from directly interacting. The particle suspension, however, is expected to lubricate the surfaces utilizing a ball-bearing mechanism where the individual hydrogel particles roll while collectively sustaining the load and keeping the surfaces apart (Figure 4.1). For the hydrogel particle suspension, we find that the friction coefficient transitions through multiple regimes, beyond the expected boundary, mixed and hydrodynamic regimes for most fluid lubricants, as also seen for the gelatin solution. For our particle suspensions, the friction coefficient is initially rather constant as expected in the boundary regime. We find a decrease in friction with increased speed, followed by an increase in the friction coefficient upon further increasing the velocity up until around 2 mm/s. The steep decrease after 20 mm/s again resembles typical Stribeck behavior in the mixed regime; a strong decrease in friction is seen as the thickness of the lubricating layer increases. At the maximum velocity of 500 mm/s, the system still appears to be in the mixed regime. If the system had entered the hydrodynamic regime, an increase in friction coefficient would be expected. These velocity dynamics highlight the complexity of lubricants containing soft ball bearings.

Similar frictional regimes have been found for other soft dispersed systems,

Uncovering friction dynamics using hydrogel particles as soft ball bearings

such as agar particles and whey protein solutions. [21, 26, 28] In these works, these regimes were suggested to originate from the different fluid or gel particles entering the gap separately at specific velocities. In the boundary regime, at low velocities, it is expected that only fluids or small hydrocolloids can enter the gap. [21, 26, 40] As the velocity increases, the gap size is also thought to increase, and once the gap size increases beyond a critical gap size, particles begin to enter the contact zone. [6, 30, 41, 42] This may initially lead to an increase in friction due to decreased mobility of the two surfaces. Once the lubricant is able to form a uniform layer, the friction decreases steeply as one would expect in the mixed regime. The descriptions found in literature as summarized above, however, do not fully capture the behavior we find for our gelatin particle suspensions. We find different friction coefficients for all of our samples in the boundary regime as will be described in the following sections. These results indicate that particles are already present in the gap at low velocities, suggesting that the mechanisms currently described in literature are unable to explain the dynamics in our soft hydrogel lubricant. By varying the particle volume fraction, deformability, and size of the particles we will now systematically investigate the main contributors to the frictional behavior of soft ball bearings. An overview of the hydrogel microparticle suspensions that will be described in the following sections are displayed in Table 4.2.

Uncovering friction dynamics using hydrogel particles as soft ball bearings

Table 4.2: Gelatin microparticle characteristics for the different samples used. For the deformability series, YM refers to the Young's modulus of the macroscopic gelatin disks in kPa. The viscosity (Pa·s) of the suspensions at a fixed shear rate of 1 s^{-1} is also shown here.

Sample	Gelatin concentration (wt%)	Particle size D[4,3] (μm)	Viscosity (Pa·s) at shear rate 1 s^{-1}
Microparticle content			
"100%"	15	8	12.5
Microparticle deformability			
YM50	10	6	0.1
YM90	15	8	12.5
YM150	20	11.2	127.7
YM500	15	8	76.5
Microparticle size			
Small	15	12	16
Medium	15	33	12.5
Large	15	150	20

Particle packing fraction

Friction coefficients are expected to be lowest when direct contact between interacting surfaces is minimized. For (semi-)solid spheres as ball bearings, varying the number of spheres separating the surfaces would thus be an efficient way to influence the friction coefficient. We vary the volume fraction of particles present in the suspension to study the effect of particle number on the lubricating ability of soft spheres. The particles used contained 15% gelatin and had an average particle size of $8 \mu\text{m}$. A densely packed suspension with maximum packing fraction was obtained by removing as much water as possible by means of centrifugation and subsequent draining of the fluid suspension through a filter. Figure 4.5 shows the

Uncovering friction dynamics using hydrogel particles as soft ball bearings

friction coefficients measured for the different volume fractions.

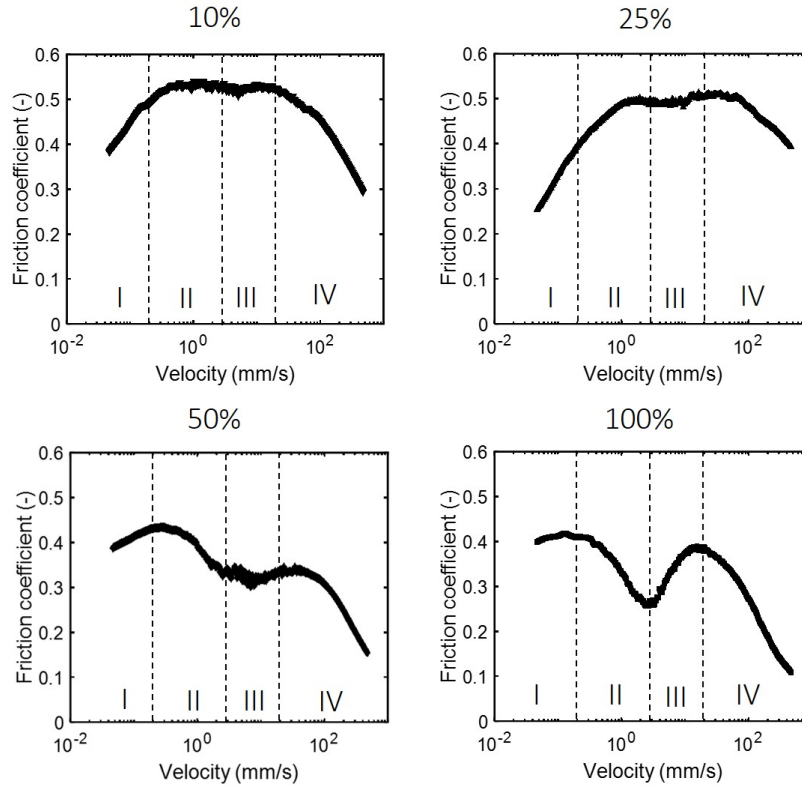


Figure 4.5: Tribological behavior of densely packed suspensions (100%) and suspensions diluted to 50%, 25% and 10%.

The sample with the highest volume fraction of hydrogel particles, “100%”, gives the lowest friction coefficients if we take all regimes into account. When the volume fraction decreases, the maximum friction coefficient increases from $\mu_{max} = 0.42$ for the 100% samples to $\mu_{max} = 0.53$ for the 10% sample. An increase in friction coefficient with a decrease in particle volume fraction has also been found previously for whey protein particles, which were made by fracturing hydrogels using a hand blender. [22] This increase in friction coefficient with decreasing particle volume fraction is not surprising as the particles are largely responsible for keeping the surfaces separated. With a decreasing volume fraction, the friction coefficient is mostly determined by the lubricating ability of water. As water has a low affinity for the hydrophobic PDMS interface, the measured friction coefficients become as high as 0.7 for pure water (Figure 4.4). When diluting the particle suspension to 10% particles, the viscosity decreases more than 600 times compared to the original densely packed suspension. The difference in frictional behavior cannot be explained by this large decrease in viscosity as was also seen in the previous section. It thus appears that the friction coefficient is a result of the lubricating ability of the ball-bearing particles and not the viscosity.

The hydrogel particle suspensions transition through multiple frictional regimes, especially at high particle volume fractions (Figure 4.5). At lower volume fractions, the four regimes are less easy to distinguish. Particularly, the separation between the second and third regime becomes less obvious and the drop in the friction coefficient in the second frictional regime decreases. This can be explained by the deformable nature of the particles. The applied load, the same in all experiments is divided over the present particles, so as the number of particles decreases, the load on each particle increases proportionally. Such a higher load would cause a higher degree of deformation of the gelatin hydrogel particles, leading to a lower ability of the particles to separate the surfaces and to roll. This decreased rolling ability and a smaller gap size leads to more asperity contact between the surfaces, which explains the higher friction coefficients for suspensions with a lower volume fraction of soft hydrogel particles (Figure 4.6). The deformability of the particles, therefore, seems to play an important role in the frictional behavior of the suspensions.

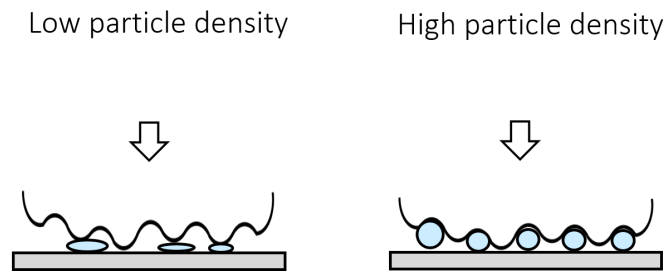


Figure 4.6: A comparison between low particle volume fractions and high particle volume fractions. At low volume fractions, the load per particle is relatively high leading to geometrical deformations of the particles. At higher volume fractions the load per particle is relatively low and particles retain their spherical shape.

Particle deformability

The ball-bearing mechanism is strongly dependent on the ability of a particle to retain its spherical shape during rolling and sliding. The results in the previous section already indicated that the load applied on each sphere influences the frictional behavior: particles that are more likely to deform give higher friction coefficients. When particles deform into an ellipsoidal shape, the contact area between the particles and the glass and PDMS surface increases, and limits rolling and sliding. To examine how the deformability of soft spheres influences their ball bearing-ability, we have varied the stiffness of the gelatin hydrogel particles in suspension. This was done by using a range of gelatin concentrations (10 to 20%) in the initial solution used to make the gelatin-in-oil emulsion, which consequently

Uncovering friction dynamics using hydrogel particles as soft ball bearings

altered the gelatin content in the hydrogel particles. As it is challenging to measure the modulus of a single soft particle on a micrometer scale, we measured the Young's modulus of macroscopically large gelatin disks of similar gelatin concentration. The Young's moduli for gels with different gelatin concentrations are given in Figure 4.7a. The suspension packing fraction used in all these experiments, was "100%" as previously defined. As the volume fraction of particles in the suspension is assumed to be the same, but the gelatin concentration within the particles differ, the total gelatin concentration of the suspension should also change proportionally.

Particle characterisation

To determine if the suspensions of different gelatin microparticles indeed had a similar volume fraction, we measured the dry weight of the particle suspensions. After evaporating the water from the suspensions overnight, we found that the dry gelatin content in 20% gelatin particle suspensions was indeed twice as much as found in the 10% particle suspension. We therefore assume that the gelatin microparticles indeed contained the desired gelatin content, i.e., no particle swelling or shrinking occurred, and that the Young's moduli of the particles in the suspension are well represented by the moduli of the macroscopic gels. The different particles had a similar particle size ranging from 5 to 11 μm , where the particles with a higher gelatin content were slightly larger than the ones with low gelatin content. We assume that the relatively small differences in average particle size have a limited effect and that these particles thus mainly vary in their deformability. An additional sample with particles with a much higher stiffness was obtained by chemically cross-linking the 15 wt% gelatin samples using glutaraldehyde. The Young's modulus of the chemically cross-linked samples (YM500) is 500 kPa as we described in **Chapter 2**. [2] This value is a factor five higher than the modulus for the original 15 wt% gelatin gel (YM90). The chemical cross-linking of gelatin did not change the particle size (Table 4.2). The viscosity profile of these particle suspensions with particles with different Young's moduli (YM) is shown in Figure 4.7b. As can be seen, the viscosity increased for stiffer particles, although the difference in viscosity between samples with particles of Young's modulus 150 kPa and 500 kPa was limited.

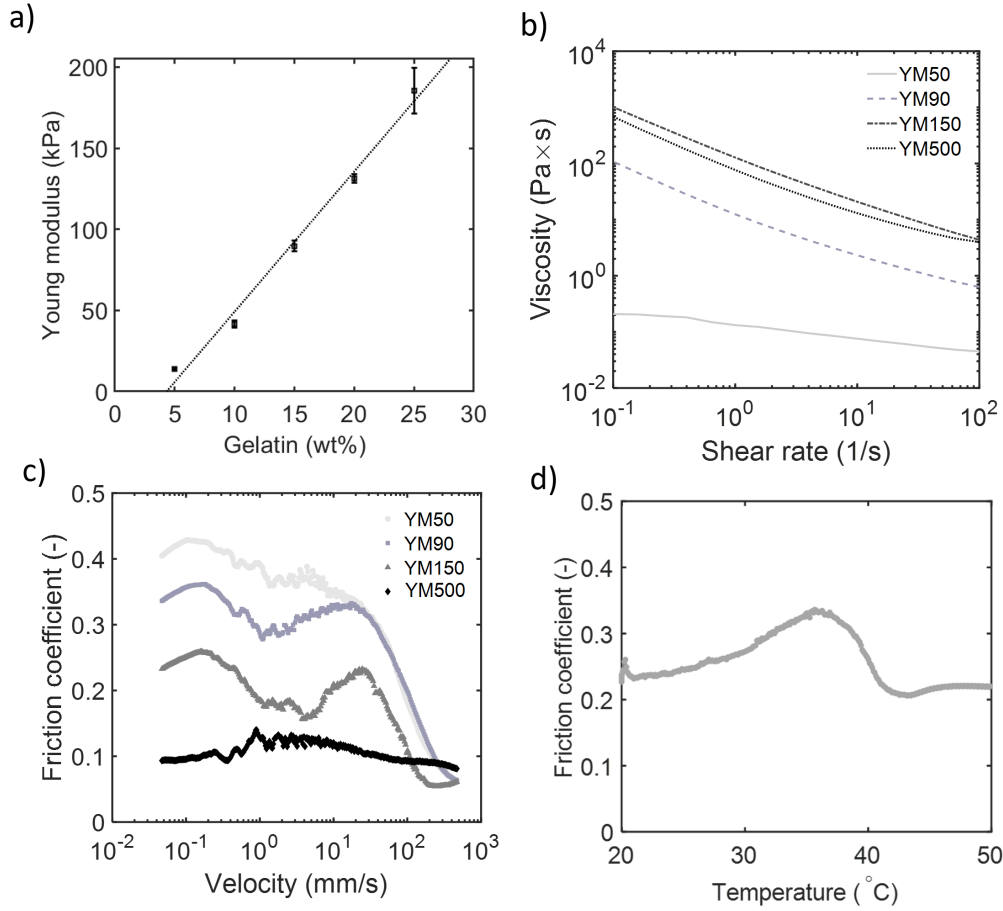


Figure 4.7: a) Young's moduli of physically cross-linked gelatin gels at different concentration. b) Flow curves of microparticle suspensions of particles with different Young's moduli. c) The friction curves for particles of Young's moduli 50, 90, 150 kPa physically cross-linked gelatin and 500 kPa chemically cross-linked gelatin. d) A temperature sweep of particles of 90 kPa at 50 mm/s.

Friction depends on particle modulus

The tribological data of the suspensions with particles varying in deformability are displayed in Figure 4.7c as a function of velocity. The softest particles with a low modulus of 50 kPa (YM50) show the highest friction coefficients, especially at lower velocities. We find that the friction coefficient decreases with decreasing particle deformability (increasing modulus). The lowest friction coefficients are found for the stiffest particles (YM500). These stiff particles are able to provide a low friction coefficient of around 0.1 already in the boundary regime. These results strongly suggest that deformability is the main contributor to the differences in frictional behavior, especially for lower velocities, i.e. boundary regime. In literature, it is often argued that in the boundary regime the gap size is too narrow for particle entrapment, and that friction is mainly dominated by the continuous fluid phase.

Uncovering friction dynamics using hydrogel particles as soft ball bearings

[21, 26] In our case, we measure distinctly different friction coefficients in regime I. For the softest particles, we find $\mu_{regime I} \approx 0.4$ and for the hardest particles, we find $\mu_{regime I} \approx 0.1$, even though the continuous fluid phase is the same. It thus appears that particles are already present between the surfaces at low velocities (regime I or boundary regime). The continuous aqueous phase would give relatively high friction coefficients, therefore water alone cannot be responsible for lubricating the surfaces in the first regime.

Interpreting the frictional curves

The suspensions containing softer particles give higher friction coefficients and appear to be less able to act as ball bearings. We expect these particles to be deformed easily during compression and shear, leading to a more ellipsoidal shaped particle. Due to this geometrical change, the particles have a decreased rolling ability, limiting the mobility of the glass-PDMS contact surfaces. This leads to high friction coefficients for the soft particles. For the stiffer, chemically cross-linked samples (YM500), the particles are hard enough to retain their spherical shape under the applied load, which gives low friction coefficients over the entire velocity range (Figure 4.7c). We also see that these particle suspensions do not display the four regimes we previously observed. Instead, the friction coefficient remains rather constant over the entire velocity range. The four regimes are present for the soft (YM90, YM150) particles. For the softest YM50 particles, however, the second and third regimes are less pronounced. This is probably due to differences in the gap size as a result of the deformation of the particles. The deformation of the particles (δ) can be approximated with Hertzian-type contact mechanics, adapted to the deformation of soft spheres (equation 4.2). [43, 44]

$$\delta = \left[\frac{3(1 - \nu^2)}{4ER^{1/2}} \right]^{2/3} F_N^{2/3} \quad (4.2)$$

In this equation E is the Young's modulus of the particles, F_N is the applied load, R is the radius of the particles and ν is the Poisson ratio. Here, we assume a value for $\nu = 0.5$ for incompressible materials. [45] From the light wear track observed on the PDMS pins after the measurement, we estimate the contact area between the glass ball and the three PDMS pins to be 7 mm². Using the average particle sizes, we estimate the force per particle: the deformation for the hardest particles with a Young's Modulus of 500 kPa is then around 24% while the softest particles are fully flattened with calculated values over 100% deformation with respect to their original size. To more accurately calculate these values, the exact number of particles present between the surfaces needs to be known at each velocity, as well as the presence of multiple lubricating layers. This is however currently not

possible for us to measure *in situ*. The equation used here does not include the roughness of the surfaces, which may alter the exact contact area and with that the number of particles. With the current estimation, however, we do get a better perception of the difference in deformation between relatively hard and relatively soft particles. When the particles are flattened to a larger extent, the gap size remains small, and the surfaces come in closer contact. This explains the high friction coefficients found for the softest hydrogel particles and the absence of four distinct frictional regimes.

Thus far, we have found that the multiple regimes disappear in two cases: (I) when the particle number is small or the particles are too soft to separate the surfaces, leading to glass – pdms contact and (II) when the particles are hard enough to continuously separate the surfaces under the applied load. In the first case, there is a high degree of constant contact between the surfaces, while the latter case describes a situation where the surfaces are at distance with a low degree of contact over the entire velocity range. It seems that the regimes are visible when there are fluctuations in contact (area) between the glass ball and the PDMS pins instead of continuous contact or separation.

The role of effective suspension viscosity

To ensure that the differences in friction coefficients are caused by surface properties and not by bulk or rheological properties, we measured the viscosity of our samples as shown in Figure 4.7. For many lubricants, high viscosity is thought to allow the creation of a stable film to avoid direct contact between the entraining surfaces and as such decrease friction [35, 37], or to shift the regimes commonly observed on the Stribeck curve. Here, we find similar viscosities for the YM150 and YM500 samples, with the latter showing a slightly lower viscosity (Figure 4.7b). The YM500 suspension with the lower viscosity, however, gives much lower friction coefficients and different friction dynamics with a rather monotonous curve. In the case of our particle suspensions, the viscosity is therefore not responsible for the differences in the frictional behavior. Instead, the presence of rolling particles most likely plays the most important role when it comes to lubrication.

Melting particles

We change the particle deformability *in situ* by changing the temperature during a constant rate tribological test. To test the temperature dependence, we performed measurements at a fixed velocity of 50 mm/s and 1 N while we gradually increased the temperature from 20 to 50 °C (Figure 4.7d). As the temperature increases, the

Uncovering friction dynamics using hydrogel particles as soft ball bearings

thermosensitive gelatin particles become softer as the gelatin network destabilizes. This process continues until a polymer solution is obtained at around 40 °C due to disruption of hydrogen bonds responsible for the network formation. During the initial stages of the temperature increase from 20 to 35 °C, the friction coefficient increased from around 0.25 up to 0.33. As the particles become softer at higher temperatures, they easily deform, making the particles less able to roll and keep the surfaces apart. As the temperature further increases, the particles start to melt, which decreases the particle size and stiffness even further. This reduced the rolling ability and led to an increase in friction. Above 37 °C, we observe a decrease in the friction coefficient. This is above the melting temperature for the type of gelatin used here. [46] Upon melting, the gelatin network collapses and the particles completely disintegrate, turning the suspension into a gelatin solution. We thus exploit the low melting point of gelatin to test the role of particles in lubrication. A transition occurs from a ball-bearing type mechanism to a simple fluid film separating the surfaces as was seen in Figure 4.4. Once the fluid film has formed, a friction coefficient of 0.23 is obtained. A closer look at Figure 4.7d reveals more fluctuations in the friction coefficient at low temperatures, when the particles are still solid. Solid particles can be expected to give changes in gap size as particles enter and exit the gap. This explains why fluid samples give smoother frictional curves. Once the particles melt at 37 °C a smoother curve is obtained. The increase in frictional values for the softened particles around 35 °C strengthens our hypothesis that the ball-bearing ability is decreased with decreased particle stiffness.

Particle size influences the friction coefficient

From previous sections, it appears that the friction coefficient is determined by the ability of the soft spherical particles to keep the sliding surfaces apart. Here, we try to vary the distance by using particles of different sizes. We prepared hydrogel particles of different average sizes by varying the mixing speed when making the initial gelatin-in-oil emulsion (Table 4.1). We have labeled the samples based on the D[4,3] average radii of the particles: small (12 μm), medium (33 μm), and large (150 μm). The particles were made with 15% gelatin and the particle suspensions were prepared at the maximum packing fraction (100%). The friction coefficients of the hydrogel particle suspensions, with particles varying in size, are shown in Figure 4.8a. Measured particle size distribution and viscosity profiles of the suspensions can be found in Figure 4.8b. By varying the particle sizes we find differences in the actual friction coefficients and more importantly, in the overall frictional behavior. The viscosity profiles of these particle suspensions however only

show minor differences (Figure 4.8b), again showing that the viscosity is not the main contributor to the frictional behavior observed here.

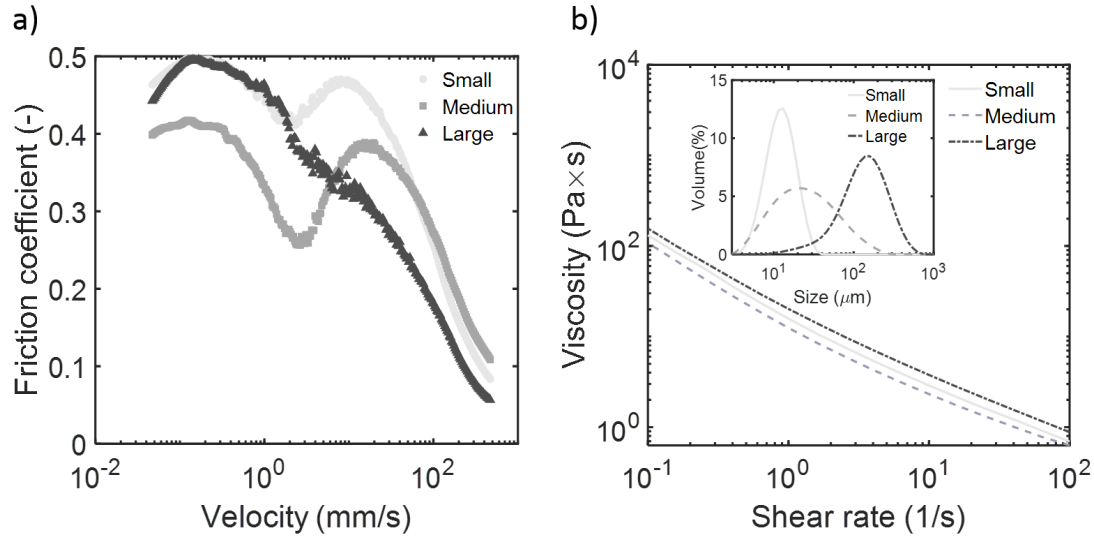


Figure 4.8: Friction coefficients (a) and flow curves (b) obtained for suspensions with microparticles with varying particle sizes. Inset shows the particle size distribution. Particle characteristics can be found in Table 4.2.

We find the lowest friction coefficients for the largest particles. This was expected as large particles are able to keep the surfaces at a larger distance, leading to minimal direct contact between the surfaces. However, the low friction coefficient for the large particles is only observed after a velocity of around 5 mm/s, and the suspension does not transition through the four frictional regimes. The suspensions with small and medium-sized particles (12 and 33 μm , respectively) do display the frictional curves consisting of the four regimes, as expected based on the previous results.

Surface – particle interactions

In the first lubrication stages, the largest particles and smallest particles show similarly high friction coefficients. For the small particles, this may be caused by asperity contact between the glass ball and PDMS pins. Atomic force microscopy of the PDMS surface showed that the peak height and width of the surface asperities was around 500 nm, much smaller than the size of the particles. The surface roughness of the glass probe is shown in Figure 4.9.

These asperities are larger than the smallest particles (12 μm). These small particles are therefore small enough to be trapped between the surface asperities of the glass ball. The entrapped particles would then be unable to separate the surfaces, which results in a high degree of contact between the substrate and the probe.

Uncovering friction dynamics using hydrogel particles as soft ball bearings

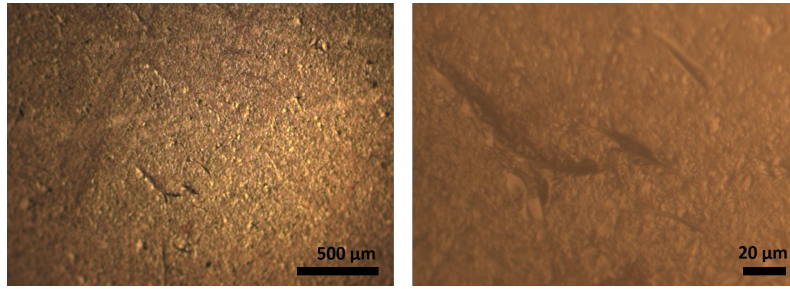


Figure 4.9: Microscopy image of the spherical glass probe, showing the relatively high degree of roughness of the surface.

This makes these small particle suspensions a less efficient ball-bearing lubricant. The large particles with an average size of $150\ \mu\text{m}$ also show lower lubricating ability in the boundary regime. As the large particles are expected to be larger than the surface asperities of the glass ball and PDMS pins, these particles are not trapped between asperities and do have the ability to separate the surfaces. Due to the larger particle size, however, fewer particles fit on the same surface area, which increases the applied load *per particle*. Under this relatively high load, these particles may be deformed to a more elliptical shape. Using equation 4.2, we estimate the large particles ($150\ \mu\text{m}$) to be deformed to a final height of $35\ \mu\text{m}$. This deformation reduces the lubricating properties as the contact area between the particles and the surfaces increases and the rolling ability decreases. Although the deformed large particles have a similar height ($35\ \mu\text{m}$) as the size of the medium particles ($33\ \mu\text{m}$), the friction coefficient for the medium particle suspensions is lower. This can be explained by the number of particles. The number of medium-sized particles is at least 100 times larger than the number of large particles. The expected load per medium particle is therefore much smaller than for the large particles and as a result, the deformation of these particles is also expected to be smaller. The medium-sized particles, therefore, remain mostly spherical. We attribute the low friction coefficients of the medium particles thus to their ability to roll due to a lower deformation, and inability to be trapped between surface asperities. These results show that there is an optimum in particle properties; they should be small enough to provide a large number of particles that do not deform, but they should be large enough not to get trapped within the asperities. This makes the suspension with the medium particles an efficient ball-bearing lubricant, especially in the first regimes as shown in Figure 4.8a.

Frictional regimes for different particle sizes

Both the medium-sized ($33\ \mu\text{m}$) and small particles ($12\ \mu\text{m}$) show the four frictional regimes as described in previous sections. For the large particles, the

frictional behavior is noticeably different and the four regimes are less pronounced. Specifically, the increase in friction in regime III is absent. The phenomenon responsible for the increase in friction thus does not occur in suspensions with large particles as the increase in friction expected for the third regime is not seen here. In regime IV, the last regime, the friction coefficient becomes the smallest for the large particles. In this regime, we assume that a large number of particles can be present between the surfaces as the gap size increases. As the large particles are well able to keep the surfaces at a relatively large distance, these low friction coefficients are to be expected. Again, we find that the low friction coefficients are obtained with particles that can act as ball bearings by keeping a distance between surfaces while rolling over the surfaces easily, regardless of the rheological properties of the suspension.

Interpretation of soft particle lubrication

For soft ball-bearing systems, small particles, soft particles and a low volume fraction of particles in suspension lead to relatively high friction coefficients. On the other hand, low friction is found for hard, large particles and when particles are present in large amounts. The systems with high friction coefficients have an important characteristic in common: a poor ability to separate surfaces and particles with a low ability to roll. These aspects are of high importance for the ball-bearing mechanism. Instead of the well-known three regimes, e.g. boundary, mixed and hydrodynamic regime, our particle suspensions transition through four frictional regimes. Similar frictional zones have been found before for lubricants containing solid-like particles. [21, 26] We have shown the importance of the particle properties in the occurrence of the different frictional regimes. When particles are too soft, too hard, or too large, the particle suspensions do not transition through all four frictional regimes.

Based on our findings with systematic variations in particle properties, we provide new insights regarding the interpretation of the different frictional regimes for soft particles in a fluid matrix. In previous works, it has been suggested that high friction arises from low particle number entrainment [21, 26], due to a large particle size compared to the gap size or a result of local build-up of particles around the probe [27]. However, we find different friction coefficients for all of our samples in the boundary regime or regime I, and the most solid-like, chemically cross-linked particles, are unaffected by the changes in gap size (Figure 4.7). This strongly indicates that particles are already present between the sliding surfaces even at relatively small gap sizes at low speeds. High friction coefficients are

Uncovering friction dynamics using hydrogel particles as soft ball bearings

therefore expected to arise from the deformation of the soft particles. Low friction coefficients are then found in the case the particles are spherical and able to roll. The increase in gap size will also lead to the presence of a large number of particles, collectively acting as a good lubricant due to good rolling ability and large separation of the surfaces. As the particles have less contact with the surfaces, the properties of the particles become less relevant. Based on these observations, we, therefore, propose the following lubrication mechanisms for the four different regimes for soft hydrogel particle suspensions between rough surfaces as shown in Figure 4.10.

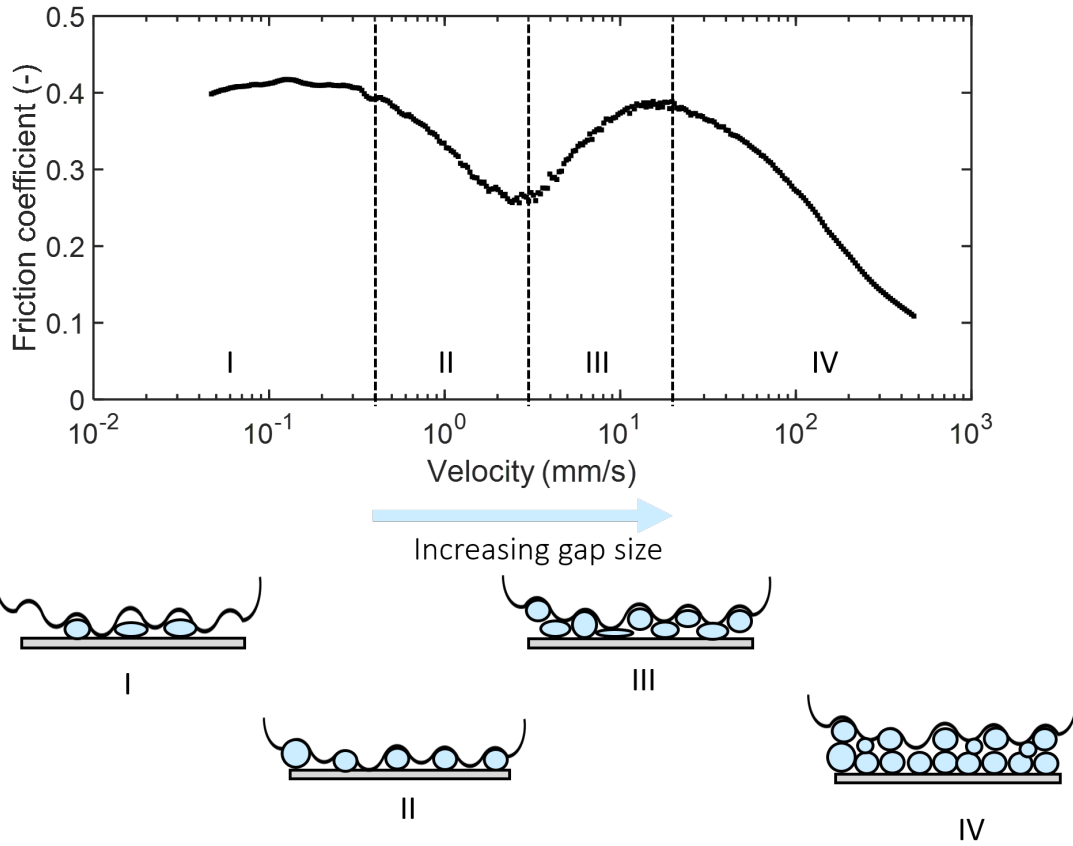


Figure 4.10: Schematic representation of our proposed four frictional regimes of hydrogel microparticle suspensions as the velocity and gap size increase.

Regime I : At these small gap sizes, a limited number of particles is present between the surfaces and depending on their size, the particles may become trapped within the cavities on the rough glass surface (Figure 4.9) carrying relatively high loads. The compressed particles lose their spherical shape and rolling ability and are dragged along the PDMS surface. In this case, relatively large contact areas between the glass and PDMS surfaces are expected, leading to rather high friction coefficients in this boundary regime.

Regime II: As the velocity increases, the gap size increases. More particles enter between the glass – PDMS surfaces and the deformable particles regain their original spherical shape. The improved rolling ability of the particles provides sufficient lubrication and gives rise to a decrease in the friction coefficient until a certain minimum value where the particles are assumed to be completely spherical.

Regime III: At even higher velocities, the change in friction coefficient can be attributed again to geometrical changes of the particles during sliding. As the velocity increases in regime III, more space between the PDMS and glass surfaces is

Uncovering friction dynamics using hydrogel particles as soft ball bearings

created, probably at a distance comparable to or larger than the particle size. Such an increase in gap size leads to an inflow of more particles. An excess of particles between the surface may lead to jamming of the particles, compression of particles, and perhaps even the formation of multiple lubricating layers. All effects would limit the ability for the particles to roll, hence an increase in the friction coefficient is expected.

Regime IV: In the mixed regime, the gap size is thought to further increase. Firstly, this causes the layered particles to regain their original shape and rolling ability. Secondly, this makes it possible for more particles to enter the gap quickly as the velocity increases. The suspension can now form a viscous lubricious layer where direct contact between the surfaces and the particles is reduced. The ball-bearing mechanism becomes less relevant, and lubrication by a fluid film becomes more dominant. The strong decay in friction coefficient in the mixed regime (regime IV) is typical for rate-dependent frictional curves and shows similarities to a gelatin solution or water (Figure 4.4). We summarize our proposed mechanism schematically in Figure 4.10.

This mechanism explains the important role of the particle properties combined with the surface properties in the lubrication behavior of hydrogel particle suspensions. We point out the importance of the deformable nature of the particles for the appearance of the specific behavior observed in regime II and III. These regimes are absent for particles that are less sensitive to deformation. For small particles, we find high friction, likely because particles are trapped between surface asperities.

Smooth surface lubrication

To demonstrate the important role of particle trapping within the surface asperities, we carried out measurements using a smooth steel ball instead of a rough glass ball. Using a different surface allows us to study the effect of surface properties. For this polished steel ball, we expect the surface asperities to be far smaller than our particles which are several μm in size. Particle trapping will thus be less probable in the case of this smooth steel ball. Indeed our measurements performed with the smooth steel ball show different rate-dependent lubrication behavior than previously seen; the frictional regimes observed when using a smooth steel ball are different from those seen for the glass ball (Figure 4.11). For the rough glass ball, we related the decrease in the second regime and increase in the third regime to particle trapping and deformation. The steel ball however shows a rather steady decrease in friction coefficient in regimes II and III. It thus appears that the fluctuations in particle trapping that result in changes in contact between the sliding surfaces are different for a smooth ball.

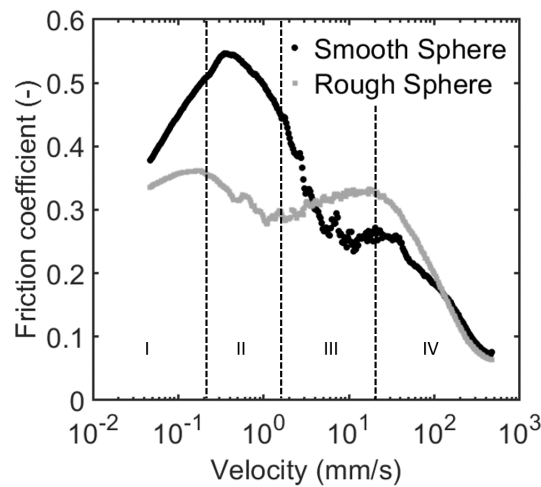


Figure 4.11: Frictional curves of hydrogel particles of 90 kPa measured with different spherical probes. We use a smooth steel probe and a rough glass probe against relatively smooth PDMS pins. Dashed lines are placed at the transition points for the rough glass spherical probe.

Aside from the different frictional regimes, the steel ball also seems to display higher friction coefficients for the majority of the measured velocities. With the smooth ball, fewer particles are being trapped between the surfaces meaning more particles are excluded from the sliding interface. This leads to more contact between the steel ball and the PDMS surface resulting in higher friction coefficients. The smooth ball has a larger contact area with the PDMS surface than a rough ball where only several asperities are in contact with the flat substrate. Sliding experiments with PDMS using rough surfaces have shown lower friction coefficients compared to friction with smooth surfaces [47, 48] which is also observed here. This decrease

Uncovering friction dynamics using hydrogel particles as soft ball bearings

in friction is likely due to the relatively high adhesive forces of PDMS. [49, 50] In addition, with the smooth ball, fewer particles could be trapped between the surfaces meaning more particles are excluded from the sliding interface. This leads to more contact between the steel ball and the PDMS surface resulting in higher friction coefficients. By varying the surface properties and the particle properties we have shown how the complex frictional behavior of particle suspensions depends on both the properties of the lubricant and the surface properties of the interacting bodies.

Conclusions

In this chapter, we elucidated how and why soft hydrogel suspensions act as good lubricants. We find four frictional regimes as a function of velocity. By systematically exploring the relevant physical characteristics of particles and surfaces involved we can propose a physical lubrication mechanism for each regime. We identified variations in gap size and particle deformability as the main cause for the rate-dependence. Additionally, we showed that when a large degree of contact between the interacting surfaces is to be expected (presence of small, soft, and limited number of particles), large friction coefficients are obtained. Low friction coefficients are measured when particles diminish surface-surface interaction, and in addition, easily roll over the surfaces. This is the case for large particles, hard particles, and particles present in high volume fractions. Additionally, we show that different surface characteristics give way to entirely different friction dynamics. Our hydrogel particle suspensions are thus efficient lubricants and are also a useful model system to better interpret the complex frictional behavior of soft materials.

References

1. Urueña, J. M. *et al.* Normal load scaling of friction in gemini hydrogels. *Biotribology* vol. 13, 30–35 (2018).
2. Rudge, R. E. D., Scholten, E. & Dijkman, J. A. Natural and induced surface roughness determine frictional regimes in hydrogel pairs. *Tribology International* vol. 141, 105903 (2019).
3. Berman, D., Erdemir, A. & Sumant, A. V. Graphene: a new emerging lubricant. *Materials Today* vol. 17, 31–42 (2014).
4. Biswas, S. & Vijayan, K. Friction and wear of PTFE—a review. *Wear* vol. 158, 193–211 (1992).
5. Upadhyay, R. K. & Kumaraswamidhas, L. A. in *Handbook of Materials Failure Analysis* 209–233 (Elsevier, 2018).
6. Liu, K., Tian, Y., Stieger, M., van der Linden, E. & van de Velde, F. Evidence for ball-bearing mechanism of microparticulated whey protein as fat replacer in liquid and semi-solid multi-component model foods. *Food Hydrocolloids* vol. 52, 403–414 (2016).
7. Johnson, K. The influence of elastic deformation upon the motion of a ball rolling between two surfaces. *Proceedings of the Institution of Mechanical Engineers* vol. 173, 795–810 (1959).
8. Deng, F., Tsekenis, G. & Rubinstein, S. M. Simple law for third-body friction. *Physical Review Letters* vol. 122, 135503 (2019).
9. Ginty, B. Bearing materials for small electric motors. *Tribology International* vol. 15, 85–88 (1982).
10. Roberts, E. Space tribology: its role in spacecraft mechanisms. *Journal of Physics D: Applied Physics* vol. 45, 503001 (2012).
11. Stribeck, R. Die wesentlichen eigenschaften der gleit-und rollenlager. *Zeitschrift des Vereines Deutscher Ingenieure* vol. 46, 1341–1348 (1902).
12. Gong, J. P. *et al.* Synthesis of hydrogels with extremely low surface friction. *Journal of the American Chemical Society* vol. 123, 5582–5583 (2001).
13. Gong, J. P. Friction and lubrication of hydrogels—its richness and complexity. *Soft Matter* vol. 2, 544–552 (2006).
14. Workamp, M. & Dijkman, J. A. Contact tribology also affects the slow flow behavior of granular emulsions. *Journal of Rheology* vol. 63, 275–283 (2019).
15. Bahrami, M., Le Houérou, V. & Rühe, J. Lubrication of surfaces covered by surface-attached hydrogel layers. *Tribology International* vol. 149, 105637 (2020).
16. Pitenis, A. *et al.* Polymer fluctuation lubrication in hydrogel gemini interfaces. *Soft Matter* vol. 10, 8955–8962 (2014).
17. Klein, J., Kumacheva, E., Mahalu, D., Perahia, D. & Fetters, L. J. Reduction of frictional forces between solid surfaces bearing polymer brushes. *Nature* vol. 370, 634 (1994).
18. Banquy, X., Burdyska, J., Lee, D. W., Matyjaszewski, K. & Israelachvili, J. Bioinspired bottle-brush polymer exhibits low friction and Amontons-like behavior. *Journal of the American Chemical Society* vol. 136, 6199–6202 (2014).
19. Gong, J., Higa, M., Iwasaki, Y., Katsuyama, Y. & Osada, Y. Friction of gels. *The Journal of Physical Chemistry B* vol. 101, 5487–5489 (1997).

20. Meier, Y. A., Zhang, K., Spencer, N. D. & Simic, R. Linking Friction and Surface Properties of Hydrogels Molded Against Materials of Different Surface Energies. *Langmuir* vol. 35, 15805–15812 (2019).
21. Gabriele, A., Spyropoulos, F. & Norton, I. A conceptual model for fluid gel lubrication. *Soft Matter* vol. 6, 4205–4213 (2010).
22. Sarkar, A., Kanti, F., Gulotta, A., Murray, B. S. & Zhang, S. Aqueous lubrication, structure and rheological properties of whey protein microgel particles. *Langmuir* vol. 33, 14699–14708 (2017).
23. Wu, Y. *et al.* An experimental study of interaction between surfactant and particle hydrogels. *Polymer* vol. 52, 452–460 (2011).
24. Andablo-Reyes, E. *et al.* Microgels as viscosity modifiers influence lubrication performance of continuum. *Soft Matter* vol. 15, 9614–9624 (2019).
25. Lee, S., Heuberger, M., Rousset, P. & Spencer, N. D. A tribological model for chocolate in the mouth: General implications for slurry-lubricated hard/soft sliding counterfaces. *Tribology letters* vol. 16, 239–249 (2004).
26. Nguyen, P. T., Kravchuk, O., Bhandari, B. & Prakash, S. Effect of different hydrocolloids on texture, rheology, tribology and sensory perception of texture and mouthfeel of low-fat pot-set yoghurt. *Food Hydrocolloids* vol. 72, 90–104 (2017).
27. Farrés, I. F. & Norton, I. The influence of co-solutes on tribology of agar fluid gels. *Food Hydrocolloids* vol. 45, 186–195 (2015).
28. Zhang, B. *et al.* Tribology of swollen starch granule suspensions from maize and potato. *Carbohydrate polymers* vol. 155, 128–135 (2017).
29. Rudge, R. E. D., Scholten, E. & Dijkman, J. A. Advances and challenges in soft tribology with applications to foods. *Current Opinion in Food Science* vol. 27, 90–97 (2019).
30. Shewan, H. M., Pradal, C. & Stokes, J. R. Tribology and its growing use toward the study of food oral processing and sensory perception. *Journal of Texture Studies* vol. 51, 7–22 (2020).
31. Scott, G. & Kilgour, D. The density of random close packing of spheres. *Journal of Physics D: Applied Physics* vol. 2, 863 (1969).
32. Cassin, G., Heinrich, E. & Spikes, H. The influence of surface roughness on the lubrication properties of adsorbing and non-adsorbing biopolymers. *Tribology Letters* vol. 11, 95–102 (2001).
33. Gallego, R., Cidade, T., Sánchez, R., Valencia, C. & Franco, J. Tribological behaviour of novel chemically modified biopolymer-thickened lubricating greases investigated in a steel–steel rotating ball-on-three plates tribology cell. *Tribology International* vol. 94, 652–660 (2016).
34. Shoaib, T. *et al.* Stick–slip friction reveals hydrogel lubrication mechanisms. *Langmuir* vol. 34, 756–765 (2017).
35. Bongaerts, J., Fourtouni, K. & Stokes, J. Soft-tribology: lubrication in a compliant PDMS–PDMS contact. *Tribology International* vol. 40, 1531–1542 (2007).
36. Selway, N., Chan, V. & Stokes, J. R. Influence of fluid viscosity and wetting on multiscale viscoelastic lubrication in soft tribological contacts. *Soft Matter* vol. 13, 1702–1715 (2017).

37. Kim, J. M., Wolf, F. & Baier, S. K. Effect of varying mixing ratio of PDMS on the consistency of the soft-contact Stribeck curve for glycerol solutions. *Tribology International* vol. 89, 46–53 (2015).
38. De Vicente, J., Spikes, H. & Stokes, J. Viscosity ratio effect in the emulsion lubrication of soft EHL contact. *Journal of Tribology* vol. 128, 795–800 (2006).
39. Bett, K. & Cappi, J. Effect of pressure on the viscosity of water. *Nature* vol. 207, 620–621 (1965).
40. Selway, N. & Stokes, J. R. Insights into the dynamics of oral lubrication and mouthfeel using soft tribology: Differentiating semi-fluid foods with similar rheology. *Food research international* vol. 54, 423–431 (2013).
41. Bonnevie, E. D., Galesso, D., Secchieri, C., Cohen, I. & Bonassar, L. J. Elastoviscous transitions of articular cartilage reveal a mechanism of synergy between lubricin and hyaluronic acid. *PloS one* vol. 10, e0143415 (2015).
42. Oppermann, A., Verkaaik, L., Stieger, M. & Scholten, E. Influence of double (w 1/o/w 2) emulsion composition on lubrication properties. *Food & Function* vol. 8, 522–532 (2017).
43. Kim, K., Cheng, J., Liu, Q., Wu, X. Y. & Sun, Y. Investigation of mechanical properties of soft hydrogel microcapsules in relation to protein delivery using a MEMS force sensor. *Journal of Biomedical Materials Research Part A: An Official Journal of The Society for Biomaterials, The Japanese Society for Biomaterials, and The Australian Society for Biomaterials and the Korean Society for Biomaterials* vol. 92, 103–113 (2010).
44. Ding, P., Norton, I., Zhang, Z. & Pacek, A. Mechanical properties of gelatin-rich micro-particles. *Journal of food engineering* vol. 86, 307–314 (2008).
45. Anseth, K. S., Bowman, C. N. & Brannon-Peppas, L. Mechanical properties of hydrogels and their experimental determination. *Biomaterials* vol. 17, 1647–1657 (1996).
46. Haug, I. & Draget, K. in *Handbook of food proteins* 92–115 (Elsevier, 2011).
47. Yu, J. *et al.* Friction and adhesion of gecko-inspired PDMS flaps on rough surfaces. *Langmuir* vol. 28, 11527–11534 (2012).
48. He, B., Chen, W. & Wang, Q. J. *Friction and Wettability of a Micro-Textured Elastomer: Poly (Dimethylsiloxane) (PDMS)* in *STLE/ASME 2006 International Joint Tribology Conference* (2006), 1053–1062.
49. Kroner, E., Maboudian, R. & Arzt, E. Adhesion characteristics of PDMS surfaces during repeated pull-off force measurements. *Advanced Engineering Materials* vol. 12, 398–404 (2010).
50. Kamperman, M. & Synytska, A. Switchable adhesion by chemical functionality and topography. *Journal of Materials Chemistry* vol. 22, 19390–19401 (2012).



5

**Rolling and sliding friction of
hard particles lubricating
soft surfaces**

Abstract

Soft materials often have interesting and unexpected frictional behavior owing to their deformable nature as has we have shown using hydrogel materials in the previous chapters. In this chapter, we use soft polydimethylsiloxane (PDMS) surfaces lubricated by hard glass spheres to study how this deformability influences particle-based lubrication. For particles between 100 and 2000 μm in size, we observe a nontrivial rate dependence and three frictional regimes. (I) A rolling friction regime where the rolling particles keep the surfaces apart sufficiently to give low friction coefficients. This is mainly found for large particles and smooth surfaces. (II) A sliding friction regime with high friction coefficients where the surfaces are partially in contact, which is found for small particles, rough surfaces and high normal forces. (III) A PDMS – PDMS contact regime where the particles are fully inserted into surfaces and the surfaces are in contact. We interpret the friction dynamics in terms of the Hertzian contact deformation effects in the indentation of the PDMS surfaces.

This chapter was accepted for publications as:

Rudge, R.E.D., Theunissen, K., Stokes, J.R., Scholten, E., and Dijksman, J. A. (2021), Tribology of hard particles lubricating soft surfaces., Physical Review Materials.

Introduction

To reduce the friction between two sliding surfaces under given normal load, typically one uses either a lubricating fluid film or solid ball bearings. Lubrication films have been studied for a long time; Reynolds already proposed an equation based on hydrodynamic pressure for such films. [1, 2] Ball bearing lubrication has also been a subject of much interest throughout the past century. [3–7] The ability of ball bearings to reduce friction, wear, and subsequent energy losses have made these rolling elements of great importance to society with applications from computer components [8] to aerospace machinery. [9, 10] In many fluid lubricated tribological systems, complex mechanics and nontrivial lubricant properties dictate the frictional behavior, and complexity is often the rule rather than the exception. The use of particles or *third bodies* between sliding surfaces should simply lead to a smaller real contact area between the sliding surfaces and subsequently decreases the friction coefficient. Many third-body lubrication studies consider only hard surfaces with hard particles for which surface deformation is negligible. [11–13] In soft material friction, however, the deformability of the involved materials becomes an additional important factor when third bodies are introduced, which should add interesting physics and potentially make it easier to clarify the physics of third body friction, as pressures and time scales in tribological dynamics are reduced.

Several soft surfaces have been studied for their tribological behavior recently, including rubbers, [14–16] hydrogels [17–19] and elastomers. [20–22] Such soft materials are found in a variety of applications, such as biomimetics, [23] soft robotics, [24] cosmetics [25] and food materials. [26] The majority of particle-tribology studies involving soft materials use particles suspended in fluids instead of dry particles. [27–31] For soft (hydrogel) particles in suspension it was found that particle properties such as hardness, size and volume fraction cause significant changes in the frictional behavior. [27, 28] Using hard particles suspended in aqueous media it was found that continuous phase viscosity, volume fraction and particle/matrix entrainment are important parameters influencing the friction coefficient. [29] In general, more particles and less fluids leads to lower friction coefficients. In addition, under thin-film (boundary) conditions, deformation of the substrate promotes entrainment of spherical particles, which have the ability to roll. Entrainment in the thin-film regime is also found to depend on fluid – particle – surface interactions. [29]

Rolling and sliding friction of hard particles lubricating soft surfaces

Due to the complex interplay of the effect of suspended particles, fluid and substrate, most studies, however, shed little light on how the particle phase influences the tribological behavior of the system in the absence of fluids. In the current chapter, we aim to uncover the particle contribution to friction and, in particular, the contributions of rolling/sliding mechanisms behind dry particle lubrication. To isolate particle – substrate interactions from fluid hydrodynamics and focus specifically on the effect of the lubricating particles on the frictional behavior of soft surfaces, we use dry hard glass particles and soft polydimethylsiloxane (PDMS) surfaces. Using this hard-soft tribosystem, we also consider the changes in contact area associated with hard particles contacting soft substrates. Soft surface deformation is expected to cause (partial) particle penetration into the surfaces, which leads to increased contact area between the particles and the surfaces but also between surfaces for large degree of deformation. These changes in contact dynamics could limit particle rolling ability. We test this hypothesis by systematically varying the surface roughness (smooth and rough) of the PDMS substrate, the measuring speed (4 mm/s to 100 mm/s), particle size (100 to 2000 μm), particle number (10 to 100% surface coverage) and the ratio at which the surfaces slide alongside one another. Using such a systematic approach allows us to study how particles influence the frictional behavior in the absence of fluids. The results are presented in terms of probe roughness, normal force and number of spherical particles covering the surfaces.

Experimental section

In this study a Bruker UMT Tribolab tribometer (BTL, Figure 5.1a) was used to measure the friction coefficient between a rough or smooth hemispherical probe ($R = 2 \text{ cm}$) and flat substrate ($5.9 \times 4.4 \times 0.4 \text{ cm}$) all made of polydimethylsiloxane (PDMS, Sylgard 184 elastomer kit, 1:10 base:catalyst ratio). The rough probe (asperity size $\approx 100\text{-}400 \mu\text{m}$) was obtained using a stainless steel mold (Eppicotispai Kitchenware). The tribological set-up used here consists of a reciprocating substrate and a stationary probe. The oscillatory sliding distance is fixed at 10 mm and measurements take place at velocities from 4 mm/s to 100 mm/s at a fixed load of 0.5 N. The lubricant used here consists of dry glass spheres in sizes of $\leq 106 \mu\text{m}$ (140-finer U.S. sieve), 212-300 μm , 425-600 μm (Sigma-Aldrich) and approximately 2000 μm (manufacturer unknown) to completely cover the substrate surface. The number of particles needed by weight is determined using the area of the substrate and the diameter of the particles together with the density of the particles. These spherical particles are referred to as 100, 300, 600 and 2000 μm particles, respectively throughout the paper. The smooth PDMS probe

combined with the smallest and largest particles are shown in in Figure 5.1b as well as schematically in Figure 5.1c. It should be noted that the presence of the metal screw inside the PDMS probe may decrease the deformability of the elastomer.

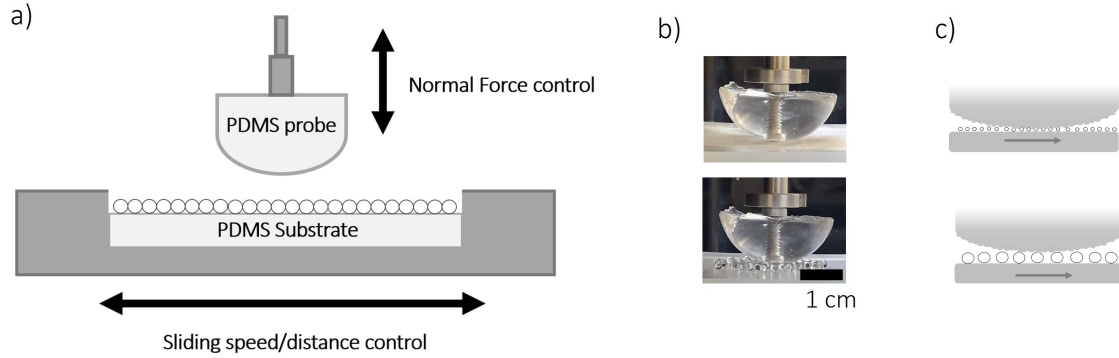


Figure 5.1: a) Schematic image of the measuring segment of the BTL tribometer. b) Image of the 2000 and 100 μm particles between PDMS surfaces together with c) a schematic representation of the particles between the surfaces.

To evaluate the effect of the relative speeds of sliding surfaces, we also use a PCS Instruments Mini Traction Machine (MTM) tribometer with a PDMS probe and substrate. The probe and the substrate on the MTM are driven by separate motors, allowing for variations between the speed ratio of the two. This ratio is known as the slide-to-roll ratio (SRR). The SRR is defined as $SRR = (U_{disk} - U_{ball})/U_{mean}$ and $(U_{mean} = (U_{disk} + U_{ball})/2)$. [32–34] An $SRR = 0$ corresponds to so-called “pure rolling”, the case where the ball and the disk rotate at the same speed in the same direction. An $SRR = 2$ refers to the ball rotating while the disk is stationary and vice versa. This is called “pure sliding”. This pure sliding movement is most similar to the measurements performed with the BTL tribometer where the substrates oscillates while the probe remains stationary.

Results

Dry PDMS surfaces in direct contact can give friction coefficients as high as $\mu = 3$ due to the self-adhesive nature of PDMS. [20, 35] To modulate the friction coefficient, we use spherical glass particles as our dry, solid lubricants. These particles are placed on the flat substrate to fully cover the surface (referred to as 100%). The particle sizes are 2000, 600, 300 and 100 μm . As shown in Figure 5.2a, these particles are able to generate a 100-fold decrease in friction coefficient with respect to bare PDMS – PDMS contacts to values as low as 0.02.

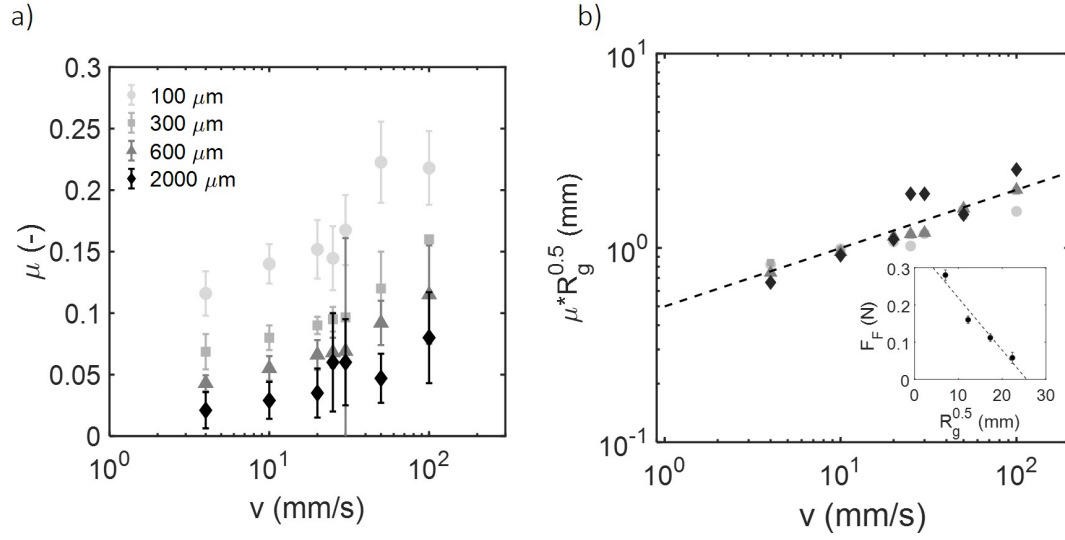


Figure 5.2: a) The friction coefficient as a function of maximum velocity for a range of lubricating particle diameter at 0.5 N measured with a rough (asperity width 100-400 μm) PDMS probe. b) The collapsed data obtained when μ is multiplied by $R_g^{0.5}$. The scaling of $R_g^{0.5}$ with F_F is shown in the inset. The dashed lines represent an empirical fit through the data.

Particle size and sliding speed dependence

The results show that friction coefficient decreases with increasing particle size. For the largest particles, the friction coefficient ranges from 0.02 to 0.08 over the entire range of speeds, for the small particles from 0.12 to 0.22 (Figure 5.2a). In the case of smaller particles, a larger number of glass particles is required to obtain the same surface coverage. This gives a larger number of separate surface – particle contacts which contributes to a higher friction coefficient of the entire system. The number of contacts scales with glass particle radius R_g^2 , hence the strong particle size dependence. The surface – particle contact area can be estimated by calculating how much the particle is pushed into the soft material due to the applied load. Using Hertzian theories, the displacement, d , can be estimated. This value shows how much each particle is inserted into the PDMS surface as $F_N = \frac{4}{3} E^* R_g^{\frac{1}{2}} d^{\frac{3}{2}}$. [36] Here, F_N is the load per particle (0.5 N distributed over all particles on 2 mm^2), E^* is the effective Young's modulus of the PDMS (2.5 MPa). We use 2 mm^2 here because this well above the estimated Hertzian contact area between the 2000 μm glass particle and the PDMS surface at 0.5 N ($\approx 1 \text{ mm}^2$). At 2 mm^2 we can thus assume that at least one 2000 μm particle will be present between the PDMS surfaces. For the particles of sizes 2000, 600, 300 and 100 μm , indentation depths are estimated to be 282, 85, 42 and 14 μm , respectively. The increase in friction coefficient with decreasing particle size is thus likely due to the corresponding increase in particle – substrate contact area. The theoretical contact area diameter, a , of a glass particle indenting the PDMS surface is defined as $a = (R_g d)^{0.5}$ with R_g

the radius of the glass particle. Values of 481, 145, 72 and 24 μm are found for the 2000, 600, 300 and 100 μm sized particles, respectively. The friction coefficient thus appears to decrease with increasing contact area.

The speed curves for the different particle sizes all appear to follow a similar increasing trend. When we multiply μ by $R_g^{0.5}$ we find that the data collapse onto a single line, shown here with a (dashed) trend line (Figure 5.2b). To understand the origin of this dependence of μ on $R_g^{0.5}$ we assess the friction and normal forces acting on the probe and a single particle (Figure 5.3) using the Hertzian approach. For this we use the normal force the PDMS probe (F_{Np}) exerts on each particle: $F_{Np} = (a/R^2)F_{Ng}$. We determine the normal force per glass particle as $F_{Ng} = E^*R_g^{0.5}d^{3/2}$. Using these two equations we obtain $F_{Np} = aE^*(d/R_p)^{3/2}$. A similar approach as used here for the normal force, can be used for the friction force resulting in $F_{Fp} = (a/R^2)F_{Fg}$. Assuming that $F_F \propto$ contact area, we then find that $F_{Fg} \propto R_g d$ and thus $F_{Fp} \propto a(d/R_g)$. Since $\mu = F_F/F_N$, we then find that $\mu = F_{Fp}/F_{Np} \propto E^*(d/R_g^{0.5})$. This would mean that $\mu R_g^{0.5}$ should be constant at given speed and normal force. This scaling with R_g is verified in Figure 5.2b).

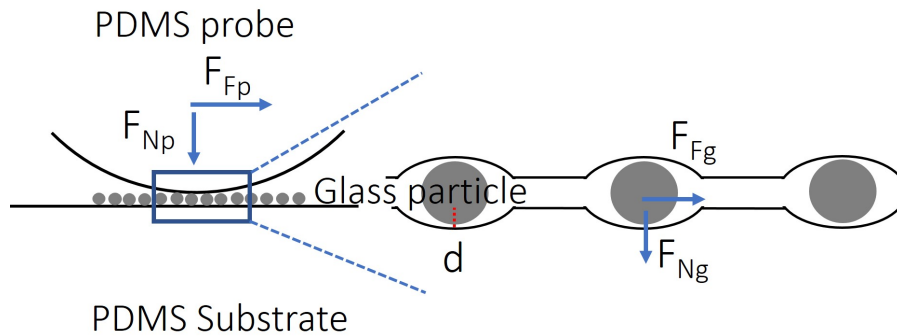


Figure 5.3: Schematic view of the normal and friction forces acting on the probe (F_{Np} , F_{Fp}) and on the particles (F_{Ng} , F_{Fg}) and the indentation depth, d .

When we increase the sliding speed, we see an increase in the friction coefficient for all particle sizes (Figure 5.2a). At high speeds, particles may easily be pushed out of the contact which could potentially lead to PDMS – PDMS contact. As the escaping of particles from between the surfaces occurs at random, the relatively large error bars observed here are to be expected. For the rough surfaces used here, we expect smaller particles to be able to enter the space between the asperities. When particles become trapped between asperities, their ability to roll could be inhibited and friction coefficients are expected to increase. This was also found in a previous study, where the friction coefficient of rough PDMS surfaces lubricated by solid particles increased when particles were of similar size as the surface asperities. [7] When we compare friction coefficients of rough surfaces lubricated by 100 μm

Rolling and sliding friction of hard particles lubricating soft surfaces

particles to smooth surfaces lubricated by the same particles, friction coefficients that are twice as high for the rough surfaces at high normal forces are found as will be discussed in the next section. This shows that an increase in surface – surface and particle – surface contact area causes an increase in the friction coefficient. We will discuss this further in the following section. Although particles enter the space between asperities, we do find that the friction coefficients of particle-lubricated contacts are still far lower than the friction coefficient of a dry PDMS – PDMS contact. This is an indication that the particles are still able to prevent complete PDMS – PDMS contact.

Normal force dependence

Particle inclusion between the asperities is expected to be enhanced at higher normal forces, due to the deformable nature of the surfaces. As the load increases, the elastic substrates can cover and entrain the lubricating particles due to deformation of the PDMS around the particles, causing increased direct PDMS – PDMS contact. From measurements at normal forces ranging from 0.25 to 1.5 N using both a rough probe and a smooth probe, we indeed find that higher normal forces give higher friction coefficients for the smallest (100 μm) particles (Figure 5.4a,b). The increase in friction coefficient as function of the normal force is modest for larger particles, suggesting only a small contribution to the total dissipation from the few normal-force strengthened surface – particle contacts.

For the 100 μm particles we a three-fold increase in friction coefficient from $\mu = 0.15$ to $\mu = 0.45$ was found when the normal force is increased from 0.25 to 1.5 N using the rough surface. While the contact area is expected to increase gradually with increasing normal forces, there appears to be a threshold F_N above which the friction coefficient increases strongly. This threshold force is most likely related to particles becoming entrained between the asperities of the rough PDMS (asperity size $\approx 100 - 400 \mu\text{m}$) and the deformability of PDMS, which leads to a sudden change in contact dynamics with changes in F_N . When the normal force increases, the indentation of the PDMS surfaces by the particles facilitates particle inclusion between the asperities and generates larger contact areas between the two surfaces and between the surfaces and the particles.

Rolling and sliding friction

An increase in normal force from 0.25 N to 1.5 N for a glass particle on a PDMS plane gives an increase in contact area from 115 to 380 μm^2 . This is related to an increase in indentation depth from 7 to 24 μm . For the rough surfaces the actual contact area will be higher as particles enter the space between the asperities, and therefore more direct PDMS – PDMS contact will occur. In Figure 5.4b it can be seen that the normal force dependence for smooth surfaces is much less pronounced compared to surfaces with asperities. For surfaces under higher load, two separate mechanisms are proposed that may affect the friction coefficient: (I) reduction in rolling capacity of particles due to inclusion between asperities causing particles to slide over the surface with increased particle – surface contact area, (II) direct PDMS – PDMS sliding contact.

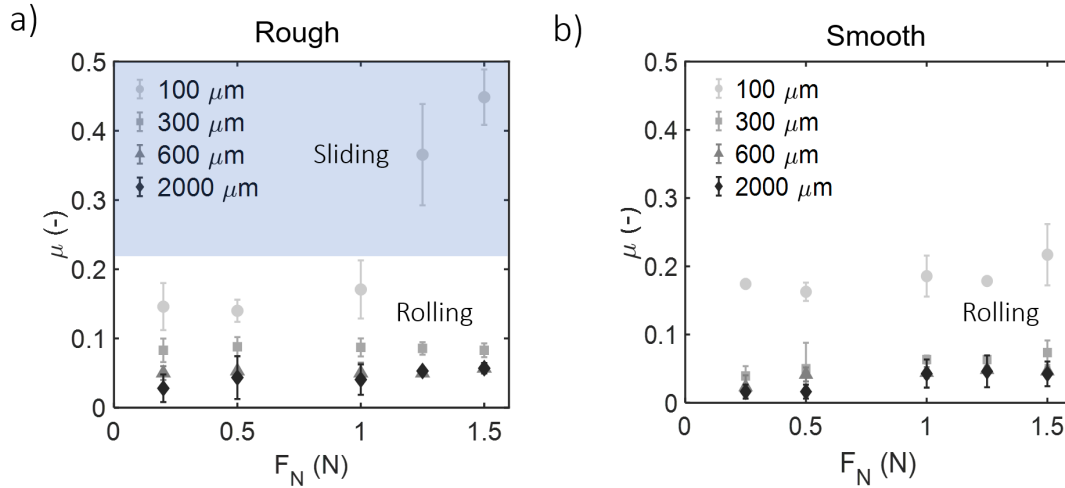


Figure 5.4: Normal force F_N dependent friction for all particle sizes using a) a rough and b) a smooth probe. The transition from rolling to sliding friction is highlighted in blue.

The transition from rolling to sliding friction is visible in Figure 5.4a where the contact regime (sliding friction) is highlighted in blue. This shows the contact area dependence of the friction coefficient. The smallest particles paired with the rough surface are most sensitive to changes in normal force as the particle – surface contact area increases rapidly for these surfaces where the asperities are of similar dimensions as the particles. To observe how particles may be inserted between PDMS asperities, we place particles between a (rough or smooth) PDMS probe and a flat glass microscope slide. The particles are then pushed against the PDMS surface at 0.5 and 1.5 N. In Figure 5.5a, in the top row, we observe PDMS-particle contact at 0.5 N compared to 1.5 N for the smooth probe. The difference in contact for the two forces is not very obvious, which is consistent with the similarity of the friction coefficients.

Rolling and sliding friction of hard particles lubricating soft surfaces

Note that to be able to obtain informative images, a lower surface coverage of particles was used during imaging than used in the tribology experiments.

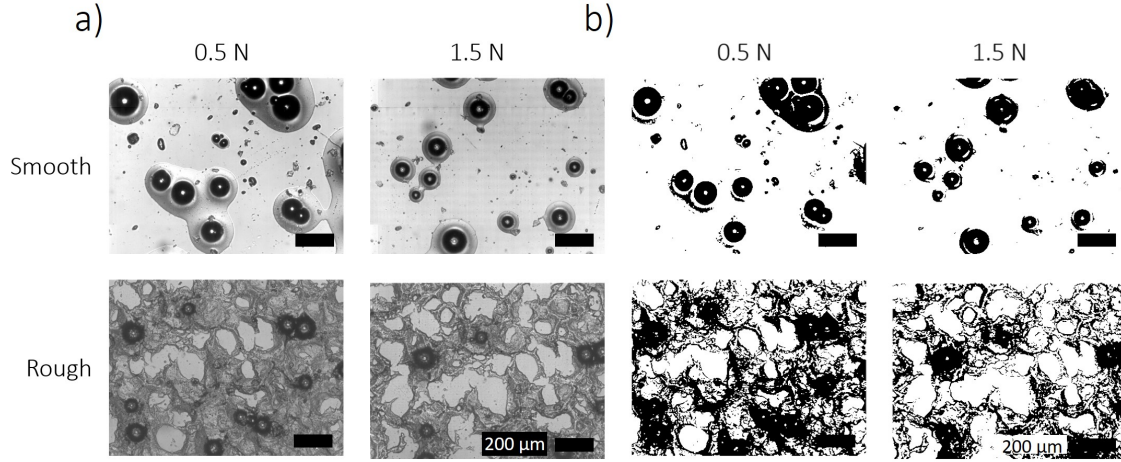


Figure 5.5: a) Microscopy images of smooth and rough PDMS surfaces in contact (white areas) with particles (dark areas) at 0.5 N and 1.5 N for smooth (upper row) and rough (lower row) surfaces. In b) the same images are shown with a black and white filter applied to emphasize PDMS contact and particle contact. Larger white areas are seen at high F_N indicating larger contact areas and particle insertion between asperities. Low surface coverage was used here for imaging purposes. Scale bar represents 200 μm .

For the rough probe we see that particles are inserted between the asperities at both low and high normal force. Additionally, we observe an increase in contact area at higher normal forces. Applying a black and white image filter makes it even more evident that more contact (white) is obtained at higher normal forces as particles (black) are pushed further into the PDMS surface (Figure 5.5b). These results show the major role that particle inclusion between the asperities and contact area play in the frictional behavior of deformable surfaces.

Partially covered surfaces

We previously suggested that the friction coefficient increases with increasing PDMS contact, for example due to increased normal forces or enhanced particle insertion between asperities. To verify how the friction coefficient responds to increasing PDMS – PDMS contact, we designed an experiment where we vary the number of glass particles present on the surface. We eliminate the effect of particle trapping by using a smooth PDMS probe against a smooth PDMS surface and limit sliding speed to 10 mm/s and the normal force to 0.5 N. To maximize changes in surface – surface contact, we use the smallest particles which initially already give a small gap size of maximum 100 μm , i.e. the diameter of the particles. We quantify surface coverage via the total area of particles covering the flat PDMS surface; we used

the particle diameter to calculate its effective surface coverage and present surface coverage as a percentage of the total surface coverage (Figure 5.6).

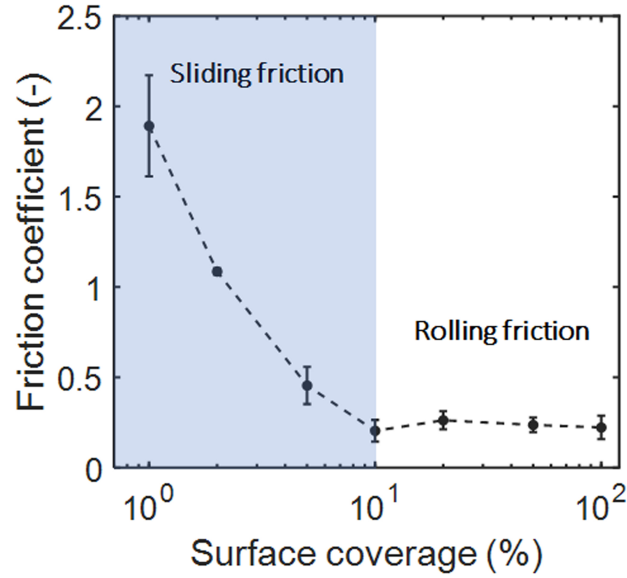


Figure 5.6: Friction coefficient as function of surface coverage for the 100 μm particles between a smooth hemispherical PDMS probe and a smooth flat PDMS substrate. Surface coverage is defined with respect to the maximum number of particles that geometrically fit in a single layer.

Here, 100% refers to the substrate being completely covered with a randomly packed monolayer of particles. At a low surface coverage of 1%, the friction coefficient is rather high ($\mu \approx 2$) and approaches the friction coefficient of dry PDMS ($\mu \approx 3$). As there are only a few particles present to separate the surfaces, direct PDMS – PDMS sliding contact is likely the cause for these high frictional values due to surface deformation or indentation. We find a steep decrease in friction coefficient as the percentage of particles increases. Higher particle surface coverage corresponds to less deformation, i.e. larger gap sizes, and less PDMS – PDMS contact, which leads to a decrease in friction as also seen in previous sections (Figure 5.4). At a surface coverage of 1, 2, 5 and 10% and a normal force of 0.5 N the estimated indentation depth using Hertzian theories equals 12, 18, 157 and 250 μm . As the latter values of indentation are larger than the particle size (100 μm) the particles become fully enveloped by the PDMS surfaces and direct PDMS contact arises.

The glass particles between PDMS surfaces already show optimal lubrication at only 10% surface coverage. For surface coverage values higher than 10% of particles, we see a constant friction coefficient. We can thus expect that 10% particles distributes the total normal force over enough particles that the PDMS substrates do not deform enough to completely envelope the particles. Thus PDMS – PDMS contact is limited, and the particles are able to roll between the PDMS surfaces. This

Rolling and sliding friction of hard particles lubricating soft surfaces

regime of constant friction coefficient represents the rolling friction regime; values for μ here are indeed consistent with those shown in Figure 5.4. The surface coverage dependence measurements of hard particle-lubricated soft substrates are an additional confirmation that for these soft surfaces, there is a strong indentation depth or contact area dependence. Contact area dependencies are not uncommon for either soft or hard materials, and have been shown to occur in different systems, such as elastic contacts [37] and, more specifically, hydrogels. [17, 18, 38]

Varying the tribometer motion

To assess the robustness of the observations under different tribological circumstances, we vary the relative sliding and rolling motion of the sliding surfaces. To do this, we introduce an additional friction tester, the Mini Traction Machine (MTM, Figure 5.7a), which is a double drive tribometer. This tribometer can give additional insights into the sliding-rolling effects as the MTM is able to control the rotating PDMS ball and the sliding PDMS disk independently. [20, 32, 34] The MTM also allows us to answer an additional question: how does the surface motion (e.g. rolling or sliding probe and substrate) influence the contact area dependent friction coefficient? We use the 100 μm particles entrained between two smooth PDMS surfaces at 10 mm/s as used previously, at a surface coverage of 100%. In this case a normal force of 1 N is used to stay within the measuring range of the tribometer and the probe is very similar to the probe used on the BTL (diameter (hemi-)sphere on MTM tribometer: 19 mm, on the BTL: 20 mm). With the ability to drive the probe and substrate separately, we have the possibility to vary the ratio between the speed of the ball and the speed of the disk, also known as the slide-to-roll ratio (SRR).

At a SRR of 2, where pure sliding of the surfaces takes place, the frictional values are within the same range as observed previously for the same particles of 100 μm in diameter ($\mu_{max} \approx 0.17$, Figure 5.7b). The expected transition from sliding to rolling friction is also seen using the MTM. A strong decrease in friction coefficient from 0.2 to about 0.008 is observed when decreasing the SRR from 2 to 0. When the ball and disk are rotating at equivalent velocities, i.e. SRR = 0, the spherical particles are easily maintained between the surfaces and are allowed to roll along with the imposed motion of the PDMS surfaces. The rolling of the particles is then driven by both the ball and the disk which results in extremely low friction coefficients. At higher SRRs, the rolling of the particles is mainly driven by only one of the surfaces at a time, while the stationary surface counteracts the rolling motion of the particles. Additionally, at high SRR values, particles can be expected

Rolling and sliding friction of hard particles lubricating soft surfaces

to leave the contact regime and accumulate around the probe which would result in high friction as well. Once particles exit the gap, large PDMS contact areas lead to increased friction coefficients. Particles exit the gap at different times and speeds during each measurement, which explains the large error bars observable in Figure 5.7b. The increase in friction with decreased particle rolling ability shows that restricted particle rolling motion causes an increase in friction coefficient, which was also seen when varying measuring parameters including the normal force in previous sections.

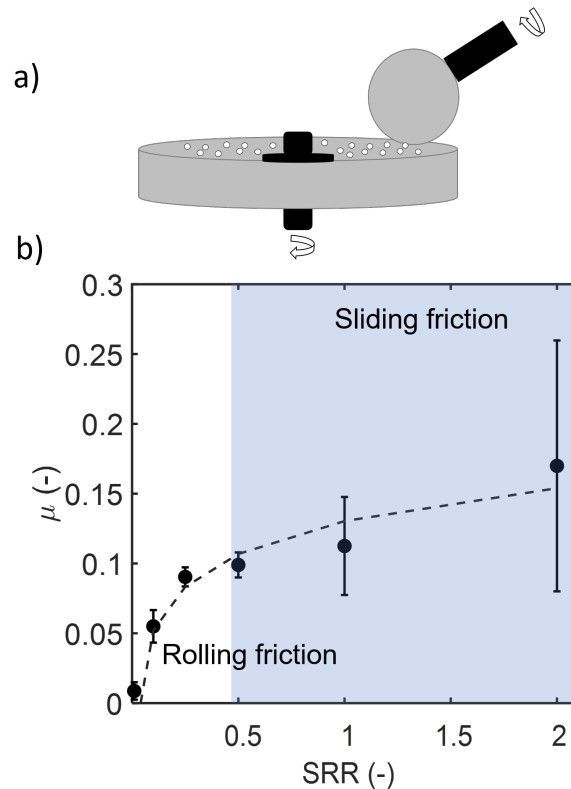


Figure 5.7: a) Schematic view of the Mini Traction Machine with two PDMS surfaces and glass particles as lubricant. b) Friction coefficient obtained using a double drive tribometer at various slide to roll ratios.

Relating the friction coefficient to the contact area

We have highlighted the transition from rolling (particle) friction to sliding (surface dominated) friction by varying the particle size, normal force, surface roughness, number of particles and even by using an additional tribological device. As the friction coefficient is often related to the contact area, we combine the friction coefficients from the measurements in previous sections performed with the smooth probe into one figure, as function of the contact area radius estimated using a Hertzian approach (Figure 5.8).

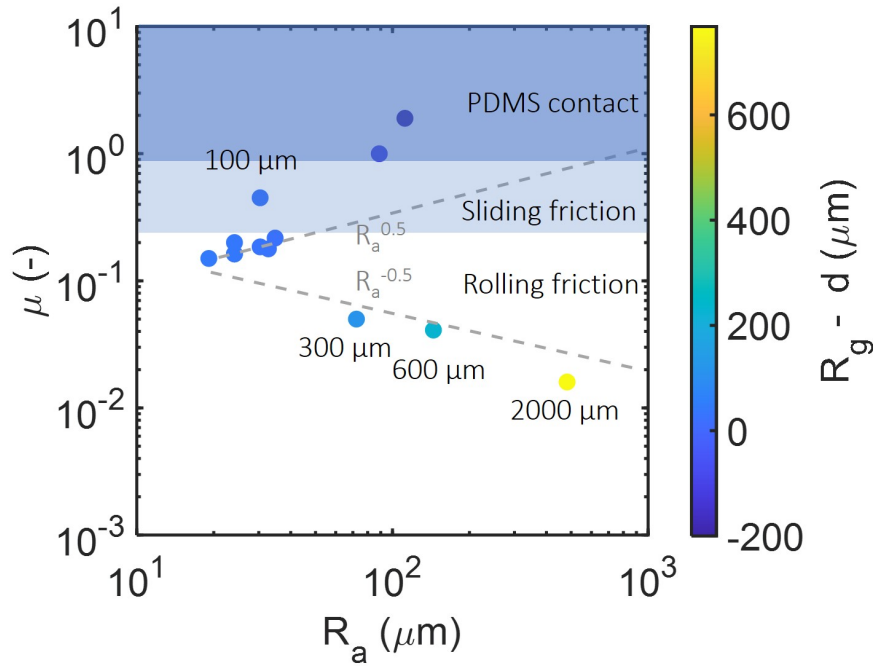


Figure 5.8: Frictional values of Figures 5.2, 5.4, 5.6, and 5.7 are combined to display the friction coefficient as function of contact area radius (R_a). The color bar represents $R_g - d$, which results in rolling, sliding or PDMS – PDMS contact friction.

Using this approach, we find that the friction coefficient in the rolling regime scales with $R_a^{-0.5}$ with R_a the radius of the contact area. The friction coefficient thus decreases with increasing contact area for the particles with different particle sizes. When the contact area increases due to increases in normal force or decrease in surface coverage, the friction coefficient increases. In the latter case, particle insertion and PDMS – PDMS contact causes the increase in friction coefficient. We attempt to quantify the increase of particle - particle and surface – particle contact and calculate the separation distance between the two PDMS surfaces by subtracting the indentation depth from the particle size; when the indentation depth is larger than the particle size, the PDMS surfaces are allowed to contact one another.

From the colorbar in Figure 5.8 showing $R_g - d$ we see that an increase in this value causes a decrease in the friction coefficient for the particles of different sizes. For the 100 μm particles, we find that when particles are pushed into the soft surfaces and are still able to keep the surfaces separated ($R_g - d \approx 40 \mu\text{m}$) relatively low friction coefficients are obtained. Once PDMS – PDMS contact is established ($R_g - d < 0 \mu\text{m}$), a strong increase in the friction coefficient is seen in this PDMS contact regime. This shows that each frictional regime has its own complex relation with the contact area depending on the particle – surface and

surface – surface dynamics.

The lowest friction coefficients are seen for the larger particles that are well able to keep the surface apart (large $R_g - d$ values) in the rolling friction regime. When the separation distance falls below $100\ \mu\text{m}$, the particles are less able to separate the surfaces. Below this gap size, particle insertion into the PDMS surface begins to take place due to elastomeric surface deformation, and PDMS – PDMS contact is enlarged. We therefore propose the following mechanism: As particles have limited rolling ability, friction is dominated by sliding surfaces. This change from rolling particles to particles being pushed into and deforming the surfaces marks the onset of the sliding regime as indicated in Figure 5.8 in blue. Sliding here refers to the limited rolling ability of the particles due to insertion into the surfaces and enhanced particle – PDMS contact. The separation distance between the surfaces decreases further as the normal force increases or when there are less particles present on the surface. Both conditions lead to a higher normal force per particle, i.e. more surface deformation and higher surface – particle contact area, and with that, higher friction coefficients. When the glass-PDMS indentation depth is larger than the particle size, negative values are found for the indentation depth. We find indentation depths larger than the particle size at a surface coverage of 2% and 1%. At these percentages of surface coverage, particles are fully enveloped by the surfaces and direct PDMS – PDMS sliding contact occurs.

This supports our suggested frictional mechanism: For large separations, low (or even no) direct PDMS – PDMS contact occurs and low friction coefficients are found. As the separation distance decreases due to a decrease in particle size, particle number, or an increase in normal force, the overall indentation increases and the friction coefficient increases accordingly. Once the surfaces are in contact a large increase in the friction coefficient is measured. We thus show that the degree of separation between the PDMS surfaces as caused by changes in normal force, particle size or surface coverage determines in what contact regime the frictional system is located. Based on the contact regime (PDMS contact, sliding or rolling), the friction coefficient shows a positive or negative dependence on the contact area of the contact between the glass particles and the PDMS surface.

Conclusions

In this chapter, we used two tribometers to assess the frictional dynamics of dry hard spherical particles lubricating soft surfaces. We find that the friction coefficient increases with increasing normal force, when we decrease the number of particles on the surface and when smaller particles are used. The increase in friction coefficient in these cases is caused by enhanced surface – surface and particle – surface contact. By manipulating different aspects of this soft-hard tribosystem, we display three different frictional regimes: a rolling regime, a sliding regime and a PDMS – PDMS contact regime. The rolling regime displays low friction coefficients, attributed to the rolling motion of the particles. In the sliding regime, an increase in friction coefficient is found as particles are inserted between asperities due to similarity in size between particles and deformation of the surfaces. In this regime, particle – surface and surface – surface interactions arise, leading to an increase in friction coefficients. When the particles are fully covered by the surfaces (particle insertion and PDMS deformation), direct PDMS – PDMS contact occurs and the friction coefficient increases accordingly.

References

1. Reynolds, O. IV. On the theory of lubrication and its application to Mr. Beauchamp tower's experiments, including an experimental determination of the viscosity of olive oil. *Philosophical transactions of the Royal Society of London* vol. 177, 157–234 (1886).
2. Lugt, P. M. & Morales-Espejel, G. E. A review of elasto-hydrodynamic lubrication theory. *Tribology Transactions* vol. 54, 470–496 (2011).
3. Stribeck, R. *Kugellager für beliebige Belastungen* (Buchdruckerei AW Schade, Berlin N., 1901).
4. Dowson, D. *History of tribology* (Addison-Wesley Longman Limited, 1979).
5. Katz, R. N. & Hannoosh, J. G. Ceramics for high performance rolling element bearings: a review and assessment. *International Journal of High Technology Ceramics* vol. 1, 69–79 (1985).
6. Singh, A., Chauhan, P. & Mamatha, T. A review on tribological performance of lubricants with nanoparticles additives. *Materials today: proceedings* vol. 25, 586–591 (2020).
7. Deng, F., Tsekenis, G. & Rubinstein, S. M. Simple law for third-body friction. *Physical Review Letters* vol. 122, 135503 (2019).
8. Fussell, B. K. *Analysis and performance comparison of a tooth wound brushless CPU cooling fan motor in Proceedings: Electrical Insulation Conference and Electrical Manufacturing and Coil Winding Technology Conference (Cat. No. 03CH37480)* (2003), 379–386.
9. Ebert, F. *Performance of silicon nitride (Si₃N₄) components in aerospace bearing applications in ASME 1990 International Gas Turbine and Aeroengine Congress and Exposition* (1990).
10. Guo, C. Nonlinear dynamic response analysis of unbalance-rubbing coupling faults of rotor-ball bearing-stator coupling system. *Journal of Aerospace Power* vol. 22, 1771–1778 (2007).
11. Peña-Parás, L. *et al.* Effects of substrate surface roughness and nano/micro particle additive size on friction and wear in lubricated sliding. *Tribology International* vol. 119, 88–98 (2018).
12. Kim, S.-T., Woo, J.-Y. & Lee, Y.-Z. Friction, wear, and scuffing characteristics of marine engine lubricants with nanodiamond particles. *Tribology Transactions* vol. 59, 1098–1103 (2016).
13. Aghababaei, R. Effect of adhesion on material removal during adhesive wear. *Physical Review Materials* vol. 3, 063604 (2019).
14. Persson, B. N. Theory of rubber friction and contact mechanics. *The Journal of Chemical Physics* vol. 115, 3840–3861 (2001).
15. Persson, B. N., Tartaglino, U., Albohr, O. & Tosatti, E. Rubber friction on wet and dry road surfaces: The sealing effect. *Physical Review B* vol. 71, 035428 (2005).
16. Schallamach, A. The load dependence of rubber friction. *Proceedings of the Physical Society. Section B* vol. 65, 657 (1952).
17. Gong, J. P. Friction and lubrication of hydrogels—its richness and complexity. *Soft Matter* vol. 2, 544–552 (2006).
18. Rudge, R. E. D., Scholten, E. & Dijkman, J. A. Natural and induced surface roughness determine frictional regimes in hydrogel pairs. *Tribology International* vol. 141, 105903 (2019).
19. Urueña, J. M. *et al.* Mesh size control of polymer fluctuation lubrication in gemini hydrogels. *Biotribology* vol. 1, 24–29 (2015).

20. Bongaerts, J., Fourtouni, K. & Stokes, J. Soft-tribology: lubrication in a compliant PDMS–PDMS contact. *Tribology International* vol. 40, 1531–1542 (2007).
21. Selway, N., Chan, V. & Stokes, J. R. Influence of fluid viscosity and wetting on multiscale viscoelastic lubrication in soft tribological contacts. *Soft Matter* vol. 13, 1702–1715 (2017).
22. Yu, J. *et al.* Friction and adhesion of gecko-inspired PDMS flaps on rough surfaces. *Langmuir* vol. 28, 11527–11534 (2012).
23. Damm, P., Bender, A., Duda, G. & Bergmann, G. In vivo measured joint friction in hip implants during walking after a short rest. *Plos one* vol. 12, e0174788 (2017).
24. Whitesides, G. M. Soft robotics. *Angewandte Chemie International Edition* vol. 57, 4258–4273 (2018).
25. Bhushan, B. & Tang, W. Surface, tribological, and mechanical characterization of synthetic skins for tribological applications in cosmetic science. *Journal of Applied Polymer Science* vol. 120, 2881–2890 (2011).
26. Rudge, R. E. D., Scholten, E. & Dijkman, J. A. Advances and challenges in soft tribology with applications to foods. *Current Opinion in Food Science* vol. 27, 90–97 (2019).
27. Rudge, R. E. D., Van De Sande, J. P., Dijkman, J. A. & Scholten, E. Uncovering friction dynamics using hydrogel particles as soft ball bearings. *Soft Matter* vol. 16, 3821–3831 (2020).
28. Sarkar, A., Kanti, F., Gulotta, A., Murray, B. S. & Zhang, S. Aqueous lubrication, structure and rheological properties of whey protein microgel particles. *Langmuir* vol. 33, 14699–14708 (2017).
29. Yakubov, G., Branfield, T., Bongaerts, J. & Stokes, J. Tribology of particle suspensions in rolling-sliding soft contacts. *Biotribology* vol. 3, 1–10 (2015).
30. Nguyen, P. T., Kravchuk, O., Bhandari, B. & Prakash, S. Effect of different hydrocolloids on texture, rheology, tribology and sensory perception of texture and mouthfeel of low-fat pot-set yoghurt. *Food Hydrocolloids* vol. 72, 90–104 (2017).
31. Andablo-Reyes, E. *et al.* Microgels as viscosity modifiers influence lubrication performance of continuum. *Soft Matter* vol. 15, 9614–9624 (2019).
32. Myant, C., Spikes, H. & Stokes, J. Influence of load and elastic properties on the rolling and sliding friction of lubricated compliant contacts. *Tribology International* vol. 43, 55–63 (2010).
33. De Vicente, J., Stokes, J. & Spikes, H. The frictional properties of Newtonian fluids in rolling–sliding soft-EHL contact. *Tribology Letters* vol. 20, 273–286 (2005).
34. De Vicente, J., Stokes, J. & Spikes, H. Rolling and sliding friction in compliant, lubricated contact. *Proceedings of the Institution of Mechanical Engineers, Part J: Journal of Engineering Tribology* vol. 220, 55–63 (2006).
35. Penskiy, I., Gerratt, A. & Bergbreiter, S. Friction, adhesion and wear properties of PDMS films on silicon sidewalls. *Journal of Micromechanics and Microengineering* vol. 21, 105013 (2011).
36. Johnson, K. L. *Contact mechanics* (Cambridge university press, 1987).
37. Weber, B. *et al.* Molecular probes reveal deviations from Amontons’ law in multi-asperity frictional contacts. *Nature communications* vol. 9, 1–7 (2018).
38. Urueña, J. M. *et al.* Normal load scaling of friction in gemini hydrogels. *Biotribology* vol. 13, 30–35 (2018).



6

**Lubrication properties of
hard particle suspensions
between soft surfaces**

Abstract

Interpreting the frictional behavior of soft surfaces is complex as a broad range of parameters simultaneously influence the friction coefficient. The deformation of the surfaces, the degree of wetting by the lubricant, and the viscosity of the lubricant are examples parameters that strongly influence soft lubrication. This chapter aims to reveal the interplay between the aforementioned parameters by evaluating the frictional behavior of particle suspensions between PDMS sliding surfaces. We use different percentages of hydrophilic and hydrophobic particles suspended in water, oil and glycerol. Using these different particulate lubricants, different fluid – surface, fluid – particle, and particle – particle interactions could be measured. The results show that competition exists between fluid entrainment and particle entrainment, leading to two frictional regimes; a sliding surface (fluid-dominated) and a rolling particle (particle-dominated) regime. Fluid polarity as well as particle hydrophobicity are key parameters leading to fluid and particle entrainment. A fluid-dominated regime was observed in the case of low particle numbers, good fluid – particle wettability and low matrix viscosities. We find that particle entrainment depends on the ability of the matrix fluid to wet the particles as well as the number of particles present in solution. Using different percentages of glycerol, it was found that fluids with high viscosities facilitate particle entrainment as both the fluid and particles are able to increase the gap size.

This chapter is in preparation for submission as:

Rudge, R.E.D., Shewan, H. M., Stokes, J. R., Dijksman, J. A., and E. Scholten.
Lubrication properties of hard particle suspensions between soft surfaces.

Introduction

The friction or lubrication properties of particle suspensions are of interest because of their applications in industries such as coatings [1, 2], cosmetics or pharmaceuticals [3, 4], and foods. [5, 6] These frictional properties strongly influence how the end-user appreciates the product. For example, a skin cream requires specific lubrication properties to be applied to the body and remain on the skin while forming a thin film. [7, 8] Similarly, a cream-based dessert is expected to have specific in-mouth lubrication properties, which contribute to the liking of the product. [9, 10] These lubricants often consist of multiple components, such as deformable droplets or particles dispersed in a viscous fluid, and the surfaces (tongue, skin) are relatively soft. In this chapter, we assess the lubrication behavior of such multi-component lubricants. As discussed in previous chapters, a regular Stribeck curve for simple Newtonian lubricants commonly consists of a boundary regime, mixed regime and elastohydrodynamic (EHL) regime. [11, 12] Viscosity and hydrophobicity play an important role in the progression of the lubrication curve. [13, 14] Correcting the Stribeck curve for the viscosity often leads to a collapse of the data onto a single frictional curve for Newtonian fluids as was very well illustrated by Bongaerts and coworkers. [15] The frictional mechanisms become more complex for soft surfaces, especially when particle suspensions are used instead of Newtonian fluid lubricants as we have shown in the previous chapters. The presence of particles as an additional component leads to a mechanism that is commonly referred to as third-body friction. [16, 17] While the rheological behavior of such particle suspensions is relatively well understood, [18–21] the tribological behavior of such suspensions, however, has received less attention in the available literature. As we have shown previously, the lubrication behavior of such suspensions is affected by many parameters such as the size of the particles, the hardness of the particles, the roughness of the surfaces, etc, which provide different contact areas and interlocking events. [22–25]

In this chapter, we test hypotheses developed based on previous chapters where particle lubrication was studied. For particle lubrication, we found in **Chapters 4** and **5** that the friction coefficient is mainly determined by the surface – surface and particle – surface interactions. [22] The deformation of soft surfaces, such as the surface of hydrogels or elastomers, causes changes in contact areas and, with that, changes in the friction coefficient. This often leads to multiple frictional regimes, different from the commonly reported Stribeck regimes. [22, 26] It has also been shown that fluid-matrix properties and surface properties are important in determining the lubrication behavior. In a study by Yakubov et al., it was

shown that the hydrophobicity of the surfaces influences the entrainment of 10 μm particles in the boundary regime while in the EHL regime, fluid lubrication dominated the lubrication behavior. [27] These results were interpreted in terms of adhesive contact between the particles and the surfaces and hydrodynamic drag forces, which either cause particles to enter or escape from the gap. So far, limited knowledge exists on the effect of fluid viscosity, polarity of the fluid molecules, and particle hydrophobicity on particle entrainment and the overall friction coefficient. In this chapter, we aim to further elucidate the effects of surface – particle – fluid interactions and how these interactions influence particle entrainment and the overall frictional behavior. To change the interactions within the third body system, hydrophilic and hydrophobic glass particles (diameter 100 μm) suspended in various Newtonian fluids varying in viscosity and hydrophobicity, are used in this third-body lubrication system. With these suspensions, the effect of hydrophobicity, particle interactions, particle volume fraction, and fluid viscosity on fluid and particle entrainment is investigated. We hypothesize that particles can be entrained into the contact together with the lubricating fluids at sufficiently large gap sizes. Additionally, we expect low friction when the surfaces have favorable (attractive) interactions with the fluid and the particles present in the suspension. With the results obtained, we construct a schematic lubrication curve that represents the different frictional regimes and the corresponding mechanisms.

Experimental section

PDMS preparation

Hydrophobic polydimethylsiloxane (PDMS) surfaces are used to measure the friction coefficients. These relatively soft surfaces (≈ 3 MPa) surfaces are made using Sylgard 184 in a 10:1 ratio following a commonly used protocol [28], and as explained in **Chapter 4**, the fluid PDMS is then poured into the respective molds to obtain spherical probes and smooth and patterned substrates used for rheology and tribology.

Particle suspensions

The particle suspensions used here were made of glass particles (unwashed glass particles <106 μm , Sigma-Aldrich) suspended in Newtonian fluids. We used 10% or 50% particles by weight, combined with the matrix fluid, and the particles were dispersed into the fluid using a spatula. When sedimentation occurred, the suspension was mixed again prior to measuring to ensure homogeneity of the

system. The fluid matrices used were (mixtures of) ultra pure water (Milli-Q), glycerol (ChemSupply), mineral oil (light, Sigma-Aldrich), corn syrup (Queen, glucose syrup from corn), and ethanol (Merck).

Rheological measurements

A Haake MARS III stress-controlled rheometer was used to measure the viscosity of Newtonian fluids and suspensions. This rheometer was equipped with a parallel plate geometry. The 35 mm parallel plates were made of steel with a 35 mm sandpaper disk attached to the bottom plate and a 35 mm PDMS disk attached to the upper plate surface. Measurements were performed with a 1 mm gap and a temperature of 20 ° C. The viscosity of the suspensions was measured between a smooth PDMS plate and a rough sandpaper plate to simulate the wetting properties of the tribometer while using a rough surface to keep poorly wetting fluids and particles from being expelled from the gap. The measured viscosities for the Newtonian fluids were similar to those obtained using smooth, solid surfaces.

Tribological measurements

The tribometer used here is the PCS Instruments Mini Traction Machine (MTM). This setup consists of a rotating ball (diameter: 19 mm) and disk (diameter: 46 mm). The device operated at speeds between 1 and 1000 mm/s and at a load of 1 N. We set the slide-to-roll ratio (SRR) to be fixed at 0.5 and is calculated as $SRR = U_{ball} - U_{disk} / U_{total}$. The measurements were carried out in bidirectional mode, which means that both the probe and the substrate rotate in opposite directions. This provides a sliding friction coefficient and a rolling friction coefficient. [29] Here, we only report the sliding friction coefficient. We obtain an average friction coefficient from five data points per sliding velocity. Our measurements were performed in triplicate. Measurements were performed at decreasing speed from 1000 to 1 mm/s followed by increasing speed from 1 to 1000 mm/s. For most particle suspensions, however, a limited speed range from 100 to 1 mm/s was used as particles were excluded from the gap at high speeds, making it impossible to obtain accurate data at these high speeds. All measurements were performed at 20 °C.

Results

Glass particles and glass particles suspended in water

Dry glass particles

The frictional behavior of glass particles between two PDMS surfaces was assessed at complete surface coverage. Friction coefficients of around 0.1 were found for this sliding system (Figure 6.1). With dry particles, we refer to 100% surface coverage, the situation where a complete layer of glass particles covers the PDMS substrate. As we showed in **Chapter 5**, above a certain particle percentage (10 %), the friction coefficient remains unaffected by the addition of extra particles. The frictional values we measured here on the MTM tribometer are very similar to our findings presented in **Chapter 5** where we discussed dry glass particles lubricating PDMS surfaces measured on the Bruker tribometer. Such rolling particles can greatly reduce the friction coefficient of dry PDMS contact ($\mu > 2$). The glass particles used here, i.e. 100 μm , are much larger than the theoretical gap size in which was estimated to be smaller than 5 μm for these surfaces on the MTM at the sliding velocities used here. [27] As such, it is not that straightforward that particles would be entrained in the gap. However, due to the hard nature of the particles (Young's modulus (E) \gg 1 GPa) compared to the much softer nature of the PDMS surface ($E = 3$ MPa), the PDMS surfaces can deform in such a way that glass particles can enter the contact zone, separate the PDMS surfaces entirely and thus lubricate the surfaces. [27]

These dry glass particles show a rather constant friction coefficient of around 0.15, which indicates that no changes occur in terms of particle entrainment or surface deformation over the entire velocity range. With these dry particles lubricating elastomeric surfaces, the surface – particle interactions that decrease direct surface – surface interactions dominate the lubrication behavior observed here.

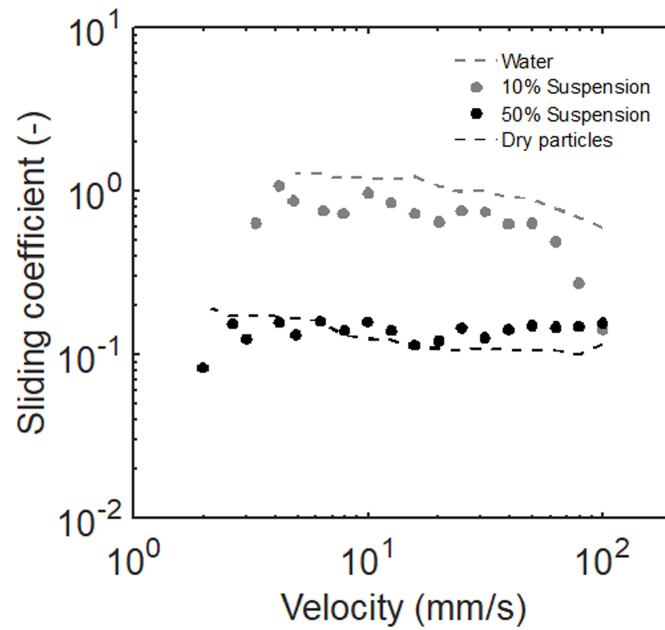


Figure 6.1: Tribological properties of water (grey dashed line), 10% (10% P in W) and 50% (50% P in W) particles suspended in water (black circles) and dry particles (100% P, black dashed line). In the case of dry particles, the substrate surface is completely covered with particles.

Glass particles in water

When combining glass particles with water and making a suspension of 50% particles, the friction coefficient strongly resembles that of dry particles (Figure 6.1). This indicates that the fluid matrix has a limited effect in this case and does not cause any significant changes in the frictional mechanisms behind glass particle lubrication. This indicates that the frictional mechanisms behind both the suspension and the dry particles are similar. This can be explained by the wetting ability of the fluid. Water is poorly able to wet both the tribopairs and the particles, [13, 30] hence the lubrication behavior of the suspension is similar to the case where water is absent (dry particles). Even though the hydrophobic interactions between the particles in water enhances particle – particle interactions than for the dry particles, these interactions thus do not affect the rolling ability of the particles, once present in the gap. It appears that the surface – particle interactions dictate the friction coefficient, while the effect of particle – particle, fluid – particle, and fluid – surface interactions remain limited due to the poor wetting properties of water on glass and PDMS.

To potentially enhance the participation of the fluid matrix in the overall frictional behavior, a suspension that consists of 90% water and only 10% of particles was also measured (Figure 6.1). When fewer particles are present, the load per particle is higher leading to larger surface deformations and larger contact areas. These

Lubrication properties of hard particle suspensions between soft surfaces

suspensions show different frictional behavior than observed for the dry particles indicating that fluid interactions or deformation effects begin to play an increasingly large role. For 10% particles, we first observe a plateau (Figure 6.1, grey symbols) around a friction coefficient of $\mu \approx 0.8$. This is lower than the friction coefficient of $\mu \approx 1.5$ for water in the boundary regime (Figure 6.1, dashed line). Even at such low concentrations of particles, particles can alter the lubrication behavior of water by almost a factor 2. As fluid dominates the lubrication here, similar frictional regimes are found for water and for 10% particles suspended in water. After the boundary regime, both water and the 10% suspension show a steep decrease in the friction coefficient, which resembles the Stribeck mixed regime. For pure fluids lubricating (semi-)solid surfaces, this represents a transition from a surface – surface contact dominated boundary regime, to a mixed regime where both asperity contact and fluid – surface interactions play an important role, as the fluid starts to form a lubrication layer. For the glass particle suspensions, a different mechanism may be at play. In the first regime of the 10% particle suspension, particles must be present between the surfaces, which is hypothesized based on the lower friction coefficient found for particles compared to that of water alone, indicating that both fluid – surface and particle – surface interactions are driving the frictional behavior. Besides the fluid lubrication, the rolling ability of the particles also plays a role. As the “mixed” regime starts around the same velocity, the fluid – surface interactions appear to be more important. Using these particle suspensions, we thus find that particle lubrication dominates at high particle percentages as the particles can enter the gap due to surface deformations. For low particle concentrations, the contribution of the fluid is more evident and Stribeck-type regimes are found.

Viscosity effects on particle lubrication

The properties of the tribosystem are changed by using a high viscosity fluid matrix. As matrix fluids, glycerol solutions of 0, 1, 25, 50, 75, and 95% are used combined with 50% particles. We first characterise the suspensions in terms of their viscosity and then proceed to discuss the friction coefficients measured.

Rheological properties

The results in Figure 6.2 show how the low-shear viscosity of glycerol solutions increases at higher percentages of glycerol in water (open symbols). Our results are consistent with literature values. [31] Comparing the glycerol solutions to the particle suspensions with glycerol, reveals that the addition of glass particles increases the viscosity (Figure 6.2, closed symbols), as expected. For the particle suspended in 25% of glycerol, we were unable to measure the viscosity, as the

suspension was removed from the gap during measurement likely due to poor wettability, low fluid viscosity and limited particle cohesion. The viscosity of the particle suspension of 25% glycerol (Figure 6.2, dashed line) is estimated by using the measured values of the other glycerol solutions and the Quemada model [18, 19]. The Quemada model gives the viscosity of the suspension based on the viscosity of the matrix and the particle volume fraction as $\eta_S = \eta_M / (1 - \phi/\phi_{max})^{-2}$. The value for ϕ_{max} used here is 64% assuming randomly packed hard spheres. [32] It is important to note that we keep the particle weight percentage constant at 50%. For the particles in glycerol, this means that the particle volume fraction is between 28 and 32% depending on the density of the glycerol/water mixtures. The Quemada expression accurately describes the behavior of our non-interacting particles in suspension as the theoretical values are in line with our experimental results. The theoretical values are thus used as an indication of the suspension viscosity. The suspensions viscosity will be used to assess the rate-dependent lubrication behavior in the following sections.

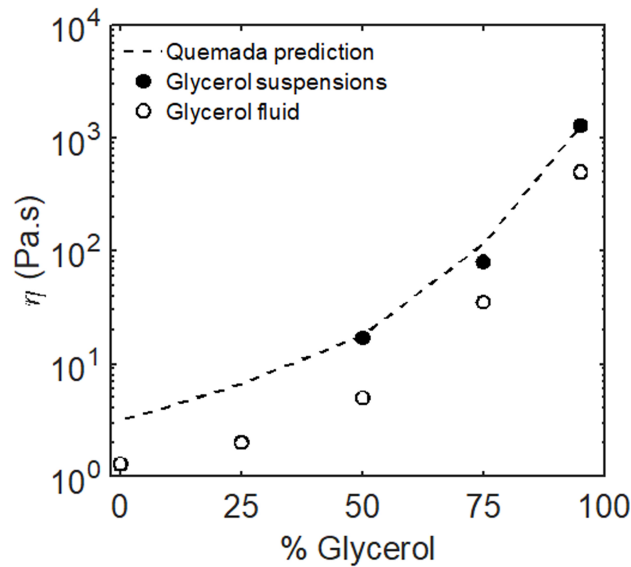


Figure 6.2: a) Measured viscosities of 50, 75 and 95% glycerol/water solutions (open symbols) and of water/glycerol solutions containing 50% glass particles (closed symbols). The dashed line represents the theoretical values obtained using the Quemada equation.

Tribological Properties

We found that the particle suspensions display the expected rheological behavior, i.e., the viscosity increases with an increase in glycerol content. We can thus now explore how the suspension dynamics affect the lubrication behavior. We measured the friction coefficients of the glycerol/water mixtures and of 50% particles suspended

Lubrication properties of hard particle suspensions between soft surfaces

in the same glycerol/water mixtures. We show the friction coefficients for different glycerol/water mixtures in Figure 6.3 (dashed lines).

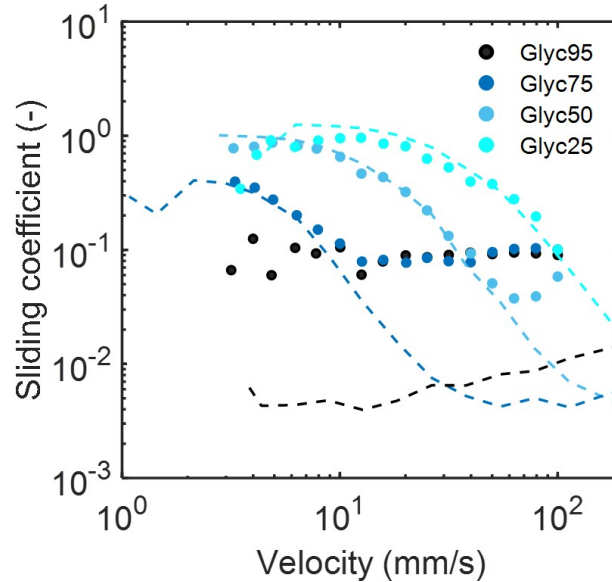


Figure 6.3: Sliding friction coefficients of 25%, 50%, 75% and 95% glycerol/water solutions (dashed lines) and of 50% glass particles suspended in 25%, 50%, 75% and 95% glycerol solutions (filled symbols).

The frictional behavior of the 50% particles suspended in 25%, 50% and 75% glycerol solutions show a strong resemblance to that of the glycerol fluids without particles, especially at low velocities and viscosities as shown in Figure 6.3 (filled symbols). This indicates that particles do not contribute to the lubrication behavior at this stage. At higher speeds, the curve of the suspensions start to deviate from those of the glycerol matrix and shows a plateau. This plateau indicates that particles begin to contribute to the lubrication at high speeds. For the particles in 50% glycerol/water, particle entrainment begins at 60 mm/s. The particle in a 75% glycerol/water solution shows particle entrainment at 10 mm/s as the curve transitions to a plateau. The higher viscosity of the glycerol mixture thus enables particle entrainment at lower speeds. This plateau overlaps with the friction coefficients found over the entire velocity range for the particles suspended in 95% glycerol. For 95% glycerol solutions, the viscosity is high enough to continuously entrain the particles, even at low velocities. For 95% glycerol suspension, the friction coefficient is determined by the glass particles over the entire velocity range and is higher than the friction coefficient of the solution itself.

By multiplying the velocity by the viscosity of the glycerol/water matrix, a typical Stribeck curve is obtained for the glycerol solutions in Figure 6.4. A collapsed curve is obtained with a mixed, boundary and hydrodynamic regime. This

hydrodynamic regime exists as the high viscosity lubricant separates the surfaces completely at these velocities due to the increased hydrodynamic pressure. These Newtonian lubricants thus show classical Stribeck behavior. For the suspensions (filled symbols), however, we observe different regimes than the regular Stribeck regimes. For the lubrication curves of the particle suspensions, we can either use the matrix viscosity or the suspension viscosity to obtain a collapsed curve. When correcting for the matrix (glycerol/water solutions) viscosity, the curves of the suspensions and the fluids overlap in the boundary and the mixed regime in Figure 6.4a. Where the fluid shows a hydrodynamic regime, the particle suspensions show a particle lubrication regime. This is similar to what the uncorrected data indicates.

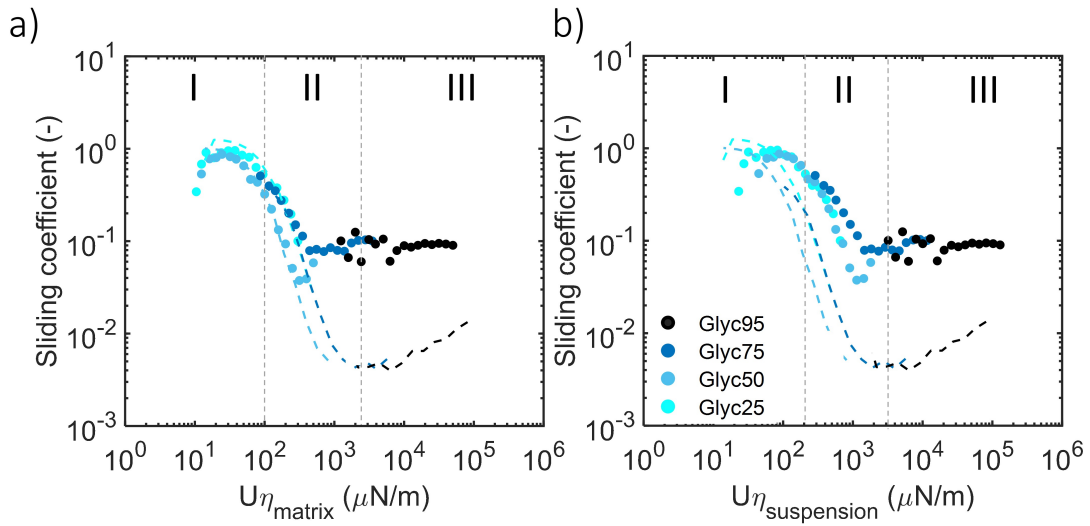


Figure 6.4: The sliding friction coefficients of glycerol/water solutions (25, 50, 75 and 95% dashed lines) and 50% particles suspended in the different glycerol/water solutions (filled circles). The viscosity was corrected for a) the matrix viscosity and b) the suspension viscosity. In both curves, we find three frictional regimes: (I) boundary, (II) mixed, and (III) particle lubricated.

These results thus show that the fluid matrix lubricates the surfaces and determines the frictional behavior at low $U\eta$ values and particle lubrication dominates at high values. When we use the viscosity of the suspension instead of the fluid, we find two separate collapsed curves for the fluids and the particle suspensions with very limited overlap (Figure 6.4b). Using the suspension viscosity as a scaling factor, gives results that are not in line with the uncorrected data (Figure 6.4a), as fluid and suspensions overlap at low velocities in the uncorrected case (Figure 6.3). This shows that the fluid matrix viscosity is the main driver behind the friction coefficient in the fluid dominated regime. When we use the matrix viscosity as a correction factor as shown in Figure 6.4a, we observe that particles are fully entrained at $U\eta$ values of $400 \mu\text{N/m}$. At a value of $400 \mu\text{N/m}$, we estimated the gap size to be below $5 \mu\text{m}$ using a method as presented in literature. [27, 29, 33] Particle entrainment at these $U\eta$ values are not trivial as the gap size is far smaller

Lubrication properties of hard particle suspensions between soft surfaces

than the size of the particles (100 μm). In this case, particles can be entrained due to the deformability of the surfaces. This suggests that with softer surfaces or softer particles, particle entrainment occurs at even lower values of the gap size. The contribution of the viscous matrix fluid is especially important at low sliding speeds. At these speeds, we see a similar behavior for the solutions and the suspensions. At high sliding speeds, the contribution of the particles becomes more visible, as we find two different sliding regimes for particle suspensions and for glycerol solutions without particles. The effect of the particles is especially observed for the suspension with 95% glycerol. As a hydrodynamic regime is absent for the 95% glycerol suspensions, the contribution of the continuous viscous fluid becomes less relevant: the size of the gap is caused by the particles and not by the hydrodynamics of the fluid. A high matrix (fluid) viscosity allows particles to be entrained between surfaces as the hydrodynamic pressure already increases the gap size. Additionally, at high viscosities, drag forces on the particles are high which means fluids can drag the particles into the gap. The drag force is quantified as $F_d = 6\pi UR\eta$ with U the sliding velocity and R the particle radius and η the matrix viscosity. Hence, at high viscosities, i.e. high drag forces, particles remain suspended in the fluid as migrating through the fluid is energetically unfavorable. [34] For our particles suspended in glycerol, we thus find three frictional regimes. (I) boundary regime where the lubricant determines the frictional behavior, (II) A mixed fluid lubricated and asperity contact regime, (III) a regime where the friction coefficient is dominated by particles lubricating the surfaces.

Comparing suspensions in water to suspensions in glycerol: wetting and viscosity

It should come as a surprise that a 50% particles in 25% glycerol/water suspension show such a different behavior than a 50% particles in pure water suspension: the viscosity of 25% glycerol is very similar to that of water, as is the (normalised) polarity (water: 1, 100% glycerol: 0.8). [35] Here we perform frictional measurements using low percentages of glycerol and other solvents to better understand the lubrication behavior. In this section, a 1% glycerol/water solution (1 mPa·s) is measured. This solution is very similar to water in terms of polarity and viscosity. We find that the friction coefficients of 1% glycerol and water without particles overlap almost completely (not shown here). The friction coefficients for particle suspensions with the previously mentioned solvents as the matrix, however, again show large differences (Figure 6.5). For water the friction coefficient is 0.1, while 1% glycerol, shows a much higher friction coefficient of roughly 1 in the boundary regime.

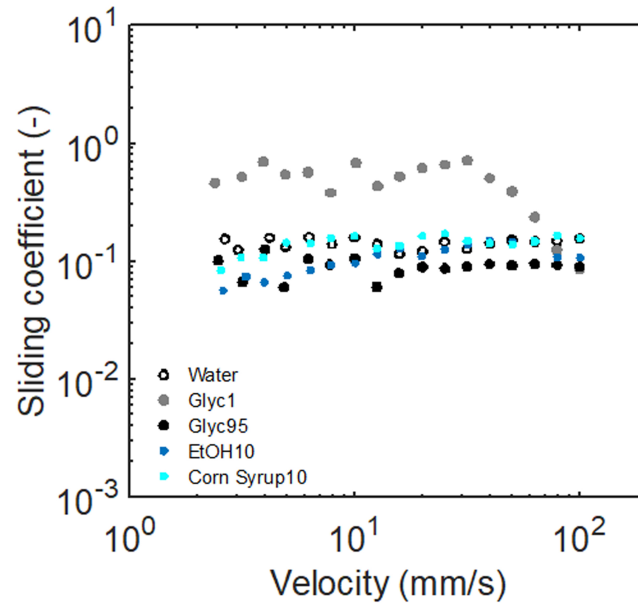


Figure 6.5: Friction coefficients of 50% particles suspended in 100% water, 1% (Glyc1), 95% glycerol (Glyc95), 1% ethanol (EtOH1), and 1% corn syrup (corn syrup1) in water.

The addition of 1% glycerol to water completely changes the frictional behavior of the glass particle suspension between two PDMS surfaces. As the differences in frictional behavior between 1% glycerol/water suspensions and pure water suspensions cannot be explained by viscosity or wettability, the difference must be due to specific interactions between the particles and surfaces and the glycerol. One option would be specific hydrogen bond formation with the fluid. To test this hypothesis, we perform an additional test using a 1% corn syrup (glucose) solution in water (Figure 6.5). Glucose has multiple -OH groups, as does glycerol. These -OH groups could be influencing the fluid – particle, fluid – surface, and fluid – fluid interactions by means of hydrogen bonding. The viscosity of the corn syrup solution is similar to that of 1% glycerol solution and pure water. The suspension containing glass particles in 1% corn syrup shows similar behavior to particles in pure water, but different than in a 1% glycerol solution. The differences, therefore, seem to be very specific for glycerol.

For further comparison, we also used a 1% ethanol solution (relative polarity ethanol: 0.65), [35] which slightly changes the overall polarity of the mixture to a less polar fluid. In Figure 6.5, however, we find that the particle suspension in 1% ethanol shows very similar behavior to the particle suspension with water. It thus appears that the fluid polarity does not influence the friction. The differences between the different suspensions are thus more related to the particle lubrication.

Lubrication properties of hard particle suspensions between soft surfaces

It remains unclear why 50% of particles in 1% glycerol show such striking differences in their lubrication behavior based on the range of frictional measurements we have carried out. Glycerol appears to alter specific interactions between the particles or the surface properties of the PDMS causing fluid lubrication to be preferred over particle lubrication at low velocities. Further investigation into the physical-chemical interactions between water and glycerol, glycerol and the particles, and glycerol and the PDMS surfaces are needed to accurately describe the behavior of glycerol/water suspensions compared to pure water suspensions.

Glass particles suspended in oil

In the previous sections, aqueous solutions of water and glycerol were discussed. These fluids are poorly able to wet the hydrophobic surface and particles due to their high polarity. To probe the role of fluid – surface interactions, we assemble a tribosystem where good wetting between both the fluid and the particles and the fluid and the surfaces exist. This is done by suspending hydrophobic glass particles in mineral oil, measured between hydrophobic PDMS surfaces.

Water and oil lubrication

We first compare the lubrication behavior of mineral oil, the fluid matrix (Figure 6.6, yellow dashed line) to water (Figure 6.1, grey dashed line). It is immediately clear that mineral oil is much better able to lubricate the PDMS surfaces and lower friction coefficients are found for oil ($\mu_{max} = 0.1$) compared to that of water ($\mu_{max} = 1.5$). This is easily explained by the better wettability of the hydrophobic surface for oil, a non-polar fluid. While water shows a boundary and a mixed regime, for oil the boundary regime seems absent, likely due to the differences in wettability and viscosity (η), which allows oil ($\eta = 17$ mPa·s) to separate the surfaces at lower velocities and gap sizes than water ($\eta = 1$ mPa·s). For these pure fluids, the fluid – surface interactions drive the friction coefficient.

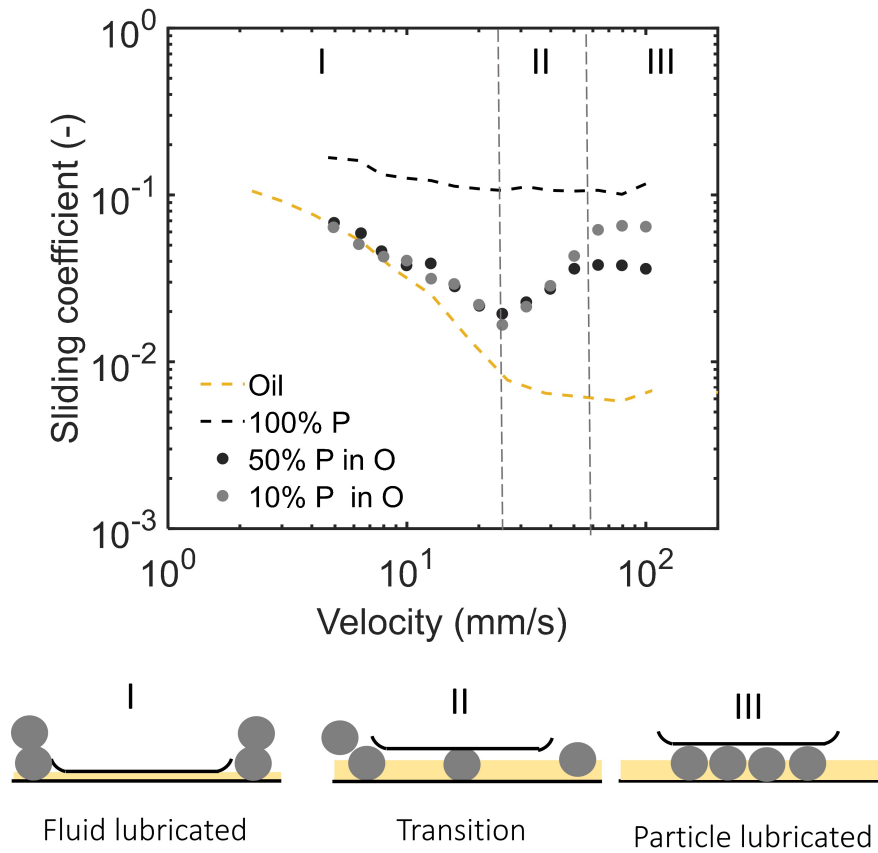


Figure 6.6: Lubrication curves of oil (yellow dashed line), dry glass particles (black dashed line), and 10% and 50% glass particles (grey and black filled symbols respectively) in oil. The three different sliding regimes are indicated with the grey dashed lines and the mechanisms for each regime are shown below the graph. Regime I is fluid dominated, regime II is a mixed fluid – particle lubricated regime and regime III is the particle lubrication regime.

Particle suspension lubrication

In Figure 6.6, the lubrication properties of 10% and 50% glass particles in oil (grey and black filled symbols, respectively) are shown. Upon the addition of particles to mineral oil, we find three frictional regimes for both the 10 and 50% particle suspensions. These regimes consist of (I) a decrease in the friction coefficient with an increase in velocity, followed by (II) an increase in the friction coefficient and (III) a subsequent plateau. The curves for 10% and 50% particles in oil overlap in regimes I and II. However, in regime (III) a higher friction coefficient is found for the 10% suspension than for the 50% suspension. All the oil-based lubricants do show lower friction coefficients than the water-based lubricants and the dry particles. The potential mechanisms behind the three frictional regimes observed here will be discussed in the next section.

The first regime in Figure 6.6 strongly resembles the first section of the mea-

surement conducted with pure oil and the curves show some overlap. This is an indication that particles are not yet present in this fluid lubricated regime and that the behavior is just dominated by oil. This potential particle exclusion might be a result of the good fluid – surface contact. Entraining a fluid with good wetting properties is energetically favorable as it spreads easily over the surface. This fluid lubrication is favored at low gap sizes. A second regime arises at 25 mm/s. At this point, an increase in the friction coefficient is observed and the curve strongly deviates from that of oil alone (Figure 6.6). This increase in the friction coefficient in regime II is an indication of particle inclusion within the gap. This requires the surfaces to deform, and once the particles are present between the surfaces, they will contribute to the friction coefficient. As the oil itself has a lower friction coefficient than the particles, particle inclusion thus causes an increase in the overall friction coefficient. The second regime begins when particles are entrained which gives way to an increase in the friction coefficient. This is quite the opposite of what we saw for the water-lubricated surfaces where particle entrainment caused a decrease in the friction coefficient. This increase in friction coefficient appears to arrive at a plateau at 60 mm/s.

At this plateau, regime III begins. The friction coefficient remains constant, indicating that no changes are taking place in terms of fluid entrainment, particle entrainment, or surface deformation as particles are fully entrained. A particle-dominated frictional regime was also observed for dry particles where no changes in frictional dynamics occurred over a range of velocities. In this particle-dominated regime, the friction coefficient is much higher than that of oil alone ($\mu = 0.006$). For 10% glass particles, we find a plateau value of 0.06 and for 50% glass particles in oil, this value is around 0.03. The lower value for the suspension with more particles is likely a cause of more surface separation and less surface deformation due to the presence of more load-bearing particles, as was also discussed in **Chapter 4** and **5**. In this regime, the surface – particle interactions are most important. Surface – particle interactions are also the dominating interactions for the dry glass particles. However, the oil-suspended particles show a much lower friction coefficient than dry particles ($\mu = 0.15$). This suggests that the surface – particle interactions are more favorable in the presence of oil than for dry particles and particles in water. Additionally, particle – particle friction is also expected to be lower in the presence of oil, as oil is well able to wet these slightly hydrophobic glass particles. For particles suspended in oil, lower friction coefficients than for particles in water and for dry particles are thus found, owing mainly to the good surface – fluid and surface – particle contact due to the compatibility of the non-polar fluid with the hydrophobic PDMS surfaces and hydrophobic glass particles.

Hydrophilic glass particles suspended in water and oil

The results so far showed that the interactions between the fluid with the surfaces and the particles lead to diverse frictional behavior. In the previous experiments, both particles and surfaces were hydrophobic. Next, the hydrophobicity of the particles is adapted. To change the particle – fluid, particle – surface, and particle – particle interactions, particles are made hydrophilic by coating the particles with Decon 90, a surfactant. Treating glass with surfactants makes the glass surface more hydrophilic, as the hydrophobic sites attach to the particles, while the hydrophilic sites are present on the outside. [30] We refer to these surfactant coated particles as hydrophilic particles for simplicity. We assume that the surfactants stay present on the particles. However, we must note that surfactants may also detach from the particles. These detached surfactant molecules could then remain in solution or attach to the hydrophobic PDMS surface making the surface slightly hydrophilic.

Hydrophilic particles in water

As mentioned previously, we acknowledge that surfactant molecules may be present in the solution. We, therefore, measure the frictional behavior of a 1% Decon 90 solution to gain insight in the effect of the surfactant alone. We find that the surfactant solution (Figure 6.7, blue dashed line) shows lower friction coefficients than water (1.5 in the boundary regime, Figure 6.1). We attribute this finding to the adhesion of the hydrophobic segments of the surfactant to the PDMS surface. These surfactants then form a lubricating film which renders lower friction coefficients than pure water. [36] For our hydrophilic particles suspended in water, again we observe multiple regimes. We first find a decrease in the friction coefficient from 0.4 to 0.04 up until 5 mm/s. Between 5 mm/s and 30 mm/s, an increase in the friction coefficient is seen from 0.04 until 0.1. At this value, the friction coefficient appears to plateau, something we have also seen in previous sections.

The first regime for these hydrophilic particles in water follows the lubrication curve of the Decon 90 solution. This is similar to regime I in Figure 6.6 where we measured hydrophobic particles in oil and saw that the first regime overlapped with the oil curve in that regime. Both oil and Decon 90 could be considered good lubricants for these surfaces, which explains why their entrainment is favored over particle entrainment. It thus appears that, in this first regime, limited or even no particles are entrained as fluid – surface interactions dominate. The friction coefficient increases again when particles begin to enter the gap as was the case in regime II in the previous section (Figure 6.6). The friction coefficient increases due to the surface deformations induced by the particles and the disruption of the

Lubrication properties of hard particle suspensions between soft surfaces

lubricating layer by the particles as we previously discussed. The plateau-regime is then the regime where particle-driven lubrication dominates the friction coefficient, similar to regime III for the hydrophobic particles in oil (Figure 6.6). The friction coefficient of hydrophilic particles suspended in water is lower than that of dry particles, indicating that the fluid and/or the surfactant are contributing to the lubrication behavior as well. For suspensions with fluids that are well able to wet the surface (oil, surfactant solution), fluids lubricate the sliding surfaces at small gap sizes. At larger gap sizes, more fluid enters the gap and particles can enter the gap with the fluids as a result of the good fluid – particle contact. Once enough particles have been entrained, particle lubrication dominates and the friction coefficient reaches a constant value.

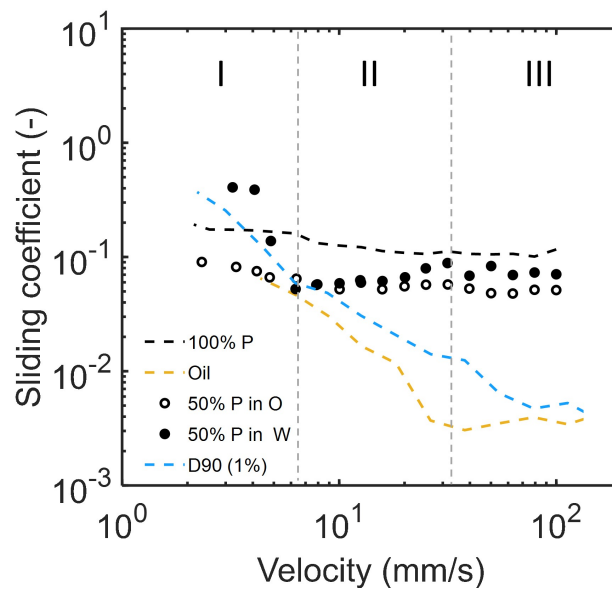


Figure 6.7: Sliding friction coefficients of hydrophilic (surfactant coated) particles. Glass particles (50%) were suspended in water and in oil (filled and empty circles respectively). We show oil (yellow dashed line) as a reference as well as a 1% Decon 90 (D90) solution (blue dashed line) as particles may become detached from the glass surface and dissolve in the fluid matrix. Dry particles are added as a reference (black dashed line).

Hydrophilic particles in oil

In this section, a situation where poor fluid – particle wettability exists is investigated. This is the case for hydrophilic (Decon 90 coated) particles in oil, and the results are displayed in Figure 6.7. For these particles, a constant friction coefficient is measured. The friction coefficients found here are lower than those of hydrophobic glass particles in water and dry glass particles especially at lower speeds. Both the hydrophilic particle suspension in oil and the dry particles show a rather constant friction coefficient (Figure 6.7). We previously attributed such

a constant friction to particle lubrication with limited effects of the surrounding lubricant due to poor fluid – particle wetting. Poor fluid – particle wetting also exists for the hydrophilic particles suspended in hydrophobic oil (Figure 6.7, open symbols). In the case of poor fluid – particle wetting, the gap size is determined by the entrained particles, independent on the interactions between the fluid and the surface. As the fluid is unable to wet the particles, the fluid contribution is limited in this case. One could, however, expect fluid (oil lubrication), to be preferred over particle lubrication, especially at small velocities and gap sizes. Considering that measurements start at high velocities, particles are immediately entrained at the beginning of the measurement. As we decrease the velocity, the gap size decreases, and fluids are expected to be squeezed out of the contact. However, as the oil is unable to wet these hydrophilic particles, the particles remain between the surfaces while the fluids are squeezed out of the contact. This effect becomes even larger when we assume that free surfactants can also make the surface more hydrophilic. We thus find that the gap size here is driven by the particles present in the gap.

Overview of mechanisms behind particle suspension lubrication

Using hydrophobic and hydrophilic glass particles suspended in various Newtonian fluids, we find that different frictional regimes arise depending on the fluid properties and the particle properties. We have found fluid lubricated regimes, particle lubricated regimes, and transition/mixed regimes. In this section, we will provide an overview of the various mechanisms we have observed for these glass particle suspensions in the different regimes.

Particle percentages

Using dry particles results in particle entrainment and lubrication over the entire velocity range. This is represented by the black line in Figure 6.8 where the friction coefficient is velocity (gap size) independent. For particles suspended in water and in oil, we observed a fluid-dominated and a particle-dominated regime depending on the measuring conditions. Particle entrainment occurs more readily at high volume fractions (Figure 6.1 and 6.6). As there are more particles present, it is more likely that particles become entrained between the surfaces reducing the surface – surface contact while increasing the (rolling) particle – surface interactions. As discussed in **Chapter 4** and **5**, with a low number of particles, the load per particle remains relatively high, and larger surface deformations lead to larger surface – particle contacts with subsequent higher friction coefficients. For the glass

Lubrication properties of hard particle suspensions between soft surfaces

particles used here, we found two sliding regimes for low particle percentages: fluid lubrication dominates at low velocities and particles are entrained as the velocity-dependent gap size increases.

Fluid matrix viscosity

Using glycerol solutions to study the effect of matrix viscosity on particle suspension lubrication, it was found that particle entrainment depends on matrix viscosity. At high viscosities, fluid entrainment occurs as fluids are less likely to be squeezed out and a steady fluid film is formed. This leads to low friction coefficients. At low matrix viscosities, fluid film formation is less evident, and friction coefficients are higher. When the viscosity of the matrix is high, particles remain entrained with the fluid matrix, This leads to particle entrainment already at low velocities, and the friction coefficient is then dominated by particle lubrication over the entire velocity range. At low viscosity, even if the fluid is entrained, particle entrainment does not occur until the gap size increased at relatively high velocities (Figure 6.8, blue dashed line). In this case, the friction is mostly fluid-dominated, and particle lubrication is only obtained at high velocities.

Wettability

Hydrophobic particles suspended in water and hydrophilic particles suspended in oil were also considered. The contribution of the fluid matrix in both cases was limited due to the poor wetting between the fluid matrix and the particles. This led to constant particle lubrication over the entire speed regime as the gap size was determined by the entrained particles. Poor fluid – particle wetting thus leads to particle entrainment with limited effects of fluid – surface and fluid – particle interactions. When there is good fluid – particle contact (good wetting), several sliding regimes arise. At low velocities, fluid lubrication dominates and at higher velocities, particles begin to enter the gap due to the increased gap size as indicated in Figure 6.8. The effect of particle entrainment on the friction coefficient then depends on the wettability of the fluid for the surface. When there is good fluid – surface contact in terms of wettability (as in the case oil on PDMS surfaces), particle entrainment leads to an increase in the friction coefficient (Figure 6.8, yellow dotted line). In the case of poor fluid – surface contact (as in the case of water on PDMS surfaces), particle entrainment gives a decrease in the friction coefficient (Figure 6.8, blue dashed line).

To summarize, when good fluid – particle interactions exist, fluid entrainment occurs at low velocities and particles enter the gap at higher velocities. Particle

entrainment dominates in several cases: (I) high particle volume fractions, (II) Poor fluid – particle wettability, (III) high viscosity. In Figure 6.8, we show a schematic lubrication curve that shows the most important frictional regimes for particle suspensions; a fluid lubrication regime and a particle lubrication regime. The fluid regime shows characteristics of a Stribeck curve for Newtonian fluids. The particle regime shows constant values of the friction coefficient due to a constant gap size. In the figure, we have also displayed the mechanisms associated with each regime and the specific conditions for these mechanisms.

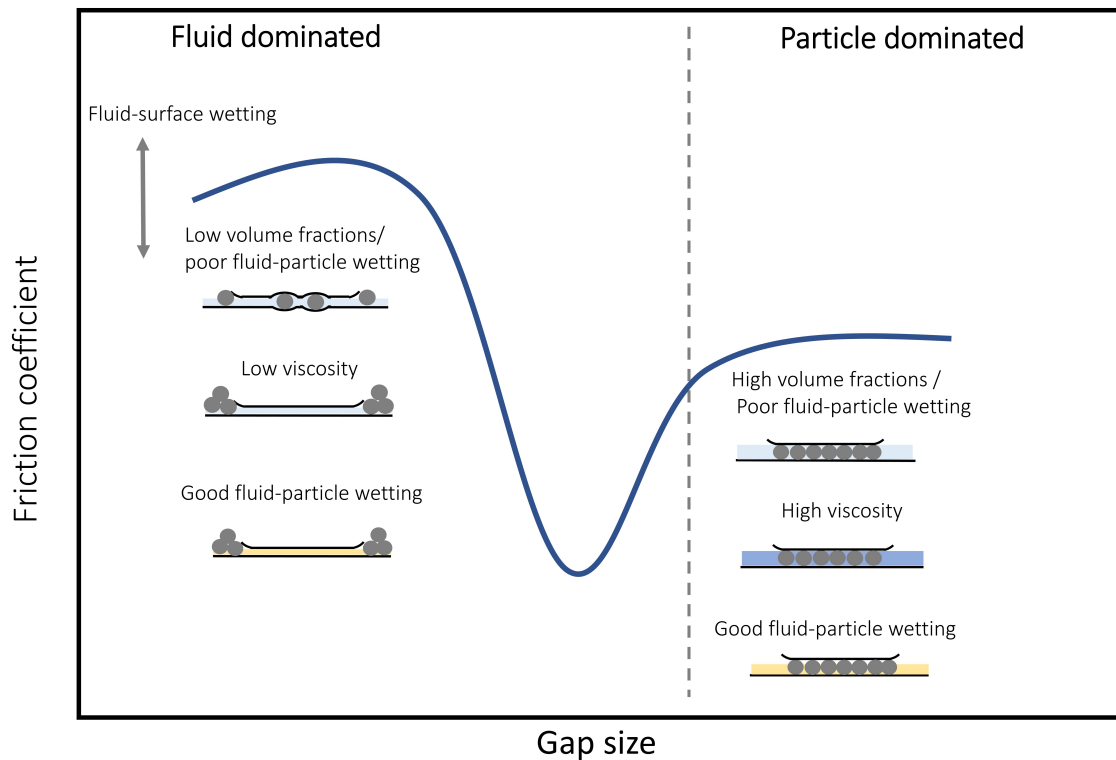


Figure 6.8: Schematic lubrication curve with the different regimes observed for particles in suspension; Fluid dominated and particle dominated. The progression of the fluid-dominated regime depends on the fluid – surface wettability and on the fluid viscosity. We show the mechanisms behind fluid lubrication and particle lubrication schematically in the figure. The gap size in the particle dominated regime is the size of the particles.

The results shown here were obtained using solid glass particles that are 100 μm in size. When we compare our results to findings in literature obtained using suspensions made of hollow 10 μm glass particles [27], deviating frictional regimes are found. In case of smaller particles, particle lubrication dominates at low gap sizes, whereas an EHL regime is found due to the fluid formation of high viscosity fluids. [27] Such an EHL regime is found as the fluid film thickness exceeds the particle diameter. For our larger particles, the viscous fluid is unable to increase the gap size to values larger than the particle size, and an EHL regime is not obtained. These differences highlight the importance of the particle size on the frictional

properties of suspensions. The friction coefficient is thus strongly dependent on the characteristics of the system, including the type of particles and fluids used.

Conclusions

The frictional behavior of hard particles in suspension between two soft surfaces was investigated in this chapter. The aim was to create a better understanding of particle entrainment in relation to fluid – particle – surface interactions. It was shown that particles can enter the gap in different situations, even at gap sizes that are theoretically far smaller than the size of the particle. Particles and fluids can enter the gap separately or simultaneously depending on the suspension properties. When poor fluid – particle wetting exists, particles enter and remain in the gap while fluids are excluded. However, when fluids are able to wet the particles, particles can be dragged in and out of the contact with the surrounding fluids. These interactions thus determine at what velocities the particles are entrained. Due to the differences in the particle entrainment, we observed two main lubrication regimes; fluid lubrication and particle lubrication. Fluid lubrication dominates at low particle volume fractions, and in situations where particles are not entrained. This occurs at low velocities, and when fluids are well able to wet the particles. Particle lubrication dominates at high particle percentages, high matrix viscosities, and poor fluid – particle wetting. Overall, we have shown that the frictional regimes for hard particles lubricating soft surfaces are a direct consequence of the ability of particles to entrain the surfaces. The entrainment is driven by the particle – fluid interactions as well as the fluid – surface interactions. At velocities at which particles are able to become and remain entrained within the gap, particle lubrication becomes more dominant over fluid lubrication. Future investigations into similar systems could study the effect of different particle sizes, surface hydrophobicity and surface roughness on the friction coefficients of soft surfaces and particulate lubricants.

References

1. Farrokhpay, S., Morris, G. E., Fornasiero, D. & Self, P. Titania pigment particles dispersion in water-based paint films. *Journal of Coatings Technology and Research* vol. 3, 275–283 (2006).
2. Van der Kooij, H. M. & Sprakel, J. Watching paint dry; more exciting than it seems. *Soft Matter* vol. 11, 6353–6359 (2015).
3. Bolzinger, M.-A., Briancon, S. & Chevalier, Y. Nanoparticles through the skin: managing conflicting results of inorganic and organic particles in cosmetics and pharmaceuticals. *Wiley Interdisciplinary Reviews: Nanomedicine and Nanobiotechnology* vol. 3, 463–478 (2011).
4. Timm, K., Myant, C., Nuguid, H., Spikes, H. & Grunze, M. Investigation of friction and perceived skin feel after application of suspensions of various cosmetic powders. *International journal of cosmetic science* vol. 34, 458–465 (2012).
5. Scholten, E. Composite foods: From structure to sensory perception. *Food & function* vol. 8, 481–497 (2017).
6. Shewan, H. M. *et al.* Interpreting Rheological Behaviour of Sugar-Fat Mixtures as a Function of Solids Phase Volume. *Journal of Food Engineering* vol. 297, 110474 (2021).
7. Sparr, E. *et al.* Controlling the hydration of the skin though the application of occluding barrier creams. *Journal of The Royal Society Interface* vol. 10, 20120788 (2013).
8. Ding, S. & Bhushan, B. Tactile perception of skin and skin cream by friction induced vibrations. *Journal of colloid and interface science* vol. 481, 131–143 (2016).
9. Civile, G. V. Food texture: pleasure and pain. *Journal of agricultural and food chemistry* vol. 59, 1487–1490 (2011).
10. Santagiuliana, M., Bhaskaran, V., Scholten, E., Piqueras-Fiszman, B. & Stieger, M. Don't judge new foods by their appearance! How visual and oral sensory cues affect sensory perception and liking of novel, heterogeneous foods. *Food Quality and Preference* vol. 77, 64–77 (2019).
11. Rudge, R. E. D., Scholten, E. & Dijkman, J. A. Advances and challenges in soft tribology with applications to foods. *Current Opinion in Food Science* vol. 27, 90–97 (2019).
12. Kim, J. M., Wolf, F. & Baier, S. K. Effect of varying mixing ratio of PDMS on the consistency of the soft-contact Stribeck curve for glycerol solutions. *Tribology International* vol. 89, 46–53 (2015).
13. Selway, N., Chan, V. & Stokes, J. R. Influence of fluid viscosity and wetting on multiscale viscoelastic lubrication in soft tribological contacts. *Soft Matter* vol. 13, 1702–1715 (2017).
14. De Vicente, J., Spikes, H. & Stokes, J. Viscosity ratio effect in the emulsion lubrication of soft EHL contact. *Journal of Tribology* vol. 128, 795–800 (2006).
15. Bongaerts, J., Rossetti, D. & Stokes, J. The lubricating properties of human whole saliva. *Tribology Letters* vol. 27, 277–287 (2007).
16. Berthier, Y. Third-body reality—consequences and use of the third-body concept to solve friction and wear problems. *Wear, Materials, Mechanisms and Practice* vol. 1 (2005).
17. Diomidis, N. & Mischler, S. Third body effects on friction and wear during fretting of steel contacts. *Tribology International* vol. 44, 1452–1460 (2011).
18. Quemada, D. Rheology of concentrated disperse systems and minimum energy dissipation principle. *Rheologica Acta* vol. 16, 82–94 (1977).

19. Shewan, H. M. & Stokes, J. R. Analytically predicting the viscosity of hard sphere suspensions from the particle size distribution. *Journal of Non-Newtonian Fluid Mechanics* vol. 222, 72–81 (2015).
20. Mangesana, N. *et al.* The effect of particle sizes and solids concentration on the rheology of silica sand based suspensions. *Journal of the Southern African Institute of Mining and Metallurgy* vol. 108, 237–243 (2008).
21. Guazzelli, É. & Pouliquen, O. Rheology of dense granular suspensions. *Journal of Fluid Mechanics* vol. 852, P1 (2018).
22. Rudge, R. E. D., Van De Sande, J. P., Dijksman, J. A. & Scholten, E. Uncovering friction dynamics using hydrogel particles as soft ball bearings. *Soft Matter* vol. 16, 3821–3831 (2020).
23. Deng, F., Tsekenis, G. & Rubinstein, S. M. Simple law for third-body friction. *Physical Review Letters* vol. 122, 135503 (2019).
24. Wang, Q., Xue, Q., Liu, H., Shen, W. & Xu, J. The effect of particle size of nanometer ZrO₂ on the tribological behaviour of PEEK. *Wear* vol. 198, 216–219 (1996).
25. Reeves, C. J., Menezes, P. L., Lovell, M. R. & Jen, T.-C. The influence of surface roughness and particulate size on the tribological performance of bio-based multi-functional hybrid lubricants. *Tribology International* vol. 88, 40–55 (2015).
26. Nguyen, P. T., Kravchuk, O., Bhandari, B. & Prakash, S. Effect of different hydrocolloids on texture, rheology, tribology and sensory perception of texture and mouthfeel of low-fat pot-set yoghurt. *Food Hydrocolloids* vol. 72, 90–104 (2017).
27. Yakubov, G., Branfield, T., Bongaerts, J. & Stokes, J. Tribology of particle suspensions in rolling-sliding soft contacts. *Biotribology* vol. 3, 1–10 (2015).
28. Bongaerts, J. H., Cooper-White, J. J. & Stokes, J. R. Low biofouling chitosan-hyaluronic acid multilayers with ultra-low friction coefficients. *Biomacromolecules* vol. 10, 1287–1294 (2009).
29. De Vicente, J., Stokes, J. & Spikes, H. Rolling and sliding friction in compliant, lubricated contact. *Proceedings of the Institution of Mechanical Engineers, Part J: Journal of Engineering Tribology* vol. 220, 55–63 (2006).
30. Khoshnaw, F. M., Conway, P. P., Hutt, D. A. & Williams, K. *Glass multilayer lamination for PCB manufacture using pressure assisted low temperature bonding in 2007 9th Electronics Packaging Technology Conference* (2007), 504–509.
31. Segur, J. B. & Oberstar, H. E. Viscosity of glycerol and its aqueous solutions. *Industrial & Engineering Chemistry* vol. 43, 2117–2120 (1951).
32. Farr, R. S. & Groot, R. D. Close packing density of polydisperse hard spheres. *The Journal of chemical physics* vol. 131, 244104 (2009).
33. De Vicente, J., Stokes, J. & Spikes, H. The frictional properties of Newtonian fluids in rolling-sliding soft-EHL contact. *Tribology Letters* vol. 20, 273–286 (2005).
34. Vergeles, M., Koblinski, P., Koplik, J. & Banavar, J. R. Stokes drag and lubrication flows: A molecular dynamics study. *Physical Review E* vol. 53, 4852 (1996).
35. Reichardt, C. Solvatochromic dyes as solvent polarity indicators. *Chemical Reviews* vol. 94, 2319–2358 (1994).

36. Graca, M., Bongaerts, J. H., Stokes, J. R. & Granick, S. Friction and adsorption of aqueous polyoxyethylene (Tween) surfactants at hydrophobic surfaces. *Journal of colloid and interface science* vol. 315, 662–670 (2007).

PART III

Tribological applications



7

**Lubrication properties of
hard particle suspensions
between soft surfaces**

Abstract

Astringency is one of the most complex oral sensations. This dry, puckering mouthfeel occurs when consuming wine, tea, or other foods containing polyphenols. The exact mechanism behind this dry mouthfeel is not completely understood. Here, we describe a systematic tribological approach to measure model and real saliva to understand the specific role of the salivary proteins (mucins and proline-rich proteins (PRPs)) on lubrication-based astringency. Our approach reveals that there are two routes towards lubrication losses, partly involving irreversible molecular mechanisms for which the order of reactivity matters. For human saliva, we find two lubrication mechanisms: (I) Using phenolic compounds, we find aggregation-induced lubrication losses due to hydrogen bond formation, which depend critically on phenol size: large polyphenols allow for aggregation-induced lubrication losses, but small phenols do not. (II) For metal salts combined with saliva, we observe aggregation without lubrication losses as a result of electrostatic interactions. We find that lubrication losses are caused by the specific removal of the salivary PRP layer, whereas mucin aggregation in the presence of PRPs does not lead to lubrication losses. We also show that the addition of solvents that are able to reduce protein-polyphenol hydrogen bonding (e.g ethanol) and highly viscous fluids (glycerol) are successful approaches to decrease the effect of aggregation-induced lubrication losses.

This chapter was submitted as:

Rudge, R.E.D., Fuhrmann, P.L., Scheermijer R., Van der Zanden, E. M., Dijksman, J.A., and Scholten. E.,

A tribological approach to astringency perception and astringency prevention

Introduction

An astringent sensation is perceived as a dry and rough feeling in the mouth, which can be experienced when drinking tea or red wine, eating unripe fruit, or a variety of plant protein derived products. [1–3] Mouthfeel characteristics such as astringency, dryness, and grittiness have recently gained a lot of attention, due to their relevance in plant-based foods and the strong impact these mouthfeel characteristics have on the hedonic response. [4–7] Astringency is often experienced as a negative sensation, and efforts to understand the underlying dynamics influencing this sensation have received increased attention. Currently, two models are commonly accepted to explain the perception of astringency. The first one assumes astringency is a receptor-based sensation where astringent compounds would potentially activate trigeminal or taste nerves. [8, 9] However, astringent sensations are also perceived on oral surfaces that do not accommodate receptors. [10] This indicates that astringency is not only receptor-based. The second model describes astringency as a friction-based sensation [9] Astringent compounds are believed to interact with bulk salivary proteins, forming insoluble aggregates, also relating to the word astringency itself, which is derived from the Latin term “adstringere” which translates to “to bind”. These aggregates are then believed to interact with the oral surfaces, thereby increasing the friction between oral surfaces. [2, 4, 11–15] Additionally, it has been suggested that the aggregation of the astringent compounds with the salivary proteins removes the lubricating salivary film from the tongue, and the proteins are no longer able to lubricate the oral surfaces. This provokes a dry and rough feeling. [16]

However, the exact mechanism behind salivary aggregation in the presence of astringent agents and how this contributes to the friction coefficient is currently unknown. Therefore, the objective of the present chapter is to investigate the interactions between different salivary proteins and astringent molecules and the impact these interactions have on salivary lubrication.

Although the proteins in saliva make up only 0.3% of saliva, they play an essential role in the functionality of saliva. These amphiphilic salivary proteins adhere to in-mouth surfaces and are able to form a lubricating biopolymer layer that helps to protect the surfaces from wear and facilitates masticating and swallowing foods. [17–19] Two groups of proteins are of specific interest in the context of lubrication in general and astringency in particular: mucins and proline-rich proteins (PRPs), which make up 30% and 70% of the total protein content of saliva, respectively. [12, 20] Mucins are essential in providing (extensional) viscosity to saliva and in

A tribological approach to astringency perception and astringency prevention

lubricating the oral cavity, as they are of polymeric nature. [17–19] PRPs appear to be relevant for maintaining oral homeostasis and have a very different structure than mucins. [14, 21] Although literature on macromolecular interactions underlying astringency is abundant, [9, 22, 23] limited knowledge currently exists on how these macromolecular interactions influence the frictional behavior. The latter will determine whether astringency is a receptor-based or a friction-based oral sensation (texture-based). It has previously been shown that large polyphenols can interact with (muco)proteins using hydrogen bonding leading to an increase in the friction coefficient. [12, 22, 24] It was also shown that mucins can interact with metal salts which also leads to binding interactions (aggregation) and subsequent lubrication losses. [25] Most lubrication studies have been performed with only mucin, but limited (or even no) information is currently available on the role of salivary PRPs and their interactions with astringent agents on lubrication losses. The interactions between astringents and both mucins and PRPs have been reported based on electrophoresis-based protein separation [26] and nuclear magnetic resonance. [27] Unfortunately, in the aforementioned studies, no tribological measurements were included. The exact role of the different salivary proteins and the effect of the protein-astringent interactions on the lubrication behavior therefore remains unclear.

Here, we investigate the effect of a broad spectrum of different astringents on salivary (protein) lubrication. The three types of astringent agents we use are small phenols, large polyphenols, and aluminum salts. We measure the friction coefficient and aggregate sizes of these combinations of astringent agents and saliva, and mucin solutions, and PRP solutions separately. Additionally, we explore how lubrication losses can be prevented by combining salivary-astringent mixtures with different (non-astringent) solvents to investigate the competing effects of polymer driven lubrication, aggregation, wettability, and viscous lubrication. The findings presented here deliver new insights into in-mouth lubrication in general and oral astringency specifically.

Experimental section

Collection of saliva

For our frictional measurements, we use human saliva. Human saliva was collected from three healthy, non-smoking, female subjects (age 19 - 26), following a procedure described by Silletti and co-workers. [28] The subjects were asked to refrain from eating and drinking for at least two hours before saliva was collected. Before saliva collection, the mouth was rinsed with water, and the first 1 mL of saliva was discarded. Non-stimulated saliva (10 ml) was then collected in a centrifugation tube and placed on ice before centrifugation at 10000 g for 30 min at 4 °C (Beckmann, Avanti TM J-25 I, JA-25.15) to remove debris.

Preparation of mucin solution

A mucin solution was prepared by dispersing porcine gastric mucin Type II in Ultrapure water (Milli-Q, Purelab Ultra System, Germany). This type of mucin is often used as a representative for human saliva. [29, 30] The concentration of mucin was 0.1 wt% and the pH of the protein solution was adjusted to 6.8 using 0.1 M NaOH, similar to the pH of human saliva.

Preparation of PRP solutions

The method used for the separation of proline-rich proteins (PRPs) from human saliva was adapted from a method previously developed. [31] In short, the collected saliva was treated with trifluoroacetic acid (TFA), and a 10% solution was added to reach a final concentration of 0.1%. This was done to precipitate high molecular weight proteins (e.g. mucins) and to inhibit protease activity. The obtained solution was then centrifuged for 10 minutes at 12000 g at 5 °C to remove the precipitated larger proteins and any residual particles. The supernatant containing the PRPs was collected and dialyzed using a Spectra/Por 3 Cellulose Membrane (SpectrumLabs, Sigma-Aldrich) with an exclusion size of 3.5 kDa. The dialysis process was carried out using demineralized water at 5 °C for 48 hours. Water was renewed after 4, 8, 16, 24, 32, and 40 hours. The dialyzed solution was frozen for at least 24 hours and freeze-dried overnight to obtain a dry PRP-rich protein concentrate. The PRP concentrate was redispersed in water at 0.2% to obtain a similar concentration as present in saliva. Removal of mucins was confirmed by sodium dodecyl sulfate–polyacrylamide gel electrophoresis (SDS-PAGE, data not shown). Before measurements, the pH was adapted to 6.8 using 0.5 M HCl. The salivary protein (PRP) solution was then sonicated using a Branson 450

A tribological approach to astringency perception and astringency prevention

Digital Sonifier at 20 kHz and amplitude of 50% (Branson Ultrasonics Corporation, USA) to remove possible protein agglomeration. A cylindrical titanium probe with 2.7 mm was used, which was immersed 5 mm into the sample vessel.

Tribological measurements

We measured friction coefficients using a commercial (glass) ball on a three (PDMS) pin setup, in a rheometer (Anton Paar Rheometer, MCR302). The measurements were performed in triplicate at a constant normal force of 1 N, relevant for forces occurring during oral processing. [32] Two procedures were used here. (I) Friction coefficients were measured as a function of entrainment velocity, in repeated cycles of in- and decreasing velocities of 0.047 mm/s- 470mm/s. For velocity-dependent runs, the first run was excluded to allow the system to arrive at an equilibrium state. (II) Friction coefficients were measured at a constant velocity (e.g. 1 mm/s) as a function of time. Before measurements, the PDMS pins were coated with a layer of saliva or individual salivary proteins (mucin or PRP concentrate) by allowing the glass probe to slide against the PDMS pins while lubricated by 0.5 ml of the protein solution for 300 s. The friction coefficient of this system was monitored to assure that saliva components were indeed present on the PDMS pins. After a constant friction coefficient was obtained, the astringent component (0.5 mL solution) was inserted into the tribocup in a 1:1 ratio and the friction coefficient was measured for an additional 300 s to detect changes in the lubrication behavior ($\Delta\mu$). As astringents, we used epigallocatechin gallate, kindly donated by Taiyo GmbH, tannic acid, gallic acid, caffeic acid (Sigma-Aldrich), and potassium alum ($KAl(SO_4)_2 \cdot 12H_2O$, Nederlandse Drogisterij Service B.V.).

Particle size measurements

To determine the particle size, we used dynamic light scattering (DLS). For this purpose, a Zetasizer Nanoseries (Malvern Instruments) was used. First, the particle size of saliva, solutions of salivary proteins, and astringent solutions were determined. The separate mucin, PRP, and astringent compounds solutions were diluted 100 times. After that, the astringent compounds were added to the different saliva and protein solutions in a ratio of 1:1, the same ratio as used for the tribological measurements, and particle size was determined again to evaluate changes in particle size.

Results

Saliva is a key component in keeping the oral surfaces lubricated. The bio-lubricant provides remarkably low friction coefficients ($\mu = 0.2$), despite only having about 0.3% protein present in saliva (Figure 7.1a). Its friction coefficient in the boundary regime, i.e. low velocities, is about four times lower than that of water, even though water makes up over 99% of saliva. Astringent compounds have been shown to change these good lubricating properties of saliva. [4, 11, 12, 33] To investigate what molecular interactions drive the physical changes in saliva responsible for the change in the lubrication behavior, we use a variety of compounds that are known to evoke astringency. The compounds used here are epigallocatechin gallate (EGCG), tannic acid (TA), caffeic acid (CA), gallic acid (GA), and alum. These astringent compounds can be divided into three categories: large phenolic compounds (EGCG, TA), small polyphenolic compounds (GA and CA), and cationic metal salts (alum). We measured the friction coefficient of 5 mM solutions of each compound without the presence of saliva and found large similarities to the frictional behavior of water only. The frictional curves with water as a reference are displayed in Figure 7.1b-f. Only the cationic astringent alum shows much lower friction coefficients than water (Figure 7.1f). It has been found that the lubricating properties of the anion of a salt depend on its ranking in the Hofmeister series. [34] Anions higher in the Hofmeister series, such as the sulfate anion of alum, have a better water holding capacity, which is related to a higher repulsive force and a higher local viscosity, both increasing the lubricity. [34] Overall, it is seen that the astringent agents do not contribute much to the lubrication properties of water.

A tribological approach to astringency perception and astringency prevention

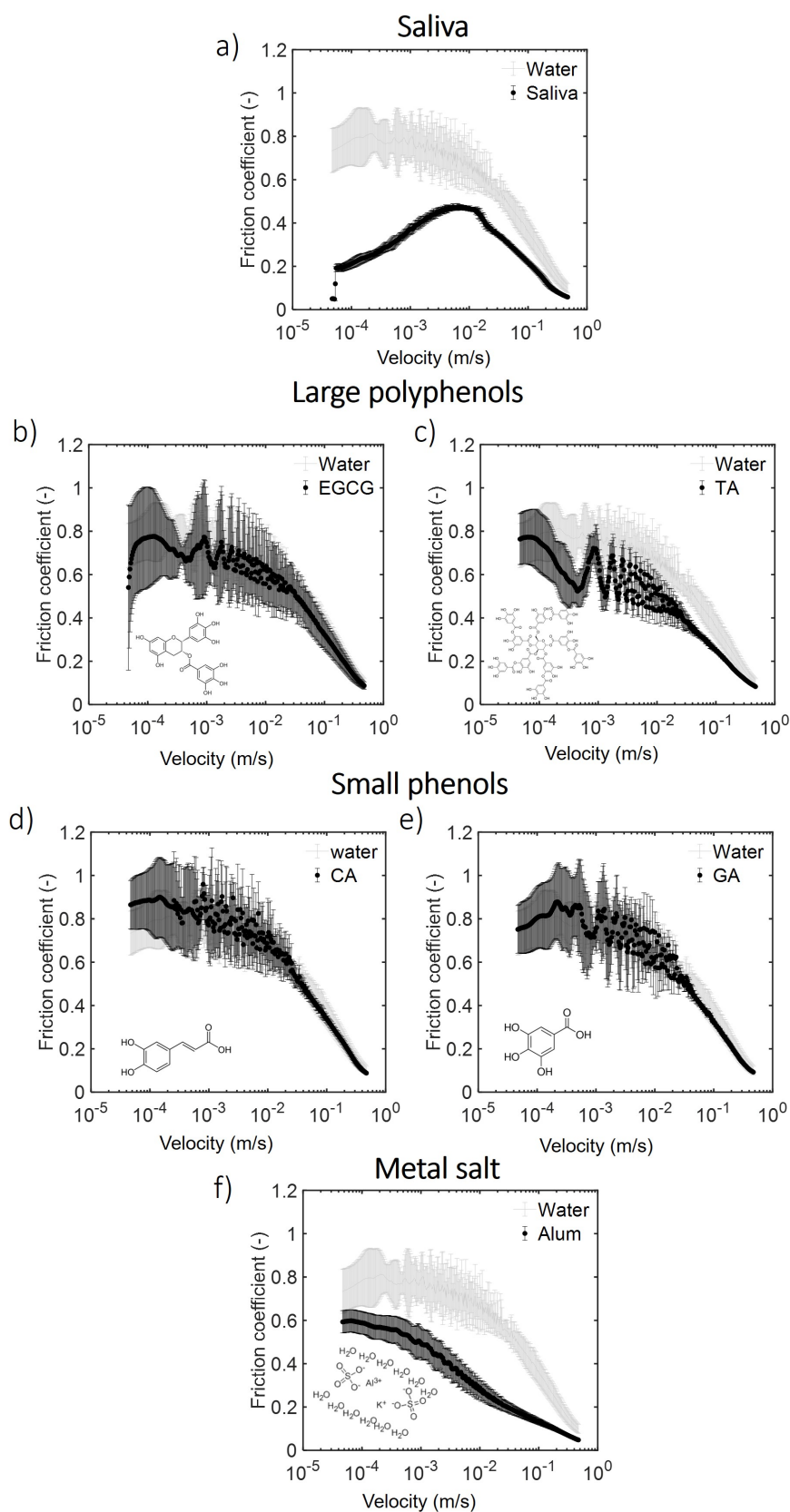


Figure 7.1: Frictional curves of a) saliva, large polyphenols: b), EGCG, c) TA, small phenols: d) CA, e) GA, and metal salt: f) alum as function of velocity measured between a rough glass ball and smooth PDMS pins. The astringent agents were dissolved in water prior to measurements. The structures of the astringent compounds are added to each graph. Water is included in all curves.

Lubrication losses caused by large polyphenols

One of the existing models to explain oral astringency suggests that astringent agents can interact with human saliva, thereby inducing aggregate formation with the salivary proteins. Here, we examine whether the aggregation is also accompanied by a change in the friction coefficient. An increase in friction can occur when saliva is not able to lubricate the surfaces, i.e. lubrication losses take place. To gain more insights into the mechanisms behind oral astringency and lubrication losses, we first measure the friction coefficient of saliva over time at a fixed speed of 1 mm/s. We observe a decrease in the friction coefficient during the first 600 seconds of measuring saliva. This is likely due to the formation of a lubricating protein layer during this period. Next, we add the large polyphenolic astringent agents TA and EGCG. After adding the polyphenols, we indeed observe the expected increase in friction coefficient as displayed in Figure 7.2a and b. This increase is likely a result of the proteins interacting with the salivary layer formed on the tribosurfaces.

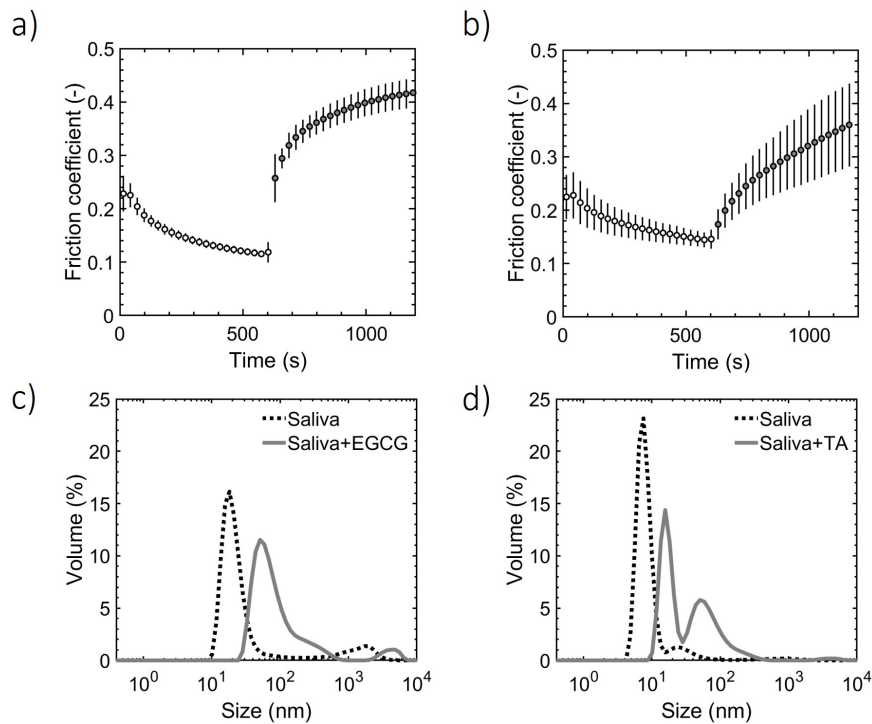


Figure 7.2: Friction coefficients of saliva (open symbols) with a) EGCG and b) TA added after 600 seconds (closed symbols). The particle size of saliva (black, dashed line) and saliva mixed with astringent (grey, solid line) are shown in c) for EGCG and d) for TA.

As a result of the addition of these large polyphenols, the friction coefficient increases from 0.1 to 0.4 in the first 30 seconds. We refer to this increase in the friction coefficient $\Delta\mu$ (note that this is a different $\Delta\mu$ than used in Chapter 2). A relatively large increase in friction coefficient ($\Delta\mu = 0.3$) is thus found,

A tribological approach to astringency perception and astringency prevention

as the interaction between large polyphenols and saliva leads to loss of salivary lubricity. This is similar to findings using mucoproteins and tannic acid where an increase in the friction coefficient, as well as the particle size, was observed as well. [22] For both EGCG and TA, we see an increase in the particle size upon mixing with saliva, indicating that protein precipitation took place. We thus confirm that the lubrication losses observed here are a direct consequence of the aggregation between the lubricious salivary proteins and EGCG or TA (Figure 7.2c and d). For large polyphenols, the astringency perception appears to come from the precipitation of salivary proteins and the polyphenols, in combination with an increase in the friction coefficient, as a direct result of the removal of the lubricious salivary protein layer. These aggregates can potentially provide rolling friction while separating the surfaces as extensively discussed in the “Particle lubrication” section (**Chapters 4, 5, and 6**) of this thesis. As the aggregates formed between saliva and polyphenols are not perfectly round or smooth, they generate relatively high friction coefficients as they do not easily roll. The presence of such large and rough particles would be perceived as dry and gritty during oral processing. [7, 35] Figure 7.3 provides a schematic overview of the tribological mechanisms, where the proteins initially provide a layer of hydrated polymer brushes, which are removed through protein precipitation by the astringent agent.

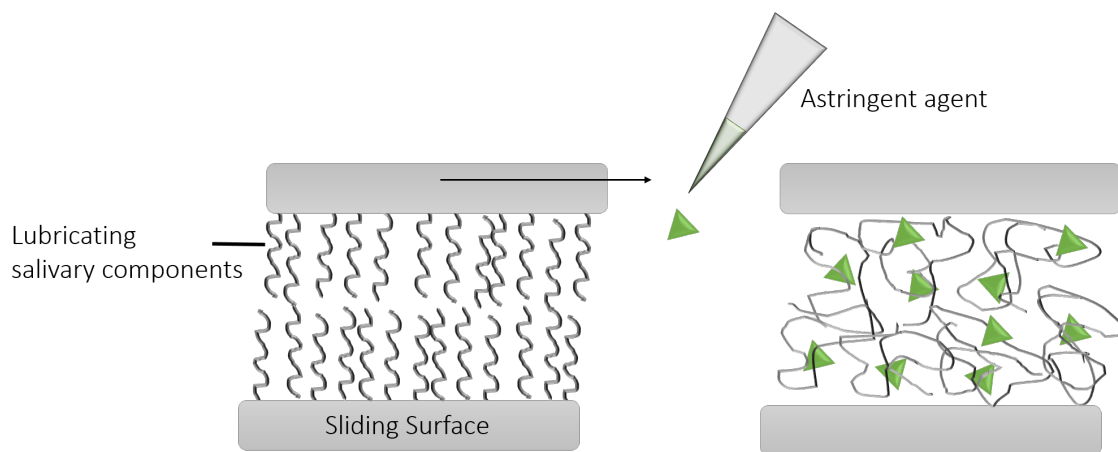


Figure 7.3: The salivary film formed on the tribometer surfaces before and after the addition of astringent agents that cause the salivary proteins to aggregate.

Small phenolic compounds are unable to aggregate proteins

To better understand how different types of astringent compounds affect both the protein precipitation and the lubrication losses, we measured the change in friction coefficient also for small phenolic compounds. The results of the increases in friction, represented by $\Delta\mu$, found for all astringent agents used here are

summarized in Figure 7.4. As a reference, the addition of water only was taken into account to be able to dismiss any dilution effects.

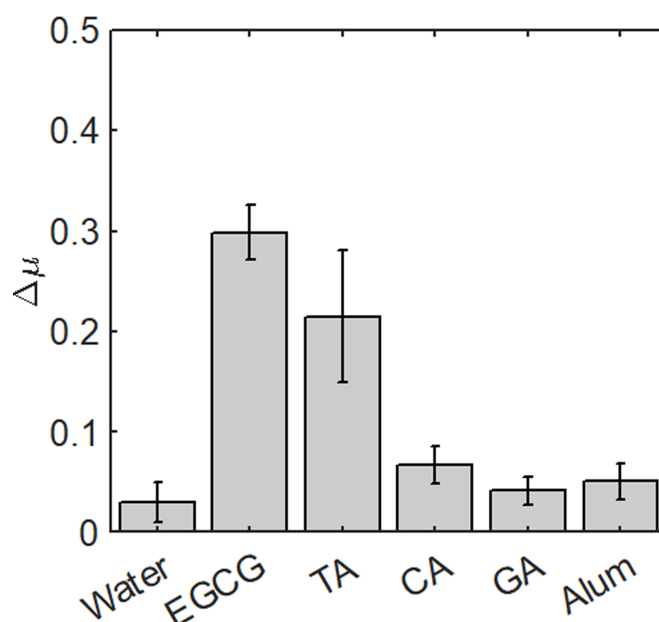


Figure 7.4: Friction coefficient increase ($\Delta\mu$) after 30 seconds of adding different astringent agents (EGCG: epigallocatechin gallate, TA: tannic acid, CA: caffeic acid, GA: gallic acid, and alum) to saliva with water as a reference.

As mentioned previously, large polyphenols induce a strong increase in the measured friction coefficient upon addition to saliva. Smaller polyphenolic moieties, however, are less likely to interact with proteins due to their limited size and insufficient protein binding sites. This was confirmed by particle size measurements, as no increase in particle size was observed when GA and CA were added to saliva (data not shown). This is also obvious from the friction measurements, as the addition of CA and GA to saliva gave only a small increase in the friction coefficient of 0.05 and 0.02, respectively (Figure 7.4). These values are similar to those found for the addition of pure water (Figure 7.4). This strongly suggests that the changes in friction coefficient are simply caused by dilution effects rather than an effect of interactions taking place between the proteins and the compounds CA and GA. Although no protein precipitation or lubrication losses were observed, CA and GA have been described as astringent during sensory evaluation [33] with astringency thresholds of 72 and 292 μM respectively, [36] which is well below the concentration used in this study (5 mM).

A tribological approach to astringency perception and astringency prevention

For these small polyphenols, oral astringency, therefore, appears not to be caused by physical changes in salivary lubrication. The astringent sensation perceived with GA and CA is more likely to be a result of the small molecule binding to a receptor, as was previously suggested. [8, 9] These results show that indeed different mechanisms are responsible for the perception of different astringent compounds. It has been reported that GA is perceived as less astringent than large polyphenols such as TA. [37] The difference in astringency perception between large and small polyphenols indicates that different astringent mechanisms are at play. Low astringency could be obtained by receptor-based sensations only, whereas enhanced astringency is related to the additional changes in friction coefficient and protein precipitation. The specific structure of the polyphenol, therefore, determines the mechanisms of action and the level of astringency. When the intramolecular interactions induce precipitation and lubrication losses, increased astringency perception occurs. This is mostly related to hydrogen bond formation between polyphenols and proline groups of the proteins. [27, 38] GA and CA are thus too small and lack sufficient degree of interactions with relevant protein binding sites to induce protein precipitation and subsequent lubrication losses.

Cationic astringents cause aggregation without lubrication losses

Potassium aluminum sulfate, better known as alum, is also known as an astringent compound. [25] As alum is a small molecule, we would not expect much protein precipitation. However, alum is a charged molecule and can interact with proteins through different interactions. This may also change salivary lubrication. Results in Figure 7.4 show that alum addition results in a small increase in the friction coefficient that is not very different from results obtained when merely diluting saliva, and is similar to the changes observed for the small polyphenols. However, when we measure the particle size of a mixture of saliva and alum, we find a shift from around 50 nm for saliva to 500 nm with the addition of alum. An unexpected increase in the particle size in combination with a limited change in friction coefficient is thus found. From the increase in particle size, it is evident that protein precipitation takes place. This observation, however, seems to be in contradiction with the results for small polyphenols that did not show any protein precipitation nor changes in lubrication behavior. Aggregation of salivary proteins can thus also take place without influencing the friction coefficient. It appears that salivary proteins can interact with the astringent agent while maintaining good lubricating properties. We present an overview of our findings for the different astringent agents when combined with saliva in Figure 7.5.

A tribological approach to astringency perception and astringency prevention

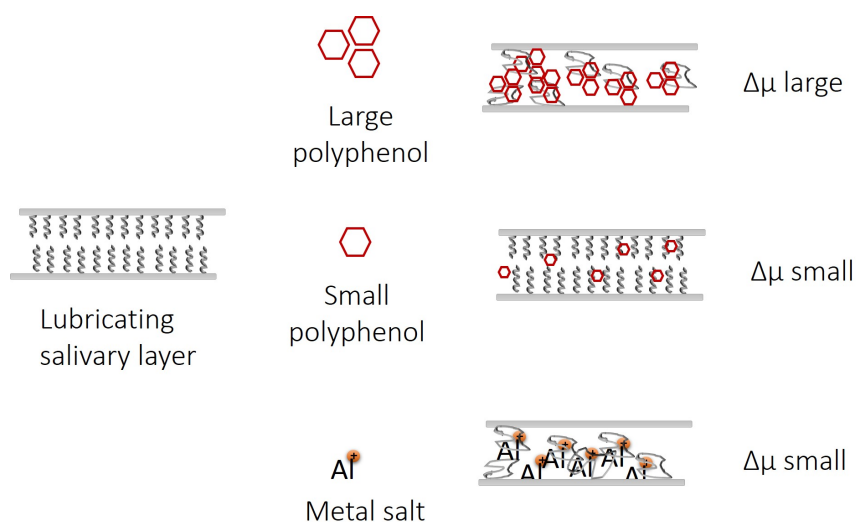


Figure 7.5: Schematic display of changes in particle size and in friction coefficient upon addition of different astringent agents to saliva during tribological measurements.

Lubrication losses of PRP and mucin solutions

Based on our current findings, the interactions between salivary proteins and astringent compounds depend on the characteristics (size, charge, conformation, etc.) of the astringent compound. For metal salts such as alum, these interactions appear to be charge driven and do not lead to lubrication losses with saliva. For large polyphenols, the molecules and salivary proteins can undergo both hydrophobic interactions and hydrogen bonding with compatible protein regions [2, 24, 39] Specifically, the proline-rich regions of salivary proteins are expected to provide good binding sites for polyphenolic rings. [27, 40, 41] In the case of large polyphenols, we do measure an increase in friction when added to saliva. This indicates that different salivary proteins interact with different astringent compounds. Although much is known about salivary aggregation, [14, 27, 38, 42, 43] limited knowledge is still available on which salivary proteins are responsible for the lubrication losses. We investigate the differences in lubrication losses when different salivary proteins are used separately in the following sections.

Large polyphenols

From our results, it seems that protein precipitation does not always lead to lubrication losses. Different salivary proteins and astringent agents appear to cause aggregation and lubrication losses by different mechanisms. To obtain information on which salivary proteins are responsible for those differences, we use solutions containing only one group of the salivary proteins. Solutions of proline-rich proteins (PRPs) or mucins were prepared, both at salivary pH (6.8). As a comparison, we use

A tribological approach to astringency perception and astringency prevention

the large polyphenol EGCG and alum, which both showed aggregation with saliva, but only EGCG led to lubrication losses. We also use the small polyphenol CA, which showed minor changes in friction and did not show an increase in particle size when combined with saliva. We combined 0.05% of our astringent solutions with solutions of 0.2% of PRPs and 0.1% of mucins in a 1:1 ratio. The salivary protein concentrations used here are similar to the concentration of those proteins present in human saliva. [29, 44] A solution of 0.05% of EGCG, CA, and alum corresponds with 1.09, 2.78, and 1.05 mM respectively. Figure 7.6 shows the changes in friction coefficient in the presence of PRP solutions and for mucin solutions when combined with different astringent components. In the case of EGCG, we measure an increase in friction coefficient in the presence of both PRPs (Figure 7.6a) and mucins (Figure 7.6b). In both cases, also an increase in particle size is observed (Figure 7.6c and d). This is similar to our findings with human saliva in the previous section (Figure 7.2). The increase in friction coefficient found for EGCG and PRPs shows roughly the same increase as the increase in friction with saliva ($\Delta\mu \approx 0.3$). For EGCG with mucins, a $\Delta\mu$ of 0.2 is observed. The contribution of mucin precipitation is thus lower than the PRP precipitation. In terms of average particle sizes, EGCG paired with PRPs also shows larger particle sizes than mucins and PRPs, and an additional peak above 1 μm is observed (Figure 7.6c and d). Larger particle sizes thus appear to correlate with larger increases in friction coefficient, which can be explained by a lower number of unaggregated proteins to act as good bio-lubricants to provide a lubricious protein film. A combination of protein precipitation and protein removal from the surface, therefore, seems to be the cause for the large increase in friction coefficient seen when EGCG is added to saliva.

A tribological approach to astringency perception and astringency prevention

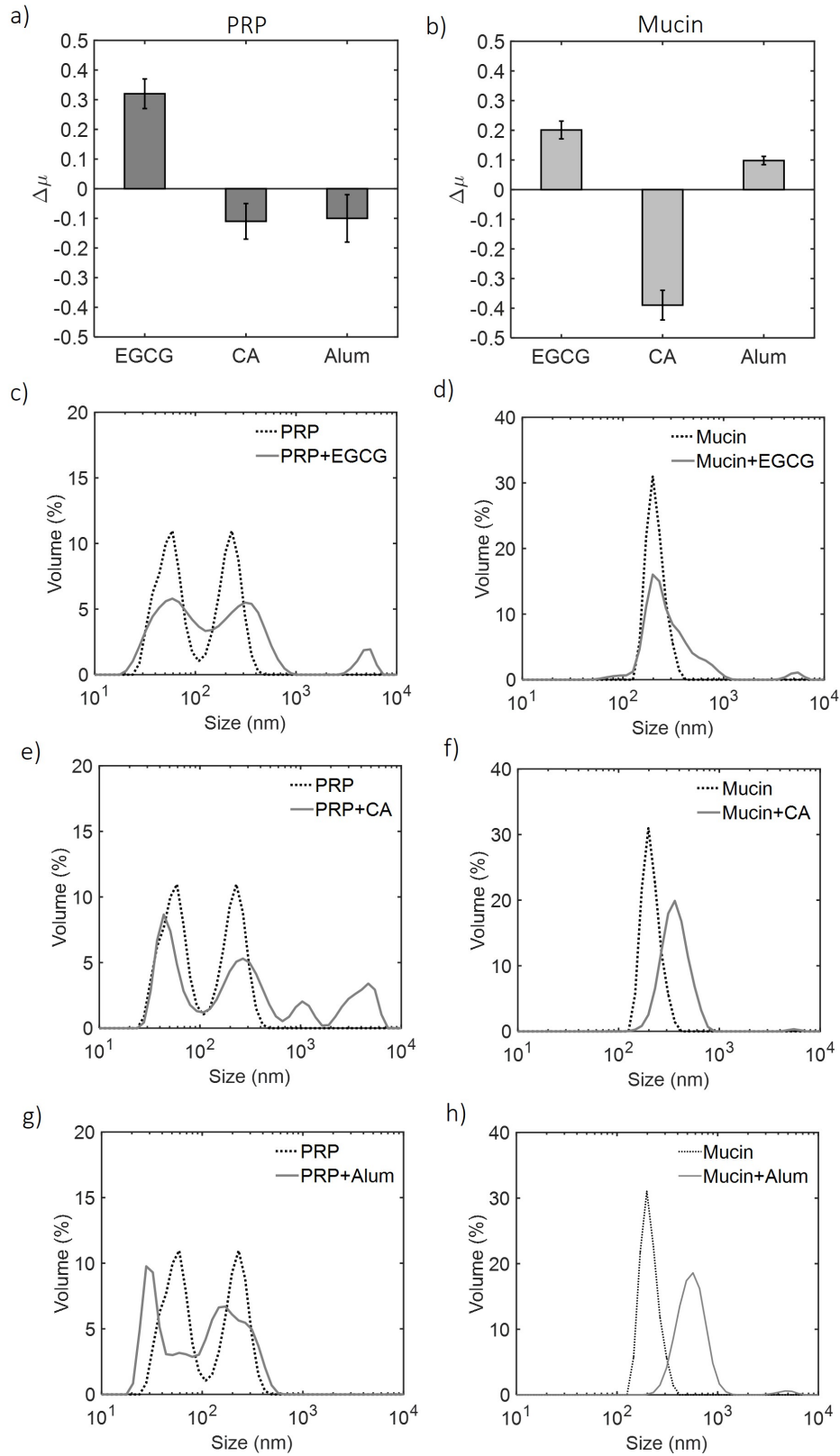


Figure 7.6: Friction coefficient increase ($\Delta\mu$) upon addition of EGCG, CA and alum to a) a 0.2% PRP solution and b) a 0.1% mucin solution. The PRP and mucin percentages used are based on their presence in saliva. The changes in particle size upon the addition of the astringent agents are shown in c-h: c) PRP + EGCG, d) mucin + EGCG, e) PRP + CA, f) Mucin + CA, g) PRP + alum h) Mucin +alum

A tribological approach to astringency perception and astringency prevention

Metal salts

As discussed, the addition of 5 mM alum to human saliva led to a minor increase in the friction coefficient ($\Delta\mu = 0.05$), while a considerable change in particle size was seen. Alum thus causes aggregation while the aggregates do not influence the friction coefficient. We first discuss the change in friction coefficient for the combination with PRPs and mucins separately. Adding alum to PRPs gives a small change in friction coefficient, and even shows a negative change, indicating improved lubrication properties. This is likely a result of the good lubricating properties of alum itself, as alum was able to lower the friction coefficient of water (Figure 7.1). When adding alum to a layer of mucins on the surface, however, an increase in friction coefficient of $\Delta\mu = 0.1$ is found (Figure 7.6a), which is an indication that alum interacts with mucins present in saliva, but not with the PRPs. This is also consistent with the changes in the particle size; no aggregates are formed when alum is combined with PRPs (Figure 7.6g), but aggregation does take place with mucin addition (Figure 7.6h). These results suggest that the observed aggregation is more related to mucin precipitation, and lubrication losses to interactions with PRP. The difference in interactions between the two astringent agents can be explained by the chemical structures of these two compounds. As mucins are negatively charged, and alum carries a positive charge, aggregate formation and the subsequent friction increase (Figure 7.6b and h) can be explained by electrostatic attraction. The multivalent ions are able to provide strong salt bridges. PRPs on the other hand interact with EGCG mainly through hydrogen bond interactions. [38, 42] Different interactions are thus responsible for the aggregate formation of the different salivary proteins.

PRP and mucin layers

In the case of alum, no aggregation with PRPs is observed. So even though mucin is removed from the salivary layer, the PRP layer remains attached to the hydrophobic surface. In this case, the remaining PRP layer still provides enough lubrication to prevent lubrication losses; aggregation of mucins alone is not enough to cause an increase in friction coefficient when PRPs and mucins are both present. Aggregation with PRPs is thus responsible for the lubrication losses measured in saliva. The proteins in the salivary layer can thus be removed separately. This is most likely due to the organization of the salivary proteins at oral surfaces. As part of the salivary pellicle, PRPs have been proposed to better adsorb onto hydrophobic surfaces than mucins, and PRPs, therefore, form a first layer of salivary proteins. Mucins in saliva are thought to interact with the PRPs with their hydrophobic patches and form a secondary layer of salivary proteins. [29, 45–47] Mucins can thus be removed

A tribological approach to astringency perception and astringency prevention

without affecting the lubrication layer provided by PRPs. The proposed location of these proteins on the oral surfaces is in line with our results as PRP precipitation causes lubrication losses while mucin precipitation does not (Figure 7.7). The PRPs mainly provide the necessary lubrication and only the removal of this layer leads to sufficient lubrication losses to cause an astringent sensation.

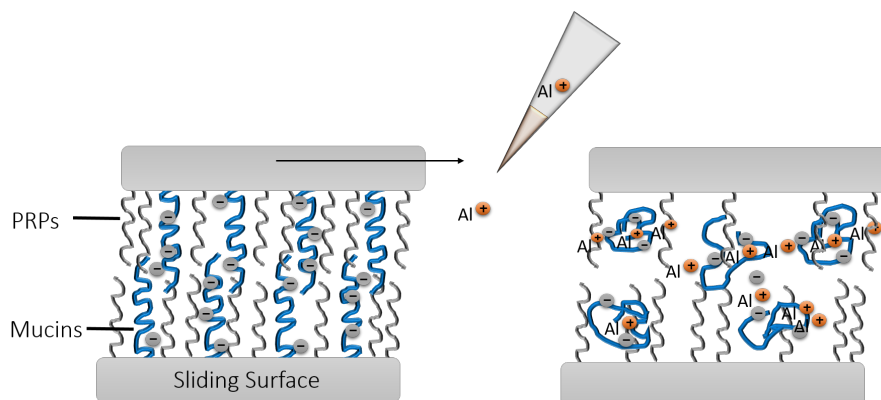


Figure 7.7: Aggregation of negatively charged mucins (large, blue) layer after addition of positively charged alum while the PRPs (small, grey) layer remain adsorbed on the surface.

Caffeic acid

In previous sections, we showed that CA mixed with saliva does not lead to an increase in particle size, nor a change in friction coefficient. When we add CA to PRPs, we find a decrease in friction coefficient of 0.1 with a relatively large error bar, suggesting enhanced lubrication. For CA paired with mucin an even stronger decrease in friction coefficient is found. Interestingly, an increase in particle size is observed for both PRPs and mucins combined with CA (Figure 7.6e and f), which is unexpected based on our previous findings with human saliva for which no protein aggregation was observed. Even though some large aggregates are formed, they do not influence lubricating properties. Although CA may be interacting with some of the PRPs, a sufficient number of salivary proteins are most likely still attached to the surface to provide good lubricating properties. The interaction between CA and mucins can be explained by the negative charge on mucins (-32.5 ± 2.9 mV). Based on a pKa of around 4 for caffeic acid, the charge at pH 6.8 will also be negative. The electrostatic repulsion between mucins and CA is a potential cause for the decrease in friction coefficient. Electrostatic repulsion could lead to a thicker protein layer and, as a result, larger separations between the sliding surfaces. Such a form of hydrated lubrication due to the presence of a water layer has been discussed in literature for other charged polymer surfaces with repulsive interactions. [48–50] We confirmed this effect of electrostatic repulsion by the simple addition of HCl (1%, 1:1 ratio) to mucins, reaching the same final pH as when combining CA and

A tribological approach to astringency perception and astringency prevention

mucin. As a result of the decrease in pH, a similar decrease in friction coefficient was found ($\Delta\mu \approx -0.4$) when adding CA to mucins. This strongly indicates that the observed changes in lubrication of CA in mucins are purely charge based. Similar findings were also reported by Sotres and co-workers. [51] They showed that at a lower pH, the friction coefficient of mucins decreased by more than an order of magnitude. This was related to an increased amount of adsorbed mucins molecules at the PDMS surface. Using circular dichroism spectroscopy (CD) the authors showed that at low pH, mucin changes its conformation in a way that exposes hydrophobic patches due to the protonation of polar regions. Having more hydrophobic regions available causes enhanced anchoring to PDMS surfaces paired with low friction coefficients.

We expect that the decrease in the friction coefficients we observed is thus related to the exposure of hydrophobic sections of the proteins. These results confirm that astringency perception and lubrication losses are related to different mechanisms. Lubrication losses occur only when PRPs are removed from the surfaces and accompanied by PRP precipitation. Mucin precipitation does not lead to lubrication losses, as long as PRPs are able to lubricate the surfaces due to a lack of PRP precipitation. When investigating the role of saliva, it is, therefore, necessary to take the role of both proteins into account. The importance of using both mucins and PRPs is also supported by other studies, which suggest that mucins alone are poorly able to reproduce tribological effects observed using saliva. [25, 29]

Protein - polyphenol hydrogen bonding

We found clear increases in friction coefficient for EGCG combined with human saliva and with PRP and mucins separately in the previous sections. The astringent sensation experienced with EGCG or TA containing foods such as tea or wine is thus related to the macromolecular interactions that cause changes in physical lubrication. Both hydrophobic interactions and hydrogen bonding have been proposed to cause salivary aggregation. [38, 52] Due to the large difference in the structure of PRPs and mucins, it is not clear to what extent such interactions affect the protein precipitation. To investigate the role of hydrogen bond formation in lubrication losses, we have measured the changes in friction coefficient when hydrogen bond formation was inhibited. To this end, we add the hydrogen bond disruptor or chaotropic agent 1,1,1,3,3,3-hexafluoroisopropanol ((CF₃)₂CHOH), also known as HFIP. [53, 54] We again first allow PRPs and mucins to form a layer on the sliding surfaces. We then add EGCG and allow the aggregates to form for 300 seconds, which is accompanied by an increase in the friction coefficient,

A tribological approach to astringency perception and astringency prevention

as discussed before. When the friction coefficient became constant, we added the hydrogen bond disruptor as a 10% solution in a 1:1 ratio and immediately a decrease in friction coefficient is observed (Figure 7.8).

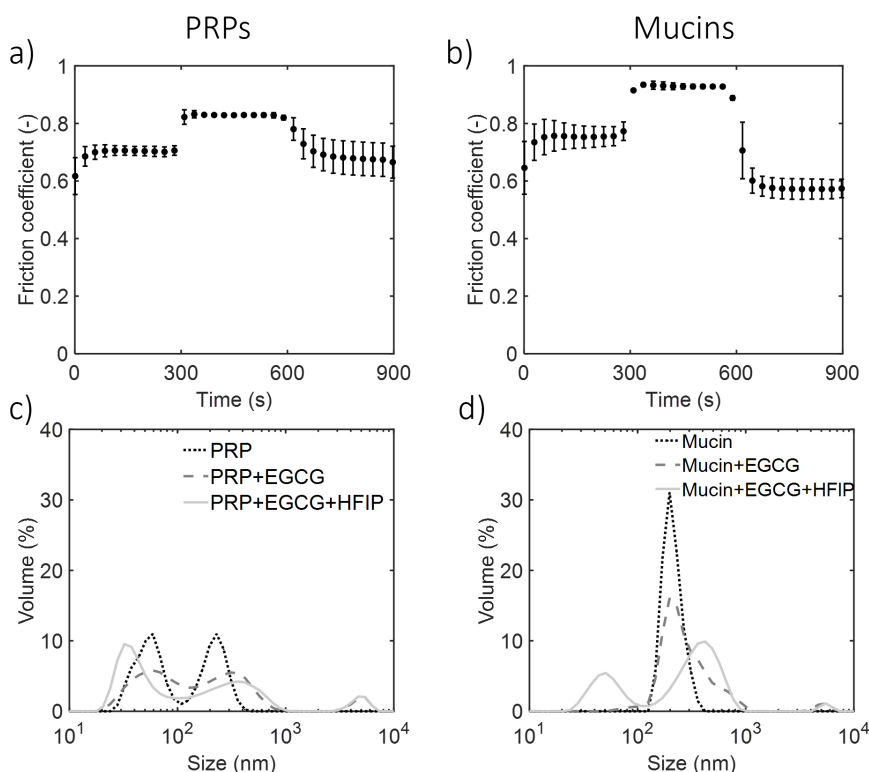


Figure 7.8: Effect of HFIP on the interaction between PRPs and mucins with EGCG added at 300s. a) Friction coefficients of PRPs with HFIP added at 600 s. b) Friction coefficients of mucins with HFIP added at 600 s. The particle size of PRPs and mucins (dotted line), after the addition of EGCG (dashed line), and the addition of HFIP (solid line) are shown in c & d, respectively.

A closer look at the friction coefficients in Figure 7.8 reveals that the friction coefficient returns to that of the PRPs and mucins before the addition of the astringent, and the salivary proteins, therefore, regain their good lubrication properties. The decrease in friction coefficient is also accompanied by the disruption of the formed protein aggregates, as the particle size again decreases. This is a strong indication that hydrogen bond formation occurs for both types of salivary proteins, and that this interaction is mainly responsible for both the protein precipitation and the lubrication losses. The lubrication losses of salivary proteins combined with large polyphenols such as EGCG and TA are thus caused by aggregate formation induced by hydrogen bonding, while aluminum salts cause aggregation by means of electrostatic interactions. Both PRPs and mucins appear to have a unique contribution to oral lubrication losses and the exact mechanism depends on the astringent agent involved. In Figure 7.9 we present a schematic overview of the manner in which salivary lubrication losses occur. This overview

A tribological approach to astringency perception and astringency prevention

highlights the importance of PRP aggregation, while mucin aggregation alone is not enough to generate lubrication losses for saliva.

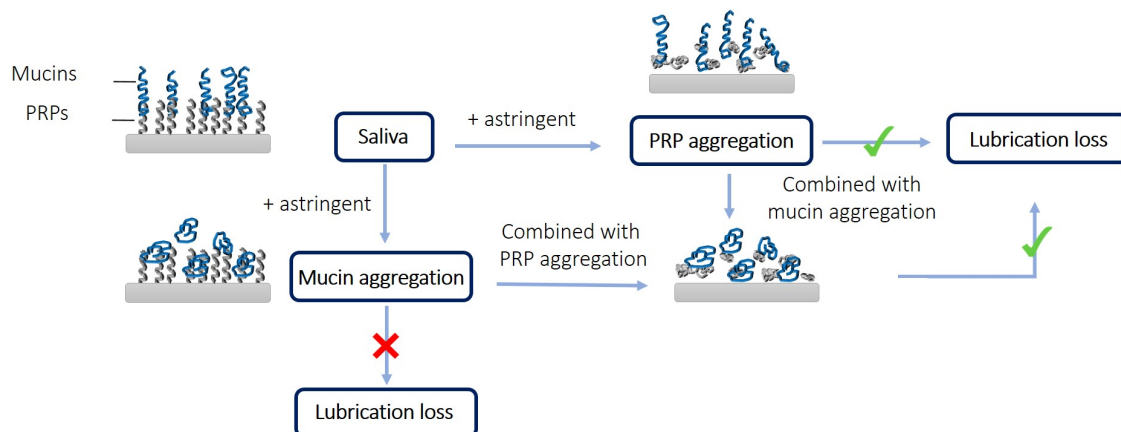


Figure 7.9: A schematic representation of the route to astringency. Lubrication losses occur when PRPs alone or both PRPs and mucins are aggregated by astringent agents. When mucin alone is aggregated, no salivary lubrication losses occur in the presence of PRPs.

Methods to prevent lubrication losses

We have highlighted that astringent lubrication losses are caused by extensive aggregation of the salivary PRPs via hydrogen bond formation. In this section, we will proceed to investigate whether hydrogen bond formation and subsequent aggregation can be prevented by the addition of different (food) components to prevent in-mouth lubrication losses. We use ingredients that are able to form hydrogen bonds and are used as food additives; ethanol (1 mPa·s) and glycerol (1400 mPa·s). Such complex mixtures are representative of red wines. [55, 56] To investigate the effect of interactions between different ingredients, we add the components in a different order, either separately, or in mixtures. In this section, the first letter indicates the first added component (usually S of saliva) followed by the additional components using their abbreviations; tannic acid (TA), glycerol (G) ethanol (E). All solutions were added in a 1:1:1 volume ratio. Combinations between brackets, for example (TA+G), refers to components that were pre-mixed before they were added. For example, the addition of a premixed TA and G mixture to saliva would be presented as S+(TA+G).

Glycerol

We explore the possibility to prevent lubrication losses by adding glycerol to saliva and tannic acid mixtures. Glycerol has a high viscosity and, as such, has a low friction coefficient of 0.01 at 1 mm/s. Glycerol is known to provide lubrication by

film formation of a thick glycerol layer in the hydrodynamic regime. [17, 57, 58] We first measure saliva and find a friction coefficient of 0.20. When TA is added, the friction increases to 0.30 (Figure 7.10a), as expected. We then add the highly viscous glycerol and find a strong decrease in the friction coefficient from 0.30 for S+TA to 0.04 for S+TA+GA ($\Delta\mu = 0.26$). The addition of glycerol is thus able to restore the good lubrication. The formation of a thick lubricating film between the surfaces contributes more to the friction than the presence of the aggregates. This film has been estimated to be around 1 μm . [57] That is larger than the size of our aggregates (in the range of 100 nm), which explains the lubrication effects seen here. When we pre-mix the astringent TA and G and add that mixture to saliva, (S+(TA+G)) we also find a decrease in the friction coefficient compared to that of saliva alone (Figure 7.10b). In this case, a $\Delta\mu$ value of 0.14 is found compared to saliva alone, which is similar to the $\Delta\mu$ value of 0.16 found in Figure 7.10a for S+TA+G. Regardless of whether aggregates were already present or not when glycerol was added, the glycerol always dominated the lubrication behavior. It is also striking that glycerol is able to decrease the friction coefficient of salivary aggregates by almost a factor of 10 (Figure 7.10a). The addition of high viscosity glycerol to an astringent agent is thus an effective way to avoid lubrication losses. Viscosity then dominates the lubrication behavior in the presence of aggregates.

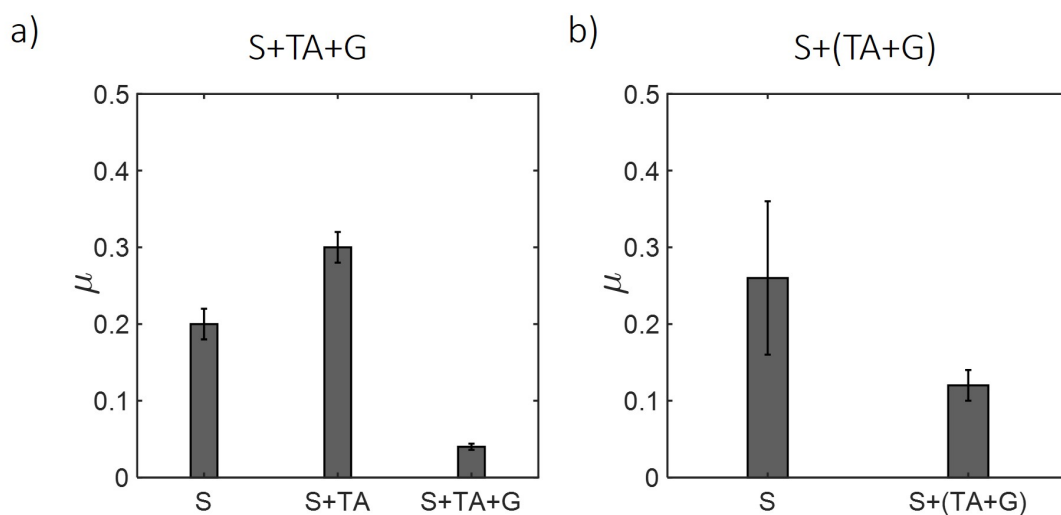


Figure 7.10: The friction coefficients of saliva (S), tannic acid (TA), and glycerol (G) when combined in different orders. a) S+TA+G and b) S+(TA+G).

Ethanol

We also examined the ability of ethanol to interact with saliva and polyphenols. Ethanol owes its good lubrication properties to its good wetting properties (contact angle of 31 °). Ethanol alone gives low friction coefficients of 0.15 at 1 mm/s. As

A tribological approach to astringency perception and astringency prevention

previously seen, S+T gives an increase in the friction coefficient (Figure 7.11a). When we add ethanol to the S+T aggregates, we find that the friction coefficient slightly increases from 0.32 to 0.37. Ethanol is unable to decrease the friction coefficient once aggregates have been formed. The friction coefficient here is thus determined by the aggregates formed between S and TA. The good wetting properties of ethanol are overruled by the presence of aggregates. The size of the aggregates is likely larger than the thickness of the fluid film formed by ethanol. In this case, the large particles separating the surfaces drive the lubrication behavior. In the case of S+E, so when the ethanol is added before the aggregates are formed, the friction coefficient of S remains unchanged (Figure 7.11b). So the ethanol does not seem to influence the lubrication protein layer. Interestingly, upon the addition of TA, the friction coefficient of S+E+TA remains constant as well. S and TA are thus unable to form aggregates in the presence of ethanol, and saliva maintains its lubrication properties. The same is found for S+(E+TA) as shown in Figure 7.11c. When ethanol and TA are premixed, S and TA are also unable to form aggregates and no lubrication losses are measured. So when ethanol is present, aggregation is prevented, and the salivary polymer brushes provide lubrication. The lack of aggregation is thus due to the interactions with ethanol. As ethanol can form hydrogen bonds, [59] ethanol addition may prevent hydrogen bond formation between S and TA.

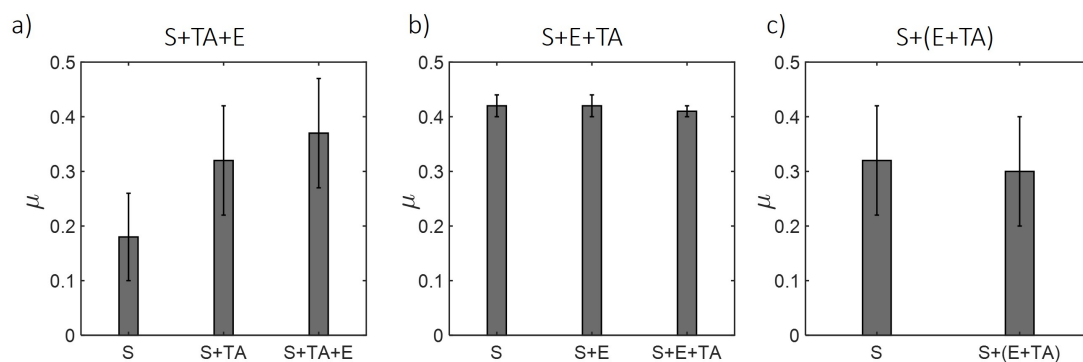


Figure 7.11: Friction coefficients obtained when mixing saliva (S), ethanol (E), and tannic acid (TA) in different orders. The combinations are a) S+TA+E, b) S+E+TA, c) S+(E+TA). Note that differences in salivary lubrication exist due to the usage of different batches and different (PDMS) surfaces.

In the presence of aggregates, the addition of ethanol does not decrease the friction coefficient, and the lubrication behavior is driven by the aggregates. However, when ethanol is already present in the mixture, TA and S are unable to aggregate to cause lubrication losses. These results suggest that ethanol does not necessarily act as a lubricating agent, but simply prevents the aggregation by interacting with tannic acid. To investigate whether ethanol can also influence the lubrication layer

A tribological approach to astringency perception and astringency prevention

itself, we also start by adding ethanol first. As expected, this gives a low friction coefficient of approximately 0.2. When we then add S, we find that the friction coefficient increases to around 0.25. This value is within the range of values we have measured for S alone. That would indicate that salivary proteins are able to migrate through the ethanol and adhere to the PDMS surface. This confirms that ethanol does not contribute to the lubrication behavior even though ethanol does have good lubrication properties thanks to its good wettability of PDMS surfaces. In this case, we find that protein brush lubrication dominates the friction coefficient in the presence of ethanol.

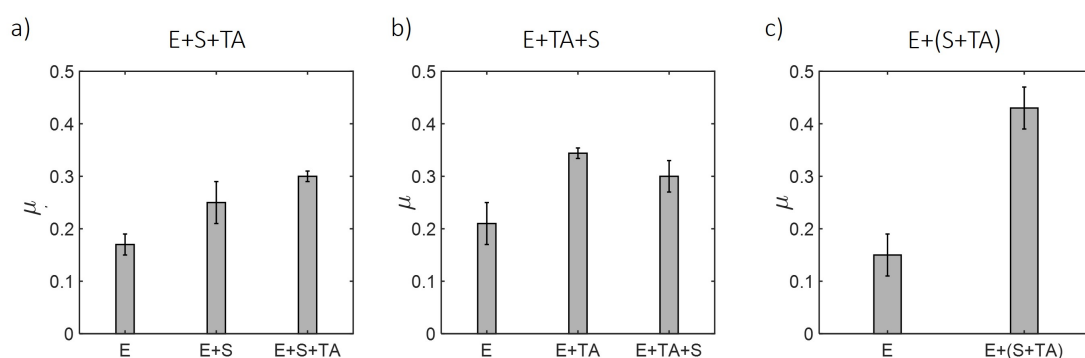


Figure 7.12: The friction coefficient of combinations of ethanol (E), saliva (S), and tannic acid (TA). The components are added to the tribometer in various orders. a) E+S+TA b) E+TA+S c) E+(S+TA).

When TA is added to ethanol first (here labeled E+TA), we find that the friction coefficient increases by 0.15, and then decreases again by 0.05 when saliva is added (in the case of E+TA+S). As we already discussed before, S and TA are unable to form large aggregates in the presence of E. The lack of large aggregates explains the minor increase in the friction coefficient. The minor increase in the friction coefficient is most likely an effect of dilutions. The lack of aggregation is also obvious from the measurement where premixed S and TA (referred to as (S+TA)) were added to E. In this case, the friction coefficient increases to 0.43, much more than in the other cases where ethanol was always present when S and TA were added together. When TA and S were pre-mixed, they aggregate more than in the case ethanol is present, which confirms that hydrogen bond formation with ethanol may indeed prevent interactions between TA and S. In this case, again, the aggregates dominate the frictional behavior as the salivary lubrication layer is disrupted by the polyphenols.

Dominating mechanisms in salivary lubrication

By mixing saliva, tannic acid, glycerol, and ethanol in different orders, we have shown the importance of the order of addition of the different components. When we begin by adding saliva, the salivary proteins provide good lubrication. This good lubrication is lost upon the addition of tannic acid due to aggregation. The obtained high friction coefficient caused by the aggregation is reduced when glycerol is added to the aggregates as caused by viscous lubrication. Without the use of a viscous fluid, lubrication losses can be prevented by limiting particle aggregation. We demonstrated this using ethanol which is able to prevent aggregation when either saliva or tannic acid is already mixed with ethanol before saliva and tannic acid are able to interact with each other.

This indicates that the viscous lubrication provided by glycerol provides a more dominating lubrication type, and is the only mechanism that dominated particle friction. These findings can be explained by the gap size the lubricant is able to provide. A low viscosity fluid such as ethanol forms a relatively thin lubricating film due to its inability to sustain large hydrodynamic pressures. Salivary protein brushes are able to form a hydrated layer that keeps the surfaces apart, but the thickness of the layer is still limited. The aggregates disrupt this salivary layer and larger aggregates are formed that are larger than both the saliva and solvent layer. Particle friction then takes over from solvent or salivary lubrication. The addition of the highly viscous glycerol, however, leads to a thick lubricating layer that lubricates the surfaces and the aggregates. We show our mechanisms in Figure 7.13, showing the lubrication hierarchy ranging from the least dominant to the most dominant mechanism.

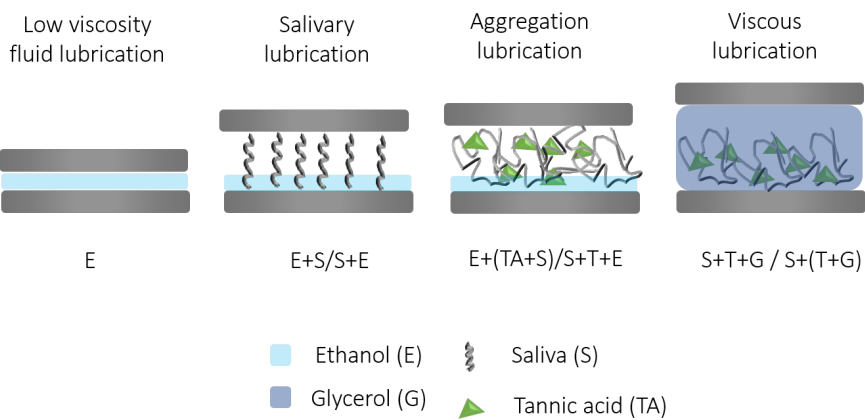


Figure 7.13: Schematic representation of the hierarchy (from left to right) between mechanisms occurring when combining ethanol (E), glycerol (G), saliva (S), and tannic acid (TA) in different orders. The mechanisms can be divided into low viscosity fluid lubrication, salivary lubrication, aggregation lubrication, and viscous lubrication.

To form a more quantitative image of the saliva-surface interactions, approaches such as Quartz crystal microbalance with dissipation monitoring (QCM-D) or atomic force microscopy (AFM) could be used. This, however, is beyond the scope of our present work. By measuring saliva and salivary proteins combined with different compounds, we have provided a framework for the mechanisms behind salivary lubrication in the presence of astringent agents, high viscosity, and good wetting fluids. The mechanisms and hierarchy of these mechanisms can be used to decrease unwanted astringency perception in foods. This can, for example, be done by adding a viscous fluid or by adding an ingredient that limits hydrogen bonding between salivary proteins and polyphenols present in food.

Conclusions

In this work, we unveiled the role of different salivary components in lubrication losses related to astringent perception. Using a tribometer configured for in-mouth conditions, we measured the lubrication behavior of saliva and different salivary proteins when combined with astringent agents and other components commonly found in astringent systems such as wine. Upon the addition of different types of astringent agents to saliva, we found that two possible events took place: (I) For phenolic compounds that have sufficient binding sites, both PRP and mucin aggregation occurred and lubrication losses were observed, and (II) for metal salts, mucin aggregation was observed without lubrication losses. To the best of our knowledge, we have here shown for the first time that PRPs are the most important proteins when it comes to salivary lubrication losses. Salivary lubrication losses only occur when PRP aggregation takes place. The removal or aggregation of the mucin layer alone does not lead to lubrication losses, as long as PRPs are still present to provide polymer salivary lubrication. The strong increase in friction coefficient measured when adding large polyphenols to saliva points towards astringency as a lubrication-based sensation. For smaller phenols and metal salts, however, different mechanisms (e.g. receptor-based responses) must be responsible for astringent perception. Understanding these mechanisms behind astringency perception and astringency prevention for different astringent agents and salivary proteins could help to reduce astringent perception of new, plant-derived foods. For these food materials, lubrication losses are often considered a negative sensory attribute and should be prevented. We show that this can be achieved by the addition of simple (food) components such as ethanol and glycerol.

References

1. Ma, W. *et al.* A review on astringency and bitterness perception of tannins in wine. *Trends in Food Science & Technology* vol. 40, 6–19 (2014).
2. Rossetti, D., Yakubov, G., Stokes, J., Williamson, A.-M. & Fuller, G. Interaction of human whole saliva and astringent dietary compounds investigated by interfacial shear rheology. *Food Hydrocolloids* vol. 22, 1068–1078 (2008).
3. Joslyn, M. & Goldstein, J. L. Astringency of fruits and fruit products in relation to phenolic content. *Advances in Food Research* vol. 13, 179–217 (1964).
4. Carter, B., Foegeding, E. & Drake, M. Invited review: Astringency in whey protein beverages. *Journal of Dairy Science* vol. 7, 5793–5804 (2020).
5. Yeom, J. *et al.* Soft and ion-conducting hydrogel artificial tongue for astringency perception. *Science Advances* vol. 6, eaba5785 (2020).
6. De Souza, V. B., Thomazini, M., Chaves, I. E., Ferro-Furtado, R. & Favaro-Trindade, C. S. Microencapsulation by complex coacervation as a tool to protect bioactive compounds and to reduce astringency and strong flavor of vegetable extracts. *Food Hydrocolloids* vol. 98, 105244 (2020).
7. Van Eck, A. & Stieger, M. Oral processing behavior, sensory perception and intake of composite foods. *Trends in Food Science & Technology* (2020).
8. Schöbel, N. *et al.* Astringency is a trigeminal sensation that involves the activation of G protein-coupled signaling by phenolic compounds. *Chemical Senses* vol. 39, 471–487 (2014).
9. Bajec, M. R. & Pickering, G. J. Astringency: mechanisms and perception. *Critical Reviews in Food Science and Nutrition* vol. 48, 858–875 (2008).
10. Green, B. G. Oral astringency: a tactile component of flavor. *Acta Psychologica* vol. 84, 119–125 (1993).
11. De Wijk, R. A. & Prinz, J. F. Mechanisms underlying the role of friction in oral texture. *Journal of Texture Studies* vol. 37, 413–427 (2006).
12. Upadhyay, R., Brossard, N. & Chen, J. Mechanisms underlying astringency: introduction to an oral tribology approach. *Journal of Physics D: Applied Physics* vol. 49, 104003 (2016).
13. Wang, S., Mantilla, S. M. O., Smith, P. A., Stokes, J. R. & Smyth, H. E. Astringency sub-qualities drying and pucker are driven by tannin and pH—Insights from sensory and tribology of a model wine system. *Food Hydrocolloids* vol. 109, 106109 (2020).
14. McRae, J. M. & Kennedy, J. A. Wine and grape tannin interactions with salivary proteins and their impact on astringency: a review of current research. *Molecules* vol. 16, 2348–2364 (2011).
15. Luck, G. *et al.* Polyphenols, astringency and proline-rich proteins. *Phytochemistry* vol. 37, 357–371 (1994).
16. Gibbins, H. & Carpenter, G. Alternative mechanisms of astringency—what is the role of saliva? *Journal of Texture Studies* vol. 44, 364–375 (2013).
17. Bongaerts, J., Rossetti, D. & Stokes, J. The lubricating properties of human whole saliva. *Tribology Letters* vol. 27, 277–287 (2007).

18. Aguirre, A. *et al.* Lubrication of selected salivary molecules and artificial salivas. *Dysphagia* vol. 4, 95–100 (1989).
19. Carpenter, G. *et al.* A study of saliva lubrication using a compliant oral mimic. *Food Hydrocolloids* vol. 92, 10–18 (2019).
20. Sarkar, A., Goh, K. K. & Singh, H. Colloidal stability and interactions of milk-protein-stabilized emulsions in an artificial saliva. *Food Hydrocolloids* vol. 23, 1270–1278 (2009).
21. McArthur, C., Sanson, G. D. & Beal, A. M. Salivary proline-rich proteins in mammals: roles in oral homeostasis and counteracting dietary tannin. *Journal of Chemical Ecology* vol. 21, 663–691 (1995).
22. Ma, S., Lee, H., Liang, Y. & Zhou, F. Astringent mouthfeel as a consequence of lubrication failure. *Angewandte Chemie* vol. 128, 5887–5891 (2016).
23. Soares, S. *et al.* Tannins in food: Insights into the molecular perception of astringency and bitter taste. *Molecules* vol. 25, 2590 (2020).
24. Laguna, L. & Sarkar, A. Oral tribology: update on the relevance to study astringency in wines. *Tribology-Materials, Surfaces & Interfaces* vol. 11, 116–123 (2017).
25. Biegler, M., Delius, J., Käschorf, B. T., Hofmann, T. & Lieleg, O. Cationic astringents alter the tribological and rheological properties of human saliva and salivary mucin solutions. *Biotribology* vol. 6, 12–20 (2016).
26. Lee, C. A., Ismail, B. & Vickers, Z. M. The role of salivary proteins in the mechanism of astringency. *Journal of Food Science* vol. 77, C381–C387 (2012).
27. Baxter, N. J., Lilley, T. H., Haslam, E. & Williamson, M. P. Multiple interactions between polyphenols and a salivary proline-rich protein repeat result in complexation and precipitation. *Biochemistry* vol. 36, 5566–5577 (1997).
28. Silletti, E., Vingerhoeds, M. H., Norde, W. & Van Aken, G. A. The role of electrostatics in saliva-induced emulsion flocculation. *Food Hydrocolloids* vol. 21, 596–606 (2007).
29. Sarkar, A., Xu, F. & Lee, S. Human saliva and model saliva at bulk to adsorbed phases—similarities and differences. *Advances in colloid and interface science* vol. 273, 102034 (2019).
30. Mystkowska, J. *et al.* Artificial mucin-based saliva preparations—Physicochemical and tribological properties. *Oral Health Prev. Dent* vol. 16, 183–193 (2018).
31. Garcíea-Estévez, I., Ramos-Pineda, A. M. & Escribano-Bailón, M. T. Interactions between wine phenolic compounds and human saliva in astringency perception. *Food & function* vol. 9, 1294–1309 (2018).
32. Ono, T., Hori, K. & Nokubi, T. Pattern of tongue pressure on hard palate during swallowing. *Dysphagia* vol. 19, 259–264 (2004).
33. Ferrer-Gallego, R., Hernández-Hierro, J. M., Rivas-Gonzalo, J. C. & Escribano-Bailón, M. T. Sensory evaluation of bitterness and astringency sub-qualities of wine phenolic compounds: Synergistic effect and modulation by aromas. *Food Research International* vol. 62, 1100–1107 (2014).
34. Garrec, D. A. & Norton, I. T. Boundary lubrication by sodium salts: A Hofmeister series effect. *Journal of Colloid and Interface Science* vol. 379, 33–40 (2012).
35. Santagiuliana, M. *et al.* Strategies to compensate for undesired gritty sensations in foods. *Food Quality and Preference* vol. 81, 103842 (2020).

36. Hufnagel, J. C. & Hofmann, T. Orosensory-directed identification of astringent mouthfeel and bitter-tasting compounds in red wine. *Journal of Agricultural and Food Chemistry* vol. 56, 1376–1386 (2008).
37. Robichaud, J. L. & Noble, A. C. Astringency and bitterness of selected phenolics in wine. *Journal of the Science of Food and Agriculture* vol. 53, 343–353 (1990).
38. Siebert, K. J., Troukhanova, N. V. & Lynn, P. Y. Nature of polyphenol- protein interactions. *Journal of Agricultural and Food Chemistry* vol. 44, 80–85 (1996).
39. Le Bourvellec, C. & Renard, C. Interactions between polyphenols and macromolecules: quantification methods and mechanisms. *Critical Reviews in Food Science and Nutrition* vol. 52, 213–248 (2012).
40. Charlton, A. J. *et al.* Polyphenol/peptide binding and precipitation. *Journal of Agricultural and Food Chemistry* vol. 50, 1593–1601 (2002).
41. Murray, N. J., Williamson, M. P., Lilley, T. H. & Haslam, E. Study of the interaction between salivary proline-rich proteins and a polyphenol by ¹H-NMR spectroscopy. *European Journal of Biochemistry* vol. 219, 923–935 (1994).
42. Canon, F. *et al.* Aggregation of the salivary proline-rich protein IB5 in the presence of the tannin EgCG. *Langmuir* vol. 29, 1926–1937 (2013).
43. Ye, Q.-Q. *et al.* A predictive model for astringency based on in vitro interactions between salivary proteins and (-)-Epigallocatechin gallate. *Food Chemistry* vol. 340, 127845 (2021).
44. Schenkels, L. C., Veerman, E. C. & Nieuw Amerongen, A. V. Biochemical composition of human saliva in relation to other mucosal fluids. *Critical Reviews in Oral Biology & Medicine* vol. 6, 161–175 (1995).
45. Lindh, L., Glantz, P.-O., Isberg, P.-E. & Arnebrant, T. An in vitro study of initial adsorption from human parotid and submandibular/sublingual resting saliva at solid/liquid interfaces. *Biofouling* vol. 17, 227–239 (2001).
46. Macakova, L., Yakubov, G. E., Plunkett, M. A. & Stokes, J. R. Influence of ionic strength changes on the structure of pre-adsorbed salivary films. A response of a natural multi-component layer. *Colloids and Surfaces B: Biointerfaces* vol. 77, 31–39 (2010).
47. Glumac, M., Ritzoulis, C. & Chen, J. Surface properties of adsorbed salivary components at a solid hydrophobic surface using a quartz crystal microbalance with dissipation (QCM-D). *Food Hydrocolloids* vol. 97, 105195 (2019).
48. Ahmed, J. *et al.* Sliding friction of zwitterionic hydrogel and its electrostatic origin. *Macromolecules* vol. 47, 3101–3107 (2014).
49. Gong, J. P. Friction and lubrication of hydrogels—its richness and complexity. *Soft Matter* vol. 2, 544–552 (2006).
50. Zhang, R. *et al.* Tuning the hydration and lubrication of the embedded load-bearing hydrogel fibers. *Langmuir* vol. 33, 2069–2075 (2017).
51. Sotres, J., Lindh, L. & Arnebrant, T. Friction force spectroscopy as a tool to study the strength and structure of salivary films. *Langmuir* vol. 27, 13692–13700 (2011).
52. Authimoolam, S. P. & Dziubla, T. D. Biopolymeric mucin and synthetic polymer analogs: their structure, function and role in biomedical applications. *Polymers* vol. 8, 71 (2016).

53. Saez Talens, V. *et al.* Aromatic gain in a supramolecular polymer. *Angewandte Chemie International Edition* vol. 54, 10502–10506 (2015).
54. Purcell, K. F., Stikeleather, J. & Brunk, S. Spectroscopic studies of hydrogen bonding: Hexafluoroisopropanol. *Journal of Molecular Spectroscopy* vol. 32, 202–213 (1969).
55. Gawel, R., Sluyter, S. V. & Waters, E. J. The effects of ethanol and glycerol on the body and other sensory characteristics of Riesling wines. *Australian Journal of Grape and Wine Research* vol. 13, 38–45 (2007).
56. Shehadeh, A. *et al.* Effect of ethanol, glycerol, glucose/fructose and tartaric acid on the refractive index of model aqueous solutions and wine samples. *Food Chemistry* vol. 329, 127085 (2020).
57. Yakubov, G., Branfield, T., Bongaerts, J. & Stokes, J. Tribology of particle suspensions in rolling-sliding soft contacts. *Biotribology* vol. 3, 1–10 (2015).
58. Kim, J. M., Wolf, F. & Baier, S. K. Effect of varying mixing ratio of PDMS on the consistency of the soft-contact Stribeck curve for glycerol solutions. *Tribology International* vol. 89, 46–53 (2015).
59. Rinaldi, A., Gambuti, A. & Moio, L. Precipitation of salivary proteins after the interaction with wine: the effect of ethanol, pH, fructose, and mannoproteins. *Journal of Food Science* vol. 77, C485–C490 (2012).



8

**Fluid and suspension
lubrication using four
different tribometers**

Abstract

Soft tribology is rapidly emerging as a tool to assess the frictional properties of soft solids and dispersed systems with various applications. It is extremely challenging to predict and understand the frictional behavior of soft materials, especially when combined with complex lubricants, as the surface, lubricant, and tribometer properties combined strongly influence the friction coefficient. The aim of this chapter is to understand how the surface characteristics and the lubricant composition influence the friction coefficient when measured on different tribometers. We present a comparison of four tribometers: three state-of-the-art tribometers used in soft tribology (Anton Paar (APT), Bruker (BTL), PCS Instruments (MTM)) and a custom-made tribometer (CTT). We find that Newtonian lubricants display typical Stribeck lubrication behavior. However, the progression of the Stribeck curve (absolute values, slopes, transition points) depends strongly on the surface type and the tribometer motion. Patterned surfaces that are used here, generate lower friction coefficients in the boundary regime and a less steep curve in the mixed and elastohydrodynamic regime. These findings for patterned surfaces are related to smaller contact areas and fluid drainage between the asperities. Patterned surfaces also have a less steep slope in the EHL due to fluid drainage and the inability to efficiently form a uniform fluid layer between the surfaces. For hydrogel suspensions as lubricants, each tribometer shows different lubrication regimes. The exact progression of the curve and the resulting regimes are a result of the way in which the tribometer is able to entrain and deform particles. With the analysis exhibited here, a framework is established for understanding tribological results produced by different tribological devices.

This chapter is in preparation for submission as:

Rudge, R.E.D., Mosselman, M. J., Shewan, H.M., Stokes, J.R., Dijkman, J. A., and E. Scholten. Fluid and suspension lubrication using four different tribometers.

Introduction

Friction and lubrication play an important role in any scientific field where moving parts are involved. An enhanced understanding is therefore required concerning how different system properties influence friction. As shown in previous chapters, the friction coefficient is influenced by the nature of the interacting surfaces and the properties of the lubricant. The interacting surfaces can vary in their deformability (modulus), [1–3] adhesive properties, [4–6] and roughness. [1, 7, 8] High friction coefficients are often found for highly adhesive materials with high surface-surface contact area. [9, 10] Friction coefficients can be decreased by reducing the interactions, either by changing the surface material or by introducing a lubricant, which separates the surfaces by providing a lubricating layer. This viscosity-dependent behavior of a lubricant is captured in a Stribeck curve for Newtonian fluids where the viscosity remains constant with the speed. [7, 11] As discussed previously, the classical Stribeck regimes (boundary, mixed, elastohydrodynamic (EHL)) are usually observed for simple fluids. When the lubricant is more structurally and rheologically more complex such as in the case of suspensions, emulsions or polymeric lubricants, different frictional behavior is often found than for Newtonian fluids. [12–15]

As has become evident from previous chapters, the friction coefficient is not a fixed value but depends strongly on the conditions under which measurements are performed, and friction coefficients are therefore a system-dependent value. As tribological measurements are so dependent on the surface and lubricant properties, the majority of tribological studies focus on varying the surface material [1, 16] and surface roughness [6–8, 17, 18] or specific lubricant properties. [12–14, 19] The effect of the type of tribological motion (e.g. rolling/sliding or different sliding directions) on the friction coefficient has also been studied by several authors. [20, 21]

These studies all emphasize the system dependencies of a tribological measurement. In this chapter, we seek to address the lack of comparisons in literature on outcomes obtained of different types of tribometers. Differences in probe or substrate motion (e.g. sliding or rolling) affect the type of contact and entrainment and, with that, the overall frictional behavior. Additionally, tribometers can operate in a normal force or a gap size controlled manner. These differences in tribometer mechanisms make it challenging to compare lubrication behavior found in literature for the same lubricant system, as differences are often found to depend on the exact measuring conditions. For a simple measurement using water between

two smooth polydimethylsiloxane (PDMS) surfaces, boundary friction coefficients ranging from 0.8 to 2 were obtained from different sources in literature. [7, 19, 22, 23]

To investigate how different tribometer motions influence lubricant, we use four tribometers paired with simple Newtonian fluids as lubricants as well as complex particulate lubricants. With the different tribological devices paired with simple and complex lubricants, the aim is to elucidate how different measuring mechanisms and different surface characteristics give way to differences in the friction coefficient. Results are obtained using three commercially available tribometers that are currently the state of the art in soft tribology (manufacturers: Anton Paar, Bruker, PCS instruments) as well as a custom-made, 3D-printed rheo-tribometer as introduced in **Chapters 2 and 3**. [1] These tribometers are unique in their sliding motions (e.g. rolling, sliding, oscillating) and sliding speed range. The way the probe moves relative to the substrate can lead to differences in fluid entrainment and in the friction coefficient. We anticipate to observe changes in Stribeck behavior when varying tribometer mechanics, surface material, surface roughness and lubricant viscosity. We examine this hypothesis using four different tribometers, six different tribopairs, two Newtonian lubricants and one non-Newtonian fluid. This results in an overview of what system parameters mainly influence the friction coefficient. The results presented in this chapter can be used as a reference for tribologists who intend to compare their data with results (in literature) measured on other tribometers.

Experimental section

Tribological measurements

The tribological measurements were performed using four different tribometers with commercially available or custom-made surfaces. The probes used here were glass, PDMS, or steel (hemi-)spheres. As a substrate, smooth, rough, or patterned PDMS surfaces were used. All measurements were carried out at room temperature (20 ° C) and at a normal load of 1 N. This normal force allows for a simple conversion of the velocity to the Hersey or Sommerfeld number by simply correcting the velocity for the viscosity. The sliding velocity was adapted depending on the tribometer specifications. An overview of the tribometers and the parameters used are displayed in Table 8.1 with schematic images of all four tribometers.

Fluid and suspension lubrication using four different tribometers

Table 8.1: An overview of the four tribometers used in this study and their most important characteristics. The tribometers used are the Anton Paar Tribocell (APT), Bruker Tribolab (BTL), PCS instruments Mini Traction Machine (MTM) and a custom-made 3D-printed tribotool (CTT).

	Anton Paar Tribocell (APT)	Bruker UMT Tribolab (BTL)	PCS Instruments Mini Traction Machine (MTM)	Custom-made Tribotool (CTT)
Tribometer type	Ball-on-3-pins	Ball-on-plate	Ball-on-disk	Pin-on-disk
Speed range (mm/s)	0.05 – 500	1 – 80	1 – 1000	1 – 20
Sliding motion Probe Substrate	Rotating Stationary	Stationary Linearly sliding	Rotating Rotating	Rotating Stationary
Probe materials	<ul style="list-style-type: none"> ▪ Rough glass ▪ Smooth steel ▪ - 	<ul style="list-style-type: none"> ▪ Rough glass ▪ - ▪ Smooth PDMS 	<ul style="list-style-type: none"> ▪ Rough glass ▪ Smooth steel ▪ Smooth PDMS 	<ul style="list-style-type: none"> ▪ Rough glass ball ▪ - ▪ -
Substrate materials	<ul style="list-style-type: none"> ▪ Smooth PDMS ▪ Rough PDMS 	<ul style="list-style-type: none"> ▪ Smooth PDMS ▪ Patterned PDMS 	<ul style="list-style-type: none"> ▪ Smooth PDMS ▪ Patterned PDMS 	<ul style="list-style-type: none"> ▪ Smooth PDMS ▪ Patterned PDMS
Schematic view				

Anton Paar Tribocell

For tribological measurements using the Anton Paar Tribocell (APT), we used an Anton Paar rheometer (Modular Compact Rheometer (MCR) 302) with a MCR

Fluid and suspension lubrication using four different tribometers

tribometer base set-up (T-PTD-200). The normal force control of this device occurs via a feedback system that is installed in the tribometer base, which holds the container and the pins. In this tribometer, a spherical probe was used and three cylindrical pins. The spherical rough glass or smooth steel ball (diameter: 12.7 mm) was attached to the rheometer shaft and rotated around its own axis as driven by the rheometer. As substrates we used cylindrical pins (6 mm in diameter), which were inserted into specially made pockets. The rough pins were provided by the manufacturer and custom-made pins and rectangular plates (15 x 6 x 3 mm) had a smooth surface. Measuring speeds ranged from 0.05 mm/s to 500 mm/s. The normal force on each of individual pins was 1 N.

Bruker Tribolab

The Bruker Universal Mechanical Tester TriboLab tribometer (BTL) has a stationary probe and an oscillating substrate (60 x 40 x 4.5 mm). The normal and friction forces are measured via the sensors in the shaft attached to the tribometer probe. A vertical motion of the shaft ensures that the normal force remains constant. For these tribological measurements, we use a rough glass ball (12.7 mm, same as used on the Anton Paar device) and a smooth, custom-made PDMS probe, which slides against a smooth PDMS substrate or a patterned substrate with cylindrical pillars (diameter 500 μm , height 500 μm , and distance 1000 μm). The PDMS surfaces were prepared as described in **Chapters 2 and 3**. The sliding speed range is from 1 mm/s to 80 mm/s as this is the maximum speed range as specified by the manufacturer. Due to the oscillating motion of the sliding container, the speed varies in a sinusoidal manner and drops to zero at the extremum of each movement, where the sliding container reverses its direction. The measuring software omits these values automatically from the calculations of the friction coefficients.

Mini Traction Machine

The Mini Traction Machine (MTM) consists of a spherical probe and a flat disk-shaped substrate. Both the substrate and the probe can rotate around their respective axes and rotate separately. The friction force and normal force sensor for this tribometer are present in the shaft attached to the rotating probe. This shaft is able to move vertically to regulate the normal force. We used a slide-to-roll ratio (SRR) of 0.5. This ratio indicates the relation between the sliding speed and the average speed ($SRR = (U_{disk} - U_{disk})/U_{total}$) and ($U_{total} = U_{disk} + U_{ball})/2$). [7, 11] We perform our measurements in bidirectional mode meaning both surfaces rotate in opposite directions. As probe materials, we use a rough glass ball, a smooth PDMS ball, and a smooth steel ball (diameter: 19 mm). As a counter surface,

we used a smooth PDMS surface and a patterned PDMS surface, similar to the patterned surfaces used in the other tribometers (pillar diameter 500 μm , height 500 μm , and distance 1000 μm). The diameter of the substrate was 46 mm. For this device, we used a speed range of 1 mm/s until 1000 mm/s.

Custom-made 3D-printed tribotool

We used a custom-made 3D printed tribotool as a fourth tribometer. A detailed description of this device can be found in **Chapters 2 and 3**. The tribometer set-up consists of an arm ($R = 30\text{ mm}$) with a container to insert a hemi-spherical probe. The hemi-spherical probe ($R = 10\text{ mm}$) slides alongside a flat substrate ($R = 43\text{ mm}$), which was fastened in the container holding the probe. For this tribometer, we used a smooth PDMS probe and a smooth PDMS substrate. The sliding motion is driven by the rheometer axis (Anton Paar MCR 501), which means that the probe was in a rotational sliding motion, whereas the substrate was stationary. This tribometer was used at a speed range from 1 mm/s until 20 mm/s. The “zero-gap” distance is first determined by the rheometer. For this tribometer, the probe is fixed at a specific height meaning the tribometer does not operate at a fixed normal force. The probe height was fixed at the height where a normal force of 1 N was measured at a specific position on the substrate surface. However, due to surface irregularities and surface deformations, the normal force fluctuates during measurements. The friction coefficients were obtained from measured normal force and torque (τ) values, and were converted into friction coefficients using $\mu = F_F / F_N$ and $F_F = \tau / R_{probe}$ with R , the radius of the probe. [1]

Surface preparation

The glass and steel probes used on the APT and MTM tribometers were provided by the respective tribometer manufacturers. Rough PDMS pins for the APT tribometer were provided by the respective manufacturer as well. The rough PDMS surfaces have an undefined roughness and we refer to them as “random rough” surfaces. The smooth and patterned PDMS surfaces used on the different tribometers were custom-made. We prepared the different PDMS surfaces following a common procedure described previously (see **Chapters 5 and 6** and reference [7]). In short, we use a 1:10 (base to catalyst) ratio by weight of a two-part Sylgard 184 DOW Corning silicone elastomer to obtain a polymer fluid. The polymer fluid was then poured into molds and cured at 60 °C to obtain solid (hemi-)spheres, flat disks, or patterned disks. To obtain patterned surfaces, we used 3D printed methacrylate molds. These molds were designed using Solidworks and subsequently 3D printed using a Formlabs Form 2 3D printer. The patterned surfaces used here have pillar-

shaped asperities on the surface that are 1000 μm in height, 500 μm in width with a distance of 1000 μm between each pillar. Before use and between measurements, surfaces were thoroughly rinsed using isopropanol or ethanol to remove lubricants and possible contaminants in a similar way as described in more detail in previous work. [16]

Atomic Force Microscopy

To obtain micrographs of the used surfaces, an Atomic Force microscope (multimode 8 AFM, Bruker) was used in tapping mode. The PDMS surface was first cleaned consecutively with demineralized water and ethanol. To analyze the surface, a topography scan with an imaging size of 10 x 10 μm was made using the ScanAsyst mode. We then analyzed the images (e.g. surface height) using the NanoScope Analysis 1.5 software.

Theoretical background

When considering the lubrication behavior of Newtonian fluids such as water and glycerol, we can obtain a better overview of the viscosity effects on lubrication by constructing a Stribeck curve. In such a plot, the viscosity (η , Pa·s) is multiplied by the entrainment speed (U , mm/s). This provides a μ (dimensionless) against $U\eta$ ($\mu\text{N/m}$) curve. The curves for different Newtonian fluids often overlap in different regimes when the lubricants vary in viscosity but have similar wetting properties. [3, 7, 24] An example of the friction coefficients for a low viscosity fluid is shown in (Figure 8.1a) and a high viscosity fluid (Figure 8.1b).

A combination of the two curves (high and low viscosity), when multiplied by the viscosity on the x-axis (Figure 8.1c), provides a so-called “master curve” for Newtonian fluids with different viscosities, as shown with the red dashed line in Figure 8.1c. This Stribeck curve provides a clear overview of the three regimes and the transitions between the different regimes. These curves can be described by an empirical equation [7] as

$$\mu_{total} = \mu_{EHL} + \left(\frac{\mu_b - \mu_{EHL}}{1 + \left(\frac{U\eta}{B} \right)^m} \right) \quad (8.1)$$

using $\mu_{EHL} = k(U\eta)^n$ as the friction coefficient in the elastohydrodynamic (EHL) regime and $\mu_b = h(U\eta)^l$ in the boundary regime.

Fluid and suspension lubrication using four different tribometers

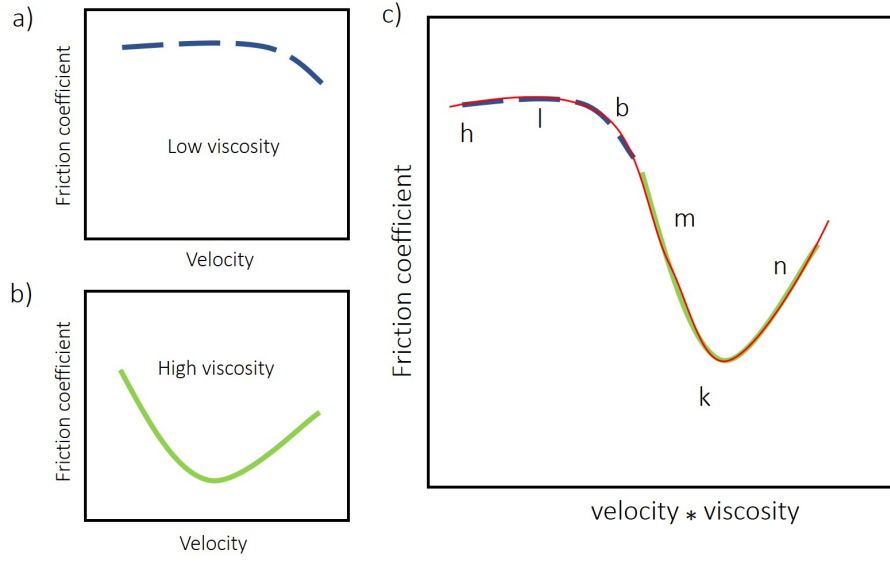


Figure 8.1: A schematic example of a) the friction coefficients of a low viscosity Newtonian fluid, b) the friction coefficients of a high viscosity Newtonian fluid, and c) a Stribeck curve obtained by combining Figure a and b and correcting for the respective viscosities on the x-axis. The red dashed line shows an example of an empirical fit of the data.

In this equation, k represents the power-law coefficient which serves as a measure for the start of the EHL regime, n the power-law exponent or the slope in the EHL regime, h the initial friction coefficient in the boundary regime, l the slope of the friction coefficient in the boundary regime and B the value of $U\eta$ that marks the end of the boundary regime (or beginning of the mixed regime). The relevant sections of the Stribeck curve for all these parameters are indicated in Figure 8.1c. Using this approach makes it possible to fit the experimentally obtained Stribeck curve and extract tribological parameters related to the different regimes.

To investigate how the surface roughness and the surface motion influences the lubricant entrainment and the friction coefficient, we use these Stribeck parameters. The results of four different tribometers are analysed when using smooth surfaces and patterned surfaces with a well-defined surface roughness of 0.5 mm in asperity width and diameter with a distance of 1 mm. This is done to relate the Stribeck parameters to various system properties including the degree of roughness of the surface (e.g. smooth, random rough, patterned) as well as the type of motion that drives the tribometer (e.g. rotational, linear).

Results

To compare the frictional behavior of different tribometers, we attempt to create a Stribeck curve that covers multiple frictional regimes. To obtain such a Stribeck curve we measure over a range of sliding velocities and viscosities. Using Newtonian fluids as lubricants, we can exclude effects of shear-dependencies. We use water and glycerol as the low and high viscosity liquid, respectively, which have similar polarities and wetting properties but very different viscosities. The viscosity of Water is 1 mPa·s and of glycerol is 1400 mPa·s. The wetting contact angle on PDMS for water 120° is and approximately 100° for glycerol. [16]

Anton Paar tribocell

We use a rough glass ball and (commercially obtained) PDMS pins as sliding surfaces in the Anton Paar tribocell. These surfaces are commonly used in various studies using this device. [25–28] The glass ball has a roughness of several μm while the roughness of the PDMS pins is an order of magnitude smaller. We show micrographs of both surfaces in Figure 8.2.

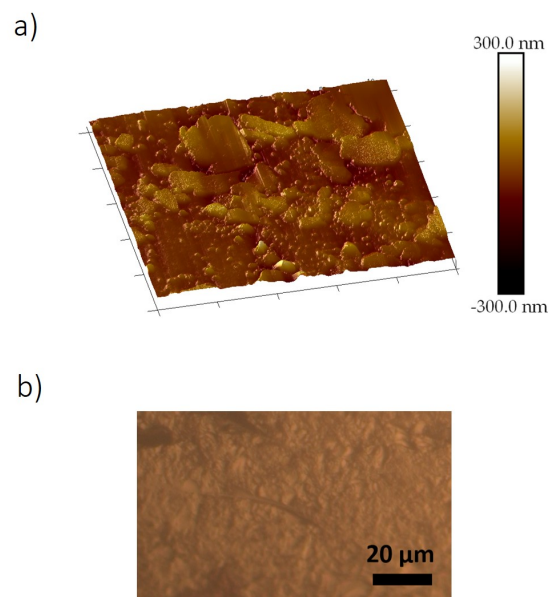


Figure 8.2: a) Atomic force microscope (AFM) image of the rough side of a commercially obtained PDMS pin. The size of the imaged section is 10000 x 10000 x 300 nm. b) Light microscope image of the commercially available rough glass ball.

These surfaces are commonly used in tribology within a soft material context, for example in the food sciences to simulate the hard, rough palate and the relatively soft and smooth tongue and deformation (elastic hysteresis) of soft tribopairs. [26, 28, 29] Hence, we use this tribopair as a reference here. Additionally, we use the rough glass ball with smooth PDMS pins and smooth PDMS plates and a steel

ball against the rough PDMS pins to evaluate the effect of surface roughness and material type on the friction coefficient. For all surfaces, we find that water shows a boundary and a mixed regime while the highly viscous glycerol shows a mixed regime and a hydrodynamic regime (Figure 8.3).

Boundary regime

In the boundary regime, surfaces are in close contact, and therefore, the surface properties strongly influence the friction coefficient. We combine the frictional results of the two aqueous lubricants (water and glycerol) by multiplying the velocities with the respective viscosities. The outcome is a collapse of the data which forms a complete Stribeck curve with three frictional regimes. Using the approach previously introduced to assess the Stribeck parameters, we will proceed to discuss the frictional results obtained using the following tribopairs: rough glass ball – rough PDMS pins (Figure 8.3a), rough glass ball – smooth PDMS pins (Figure 8.3b), rough glass ball – PDMS smooth plates (Figure 8.3c) and smooth steel ball – rough PDMS pins (Figure 8.3d). We find the largest differences in the friction coefficients in the boundary regime, as a result of the differences in the surface roughness. In the boundary regime for the smooth PDMS plates (Figure 8.3c) with a glass probe, we find a value of 0.25 and we find a much higher value of 1.5 for the glass ball against the smooth PDMS surface (Figure 8.3b).

For the rough glass ball and the smooth steel ball against the rough PDMS pins, we find similar friction coefficients of around 0.8 in the boundary regime. This is surprising as these glass and steel probes vary both in roughness and wettability. Overall, we do find that the results in the boundary regime are strongly affected by the choice of tribopair.

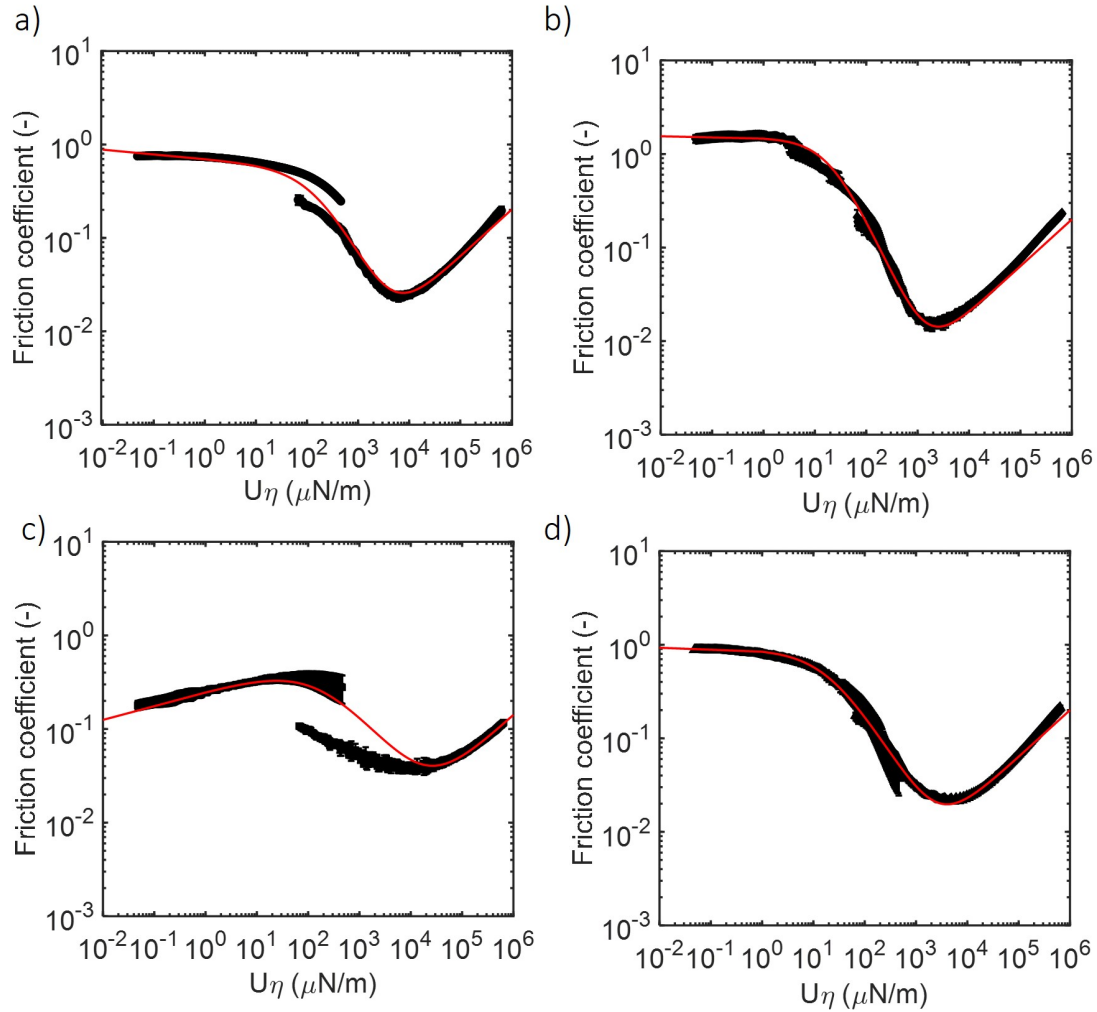


Figure 8.3: Tribological measurements obtained using the Anton Paar tribocell using different tribopairs: a) rough glass ball – rough PDMS pins, b) rough glass ball – smooth PDMS pins, c) rough glass ball – smooth PDMS plates, and d) smooth steel ball – rough PDMS pins.

PDMS pins and plates

The smooth pins and smooth plates (Figure 8.3b and c respectively) are made of the same material and have the same roughness. However, they do show large differences in the boundary regime; the pins give a friction coefficient of $\mu = 1.5$, whereas the plates give a friction coefficient of $\mu = 0.25$. As the pins and the plates have the same surface properties, the large difference in friction coefficient is therefore not only due to differences in surface roughness. We suspect the plate deformation to play a role. The PDMS plates are custom made in our lab. Because of the deformable nature of the material, the PDMS plates could not be clamped into the installation tightly which allowed the plates to move or deform during measurements. The effect of the plates moving would be most evident in the boundary regime where significant shear forces exist via large probe-plate

contact. For the PDMS plates, we also find that the measurements of water (mainly boundary regime) and glycerol give a poor collapse when corrected for viscosity, and the friction coefficient in the mixed regime (glycerol) does not overlap. We thus consider the results obtained using soft plates in the ball-on-three-plate set-up as unreliable for Newtonian fluids and would not recommend using this setup with deformable surfaces. Unlike the plates, the pins are stiffer, smaller, and can be inserted in the set-up much better in specially made cylindrical pockets, limiting the deformation and sideways movement of the substrate. The results obtained with the PDMS pins are therefore more reliable and reproducible, as also confirmed by the overlap of the two curves.

Mixed regime

To enter the mixed regime, the surfaces should become separated from one another as we move from a contact dominated regime to an asperity/fluid dominated contact. While part of a rough surface might be separated from the opposing surface, large asperities form dry patches and are still in contact with the opposing surface. This increases the critical speed for film formation and sufficient reduction of surface-surface contact. We see that each tribopair has a different starting point for the transition from the boundary to the mixed regime. The rough glass ball against the rough pins shows a transition at $100 \mu\text{N/m}$ (Figure 8.3a). For the steel ball against the rough pins, the mixed regime starts at around $20 \mu\text{N/m}$ (Figure 8.3b). The lowest value for the beginning of the mixed regime is found for the rough glass ball and the smooth pins. For these surfaces, the mixed regime starts at $U\eta$ values of around $5 \mu\text{N/m}$ (Figure 8.3b). The mixed regime thus begins earlier when the tribopairs are smoother as a fluid film is easily established.

The slope in the mixed regime also appears to be a function of the roughness of the surface. A previous study revealed that smoother surfaces show a steeper slope in the mixed regime. [7] This is in agreement with our findings. As the mixed regime represents the transition from surface – surface contact in the boundary regime to surface separation in the elastohydrodynamic (EHL) regime, the length of the mixed regime in terms of $U\eta$, also depends on the surface roughness. We find that the mixed regime is shortest for the rough PDMS surfaces: see Figure 8.3a and c. The smooth surfaces (Figure 8.3b and d) show a more extended mixed regime. For rough surfaces the mixed regime starts later and appears to be shorter than for smooth surfaces. For the smooth PDMS pins paired with the rough glass probe we also find the steepest slope in the mixed regime. The slope in this regime is thus determined by the roughness of the substrates.

EHL regime

After the strong decrease in the friction coefficient in the mixed regime, a minimum value is obtained for all surfaces (Figure 8.3). This minimum value marks the transition from the mixed to the EHL regime. In the mixed regime, there is limited asperity contact while in the EHL regime, we expect the surfaces to be fully separated as a relatively thick fluid layer begins to form between the surfaces. We find that the rough tribopairs (glass – PDMS) show higher μ values at the mixed-EHL transition point than smoother surfaces. This is similar to results previously reported using PDMS surfaces with different degrees of roughness, for which the smoothest surface also showed the lowest minimum value before entering the EHL regime. [7] The low minimum found here is related to better wettability of a smooth surface compared to a rough surface which facilitates fluid film formation. [30] After this minimum value, the system enters the EHL regime. For all of these surfaces, we find strong similarities in the hydrodynamic regime. The EHL regime begins at similar $U\eta$ values for all surfaces used (between 10^3 and $10^4 \mu\text{N/m}$). The slopes in this regime are all close to 0.5 which is the value theoretically predicted based on Reynolds' hydrodynamic theories as discussed in the work of Bongaerts et al. and De Vicente et al. [7, 11] In this regime, the surface properties appear to be of less importance than in the boundary and mixed regimes. This EHL regime is thus tribopair independent and only depends on lubricant and tribometer properties.

Bruker UMT Tribolab

We also measured the friction coefficients of water and glycerol on the Bruker UMT Tribolab (BTL). The probe of the APT tribometer discussed in the previous section rotates around its axis. The probe in the BTL tribometer is static, and the substrate moves in an oscillating sliding motion against the probe. The substrate is placed in a container that also holds the lubricating fluid. This type of linear sliding motion is more similar to certain real-life events, such as the sliding of the tongue against the palate or rubbing skin cream on the skin. The BTL tribometer has a much smaller speed range (1 mm/s until 80 mm/s) than available for the APT tribometer (0.05 – 500 mm/s). Even though the speed range of the BTL is limited, we are still able to observe a boundary regime for water and a hydrodynamic regime for glycerol (Figure 8.4).

Fluid and suspension lubrication using four different tribometers

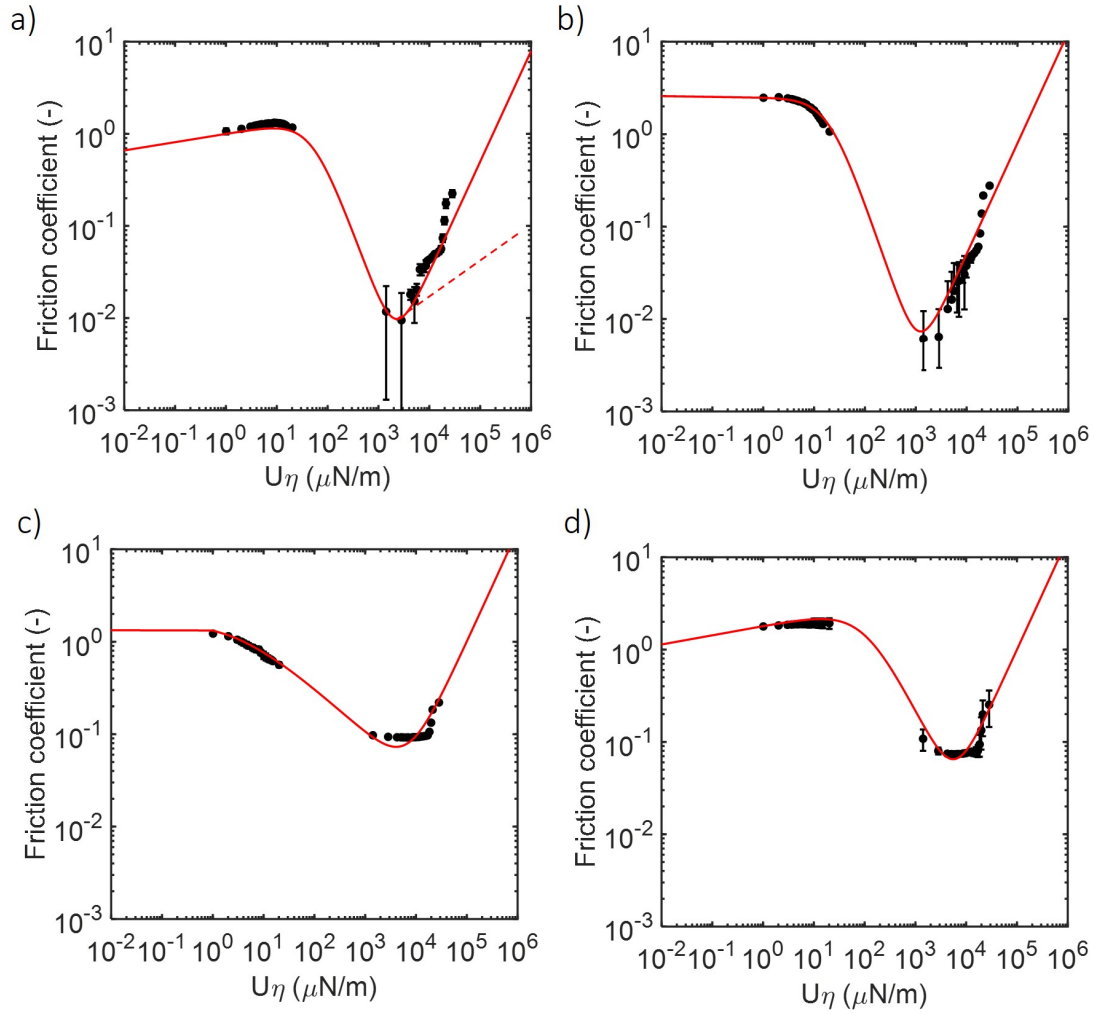


Figure 8.4: Tribological measurements obtained using the Bruker Tribolab tribometer using different tribopairs: a) rough glass ball – smooth PDMS plate, b) smooth PDMS ball – smooth PDMS plate, c) rough glass ball – patterned PDMS plate, and d) smooth PDMS ball – rough PDMS plate.

The values obtained in the mixed regime (and for some samples also in the boundary regime) are limited. Similar to our approach in the previous sections, we used the empirical formula to fit a Stribeck curve that allowed us to estimate values in the mixed regime. From findings in the previous section, the surface roughness is an important parameter when it comes to the frictional behavior. To further investigate the effect of surface roughness, next to smooth PDMS surfaces as used for the APT, we include also a patterned substrate that is covered with pillars with distinct height, width and distance. The patterned PDMS substrate has surface pillars with a diameter of $500\ \mu\text{m}$, height $500\ \mu\text{m}$, and distance $1000\ \mu\text{m}$ between each pillar. We pair these patterned substrates with both a smooth PDMS and rough glass ball as a probe. A combination of a rough glass ball and smooth PDMS surfaces was also used in the APT tribometer. Since the substrate surface area here is relatively large ($60 \times 40\ \text{mm}$), a larger number of $500\ \mu\text{m}$ pillars

Fluid and suspension lubrication using four different tribometers

could be placed on the surface than on the APT pins that are 6 mm in diameter.

The patterns on this surface are thus more regular than the random roughness on the commercially obtained PDMS pins of the APT tribometer. These well-defined micron-scale asperities allow us to gain more insights than when nano-scale random rough surfaces are used. We display the tribological results of the BTL tribometer in Figure 8.4.

Boundary regime

For the BTL, we also find rather different behavior in the boundary regime for each tribopair. The highest friction coefficient in the boundary regime is found for the smooth PDMS ball against the smooth PDMS plate ($\mu=2.5$), as can be seen in Figure 8.4b. This tribopair has the largest contact area as a result of the two smooth PDMS surfaces. PDMS also is known for being self-adhesive and high friction coefficients are found for PDMS – PDMS tribopairs. [16, 31, 32] As PDMS is hydrophobic, water poorly wets the surface and therefore water is a “bad” lubricant for PDMS tribopairs, which leads to more direct PDMS contact and high friction coefficients. For the patterned PDMS substrate, there is less direct surface contact, and therefore lower friction coefficients ($\mu=1.8$) are found. In the case of the rough glass ball, we find values around $\mu=1.2$ for both the smooth and patterned PDMS plate (Figure 8.4b and d). In this case, the surface material and not the surface roughness dictates the friction coefficient. As the adhesive forces between glass and PDMS are lower than those between PDMS and PDMS, the friction coefficient is lower as well. We thus confirm that surface roughness (contact area) and adhesive properties of the surface dominate the frictional behavior in the boundary regime regardless of the tribometer type.

Mixed regime

As the speed range was limited and a complete Stribeck curve could not be measured on the BTL tribometer, it is for most of the measurements difficult to clearly state where the mixed regime starts. We estimate the values by taking the best fit through the data points, but these values should be interpreted with extreme caution. For the APT tribometer, we saw that smoother surfaces showed an earlier transition from the boundary to the mixed regime. The smoothest surfaces used in the BTL are the smooth PDMS probe and the smooth PDMS probe (Figure 8.4b). For this pair, we are actually able to see the transition to the mixed regime. Using this tribometer, the transition for smoother surfaces also takes place at lower speeds than for the other surface combinations. Similar to the results of the APT, here, we also find the steepest slope in the mixed regime and low values for the friction coefficient at the transition to the hydrodynamic regime for the smooth

tribopairs. These results are comparable to findings in literature where it was also found that smooth PDMS surfaces show a steeper slope (m) in the mixed regime than rough surfaces. [7, 16]

For patterned PDMS surfaces, we observe different behavior at the transition between the mixed and hydrodynamic regime. Patterned surfaces show a rather flat plateau (Figure 8.4c and d). This indicates that no changes in asperity contact or fluid film thickness take place for a small range of velocities. The EHL regime starts once a sufficiently thick fluid film is formed. Having pillars on the surface makes it challenging to form a steady fluid film to separate the surfaces and enter the EHL regime. This plateau represents a transition regime where the fluid film is being built up, and larger gap sizes (higher velocity, higher viscosity) are needed to obtain hydrodynamic lubrication.

Although different characteristics (e.g. viscosity, roughness) have been investigated in various studies for their influence on the progression of the Stribeck curve [7, 16], such a plateau between the mixed and EHL regime has not been reported before. As we will see in later sections, a similar plateau is seen when using the MTM tribometer with a larger velocity range which allows to obtain data in all frictional regimes.

EHL regime

In the EHL regime as measured on the Bruker, we find slopes that are steeper than the theoretically predicted value of 0.5. The slopes we find for this linearly sliding tribometer are between 1 and 1.2. This indicates that the hydrodynamic regime is not only influenced by the viscosity of the sample and that there is an additional effect that is caused by the tribometer. We attribute this difference to the tribometer motion. While oscillating, the probe constantly slides over a new section of the substrate. This gives way to surface deformations and hysteresis should be considered as a contributor to the overall friction coefficient. Additionally, when the relaxation of the material is slower than the measurement speeds, the deformation in the opposite direction may lead to hysteresis effects, visible in the friction coefficient. Furthermore, fluids may be pushed out of the contact during oscillation. The fluid then accumulates at the edges of the container as we schematically display in Figure 8.5. The additional fluid can contribute to a drag force on the probe, which would lead to higher friction coefficients. The Stokes' drag force (F_D) is defined as $6\pi\eta RU$ with η being the viscosity, R the radius of the probe, and U the velocity. [33, 34] With the viscosity of glycerol (1.4 Pa·s), the size

Fluid and suspension lubrication using four different tribometers

of the probe (diameter: 12.7 mm) we find drag forces in the range of 10^{-3} to 10^{-2} N in the EHL regime. These drag forces are lower than the friction forces in the EHL regime, which are in the order of 10^{-2} to 10^{-1} N. Drag forces may play a role in the total shear stress measured in the BTL, yet we cannot entirely attribute the friction coefficients in the EHL regime to such non-contact forces. The origin of the steep increase in the friction coefficient in the hydrodynamic regime is thus not clear. It is evident however that the EHL regime depends on the measuring device and on the pattern on the surface when the asperities are large enough to disrupt the formation of a fluid film.

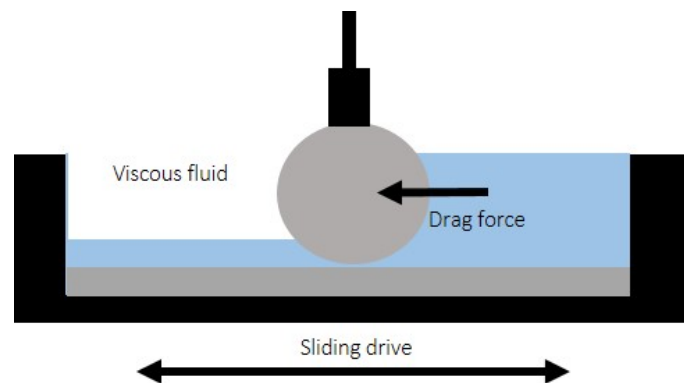


Figure 8.5: Schematic representation of fluids accumulating along the edges of the sliding reciprocating drive of the Bruker leading to an increased drag force.

Mini Traction Machine

We have discussed the results when using stationary substrates and moving probe (APT) as well as a stationary probe and moving substrate (BTL) in the previous sections. In this section, we use the Mini Traction Machine (MTM), a tribometer that operates using a rotating probe *and* a sliding substrate. Using such an additional tribometer provides more information on which system parameters determine the frictional values in each regime. In this case, we use the following tribopairs: a) rough glass ball – smooth PDMS, b) smooth PDMS – smooth PDMS ball, c) smooth PDMS ball – patterned PDMS, and d) smooth steel ball – smooth PDMS (Figure 8.6). The patterned PDMS surface contains cylindrical asperities that are 500 μm in height and diameter, with a distance of 1000 μm between each asperity, similar to those used on the BTL tribometer in the previous section. With these tribopairs, we can compare our results to those obtained by the APT (glass – PDMS, steel – PDMS) and by the BTL (PDMS – smooth PDMS, glass-smooth PDMS, and PDMS – patterned PDMS). On the MTM tribometer, we use the largest speed range of all tribometers used in this study (1 mm/s – 1000 mm/s).

Boundary regime

In the boundary regime, where the surfaces are in direct contact, the highest frictional values are obtained for the PDMS ball against the smooth PDMS substrate (Figure 8.6b, $\mu_{max}=1.6$) as we saw in previous sections. The lowest frictional value is found for smooth PDMS against patterned PDMS (Figure 8.6d, ($\mu_{max}=0.9$), due to the lower contact area. The end of the boundary regime or the start of the mixed regime occurs at the latest stage for the patterned surfaces. The trends in the onset of the mixed regime for Newtonian fluids are similar for all the tribometers we have compared so far and thus do not show strong dependencies on tribometer motion.

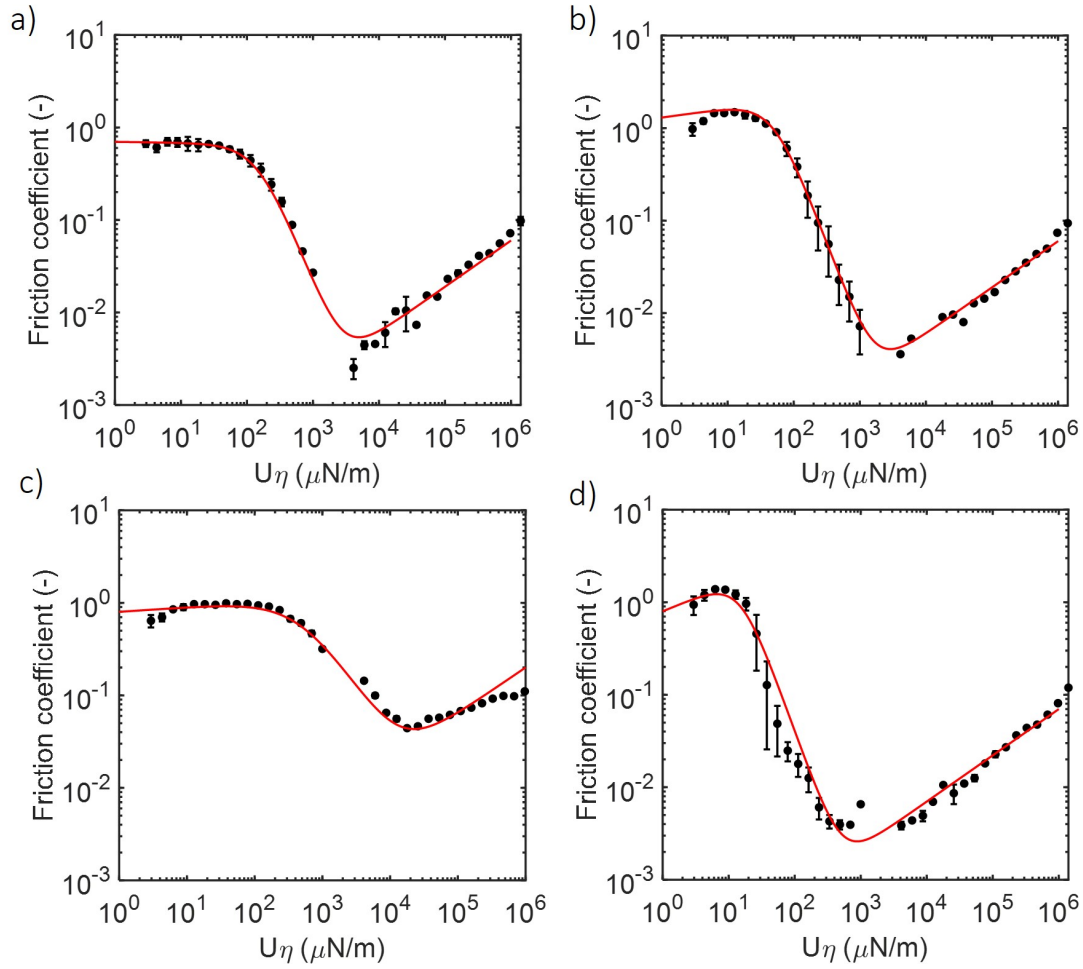


Figure 8.6: Frictional measurements performed with the MTM using four different tribopairs. Tribopairs used here are a) rough glass ball – smooth PDMS substrate, b) smooth PDMS ball – smooth PDMS substrate, c) smooth PDMS ball – patterned PDMS substrate, and d) smooth steel ball – smooth PDMS substrate. We used water and glycerol as lubricants to obtain the Stribeck curves.

The asperities on the surface, however, have a large influence on the initial boundary friction coefficient, and the transition to the mixed regime. We thus confirm the importance of surface properties in the boundary regime with our third tribometer.

Mixed regime

The mixed regime is well visible for all surfaces on the MTM. For this device, we find that the smooth steel ball against the smooth PDMS surface is the first tribopair to enter the mixed regime followed by the smooth PDMS ball against the smooth PDMS surface. Again, this is similar to what was observed for the other tribometers, where smooth surfaces have a shorter boundary regime as a fluid film is easily formed compared to a rough surface where dry asperities are still in contact with the opposing surface at higher speeds. In the mixed regime, the slope is steepest

Fluid and suspension lubrication using four different tribometers

for the smooth surfaces (smooth steel, smooth PDMS) and the least steep for rough surfaces (rough glass, patterned PDMS). For the MTM we also find that smooth surfaces show shorter mixed regimes and lower minimum values for the friction coefficient at the transition between the mixed and EHL regime, similar the other tribometers used here and similar to previous findings on the MTM. [7]

EHL regime

In the EHL regime, we find slopes close to the theoretical value of 0.5 as seen for the APT tribometer. Only the patterned PDMS surface shows a less steep slope (a slope of 0.5 is shown for comparison in the master curve in Figure 8.6c). The slope in the EHL regime is thus also related to the surface pattern. This is only the case when the roughness is large enough as the APT surfaces with smaller asperities showed no differences in the EHL regime. With the patterned surface, the fluid can easily flow into the space between the asperities. As a result, a steady fluid layer is not easily formed and, therefore, the fluid film thickness remains relatively small. In this case, not only the viscosity is important, but also the surface properties stay relevant. For all other surface combinations, we do observe an increase with a slope of 0.5 in the EHL regime, as expected from theory and also observed in previous studies. [7] Similar to what we concluded for the other tribometers, the minimum value at the transition between the mixed and EHL regime as well as the slope in the EHL regime, thus appear to be characteristics of the tribometer motion as well as the roughness of the surface that influences fluid film formation.

Smooth and patterned surfaces on the MTM and BTL

For both the MTM and BTL tribometers, we used a smooth PDMS probe against both a smooth PDMS surface and a micro-patterned surface. In this section, we will compare the results for both tribometers. We show the data of the rough and smooth PDMS surfaces from Figure 8.6 and Figure 8.4 in one graph in Figure 8.7a and b respectively. These two tribometers (BTL and MTM) show similar trends when using the same probe-substrate combinations, even though the tribometer motion is vastly different. For both tribometers, a smoother surface causes a shorter boundary regime, steeper slopes in the mixed regime, lower minimum value for the friction coefficient and an earlier start of the EHL regime. Interesting for these patterned surfaces is the plateau region in the curve before entering the EHL regime, especially for the BTL tribometer. After the plateau region (Figure 8.7b), the patterned and smooth surfaces show rather similar behavior. The last data points of the patterned surface measured on the MTM also show a very similar slope as in the case of the last data points of the smooth surface as shown in the

inset Figure 8.7a. At higher viscosities or speeds beyond the limit of this tribometer, a slope of 0.5, as found for the smooth surfaces, could potentially be obtained for the patterned surface as well. With the same surfaces, similar tribological trends are thus found on different tribometers.

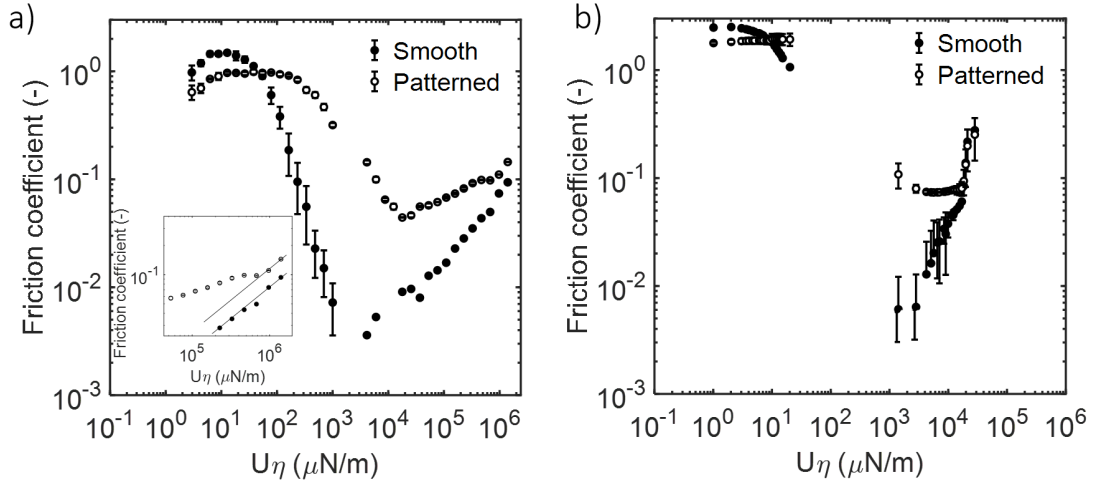


Figure 8.7: Friction coefficients measured with the smooth PDMS substrate (closed symbols) and patterned PDMS substrate (open symbols) against a smooth PDMS ball on the a) MTM Tribometer and b) BTL tribometer.

3D-printed Tribotool

The fourth tribometer we use in this study is a custom-made tribotool (CTT). As the effect of surface roughness is consistent with for the other tribometers, we use only one tribopair (rough glass ball, smooth PDMS plate) as a comparison for the tribometer mechanics. An important difference between the CTT and the other tribometers is that the CTT operates in a gap-controlled instead of a force-controlled manner. We use speeds from 1 to 20 mm/s here, as these are the speeds where reliable and reproducible results could be obtained. Due to the limited speed range, a mixed regime is absent when measuring water and glycerol (Figure 8.8). With these data, we are still able to make estimations for most of the Stribeck fit parameters in the boundary and EHL regime. The friction coefficient in the boundary regime here is 0.93 ± 0.05 , rather similar to the values previously measured using glass – PDMS combinations on the other tribometers. The results do show a dependence on the tribological device used. From the available data, it is hard to determine where exactly the mixed regime begins and what the slope in this regime is, as we do not have enough data on the mixed regimes. The limited data points we obtained in the in the EHL regime appear to follow the previously observed hydrodynamic behavior. As a reference we show a line with a slope of 0.5 in Figure 8.8. Overall, our 3D-printed rheo-tribometer delivers similar trends for

Fluid and suspension lubrication using four different tribometers

Newtonian fluids as obtained using commercially available tribometers. Due to the limited speed range, it is impossible to obtain a complete Stribeck curve with the two lubricants used here. We will, however, use the obtained data and proceed to compare the results of all the tribometers used here in the following section.

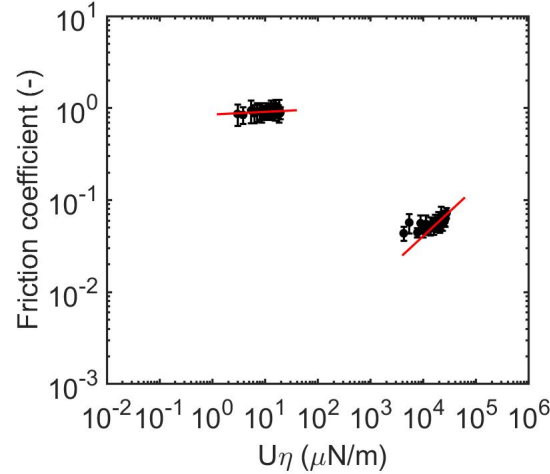


Figure 8.8: Tribological measurements obtained using a custom-made 3D printed tribotool with a rough glass ball and a smooth PDMS plate.

Stribeck parameters of different tribometers

Using the APT, BTL, MTM, and CTT tribometers, we have already observed that certain Stribeck parameters such as friction coefficients in the boundary regime (h) and the slope in the mixed regimes (m) depend on the tribopairs used, while other parameters, such as slope in the EHL regime, seem to be more related to the tribometer type. To better understand how the measuring system influences the frictional behavior, we obtain the Stribeck parameters for each tribometer from the best fit to the curves and combined them in Table 8.2. Values are those obtained for the rough glass ball and the smooth PDMS substrates as these surfaces were used on all four tribometers.

Fluid and suspension lubrication using four different tribometers

Table 8.2: Overview of the Stribeck parameters obtained for the APT, BTL, MTM and CTT tribometers with a rough glass probe and a smooth PDMS substrate. It should be noted that values for the BTL and CTT in the mixed regime are estimated based on the Stribeck fit and not obtained from actual data.

	Anton Paar (APT)	Tribolab (BTL)	Mini Traction Machine (MTM)	Tribotool (CTT)
Contact area (mm ²)	0.8	0.8	1	0.8
Sample volume (ml)	1	10	30	300
μ_{Boundary} (h)	1.52 ± 0.08	1.25 ± 0.23	0.66 ± 0.05	0.93 ± 0.05
Slope boundary regime (l)	0.01	0.02	-0.01	0.05
Begin mixed regime (B, $\mu\text{N/m}$)	20	10	50	n/a
Slope mixed regime (m)	1	2	2	n/a
Range mixed regime ($\mu\text{N/m}$)	$1.9 \cdot 10^3$	$28 \cdot 10^3$	$1.4 \cdot 10^3$	n/a
Slope EHL (n)	0.56	1.2	0.5	0.52

To obtain these values, we use the empirical Stribeck formula Eq. 8.1. When multiple parameters are used to fit a curve, small changes in one parameter can have large effects on other values, especially on a log-log scale. In addition, as in some cases we do not have experimental data in the complete regime, fitting becomes less accurate. To avoid these variations, we used several fixed values. These values were either taken directly from the lubrication curve or a theoretical value was used. One of these fixed values was the friction coefficient in the boundary regime, h (Table 8.2, μ_{boundary}). We initially also set the slope of the EHL regime (n) to the theoretically expected value of 0.5 [7, 11, 20] to obtain the remaining Stribeck parameters (l , b , m , k). We then used these obtained values to determine the actual slope in the EHL regime as reported in the table.

Boundary regime: Surface properties and surface motion

For the friction coefficient in the boundary regime, we find values between 0.66 and 1.52 for all tribometers with APT giving the highest value, whereas the MTM gives the lowest value. The lowest value for the MTM can be explained by the different sliding mechanism of the MTM compared to that of the other tribometers. The MTM measuring method is different from other tribometers because of the sliding surfaces. In this device, both surfaces rotate in opposite directions, allowing fluids to enter the contact zone more efficiently than when only one of the tribosurfaces moves. This leads to lower friction coefficients, which has been shown by MTM measurements at different relative speeds (slide-to-roll ratios) between the probe

Fluid and suspension lubrication using four different tribometers

and the substrate. [15, 35] When only one of the surfaces rotates (SRR=0, sliding), the friction coefficient is lower than when both surfaces rotate simultaneously (SRR=2, rolling). Another cause for the large difference between the MTM and the other three tribometers might be the difference in the glass ball used. For the APT, BTL, and CTT tribometers we use the same rough glass ball that is supplied by Anton Paar. For the MTM, we use a rough glass ball that is supplied by PCS instruments. It should be noted that these glass balls differ in diameter (APT: 12.7 mm. MTM: 20 mm), and may also differ in their surface structure or exact material type.

The probe of the APT tribometer is in contact with three pins simultaneously, which contributes to the higher values in the boundary regime. While the contact area of one pin is 0.8 mm^2 , the total contact area will be three times this value. The higher frictional values for the APT tribometer may be explained by a higher surface area. Alternatively, the higher friction coefficient may also be related to the specific sliding movement. [15] The APT tribometer operates in a manner that is similar to pure sliding or a SRR of 2 on the MTM tribometer. In pure sliding mode, only one of the surfaces rotates while the other remains stationary. When a SRR of 2 was used (a stationary substrate and rotating probe) the friction coefficient approached that of the APT tribometer. Similar sliding mechanisms thus results in similar friction coefficients. For the boundary regime, we, therefore, conclude, that the friction coefficient in the boundary regime predominantly depends on the surfaces used and the type of tribometer motion.

Mixed regime: Fluid flow caused by tribometer motion

We observed that the beginning of the mixed regime (B) for three of the tribometers, the APT and BTL occur at the same values of $U\eta$ (between 10 and 20 $\mu\text{N}/\text{mm}$), whereas the MTM shows a larger value of $U\eta = 50 \mu\text{N}/\text{mm}$. These differences arise due to differences in tribometer motion and the large probe size on the MTM as suggested in the previous section. However, since the entire $U\eta$ range studied here spans over eight orders of magnitude, we consider these differences to be relatively small. The length of the mixed regime in terms of $U\eta$ again varies for each tribometer. The mixed regime for the MTM and the APT appear to be rather similar at around $2 \cdot 10^3$. The BTL shows a larger range of $28 \cdot 10^3$. As the mixed regime is the transition from the surface-surface contact zone to the fully separated zone, a wide-range of the mixed regime indicates that this tribometer requires larger gap sizes to reach full surface separation by entrainment of the fluid. As the MTM has two moving surfaces, fluids are entrained more efficiently which is potentially

why the MTM shows the shortest mixed regime range. The APT tribometer also has a relatively limited range of friction coefficients in the mixed regime, which indicates efficient fluid entrainment while transitioning from the contact regime to the separated surface regime. The parameters in the mixed regime (e.g. starting point and slope) are thus influenced by the tribometer motion as well.

EHL regime: Fluid viscosity and drag forces

The behavior in the EHL regime is determined by the ability of a fluid to generate enough pressure to fully separate the sliding surfaces from one another. For the exponent n , representing the slope in the EHL regime, we find similar values around 0.5 for the three tribometers that slide in a rotational motion (APT, MTM, CTT) when the same surfaces are used. This is consistent with theories that predict a slope of 0.5 in the EHL regime.[7, 11] As discussed earlier, for the BTL we find much larger values of 1. The friction coefficient in the EHL regime depends mainly on the lubricant type and for the BTL also on tribometer motion, possibly due to the contribution of drag forces, although the exact reason for this deviating value is not completely clear.

Lubrication behavior of complex lubricants

Using simple Newtonian fluids, we found very similar trends even though the devices used operate in completely different ways. The frictional regimes and overall friction coefficients are comparable for all of the tribometers when the same tribopairs are used. These Newtonian fluids all exhibit traditional Stribeck behavior in the boundary, mixed, and hydrodynamic regime. However, many systems also contain particles to form suspensions, emulsions, etc. Such soft solid suspensions are present in foods, cosmetics, and other bio(-compatible) materials. In these systems, the frictional behavior is not just determined by the viscosity, but also by other aspects, as rolling and sliding events, particle interactions, et cetera. To demonstrate how surface motions influence particle entrainment and particle lubrication, densely-packed hydrogel microparticle suspensions are measured on the different tribometers. In **Chapter 4**, using the APT tribometer, we showed that these hydrogel particle suspensions do not show traditional Stribeck behavior but, instead, transition through four frictional regimes. [12] These regimes were attributed to the deformation and entrapment of the particles between the asperities of the glass ball. In the first regime, at low speeds and theoretically small gap sizes relative to the particle size, a small number of particles are already present between the surface asperities as we described previously in **Chapter 4**. [12] However, due to the small gap sizes, these particles can be compressed, which leads to high

Fluid and suspension lubrication using four different tribometers

values of the friction coefficient due to large particle surface contact. In the second regime, as gap sizes increase, these particles regain their spherical shape and their ability to roll leading to a decrease in the friction coefficient. An increase in friction coefficient is then seen again as a third regime arises, hypothesized to be due to jamming of particles or particle compression as more particles are able to enter the zone. When the gap size further increases, these jammed or compressed particles return to their original shape and size leading to a rapid decrease in the friction coefficient. For these systems, we have not observed a hydrodynamic regime. The different regimes appear to depend on the ability of the particle to fit within the asperities of the probe. Using these different tribometers we can also study the effect of tribometer motion on complex soft suspension tribology.

Particle-based lubrication on different tribometers

For these four tribometers, again we use a rough glass ball and smooth PDMS surfaces for comparison. As discussed before, the APT, BTL, and CTT tribometers all use a glass ball with the same roughness and size, while the glass ball on the MTM is larger in diameter (MTM: 19 mm, APT, BTL, CTT: 12.7 mm). The particles of the suspensions used on the APT, BTL, and CTT have an average size of 12 μm . The particles used on the MTM have a larger size of around 100 μm . These differences arise due to differences in available equipment at the different facilities where each tribometer is located. Although the particles are different in size, we still expect to be able to demonstrate differences in tribological behavior between Newtonian fluids and particle suspensions and to show the effect of different tribometers.

The results obtained with our four tribometers all show different frictional regimes and they do not display many similarities at first sight (Figure 8.9). The differences seen here are much larger than those observed for simple Newtonian fluids. The APT tribometer shows the four frictional regimes, with alternating decreasing and increasing friction coefficients over the entire speed range. These regimes are identical to findings presented in **Chapter 4** for particles from 10 to 150 μm in size. [12]

For the other tribometers, due to the limited speed ranges (1 – 20 mm/s for BTL and CTT, and 1 mm/s – 100 mm/s for MTM), not all four frictional regimes are visible. Using the BTL we first see a rather flat section that resembles regime I of the APT tribometer. The subsequent decrease is similar to the decrease in regime II of the APT. Alternatively, this might be related to regime IV as well. Both regimes II and IV are hypothesized to arise due to an increase in gap size. The increase in gap size allows particles to regain their rolling ability resulting in a decrease in

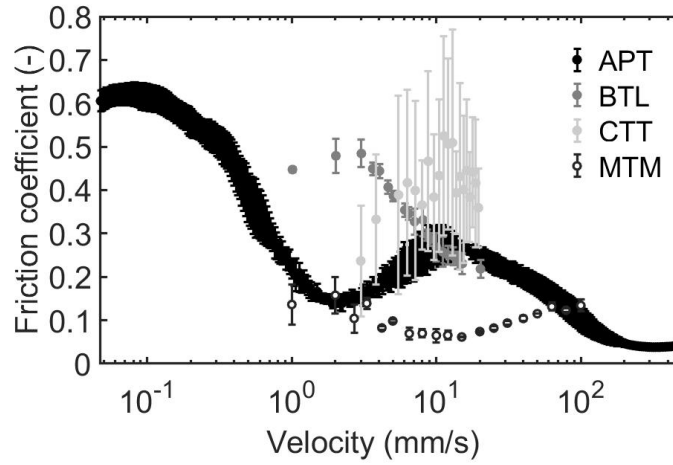


Figure 8.9: Frictional curves obtained for hydrogel microparticle suspensions on the APT, BTL, MTM and CTT tribometers with a rough glass probe and smooth PDMS substrates. The hydrogel microparticle size for the APT, BTL and CTT tribometers was $12\ \mu\text{m}$ while the particles used on the MTM were around $100\ \mu\text{m}$ in size.

the friction coefficient. We see a shift in the appearance of these regimes, which shows that although similar mechanisms take place, they do not occur at the same sliding speed. The two regimes observed for the CTT also overlap with the first two regimes of the APT but shifted to even higher values for the velocity. Alternatively, these alternating increasing and decreasing regimes could also represent regime III and IV. In this case, similar mechanisms are possibly responsible for the frictional behavior.

In the case of the MTM, we see the appearance of three frictional regimes. We must note that at speeds above $100\ \text{mm/s}$, the cohesive particle suspension was visibly removed from the contact zone, making it impossible to obtain accurate lubrication data for higher speeds. When we include a reliable speed range, we first see a regime with a rather constant friction coefficient ($1 - 3\ \text{mm/s}$), a regime with a decrease in friction coefficient ($3 - 10\ \text{mm/s}$), followed by a regime with an increase in friction coefficient (above $10\ \text{mm/s}$). These regimes strongly resemble the first three friction regimes observed for the APT tribometer. Similar to the CTT and BTL, the different regimes appear to arise at different sliding velocities and the slopes observed in the different regimes are less steep in the MTM tribometer.

If we attempt to relate our findings to the results obtained on the APT, the most apparent mechanism is that particles can roll, thereby causing a decrease in friction coefficient as happens in regime II of the curve obtained by the APT tribometer. The increase could then be caused by particle jamming/compression of particles while

Fluid and suspension lubrication using four different tribometers

more particles enter the contact zone as we hypothesized for the APT tribometer as well. [12] The MTM shows lower frictional values, which can be related to the differences in probe roughness and particle sizes used here. However, the MTM also generated lower friction coefficients than the APT for the Newtonian fluids which points towards the tribometer motion as being the main contributor for the lower friction coefficients both for particle suspensions as for Newtonian fluids. For a tribometer that has two sliding surfaces (MTM) particles can be easily entrained compared to devices that can push particles away while sliding (BTL, CTT). Due to the differences in sliding motion, particles become (de)compressed at different sliding speeds. Consequently, the entrainment of fluid and particles is changes for each tribometers, which has a large effect on the start of the frictional regimes. In this case, particle entrainment occurs at various velocities due to differences in sliding mechanisms.

Overall, we observed much more similarities for the Newtonian fluids measured on different tribometers than for the hydrogel microparticle suspensions. For more complex systems, we find that tribometer mechanics have a much larger influence on the friction coefficient than for Newtonian fluids. When using suspensions, particle entrainment, particle deformation, and particle exclusion occur under specific conditions. Particles can also be pushed out of the contact zone, causing an increase in friction coefficient or particles can become entrapped in the contact which would lead to particle compression and an increase in friction coefficient. As the tribometers differ in the sliding motion, sliding direction, and the contact area, this influences the entrainment of the particles, which affects its rolling ability due to differences in gap size. Such effects are more important for particle suspensions than for simple Newtonian fluids, which explains the large differences in the lubrication behavior found for the different tribometers. For lubricants consisting of particles, a comparison between different devices is much more complicated due to the complex nature of the lubricant. This also makes it challenging to compare results from different published studies.

Conclusions

We used four tribometers that have different types of relative sliding motions to measure the lubrication of Newtonian fluids and Non-Newtonian particle suspensions. Using this approach, we aimed to gain more insight into how different aspects of tribosystems (tribopairs, tribometer mechanics) influence the friction coefficient. For Newtonian fluids, the boundary regime is influenced strongly by the choice of surface material and roughness. The mixed regime both varies strongly with the type of surface and the type of motion of the tribometer. Smooth surfaces give a steep decrease in the mixed regime, and an early onset of the EHL regime. In the EHL regime, the slope was similar for most rotating tribometers, as expected from theory. However, for an oscillating sliding tribometer, a higher slope was found. We also found that patterned surfaces give a less steep slope in the EHL regime. The EHL regime thus responds to changes in tribometer motion as well as surface roughness above a certain asperity size. When we used a hydrogel particle suspension as a more complex lubricant, each tribometer generated lubrication curves with different frictional regimes. Although similar distinct frictional regimes were found for each tribometer, the transitions to the different regimes varied substantially between tribometers. These transitions are suggested to be related to particle entrainment and particle deformation, which strongly depends on the sliding motion. Our findings highlight the strong system dependency of a tribological measurement and shows that tribological results from different tribometers cannot directly be compared, even when the same surfaces are used.

Recommendations

It is challenging to compare results obtained using different tribological devices due to differences in surface contact and fluid entrainment between the surfaces, which yields specific lubrication curves for each tribological device or surface. As the friction coefficient is system dependent, we recommend evaluating the friction coefficient based on the characteristics of a specific device (e.g. roughness, surface motion, speed range), especially when complex multi-component lubricants are considered. Further research in this context is recommended to provide additional insights into the lubrication behavior of multi-component systems using different devices and surfaces. For both the BTL and the CTT a clear mixed regime was absent. Using lubricants with different viscosities could fill the current absence of frictional regimes. The BTL shows slopes in the EHL regime that deviate from existing theories. Additional theoretical analysis is required to predict and understand


Fluid and suspension lubrication using four different tribometers

the behavior displayed by this linear-drive tribometer. When considering particle lubrication, different particles (sizes, deformability etc) can be measured to clarify the mechanisms behind the different sliding regimes seen for different relative surface motions. These future studies can provide experimental or theoretical approaches which allow tribologists to relate their experimental (or theoretical) data to results with different tribometers and perhaps even new empirical frictional laws for soft surfaces and complex lubricants.

References

1. Rudge, R. E. D., Scholten, E. & Dijkman, J. A. Natural and induced surface roughness determine frictional regimes in hydrogel pairs. *Tribology International* vol. 141, 105903 (2019).
2. Ni, W. *et al.* Effects of the ratio of hardness to Young's modulus on the friction and wear behavior of bilayer coatings. *Applied Physics Letters* vol. 85, 4028–4030 (2004).
3. Kim, J. M., Wolf, F. & Baier, S. K. Effect of varying mixing ratio of PDMS on the consistency of the soft-contact Stribeck curve for glycerol solutions. *Tribology International* vol. 89, 46–53 (2015).
4. Maeda, N., Chen, N., Tirrell, M. & Israelachvili, J. N. Adhesion and friction mechanisms of polymer-on-polymer surfaces. *Science* vol. 297, 379–382 (2002).
5. Tabor, D. in *Advances in Polymer Friction and Wear* 5–30 (Springer, 1974).
6. Zappone, B., Rosenberg, K. J. & Israelachvili, J. Role of nanometer roughness on the adhesion and friction of a rough polymer surface and a molecularly smooth mica surface. *Tribology Letters* vol. 26, 191 (2007).
7. Bongaerts, J., Fourtouni, K. & Stokes, J. Soft-tribology: lubrication in a compliant PDMS–PDMS contact. *Tribology International* vol. 40, 1531–1542 (2007).
8. Bachchhav, B. & Bagchi, H. Effect of surface roughness on friction and lubrication regimes. *Materials Today: Proceedings, In press* (2020).
9. Yu, J. *et al.* Friction and adhesion of gecko-inspired PDMS flaps on rough surfaces. *Langmuir* vol. 28, 11527–11534 (2012).
10. Ranc, H., Servais, C., Chauvy, P.-F., Debaud, S. & Mischler, S. Effect of surface structure on frictional behaviour of a tongue/palate tribological system. *Tribology International* vol. 39, 1518–1526 (2006).
11. De Vicente, J., Stokes, J. & Spikes, H. Soft lubrication of model hydrocolloids. *Food Hydrocolloids* vol. 20, 483–491 (2006).
12. Rudge, R. E. D., Van De Sande, J. P., Dijkman, J. A. & Scholten, E. Uncovering friction dynamics using hydrogel particles as soft ball bearings. *Soft Matter* vol. 16, 3821–3831 (2020).
13. Sarkar, A., Kanti, F., Gulotta, A., Murray, B. S. & Zhang, S. Aqueous lubrication, structure and rheological properties of whey protein microgel particles. *Langmuir* vol. 33, 14699–14708 (2017).
14. Garrec, D. A. & Norton, I. T. Kappa carrageenan fluid gel material properties. Part 2: Tribology. *Food Hydrocolloids* vol. 33, 160–167 (2013).
15. Yakubov, G., Branfield, T., Bongaerts, J. & Stokes, J. Tribology of particle suspensions in rolling-sliding soft contacts. *Biotribology* vol. 3, 1–10 (2015).
16. Selway, N., Chan, V. & Stokes, J. R. Influence of fluid viscosity and wetting on multiscale viscoelastic lubrication in soft tribological contacts. *Soft Matter* vol. 13, 1702–1715 (2017).
17. Denny, D. The influence of load and surface roughness on the friction of rubber-like materials. *Proceedings of the Physical Society. Section B* vol. 66, 721 (1953).

18. Persson, B. N. J. Relation between Interfacial Separation and Load: A General Theory of Contact Mechanics. *Phys. Rev. Lett.* vol. 99, 125502 (12 2007).
19. Huang, W., Jiang, L., Zhou, C. & Wang, X. The lubricant retaining effect of micro-dimples on the sliding surface of PDMS. *Tribology International* vol. 52, 87–93 (2012).
20. De Vicente, J., Stokes, J. & Spikes, H. Rolling and sliding friction in compliant, lubricated contact. *Proceedings of the Institution of Mechanical Engineers, Part J: Journal of Engineering Tribology* vol. 220, 55–63 (2006).
21. Campbell, C. L., Foegeding, E. A. & van de Velde, F. A Comparison of the lubrication behavior of whey protein model foods using tribology in linear and elliptical movement. *Journal of texture studies* vol. 48, 335–341 (2017).
22. Røn, T. & Lee, S. Influence of temperature on the frictional properties of water-lubricated surfaces. *Lubricants* vol. 2, 177–192 (2014).
23. Yakubov, G. E., McColl, J., Bongaerts, J. H. & Ramsden, J. J. Viscous boundary lubrication of hydrophobic surfaces by mucin. *Langmuir* vol. 25, 2313–2321 (2009).
24. Xu, Y. & Stokes, J. R. Soft lubrication of model shear-thinning fluids. *Tribology International* vol. 152, 106541 (2020).
25. Pondicherry, K. S., Rummel, F. & Laeuger, J. Extended stribeck curves for food samples. *Biosurface and Biotribology* vol. 4, 34–37 (2018).
26. Oppermann, A., Verkaaik, L., Stieger, M. & Scholten, E. Influence of double (w 1/o/w 2) emulsion composition on lubrication properties. *Food & Function* vol. 8, 522–532 (2017).
27. Fuhrmann, P. L., Sala, G., Scholten, E. & Stieger, M. Influence of clustering of protein-stabilised oil droplets with proanthocyanidins on mechanical, tribological and sensory properties of o/w emulsions and emulsion-filled gels. *Food Hydrocolloids* vol. 105, 105856 (2020).
28. Kieserling, K., Schalow, S. & Drusch, S. Method development and validation of tribological measurements for differentiation of food in a rheometer. *Biotribology* vol. 16, 25–34 (2018).
29. Dresselhuys, D. M. *et al.* Tribology of o/w emulsions under mouth-like conditions: determinants of friction. *Food Biophysics* vol. 2, 158–171 (2007).
30. Zheng, Q. & Lü, C. Size effects of surface roughness to superhydrophobicity. *Procedia IUTAM* vol. 10, 462–475 (2014).
31. Mason, R., Emerson, J. & Koberstein, J. T. Self-adhesion hysteresis in polydimethylsiloxane elastomers. *The Journal of Adhesion* vol. 80, 119–143 (2004).
32. Kamperman, M., Kroner, E., del Campo, A., McMeeking, R. M. & Arzt, E. Functional adhesive surfaces with “gecko” effect: The concept of contact splitting. *Advanced Engineering Materials* vol. 12, 335–348 (2010).
33. Stokes, J. R., Macakova, L., Chojnicka-Paszun, A., de Kruif, C. G. & de Jongh, H. H. Lubrication, adsorption, and rheology of aqueous polysaccharide solutions. *Langmuir* vol. 27, 3474–3484 (2011).
34. Vergeles, M., Keblinski, P., Koplik, J. & Banavar, J. R. Stokes drag and lubrication flows: A molecular dynamics study. *Physical Review E* vol. 53, 4852 (1996).
35. Chin as-Castillo, F. & Spikes, H. Mechanism of action of colloidal solid dispersions. *Journal of Tribology* vol. 125, 552–557 (2003).



General discussion

Introduction

The complex interfaces described in this thesis, often do not show the expected Stribeck behavior (e.g. boundary, mixed and hydrodynamic regime) [1–3] commonly found for Newtonian fluids. [4–6] When soft polymeric surfaces are considered, the molecular scale fluid – surface interactions become more difficult to untangle. [3, 7, 8] Once a lubricant is included between soft surfaces, the surface-fluid interactions begin to play an increasingly important role. Effects such as wettability and viscosity can impact the friction coefficient to a great extent. [9, 10] Interactions on the nanometer scale can thus have a large impact on the friction coefficient of the entire system. When mixtures of molecules are present in solution, these molecules may even interact with one another having a deteriorating or synergistic effect on the friction coefficient. As mixtures often exist in realistic applications, the tribological field could greatly benefit from a solid scientific underpinning of the lubrication mechanisms behind these systems. When lubricants consist of (semi-)solid ball-bearing particles, this so-called third-body friction shows friction coefficients that respond to changes in particle size [11, 12] and volume fraction, [6, 13–15] as well as properties of the surrounding fluids. [13] In the presence of fluids, several frictional mechanisms play a role due to the effects of particle, fluid, and surface interactions. All of these effects, however, depend on the tribometer motion which causes lubricants to become entrained or particles and surfaces to become deformed under specific conditions. [16, 17] Soft tribological systems thus show many different mechanisms, depending on the surface-lubricant and surface – surface combinations. In this thesis, the challenge of uncovering the key mechanisms behind soft sliding systems was approached. This was done by combining soft surfaces and complex lubricants with a range of physical and chemical properties while using different tribometers.

Approach and main findings

The frictional behavior of soft materials and complex lubricants are influenced by different parameters of a tribological system. To provide a framework that interconnects the frictional behavior of different soft materials and complex lubricants, several tribosystems were studied as represented by the three sections of this thesis:

- (I) Hydrogel - Hydrogel friction (**Chapter 2** and **Chapter 3**).
- (II) Particle lubrication (**Chapter 4**, **Chapter 5**, and **Chapter 6**).

General Discussion

- (III) Tribological applications (**Chapter 7** and **Chapter 8**).

A schematic overview of the systems investigated in each chapter and their respective length scales are shown in Figure 9.1. In this figure, the main contributors to the friction coefficient are stated as well. These parameters will be further discussed in the following sections of this general discussion. We first provide a summary of the systems studied throughout the thesis.

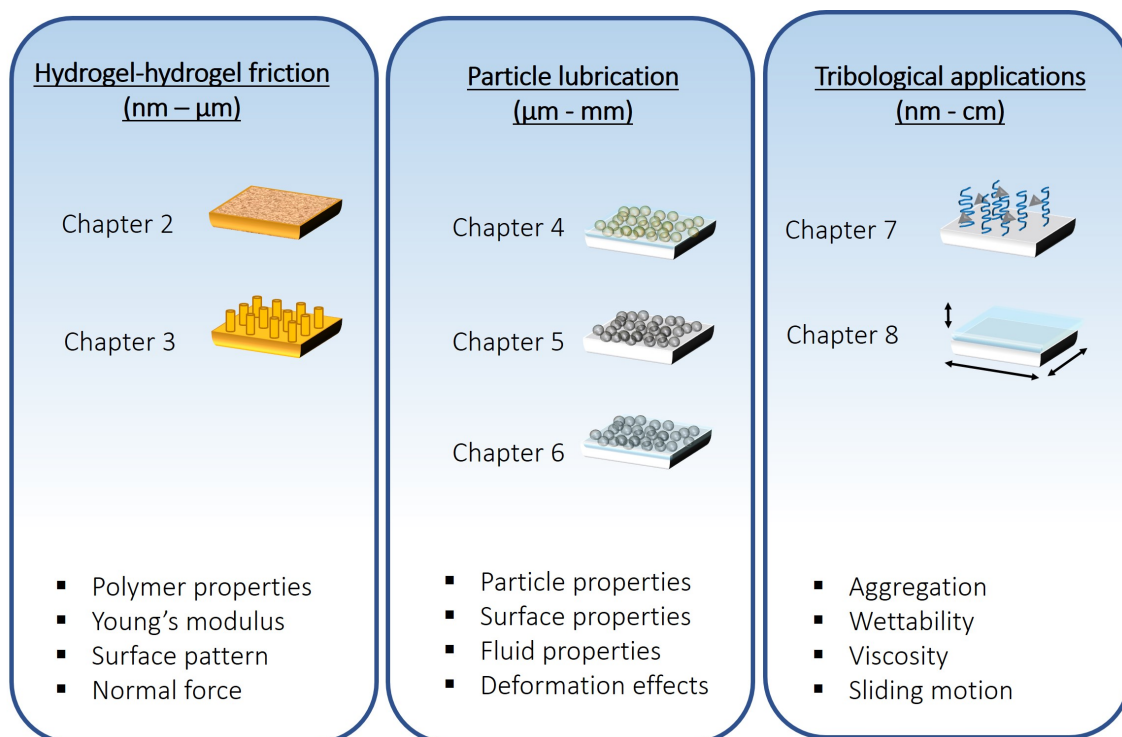


Figure 9.1: An overview of the tribological systems studied in each chapter and the most relevant control parameters that contributed to the friction coefficient. The relevant length scales are indicated in the figure.

In **Chapter 2**, we used optically smooth but microscopically rough hydrogels varying in polymer-network type and Young's modulus. We studied the effect of deformability of surface asperities and found two normal force-dependent frictional regimes as a result of asperity flattening. In **Chapter 3**, These hydrogels were modified using micro-patterning techniques which allowed us to investigate how specific surface roughness parameters influence the friction coefficient. In this chapter, it was found that the effective contact area was the most important parameter contributing to an increase in the friction coefficient. We showed how hydrogel particle properties influence lubrication behavior and give four velocity-dependent frictional regimes in **Chapter 4**. In **Chapter 5** and **Chapter 6**, the lubrication behavior dry glass particles and particles in suspension were measured, respectively. With these hard lubricants between soft surfaces two frictional regimes were found in the dry case; a rolling and a sliding friction regime, depending on

the effective gap size. For particles in suspension it was found that particles and fluids are able to enter the gap separately as a fluid-lubricated and a particle-lubricated regime was observed. The results in **Chapter 7** demonstrated how macromolecular interactions between salivary proteins and astringent agents cause significant changes in the friction coefficient depending on the type of salivary protein involved. The last experimental chapter, **Chapter 8**, we investigated all of the four tribometers used throughout the thesis. As lubricants, Newtonian fluids and hydrogel particle suspensions were measured between different tribosurfaces. The results of this chapter showed that tribometer motion strongly affects the friction coefficient and the frictional regimes found. We uncovered various mechanisms and measured a range of friction coefficients. An overview of the friction coefficients for each of the tribosystems investigated is displayed in Figure 9.2.

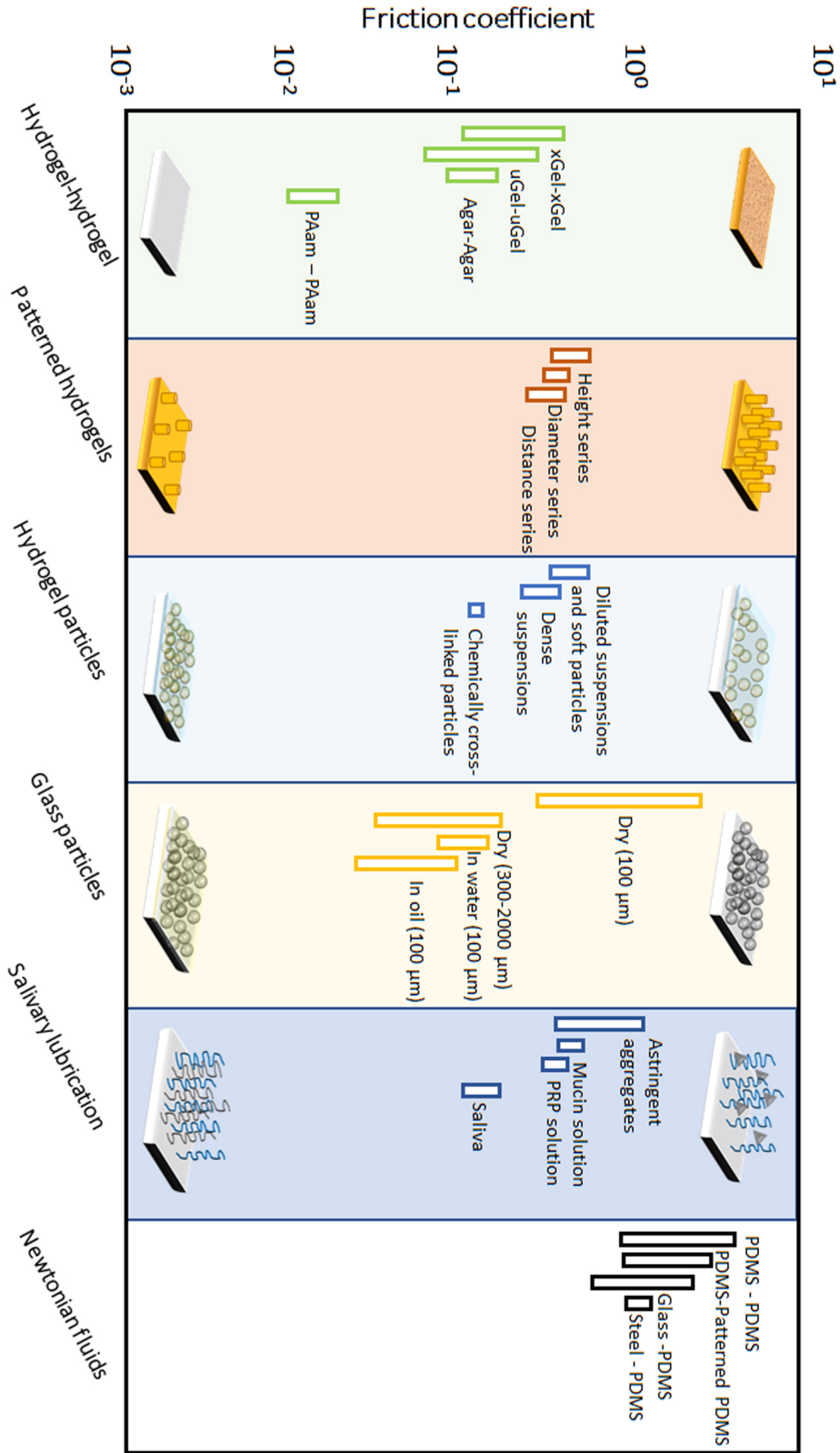


Figure 9.2: Friction coefficients of the tribosystems studied. The frictional values used are obtained in the contact regime e.g. at relatively low velocities. A schematic image of the high and low frictional systems is shown at the top and bottom of the graph respectively.

Key frictional mechanisms in soft tribology

By using different surfaces, lubricants, and tribometers, with the aim to uncover and understand the friction and lubrication mechanisms when soft surfaces and complex lubricants are involved. In this section, the three most influential frictional mechanisms are discussed: asperity contact, lubricant entrainment, and deformation effects. Concretely, (I) soft asperities influence the contact mechanics and the hydrodynamics (fluid flow) of the system, (II) lubricant and surface properties lead to lubricant entrainment which causes surface separation and, (III) deformation of the surfaces or (semi-)solid lubricants can lead to rolling and sliding friction regimes. These mechanisms often exist in parallel and directly influence one another. For example, deformation effects influence asperity contact which affects lubricant entrainment. Similarly, once particles are entrained, deformation occurs and asperity contact is enlarged leading to a transition from rolling to sliding friction. This interconnection is exactly what makes interpreting tribological results increasingly challenging.

Soft asperities, contact mechanics, and polymer networks

The majority of studies on (soft) surface roughness is carried out using randomly rough surfaces. [18, 19] These surfaces are either naturally rough or patterned using a rough counter surface. Using random rough surfaces makes it impossible to specify which roughness parameter (height, diameter, distance) plays the most important role in terms of the friction coefficient. Additionally, existing work often focuses on one specific surface material (PDMS, Polyacrylamide (PAAm), etc). For such materials it has been shown that the polymers present at the hydrogel surface contribute to the friction coefficient. [7, 8, 20, 21] We confirmed the importance of hydrogel polymer type in **Chapter 2**, as the polymer network type gave way to different degrees of roughness. Changes in surface roughness and the subsequent contact area are the main mechanisms behind the friction coefficient of soft hydrogels. This was concluded, as smooth surfaces gave much lower friction coefficient than (naturally) rough surfaces. These differences were attributed to interlocking of micron-sized asperities. Upon an increase of the normal force, the asperities were flattened and the interlocking events diminished as was observed by the decrease in the friction coefficient. Besides the micron-scale asperities, the polymers present at the surface likely also have an effect on the friction coefficient. Understanding the effect of the surface polymers requires complementary techniques such as IR spectroscopy, [22] electron microscopy, small-angle X-ray scattering (SAXS), [23] and atomic force microscopy (AFM). [24] The polymer network was kept constant, while varying the micron-scale roughness in **Chapter 3**. The friction coefficients

General Discussion

of patterned surfaces with cylindrical asperities showed that the pillar height, diameter, and distance all have a different contribution to the friction coefficient. When increasing the height of the pillar and keeping the number of pillars and the diameter constant, the friction coefficient increased. This cannot directly be related to the surface area of the sample as the surface area is the same for each sample. When bending the tall pillars, the contact dynamics and hydrodynamics change. Additionally, slender pillars bend more readily causing changes in the friction forces and the effective contact area. The contact area effectively becomes larger, as does the friction coefficient.

When considering rubbery elastomeric surfaces, similar trends were found as for our (gelatin) hydrogels; enhanced contact areas give higher friction coefficients in the boundary regime. This was shown in **Chapter 8**. In the mixed regime and in the EHL regime, the slopes of the curve were less steep for patterned than for smooth surfaces due to differences in fluid film formation. On a rough/patterned surface, it is challenging to form a uniform lubricating film due to height differences and the ability of the fluid to be drained from the surfaces. This means fluid is present between the asperities, instead of forming a film on the top of the asperities. In that case, higher speeds are needed to generate the same surface separation as for smooth surfaces. For hydrogels and elastomers the friction coefficient thus depends on the type of polymer in the polymer network, the microscopic roughness of the natural asperities, and the resulting contact dynamics.

Surface, fluid, and particle interactions

We will now discuss the mechanisms behind the various frictional regimes that arise for different lubricant types. These regimes are related to the interactions between the surfaces, fluids and particles that occur simultaneously. Currently, there is no theoretical lubrication curve that covers all the soft solid sliding regimes. Using a range of fluid and particulate lubricants we, therefore, attempt to contribute to the postulation of such soft tribological theories.

Newtonian fluids

Even when seemingly simple Newtonian lubricants are used, large influences of the viscosity and wettability on the friction coefficient can be observed. We illustrate this using preliminary results of a tribological study where we used alcohols, ketones and polyols (diols and triols) differing in carbon chain length and side groups and, with that, also in viscosity and polarity. Results of the alcohols are shown in Figure 9.3a, ketones in Figure 9.3b and polyols in Figure 9.3c. The differences in

molecular structure give rise to differences in the friction coefficient, especially at low sliding speeds.

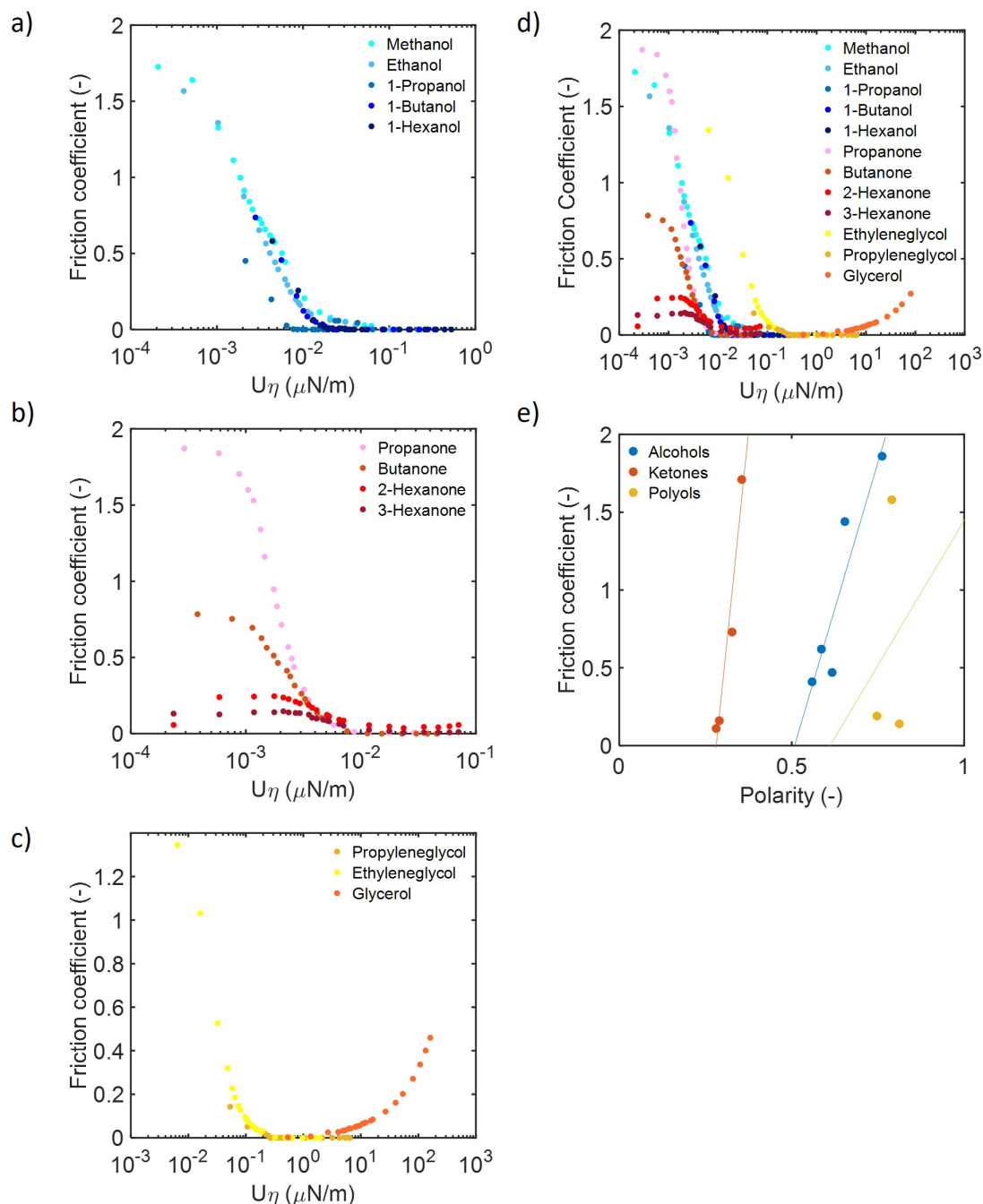


Figure 9.3: The viscosity corrected friction coefficients of organic solvents with different side groups as Newtonian lubricants. The figure shows a) alcohols, b) ketones, c) diols and triols. d) The results of all solvents into one graph. e) The friction coefficient of the organic solvents as function of the polarity of the fluids. The measurements were performed on the Bruker TriboLab tribometer (BTL) with two smooth PDMS surface at 1 N and at room temperature.

General Discussion

Alcohols have low polarities and low viscosities, ketones have high polarities and low viscosities and diols have low polarities and high viscosities. This results in entirely different lubrication curves for these Newtonian lubricants. We find a boundary regime for the ketones, a mixed regime for all categories of samples and a hydrodynamic regime for the polyols. The polyols have high polarities and are thus poorly able to wet the PDMS surface. However, their high viscosity results in efficient fluid entrainment and good lubrication in the mixed and EHL regime.

Beyond the boundary regime, polarity thus does not affect the friction coefficient and viscous effects dominate. Ketones have relatively low polarities and should be able to wet the PDMS surfaces reasonably well. Due to the low viscosity, the curve starts early in the boundary regime and distinct boundary regimes emerge. The maximum friction coefficient thus decreases with solvent polarity. For all the lubricants with different side groups, we do find that the friction coefficient decreases with the carbon chain length due to both an increase in viscosity and polarity. The friction coefficient, specifically at low velocities in the mixed and boundary regimes, also changes with the type of side group and the number of side groups and the following trend is found: $=O > -OH > \text{multiple } -OH$. The results of all the solvents as function of polarity are shown in one graph in Figure 9.3d

When considering the friction coefficients at low speeds (< 10 mm/s), we find that the friction coefficient increases with the polarity for ketones and alcohols (Figure 9.3e), here wetting properties thus dominate. For the high viscosity polyols, a poor relationship is found between the polarity and the friction coefficient as the viscous effects begin to dominate. These results with simple Newtonian fluids as lubricants highlight how even the molecular structure of fluids that have similar rheological properties can cause differences in the friction coefficient. These differences occur due to different interactions between the carbon backbone and the side groups with the PDMS surface. As we have shown with glass particles in different solvents (**Chapter 6**) and with salivary proteins mixed with different solvents (**Chapter 7**), the fluid matrix plays a large role on the friction coefficient. The friction coefficient is ultimately determined by the component that has the strongest interactions with the surfaces and becomes better entrained. In the next sections we further discuss the lubrication regimes when using complex non-Newtonian lubricants.

Fluid – surface interactions

When considering lubricants that consist of multiple components, the inter-lubricant interactions need to be taken into account besides the lubricant-surface interactions. The behavior of such lubricants was investigated in **Chapter 7** using biopolymer solutions. Upon the addition of polyphenols or metal salts to salivary

proteins, three mechanisms can take place regarding the lubricating layer: (I) protein aggregation occurs, leading to lubrication losses (II) protein aggregation occurs and good lubrication is maintained (III) no protein aggregation occurs and good lubrication is maintained. The favored mechanism depends on the type of salivary protein and astringent agent involved.

Saliva is often represented by mucin solutions in tribological studies. [15, 25, 26] We have shown that mucin alone is unable to accurately represent the components present in saliva as different trends are found between mucin solutions and human saliva. Trends between proline-rich proteins (PRPs) and saliva were much more similar indicating the PRPs are the proteins involved in astringency perception. It should be noted that our mucin/PRP solutions may not be fully representative of actual saliva either. The effect of residual proteins, cells, and even residual food particles that are present in saliva currently remains unknown. These effects should be considered as cell-polyphenol interactions may occur and if residual foods contain proteins, these may be interacting with the surfaces, proteins, and polyphenols.

Particle interactions

For dry hard (glass) particles, surface – particle interactions (e.g. the contact area between the two) are enhanced by higher normal forces, enhanced surface roughness, decreased particle surface coverage, and smaller particle size (**Chapter 5**). These parameters all yield an increase in surface – surface interactions as well and, as such, lead to an increase in the overall friction coefficient. The frictional behaviour for such systems includes (I) a regime where sliding surface – surface interactions exist and (II) a regime where rolling ball-bearing particles lubricate the surfaces. When these glass particles are present in suspension, fluid – surface and fluid-particle interactions begin to play a role which was discussed in **Chapter 6**. It was previously shown that a fluid matrix can aid in the entrainment of particles by means of drag forces.[13] We altered the hydrophobicity of the suspended particles, the hydrophobicity of the fluid matrix, and the viscosity of the fluid matrix leading to three frictional regimes: (I) fluid dominated, (II) mixed fluid/particle dominated, and (III) particle dominated. The magnitude of the friction coefficient depends on the surrounding fluid, showing that fluid-particle and fluid – surface interactions should not be disregarded. To gain more insights into the role of the surfaces, surfaces with different hydrophobicity could be paired with the suspensions as well. To effectively study the contribution of surface-particle adhesion, magnetic particles/surfaces could be considered. Ideally, such surfaces and particles would

General Discussion

have controlled magnetic properties which can be achieved via a magnetic field.

For the densely packed hydrogel (gelatin) particles suspended in water, we found in **Chapter 4** that particle and surface properties were most dominant. Even for suspensions with low volume fractions, we did not observe a fluid (water) lubrication regime. This means particles were always entrained, even at low volume fractions, or loose gelatin polymers contributed to the lubrication as well. Due to applied forces, the particles are deformed, which leads to multiple regimes. The four lubrication regimes found here with increasing speeds, were related to (I) a limited number of particles with high surface – surface and surface particle interactions due to deformation leading to high friction coefficients, (II) An increasing number of particles, less deformation, and lower friction coefficients, (III) An increase in the friction coefficient was found due to the influx of particles which enhances particle-particle interactions, and (IV) an increase in gap size caused a large number of rolling particles to effectively lubricate the surfaces with limited particle-particle and surface-particle interactions.

Entrainment caused by tribometer mechanics

As we showed in **Chapter 8** by measuring hydrogel particles on four different tribological devices, only the Anton Paar tribometer (used in **Chapter 4**), gave four frictional regimes while only two regimes were seen for the other three tribometers. The exact frictional regimes found for soft particles between hard surfaces depend on the particle properties, surface properties, and on the tribometer used to measure the friction coefficients. This is an important finding for the tribological field, as it limits the possibility to compare results between various tribological devices, especially for more complex lubricants. A specific factor can perhaps be used to correct the tribological data from different devices and, ideally, obtain a master curve where results from different tribometers overlap.

Deformation-induced frictional regimes

When semi-solid surfaces and/or lubricants are in contact, deformation is inevitable. Surface and particle deformation give way to enhanced surface – surface, surface-particle, and particle-particle interactions which influence the friction coefficient. These deformation effects often lead to multiple frictional regimes. Due to surface deformation, the naturally rough hydrogels in **Chapter 2** transition from (I) a high friction regime where asperity contact dominates, to (II) a low friction regime when asperities are deformed (flattened) due to the increase in normal force. In **Chapter 5**, we use dry surfaces and dry lubricants (PDMS surfaces and

glass particles). Deformation effects gave way to two frictional regimes in this case: (I) a rolling particle regime with low friction coefficients and (II) a sliding surface regime with high friction coefficients. Good lubrication in this case depends on the ability of particles to roll over the surface while maintaining sufficient distance between the surfaces. Even when changing different components of the tribosystem (surface coverage, normal force, tribometer type), the friction coefficient still inversely scales with the effective gap size. In the case of these dry particles with dry surfaces, enhanced normal forces cause an increase in the friction coefficient rather than a decrease as was seen for fluid lubricated hydrogel surfaces.

The effect of soft surface deformation on the friction coefficient thus depends on the nature of the surface and the lubricant. For relatively hard surfaces lubricated by soft hydrogel particles in suspension (**Chapter 4**), strong effects of particle deformations exist as well. For high loads per particle (low volume fractions) the friction coefficient is higher than for low loads per particle. These trends are similar to the deformation trends for hard particles between soft surfaces. As we discussed in the previous section, four frictional regimes were observed for the hydrogel suspensions and these regimes depend on particle deformation as well. For these hydrogel particles, an increase in load was related to an increase in friction coefficient due to enhanced particle deformations. This is different again from hydrogel surfaces where a higher load gives lower friction coefficients.

Even when similar materials are used, entirely different mechanisms occur depending on the surrounding elements of the tribosystem. These inconsistencies add to the complexity of soft material friction. The deformation effects are also relevant for patterned surfaces. For patterned hydrogel surfaces (**Chapter 3**): an increasing height of the surface pillars caused bending deformation of the pillars, which increased the friction coefficient. The (bending) deformation of these relatively large asperities shows some similarities to hydrogel particle suspensions; a larger degree of deformation gives higher friction coefficients. To fully grasp the effect of deformation on the friction coefficient of hydrogel surfaces, surfaces with different degrees of hardness could be considered as well. For a less stiff surface, an even larger difference in deformation should be expected for tall pillars compared to short pillars. When using hard surfaces where no surface deformation is expected at all, the friction coefficient should then be independent of pillar height as the effective contact area remains the same. Larger contact areas between particles and surfaces as induced by deformation give higher friction coefficients. However, when surface deformation leads to the flattening of asperities, the friction coefficient decreases with increased deformation. We show a schematic representation of the

General Discussion

key mechanisms found for these soft surfaces and complex lubricants in Figure 9.4. The exact contribution of each mechanism to the friction coefficient will also greatly depend on the measuring conditions of the tribometer.

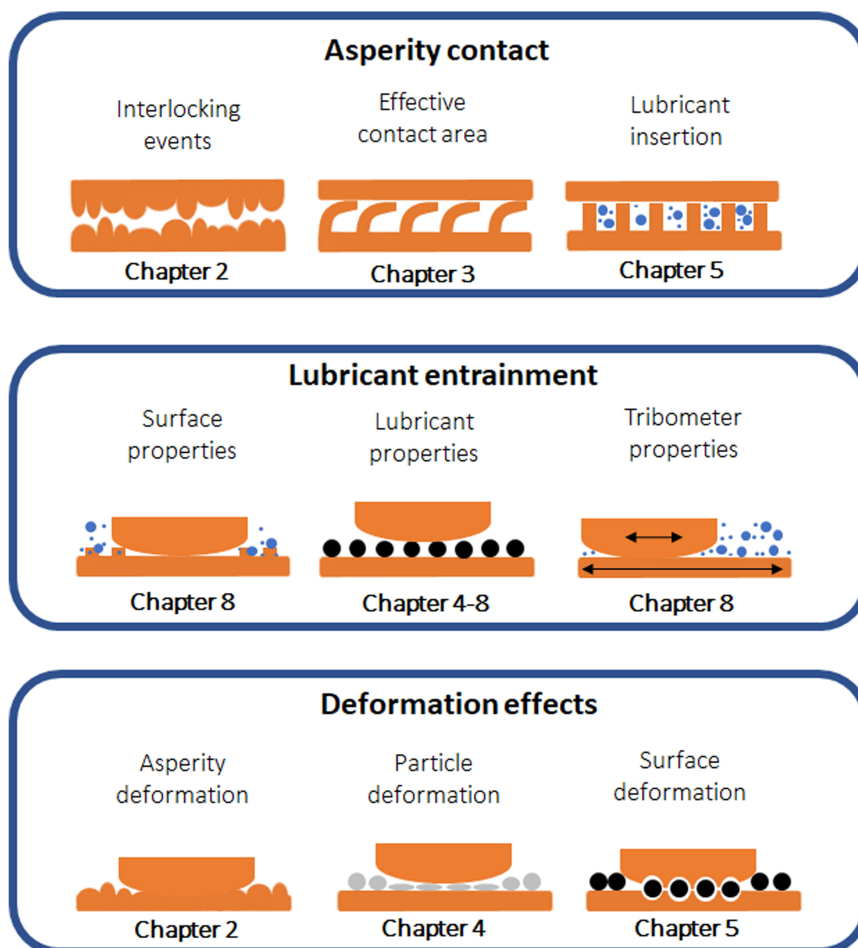


Figure 9.4: A visual representation of the three most important frictional mechanisms as we determined for soft surfaces and complex lubricants: (I) soft asperities influencing the contact mechanics and the hydrodynamics, (II) lubricant and surface properties lead to lubricant entrainment, (III) deformation of the surfaces or (semi-)solid lubricants. Each mechanism is displayed as it surfaces in the various chapters of this thesis.

Measuring friction on different tribometers

In this work, we had the advantage of having access to four tribometers: Anton Paar Tribocell, Bruker TriboLab, PCS Instruments Mini Traction Machine, and a custom-made, 3D-printed tribometer tool. We refer to these tribometers as APT, BTL, MTM, and CTT respectively. A detailed explanation of each tribometer was provided in **Chapter 8** where we combined all the tribometers in one study. We used the APT to measure hydrogel particle suspensions and salivary lubrication (**Chapters 4, 7**).

The APT ball-on-three-pins tribometer has a large speed range (0.05 – 500 mm/s), which allowed us to observe frictional regimes for complex lubricants that we were unable to capture on other devices. These frictional regimes were important for the way we interpreted particle suspension lubrication. The APT operates in a unidirectional sliding motion. Having the possibility to move the surface in two directions could give interesting new insights into the tribological properties of many systems as both wear and entrainment properties would change. This possibility exists with the linear reciprocating BTL tribometer.

The BTL was the tribometer of choice in **Chapter 5**, used to study dry glass particles. Although the tribometer has a limited speed range, it was still possible to observe a rolling particle and sliding particle regime for these glass particles. We also measured Newtonian fluids in **Chapter 8** and found differences in EHL-regime slope compared to other tribometers. The exact reason for this variation is not completely clear. Drag forces caused by the sliding drive that holds both the lubricant and the substrate appeared to contribute to this. The difference in EHL slope might also be related to the fact that this tribometer is not originally designed to accommodate soft surfaces. As such, effects that are of importance for soft surfaces, deformation or hysteresis, for example, may be measured erroneously simply as a friction force that contributes to the overall friction coefficient. An additional soft surface module for this tribometer better relate results with results obtained on other devices and existing theories, making the device more attractive for scientists studying soft materials and increase the ease with which comparisons between devices are made. For the dry glass particles, the surface coverage (number of particles on the surface) was an important parameter determining the friction coefficient. The flat, rectangular surface of the BTL was ideal for determining the number of particles on the surface. As the surface is placed flat in the container, no particles could roll or slide off the surface during measurement, which could happen when surfaces are at an angle.

General Discussion

The dry particles were also easily measured on the MTM as they could be placed on the relatively large flat substrate. The MTM has two rotating surfaces; a spherical probe and a disk-shaped substrate that is placed flat in the container that holds both the substrate and the fluid. In this case, the substrate is driven independently of the container. The speed of the probe with respect to the substrate can be varied (slide-to-roll ratio, SRR). This gives many options for the type of rotating motion, which influences fluid entrainment, contact type, and the overall friction coefficients. Surface sliding options include two surfaces rotating at the same speed in the same direction ($SRR = 0$) and one surface remaining stationary while the other surface rotates ($SRR = 2$). For dry particles, measurements with the MTM gave similar results as on the BTL when an SRR of 2 was used meaning one surface was in motion while the other was stationary. This type of motion is similar to that of the BTL which explains the similarities in friction coefficient. The MTM has a large speed range available (1 - 1000 mm/s). The main purpose of this device is to measure fluids, and limited possibilities exist when paste-like suspensions are used. When suspended particles were measured on the MTM, particles were removed from the contact by centripetal forces and we were limited to a speed range of 1 – 100 mm/s. This speed range is still far wider than for the CTT (1 and 20 mm/s) used to measure hydrogel friction in **Chapters 2 and 3**.

The CTT operates with a stationary flat substrate and a rotating probe inserted in an arm. The 3D-printed CTT is available at a fraction of the cost of most commercially available tribometers although a rheometer or other motorized device with a normal force sensor is required to operate the CTT. Such 3D-printed tools are practical when specific measuring characteristics are required or when limited funds are available. As the field of soft tribology continues to grow, we expect the emergence of more customized tribometers in the following years. However, efforts are still needed to effectively relate results from different tribometers to one another.

Lubrication curve for soft surfaces and complex lubricants

The various tribosystems described all display frictional regimes that depend on different factors including the velocity, normal force, (aggregated) particle size and fluid film thickness. Although different mechanisms are at play, ultimately there is one common variable dictating the friction coefficient of soft surfaces and complex lubricants: the gap size. We, therefore, present a lubrication curve where we summarize our main findings as function of the gap size (Figure 9.5).

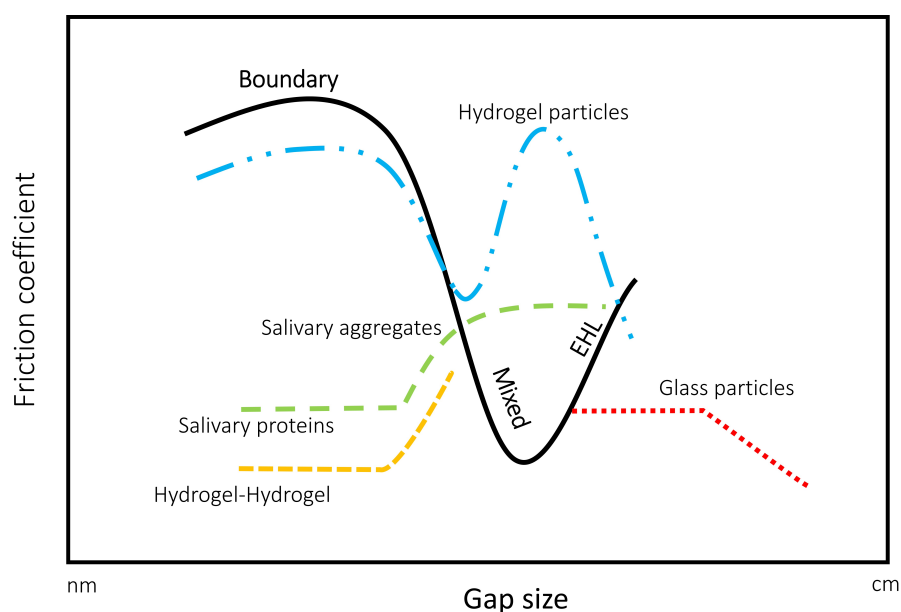


Figure 9.5: A schematic Stribeck curve for the soft surfaces and complex lubricants presented in this thesis. The friction coefficient is displayed as a function of the gap size. We show the traditional Stribeck curve (black), and lubrication curves for hydrogel-hydrogel friction (yellow), hydrogel particle suspensions (blue), salivary lubrication (green), and glass particles.

In this figure, the traditional Stribeck curve with its three gap-size dependent regimes are shown as a black curve. The different regimes as observed throughout this thesis are added to this figure as well. Hydrogel - hydrogel boundary friction is high at low normal forces and large gap sizes and decreases as the normal force increases and the gap size decreases as shown with the yellow dashed line in Figure 9.5. Hydrogel microparticle suspensions show four sliding regimes that are caused by the deformation of the particles as a result of the changes in gap size during measurement (blue dashed line). As we have shown, salivary proteins generate low friction coefficients (green dashed line). However, the friction coefficient increases when large aggregates are formed and the gap size increases. When glass particles (red dashed line) are present between the surfaces, the gap size is relatively large compared to the thickness of a fluid film. The friction coefficient decreases as the

General Discussion

gap size increases for example at lower normal forces, larger particle numbers and larger particle sizes. With the regular Stribeck regimes, an increase in the gap size is related to less surface – surface contact and decreases in the friction coefficient are found from the mixed to boundary regime. When using hydrogel surfaces, an increase in the gap size leads to the asperities resurfacing and an increase in the friction coefficient. The effect of the gap size on the friction coefficient thus depends on the type of contact between the surfaces. Whether the increase in the gap size gives way to an increase or decrease of the friction coefficient also depends on the nature of the surfaces and the components present in the lubricant. More rolling glass or hydrogel particles cause a decrease in the friction coefficient while a transition from biopolymer (saliva) lubrication to (non-spherical) particle lubrication causes an increase in the friction coefficient. The way in which the gap size influences the different systems demonstrates the complexity of the lubrication behavior of the systems studied here. More experimental and theoretical work is thus required in the field of soft tribology to fully untangle the interplay between different mechanisms that occur simultaneously. Developing a coherent physical picture to represent soft tribological parameters that predict the numerical value of μ , would be considered a large breakthrough in the field of soft tribology.

The future of food friction

The mechanisms behind food oral processing are rather challenging to comprehend and simulate. The recently awarded Nobel prize in physics on the topic of supermassive black holes, [27] suggests that we know more about events taking place thousands of light-years away than the processes inside our own mouths while eating. Making use of the key frictional concepts described in this thesis, some perspectives for the use of soft tribology in an applied context are provided.

Tribology in food science is often used to capture the friction between the soft, rough tongue and palate as lubricated by complex food systems during oral processing. [4, 5, 28–31] The friction coefficients obtained are often connected (in)directly to sensory attributes such as creaminess, fattiness, or graininess as perceived by a sensory panel. [25, 32, 33] To obtain better correlations between “man and machine”, a food tribometer is often designed to closely mimic the oral surfaces.[29, 32, 34] To accurately mimic the conditions and actions in the mouth during consumption, substrates must ideally be rough, hydrophobic, and subjected to a steady inflow of saliva. Swallowing could be represented by an outlet valve where the obtained “bolus” could be removed from the contact in a way that resembles food exiting the mouth by swallowing. Currently, different soft

surfaces are used in a food context while comparisons are made to the pillared tongue and ribbed palate. The use of surfaces and (model) lubricants that are analogous to the in-mouth surfaces and actual foods (emulsions, pastes, etc.) is also recommended. Furthermore, the measuring motions should also be selected such that the movement of the tongue is well represented.

As highlighted in this thesis, the aforementioned characteristics of a tribosystem strongly influence the frictional behavior. A schematic example of a potential mouth-mimicking tribometer that could be applied in food tribology is displayed in Figure 9.6. This tribometer includes a saliva inlet, a patterned tongue sliding surface, a rough palate stationary surface, a food sample, and an outlet for “processed” food. A food tribometer similar to the one suggested here makes it possible to study the dynamics during food oral processing as saliva secretion, bolus manipulation, and swallowing are mimicked here as well. This will further contribute to the development of new theories that predict and describe the lubrication dynamics involved in food oral processing.

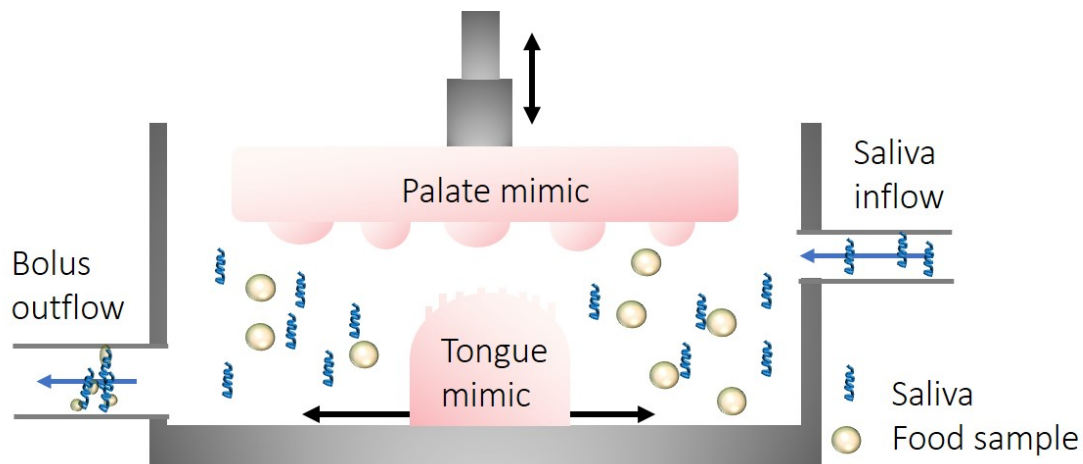


Figure 9.6: A schematic design of a potential mouth-mimicking tribometer. In this tribometer, the roughness of the tongue and palate, the movement of the tongue, the inflow of saliva, and the outflow of processed foods are represented.


Closing statements

Soft surface tribology is intrinsically different from hard, dry, solid tribology, and as such, different frictional laws apply. This thesis aimed to determine the key mechanisms that are involved in soft tribology. Using a broad range of surfaces, lubricants, and tribological devices three main mechanisms that drive the lubrication behavior of many of soft sliding systems were identified: (I) the nature of the asperity contact, (II) the ability of a lubricant to be entrained into the contact zone as caused by the surface-fluid-particle interactions, and (III) the deformation of the surfaces or soft-solid lubricants. For rough surfaces, friction is caused by interlocking effects and enlarged contact areas. The friction coefficient can thus be controlled by means of the polymer network, asperity properties, and the applied normal force. In the case of lubricant entrainment, friction is dominated by surface – surface contact, lubricant viscosity and polarity, and particle properties such as size, hardness and hydrophobicity. Varying the surface – fluid – particle dynamics offers a wide range of friction coefficients and frictional regimes where different parameters dominate. Many soft lubrication mechanisms thus exist and the dominant mechanism depends on the exact design of the tribosystem, including the type of tribometer, surfaces, and lubricant used. This makes it challenging to currently state concrete frictional laws for soft solid friction. However, for the systems used here, the frictional regimes all emerge at a critical gap size. The findings presented in this thesis in predicting results for newly fabricated tribosystems and in more specifically formulating follow up research questions to provide solutions that allow advances in science, industry, and society.

References

1. Stribeck, R. Die wesentlichen eigenschaften der gleit-und rollenlager. *Zeitschrift des Vereines Deutscher Ingenieure* vol. 46, 1341–1348 (1902).
2. Lu, X., Khonsari, M. & Gelinck, E. The Stribeck curve: experimental results and theoretical prediction (2006).
3. Bongaerts, J., Fourtouni, K. & Stokes, J. Soft-tribology: lubrication in a compliant PDMS–PDMS contact. *Tribology International* vol. 40, 1531–1542 (2007).
4. Rudge, R. E. D., Scholten, E. & Dijkman, J. A. Advances and challenges in soft tribology with applications to foods. *Current Opinion in Food Science* vol. 27, 90–97 (2019).
5. Campbell, C. L., Foegeding, E. A. & van de Velde, F. A Comparison of the lubrication behavior of whey protein model foods using tribology in linear and elliptical movement. *Journal of texture studies* vol. 48, 335–341 (2017).
6. Garrec, D. A. & Norton, I. T. Kappa carrageenan fluid gel material properties. Part 2: Tribology. *Food Hydrocolloids* vol. 33, 160–167 (2013).
7. Urueña, J. M. *et al.* Mesh size control of polymer fluctuation lubrication in gemini hydrogels. *Biotribology* vol. 1, 24–29 (2015).
8. Pitenis, A. *et al.* Polymer fluctuation lubrication in hydrogel gemini interfaces. *Soft Matter* vol. 10, 8955–8962 (2014).
9. Bongaerts, J., Rossetti, D. & Stokes, J. The lubricating properties of human whole saliva. *Tribology Letters* vol. 27, 277–287 (2007).
10. Selway, N., Chan, V. & Stokes, J. R. Influence of fluid viscosity and wetting on multiscale viscoelastic lubrication in soft tribological contacts. *Soft Matter* vol. 13, 1702–1715 (2017).
11. Deng, F., Tsekenis, G. & Rubinstein, S. M. Simple law for third-body friction. *Physical Review Letters* vol. 122, 135503 (2019).
12. Cho, K. *et al.* The size effect of zircon particles on the friction characteristics of brake lining materials. *Wear* vol. 264, 291–297 (2008).
13. Yakubov, G., Branfield, T., Bongaerts, J. & Stokes, J. Tribology of particle suspensions in rolling-sliding soft contacts. *Biotribology* vol. 3, 1–10 (2015).
14. Wang, S., Mantilla, S. M. O., Smith, P. A., Stokes, J. R. & Smyth, H. E. Astringency sub-qualities drying and pucker are driven by tannin and pH–Insights from sensory and tribology of a model wine system. *Food Hydrocolloids* vol. 109, 106109 (2020).
15. Sarkar, A., Goh, K. K. & Singh, H. Colloidal stability and interactions of milk-protein-stabilized emulsions in an artificial saliva. *Food Hydrocolloids* vol. 23, 1270–1278 (2009).
16. Prinz, J., De Wijk, R. & Huntjens, L. Load dependency of the coefficient of friction of oral mucosa. *Food Hydrocolloids* vol. 21, 402–408 (2007).
17. De Vicente, J., Stokes, J. & Spikes, H. Rolling and sliding friction in compliant, lubricated contact. *Proceedings of the Institution of Mechanical Engineers, Part J: Journal of Engineering Tribology* vol. 220, 55–63 (2006).
18. Kanca, Y., Milner, P., Dini, D. & Amis, A. A. Tribological properties of PVA/PVP blend hydrogels against articular cartilage. *Journal of the Mechanical Behavior of Biomedical Materials* vol. 78, 36–45 (2018).

19. Wang, X., Wang, X., Upadhyay, R. & Chen, J. Topographic study of human tongue in relation to oral tribology. *Food Hydrocolloids* vol. 95, 116–121 (2019).
20. Müller, M., Lee, S., Spikes, H. A. & Spencer, N. D. The influence of molecular architecture on the macroscopic lubrication properties of the brush-like co-polyelectrolyte poly (L-lysine)-g-poly (ethylene glycol)(PLL-g-PEG) adsorbed on oxide surfaces. *Tribology Letters* vol. 15, 395–405 (2003).
21. Simič, R., Yetkin, M., Zhang, K. & Spencer, N. D. Importance of hydration and surface structure for friction of acrylamide hydrogels. *Tribology Letters* vol. 68, 64 (2020).
22. Peng, D., Kang, Y., Hwang, R., Shyr, S. & Chang, Y. Tribological properties of diamond and SiO₂ nanoparticles added in paraffin. *Tribology International* vol. 42, 911–917 (2009).
23. Farias, B. V., Haeri, F. & Khan, S. A. Linking polymer hydrophobicity and molecular interactions to rheology and tribology in phospholipid-containing complex gels. *Journal of Colloid and Interface Science* vol. 584, 134–144 (2020).
24. Li, A., Ramakrishna, S. N., Kooij, E. S., Espinosa-Marzal, R. M. & Spencer, N. D. Poly (acrylamide) films at the solvent-induced glass transition: adhesion, tribology, and the influence of crosslinking. *Soft Matter* vol. 8, 9092–9100 (2012).
25. Krop, E. M., Hetherington, M. M., Holmes, M., Miquel, S. & Sarkar, A. On relating rheology and oral tribology to sensory properties in hydrogels. *Food Hydrocolloids* vol. 88, 101–113 (2019).
26. Mystkowska, J. *et al.* Artificial mucin-based saliva preparations—Physicochemical and tribological properties. *Oral Health Prev. Dent* vol. 16, 183–193 (2018).
27. Schirber, M. Nobel Prize: Facing the Reality of Black Holes. *Physics* vol. 13, 158 (2020).
28. Shewan, H. M., Pradal, C. & Stokes, J. R. Tribology and its growing use toward the study of food oral processing and sensory perception. *Journal of Texture Studies* vol. 51, 7–22 (2020).
29. Dresselhuis, D. M. *et al.* Tribology of o/w emulsions under mouth-like conditions: determinants of friction. *Food Biophysics* vol. 2, 158–171 (2007).
30. Kim, M. S. *et al.* Adapting tribology for use in sensory studies on hard food: The case of texture perception in apples. *Food Quality and Preference* vol. 86, 103990 (2020).
31. Zhang, B. *et al.* Tribology of swollen starch granule suspensions from maize and potato. *Carbohydrate polymers* vol. 155, 128–135 (2017).
32. Fuhrmann, P. L., Aguayo-Mendoza, M., Jansen, B., Stieger, M. & Scholten, E. Characterisation of friction behaviour of intact soft solid foods and food boli. *Food Hydrocolloids* vol. 100, 105441 (2020).
33. Van Eck, A. *et al.* Sauce it up: influence of condiment properties on oral processing behavior, bolus formation and sensory perception of solid foods. *Food & Function* vol. 11, 6186–6201 (2020).
34. Andablo-Reyes, E. *et al.* 3D Biomimetic Tongue-Emulating Surfaces for Tribological Applications. *ACS applied materials & interfaces* vol. 12, 49371–49385 (2020).



Summary/ Samenvatting

Summary

The friction between materials is an important aspect in any field where soft solids in contact are considered. One can think of engineering machinery, medical devices and food oral processing. Understanding the frictional or tribological behavior of specific combinations of materials and lubricants, allows for the design of new materials that have the ability to improve our daily lives. While friction of solid materials has been studied for centuries, soft solid friction is a relatively new area of study. Soft materials show complex frictional behavior due to the deformable nature of the surfaces, which leads to changes in contact areas and lubricant entrainment. A need thus exists for an enhanced comprehension of such soft materials, specifically, when paired with non-Newtonian lubricants. We approached this challenge by using soft surfaces with different degrees of deformability and by varying the surface roughness of the surfaces. To unravel the complex mechanisms behind soft tribology, soft surfaces were combined with various lubricants ranging from Newtonian fluids to dry solid particles and particle suspensions. These different surface and lubricant combinations allowed us to identify different frictional regimes. These frictional regimes are mainly caused by changes in velocity, roughness, polymer properties and deformability. All the aforementioned triboparameters cause changes in the gap size between the interacting surfaces which strongly impacts the frictional dynamics.

In **Chapter 2**, hydrogel surfaces with different degrees of roughness were used. We manipulated the surface roughness of the hydrogels by using different polymer materials and by using roughened molds. These hydrogels displayed two frictional regimes: (I) a high friction regime at low normal forces and (II) a low friction regime at high normal forces. The second regime emerges as the surface asperities are flattened at higher normal forces. The friction in the first regime is influenced by the polymer network type, the surface roughness and the hydrogel modulus. The friction coefficient in the second regime only depends on the hydrogel modulus as the asperities no longer influence the friction coefficient.

We proceeded to use hydrogel surfaces in **Chapter 3**. In this chapter, we systematically varied the surface roughness of the hydrogels. We used 3D-printed molds to obtain hydrogels with pillars on the surface that differed in height, diameter and distance between the pillars. Additionally, the type of pattern on the surface was changed from a square lattice to a star-shaped pattern. Results obtained using different surface designs, showed that the friction coefficient increases with increasing contact area and with increasing effective height. Hydrogel-hydrogel friction is thus not intrinsically low, but depends on the specific surface roughness parameters.

In **Chapter 4**, we transition from hydrogel surfaces to hydrogel particles. These hydrogel particles in suspension are efficient lubricants as they provide ball-bearing lubrication. The magnitude of the friction coefficient depends on the particle size, modulus and volume fraction. For these hydrogel particle suspensions, we observed four different frictional regimes, different from the three frictional regimes traditionally found for Newtonian lubricants. Using different surface types and particle types, we unveiled that the four regimes are caused by changes in gap size, which influences particle deformation. This deformation alters the rolling/sliding mechanisms and, with that, the friction coefficient in each regime.

The impact of rolling and sliding behavior on the friction coefficient was further highlighted in **Chapter 5** by using dry glass particles between polydimethylsiloxane (PDMS) surfaces. For this third-body frictional system, we find a rolling and a sliding frictional regime. When the gap size is large due to large particle sizes, at low normal forces and high surface coverage, the friction coefficient is low as particles are able to roll. However, when the gap size decreases and surfaces are able to directly slide against one another, the friction coefficient increases. By introducing an additional tribometer, we showed that the rolling/sliding motion of the surfaces influences the friction coefficient as well. In this chapter, it was concluded that the friction coefficient increases with decreasing gap size.

Glass particles were again used in **Chapter 6**. In this chapter, the hydrophobic glass particles were suspended in polar and non-polar fluid matrices with different viscosities. The results in this chapter show that fluid – particle interactions are the most important driving factor behind particle entrainment. When fluids are unable to wet the particles, particles remain entrained constantly. However, good fluid – particle wetting makes it possible for the fluid to drag the particles in and out of the contact zone.

Particles are also readily entrained when the matrix fluid is viscous enough to provide increased hydrodynamic pressure and separate the surfaces, making it possible for particles to enter the gap. Overall, for these particle suspensions with relatively large particles, a fluid-dominated frictional regime exists as well as a particle-dominated frictional regime. Particle lubrication dominates in the cases of high particle volume fractions, poor fluid – particle wetting, high fluid viscosity and large velocities. In all of these situations the gap size is relatively large as caused by the particles or by the surrounding fluids.

In **Chapter 7**, the tribological findings were related to in-mouth lubrication. We used saliva and salivary proteins (mucins and proline-rich proteins (PRPs)) and combined these biopolymers with compounds that are known to evoke an astringent mouthfeel: large polyphenols, small phenols and a metal salt. In this chapter, it was shown that astringency for large polyphenols is directly related to lubrication losses. Large polyphenols precipitate both mucins and PRPs which then lose their good lubricating properties. Metal salts are able to aggregate with mucins. However, this is not enough to induce lubrication losses as the PRP layer appears to be an important lubricating layer. Small phenols are unable to aggregate saliva and salivary proteins and, as such, are unable to cause changes in the friction coefficient. Besides showing the relationship between astringency perception and lubrication, we also introduced methods to reduce or remove astringency all together: (I) the addition of a viscous solvent causing viscous lubrication to dominate particle (aggregate) friction and (II) the addition of molecules that prevent protein-polyphenol interactions and lubrication losses.

As became clear from **Chapters 2-7**, the friction coefficient is a system parameter that depends on the surfaces as well as the lubricants and tribometer settings used. What influence does the tribometer motion have on the friction coefficient? This was the main research question of **Chapter 8**, where the four different tribometers used throughout the thesis were compared to one another. Three commercially-available tribometers and one tribometer that was designed and 3D-printed in-house were used in this chapter, all with surfaces with different degrees of roughness. For Newtonian fluids (water and glycerol), the boundary regime as well as the mixed regime are influenced by the surface roughness and the tribometer motion. The elastohydrodynamic (EHL) regime is mainly influenced by the fluid viscosity. However, in specific cases surface roughness and tribometer motion causes changes in the slope in the EHL regime. Besides Newtonian lubricants we also use hydrogel particle suspensions and find multiple frictional regimes on all tribometers. These frictional regimes are specific for each tribometer.

It was concluded that it is not possible to compare results obtained using different tribometers for these complex suspensions.

By examining different surfaces, lubricants and tribometers, a better understanding of frictional processes in general and of soft lubrication specifically was provided. The knowledge presented in this thesis is now available for food scientists, biomedical engineers and other soft material scientists to use to better interpret (biological) frictional processes and to create a new class of materials that industry and society will benefit from in the near future.

Samenvatting

De wrijving tussen materialen is van belang in elk veld waar zachte materialen met elkaar in contact zijn. Dit is het geval bij technische apparatuur, medische apparaten en bij het verwerken van eten in de mond. Met een beter begrip van de wrijvings- of tribologische mechanismen van verschillende oppervlakken en glijmiddelen, kunnen nieuwe materialen worden ontwikkeld die ons dagelijks leven kunnen vereenvoudigen. De wrijving van harde materialen wordt al eeuwenlang onderzocht maar de wrijving van zachtere materialen is een relatief nieuw onderzoeksveld. Zachte materialen hebben complex wrijvingsgedrag vanwege de vervormbare oppervlakken die zorgen voor veranderingen in het contactoppervlak en in het entraineren en includeren van het glijmiddel. Het is dus van belang dat er een beter begrip wordt gecreëerd van het wrijvingsgedrag van dit soort zachte materialen, vooral in combinatie met niet-Newtoniaanse glijmiddelen. Wij zijn deze uitdaging aangegaan door middel van het gebruik van zachte oppervlakken met verschillende hardheden en verschillende oppervlakte ruwheden. Om de complexiteit achter de zachte tribologische mechanismen beter te begrijpen, hebben we zachte oppervlakken gecombineerd met verschillende glijmiddelen van Newtoniaanse vloeistoffen tot droge harde deeltjes en deeltjes suspensies. Deze verschillende combinaties van oppervlakken en glijmiddelen, leidden tot verschillende wrijvingsregimes. Deze regimes ontstaan door veranderingen in snelheid, ruwheid, polymeereigenschappen en vervormbaarheid. Deze *triboparameters* zorgen voor veranderingen in de ruimte tussen de twee oppervlakken en dit heeft een belangrijke invloed op de wrijvingsdynamiek.

In **Hoofdstuk 2** is er gebruikt gemaakt van hydrogels met verschillende ruwheden op het oppervlak. De ruwheid van de hydrogels is aangepast door verschillende polymeermaterialen te gebruiken en door gebruik te maken van ruwe mallen. De hydrogels vertonen twee wrijvingsregimes: (I) een regime met hoge wrijving bij lage normaalkrachten en (II) een regime met lage wrijving bij hoge normaalkrachten. Het tweede regime ontstaat wanneer de oppervlakte ruwheid wordt platgedrukt bij hogere normaalkrachten. De wrijving in het eerste regime wordt beïnvloed door het type polymeer netwerk, de ruwheid van het oppervlak en de

modulus van de hydrogel. De wrijvingscoëfficiënt in het tweede regime is slechts afhankelijk van de hydrogel modulus aangezien de ruwheid niet langer van invloed is op de wrijvingscoëfficiënt.

We hebben ook gebruik gemaakt van hydrogel oppervlakken in **Hoofdstuk 3**. In dit hoofdstuk, veranderden we de ruwheid van de hydrogel oppervlakken systematisch. Met behulp van 3D geprinte mallen hebben we hydrogels gemaakt met pilaartjes op het oppervlak en de pilaartjes variëren in hoogte, diameter en afstand tussen de pilaartjes. De pilaartjes zijn geplaatst in een vierkant matrix en een stervormig patroon op het oppervlak. De vergaarde resultaten met oppervlakken met verschillende patronen toonden aan dat de wrijvingscoëfficiënt stijgt met toenemende contactoppervlakken en effectieve hoogte van de pilaartjes. Hydrogel-hydrogel frictie is dus niet intrinsiek laag, maar hangt af van de specifieke ruwheid van het oppervlak.

In **Hoofdstuk 4** gaan we over van hydrogel oppervlakken naar hydrogel deeltjes. Deze hydrogel deeltjes suspensies zijn efficiënte glijmiddelen door middel van een kogellager-achtige lubricatie. De omvang van de wrijvingscoëfficiënt hangt af van de deeltjesgrootte, modulus en volumefractie. Voor deze hydrogel deeltjes suspensies hebben we vier wrijvingsregimes geobserveerd, afwijkend van de drie wrijvingsregimes die bekend zijn voor Newtoniaanse glijmiddelen. Met behulp van verschillende oppervlakken en deeltjestype hebben we onthuld dat de vier regimes veroorzaakt worden door veranderingen in tussenruimte wat de vervorming van de deeltjes beïnvloedt. Deze vervorming verandert het rol/glijmechanisme en, daarmee, de wrijvingscoëfficiënt in de verschillende regimes.

Het gevolg van het rol- en glijgedrag op de wrijvingscoëfficiënt is verder onderzocht met glas deeltjes tussen polydimetylsiloxaan (PDMS) oppervlakken in **Hoofdstuk 5**. Voor dit wrijvingssysteem hebben we een rol en een glij wrijvingsregime gevonden. Wanneer de tussenruimte vergroot is door de grootte van de deeltjes, bij lage normaalkrachten en hoge oppervlaktebedekkingen is de wrijvingscoëfficiënt laag doordat de deeltjes kunnen rollen. Echter, wanneer de tussenruimte kleiner wordt en de oppervlakken direct in contact komen, stijgt de wrijvingscoëfficiënt. Aan de hand van een tweede tribometer toonden we aan dat de rol/glijbeweging van de oppervlakken de wrijvingscoëfficiënt mede beïnvloedt. In dit hoofdstuk, concluderen we dat de wrijvingscoëfficiënt stijgt wanneer de grootte van de tussenruimte daalt.

In **Hoofdstuk 6** werd er wederom gebruik gemaakt van glas deeltjes. In dit hoofdstuk, is er een suspensie gemaakt van hydrofobe deeltjes in polaire en apolaire matrix vloeistoffen met verschillende viscositeiten. De resultaten in dit hoofdstuk tonen aan dat vloeistof – deeltjes interacties de belangrijkste drijvende kracht zijn achter het entraineren van deeltjes tussen de oppervlakken. Wanneer de vloeistof de deeltjes slecht kan bevochtigen, blijven de deeltjes tussen de oppervlakken. Echter, wanneer de vloeistof de deeltjes wel kan bevochtigen, kunnen de deeltjes in en uit de contactzone worden gesleept. Deeltjes kunnen gemakkelijk tussen de oppervlakken terechtkomen wanneer de matrix vloeistof visceus genoeg is om hydrodynamische druk te leveren die de oppervlakken uit elkaar duwt zodat de deeltjes tussen de oppervlakken terecht kunnen komen. Voor deze deeltjes vinden we een wrijvingsregime dat wordt gedomineerd door lubricatie door vloeistoflubricatie regime dat wordt gedomineerd door deeltjeslubricatie. Deeltjeslubricatie komt voor wanneer er een hoge deeltjes volume fractie wordt gebruikt, wanneer de vloeistof de deeltjes slecht bevochtigt, bij vloeistoffen met een hoge viscositeit en bij hoge snelheden. In deze gevallen is de tussenruimte relatief groot als gevolg van de deeltjes- of vloeistofeigenschappen.

In **Hoofdstuk 7**, werden de tribologische metingen gerelateerd aan binnensmondslubricatie. We gebruikten speeksel en eiwitten uit speeksel (mucines en proline-rijke eiwitten (PRPs)) en combineerden deze biopolymeren met componenten die bekendstaan om hun wrange, droge mondgevoel: grote polyfenolen, kleine fenolen en een metaalzout. In dit hoofdstuk, is aangetoond dat het wrange mondgevoel voor grote polyfenolen direct gerelateerd is aan lubricatieverlies. De grote polyfenolen precipiteren mucines en PRPs die als gevolg daarvan hun goede lubricatie-eigenschappen verliezen. Metaalzouten kunnen met mucines aggregeren. Dit is echter niet genoeg om lubricatieverlies te veroorzaken aangezien de PRP laag de belangrijkste lubricatielaag blijkt te zijn. Kleine fenolen kunnen speeksel en de eiwitten in speeksel niet precipiteren en zorgen ook niet voor veranderingen in speeksellubricatie. Naast de relatie tussen wrijving en wrangheid aan te hebben getoond, hebben we ook enkele methoden geïntroduceerd om het wrange mondgevoel te bestrijden: (I) het toevoegen van een visceuze vloeistof waarbij viscuezelubricatie het overneemt van deeltjes(aggregaten)wrijving en (II) het toevoegen van moleculen die eitwit-polyfenol interacties en daarmee lubricatieverlies tegengaan.

Zoals we aangetoond hebben in **Hoofdstukken 2-7** is de wrijvingscoëfficiënt een systeemp parameter die afhangt van zowel de oppervlakken als van de glijmiddelen en de tribometerinstellingen. Hoe beïnvloedt de beweging van de tribometer de wrijvingscoëfficiënt? Dit was de belangrijkste onderzoeksvraag van **Hoofdstuk 8** waar de vier tribometers die in de verschillende hoofdstukken zijn gebruikt, met elkaar werden vergeleken. In dit hoofdstuk hebben we drie commercieel beschikbare tribometers en een zelfgemaakte 3D geprinte tribometer gebruikt met oppervlakken met verschillende ruwheden. Voor Newtoniaanse vloeistoffen wordt het wrijvingsgedrag in het grens wrijvingsregime en in het gemengde wrijvingsregime beïnvloed door de ruwheid en de manier waarop de tribometer de oppervlakken beweegt. Het gedrag in het elastohydrodynamische (EHL) regime wordt vooral beïnvloed door de viscositeit van de vloeistof. In bepaalde gevallen beïnvloeden de ruwheid van het oppervlak en de beweging van de tribometer de helling in het EHL regime. Wanneer we suspensies van hydrogel deeltjes gebruiken, vinden we verschillende wrijvingsregimes op de verschillende tribometers. De wrijvings regimes zijn specifiek voor de tribometer die gebruikt is voor het meten. Concluderend is het niet mogelijk om resultaten die vergaard zijn op verschillende tribometers met elkaar te vergelijken wanneer er complexe suspensies gemeten worden.

Door gebruik te maken van verschillende oppervlakken, glijmiddelen en tribometers, zijn er nieuwe inzichten geleverd voor wrijvingsprocessen in het algemeen en voor zachte materialen lubricatie in het bijzonder. De kennis die gepresenteerd is in dit proefschrift is nu beschikbaar voor levensmiddelenwetenschappers, biomedische technologen en andere materiaalkundigen die zich specialiseren op het gebied van zachte materialen om een beter inzicht te krijgen in (biologische) wrijvingsprocessen en om nieuwe materialen te ontwerpen waar de industrie en de maatschappij van kunnen profiteren in de nabije toekomst.



Appendix

List of publications
Acknowledgements
About the author
Completed training activities

Publications in this thesis

Rudge, R.E.D., Scholten, E., and Dijkman, J.A. (2019). Natural and induced roughness determine frictional regimes in hydrogel pairs. *Tribology International* vol. 141, 105903. (Chapter 2)

Rudge, R.E.D., Scholten, E., and Dijkman, J.A. Is there a pattern? Frictional properties of micro-patterned hydrogel., *Submitted for publication* (Chapter 3)

Rudge, R.E.D., Van de Sande, J.P., Dijkman, J.A., and Scholten, E. (2020). Uncovering friction dynamics using hydrogel particles as soft ball bearings. *Soft Matter* vol. 16, no. 15, 3821–3831. (Chapter 4)

Rudge, R.E.D., Theunissen, K., Stokes, J.R., Scholten, E., and Dijkman, J.A. (2021), Tribology of hard particles lubricating soft surfaces., Tribology of hard particles lubricating soft surfaces., *Physical Review Materials*, *Accepted* (Chapter 5)

Rudge, R.E.D., Shewan, H.M., Stokes, J.R., Dijkman, J. A. Scholten, E., Lubrication properties of hard particle suspensions between soft surfaces., *Manuscript in preparation* (Chapter 6)

Rudge, R.E.D., Fuhrmann, P.L., Scheermeijer, R., Van der Zanden, E.M., Dijkman, J.A. Scholten, E., A tribological approach to astringency perception and astringency prevention., *Submitted for publication* (Chapter 7)

Rudge, R.E.D., Mosselman, M.J., Shewan, H.M., Stokes, J.R., Dijkman, J.A. Scholten, E., Soft lubrication using four different tribometers., *Manuscript in preparation* (Chapter 8)

Other publications

Rudge, R.E.D., Scholten, E., and Dijksman, J. A. (2019). Advances and challenges in soft tribology with applications to foods. *Current Opinion in Food Science* vol. 27, 90–97.

Saez Talens, V., Davis, J., Wu, C.H., Wen, Z., Lauria, F., Gupta, K.B.S.S., **Rudge, R.E.D.**, Boraghi, M., Hagemeijer, A., Trinh, T.T. and Englebienne, P., 2020. Thiosquaramide-Based Supramolecular Polymers: Aromaticity Gain in a Switched Mode of Self-Assembly. *Journal of the American Chemical Society*, 142(47), pp.19907-19916.

Acknowledgements

Waw! I can't believe four years flew by just like that. During the past four years I have had the opportunity to meet and work with some amazing people and I will always look back at these four years with a big smile.

I could not have started or completed any of the work in this thesis without the support of my supervisors. Elke, thank you for always having your door open to me, whether it was for a deep scientific conversation, a bad pun or to organise our monthly "borrels". You have been a constant source of inspiration and motivation to me! Joshua, you have taught me many things probably without even realising it. From public speaking tricks, to linguistic skills. Thanks for always bringing your sense of humor to every meeting.

Jason and Heather, thank you for having me as a visiting PhD for much longer than we all expected. It has been a great learning experience.

A big thanks to the talented students I supervised: Annejet, Evi, Florence, Ilse, Jesse, Judith, Karlijn, Marion, Melissa, Merijn, Roos, Sera, Sybren. You have all made huge contributions to my thesis, both in and out of the lab and I will be forever grateful for that.

I would also like to thank the lovely members of the PCC and FPH secretariat for taking care of the administrative side of things. Els, Leonie en Mara, hartstikke bedankt voor alle 10000000 reminders. Ze waren hard nodig!

There are a lot more people who have contributed to the general good vibes during my PhD and I would like to thank them as well.

@FPH PhDs So much spam, so little time. You have all been great colleagues and even better friends. Has anyone booked Bornsesteeg for the next Christmas dinner? #Gourmet #hotpot #yellowcake

@PCC What a special bunch of people. Please keep reminding the world that you can be fun and smart at the same time! Thanks for always making sure there was enough juicy gossip and scientific achievements to post on the PCC screen. #kerstborrel #watiseenfysko? #hasanyoneseenmypipet?

@Labchat The puns and interesting scientific content often kept me going during long lab days. Keep up the good work and the excitement. Thanks for waking up early so I could still join the fun while I was in Australia. #nerds #butfunnerds #butnerds

@TriboTeam *Knock knock* Who's there? "Friction, lubrication and wear."... Thank you for all the patience and the feedback during the tribomeetings. I learned a lot from all of you! #boundary #mixed #hydrodynamic

@StokesLab Thanks to all of you for making me feel welcome in Australia. Your hospitality has been so amazing that I never want to leave! #UQlife #Downunder #VeL

@LabLadies You have been really great office mates, colleagues and friends during the past year! I hope we get to have a lot more lunches/dinners and other meals together and that the turkeys and magpies stay away from our food. #FunFoodFriday #PizzaCaffe #Poutine

@Fascinating Food Friends Super trots op ons dat we onze PhDs (bijna) hebben! Bedankt voor de vele fascinerende en memorabele momenten. #FFF #Leeds #posteroforal?

@bonenkruid Ik heb echt zoveel van jullie geleerd en zoveel met jullie gelachen. Elke keer als een van jullie klaar was met hun PhD heb ik een klein traantje gelaten. Gelukkig bleven we elkaar nog vaak zien :) #Gourmet #PeppaPig #Koningshof

@Cool party kids @the back Thanks for adopting me and letting me DJ at your awesome events. #CofFPEcorner #PalmIntocht #Woeste

@Fancy Ladies Probably the smartest, most elegant and classy ladies I have ever met. I am so grateful for everything you have taught me and I am happy to see you all shine!

@DJ Ryzen Zoveel gigabytes aan screenshots en voice messages. Wie had ooit verwacht dat wij een PhD zouden doen?? Wij. Je bent een topper en ik had het nooit zonder jou kunnen doen. Succes met het afronden van jouw PhD #BFFs #blackandyellow #helemaaldoorgeslagen

@I'm so excited! Thanks for all the awesome road trips and other fun adventures we went on. I can't believe we're all grown up now.... #BESTies #Arabesque #WillstDu

@Singapore & Indonesia Terimakasih! The PhD trip was a really great way to get to know you all and I'm glad we got to go through the experience together. Thanks for not leaving me behind in the Indonesian jungle. #RumahDongengPelangi #teamnosleep #Marinabay

@Laagh weekend 2027 Echt top al die weekendjes weg elk jaar! Nu al zin in 2027! #Ongelooflijk #zinin #KLMLounge

@Marly's Angels I am so lucky to have encountered you here in Australia. Thanks to you my experience here has been unforgettable. Sorry for using all the internet for my nerdy meetings... #TealPalace #Ecstaticdance #besthousematesever

@Business Class I'm not sure where we're flying to but I'm pretty sure we're going to have an awesome time. You guys are my favorites! #Octoberfest #Broccoli #Pri

@Mama Roke Thank you for being an amazing mother and for being way more interested and involved in my PhD than I ever expected. Thank you for all the life lessons and for always pushing me to invest in my education and personal development. #Sterkevrouwen #winnenwinnenwinnen

@Jeson Dankjewel voor alle motiverende woorden en alle slechte grappen! Ondanks dat we nu nog verder weg van elkaar wonen waardeert ik je steun enorm! #bestlittlebrotherever

@Papa Bedankt dat je altijd voor me klaar staat en bedankt dat je vaak interesse toonde in mijn PhD en alles er omheen.

@Paranymphs Nic and Sian, thanks heaps for being my paranymphs. You are both legends! #thanksmates #freshfeelz #faveaussies

Also a big thanks to Claudine and Melika for being my honorary paranymphs and helping to make my PhD defense unforgettable from across the globe! #Dankie #TashakkorMikonam

I would also like to thank all my friends, colleagues, cousins, aunts, uncles and other family members for their support. I hope to stay in touch and to continue making you proud!

@Sian You were definitely one of my most *interesting* discoveries during my PhD... Thank you for being caring and patient, especially in last the months of the PhD. Your enthusiasm, excitement and sense of humour kept me going! Together we can conquer the world, but let's start with Australia. #Roadtrip #Funemployed #Couplegoals

About the author

Raisa Earedice Dorien Rudge, was born in Amsterdam on March 23rd 1992. She obtained her high school degree (VWO) in 2009 from Colegio Arubano on the island of Aruba. After that, she proceeded to study Leiden University and Delft University of Technology where she completed her Bachelor's degree in Molecular Science and Technology with a major in Chemistry and a minor in Italian Language and Culture. For her Master's degree she remained at Leiden University where she studied Chemistry with a specialisation in research and supramolecular chemistry. As part of her master's degree, Raisa took elective courses in Food Technology at Wageningen University and Research as well as Research Based Business courses at Leiden University. She completed an exchange period at Universitat Politècnica de València (Spain) and at Universidad de Valladolid (Spain) where she partook in courses on materials' science and food technology.

After she completed her master's degree in 2016, she started her PhD at Physics & Physical Chemistry of Foods and Physical Chemistry & Soft Matter at Wageningen University & Research. From 2020 to 2021 Raisa was a visiting PhD student at The University of Queensland, Australia at the Rheology and biolubrication group. This thesis entitled "A slip of the tongue — Tribology of soft surfaces and complex lubricants" is the result of the work performed during her PhD.

Raisa currently remains in Australia, where she aspires to proceed her academic career as part of the Australian "Global Talent" program.



Overview of completed training activities

Discipline specific activities

Courses

COMSOL Course (COMSOL, NL)	2017
SolidWorks course (Solidworks, NL)	2018
Han-sur-Lesse Winterschool (WUR & TU Delft, BE)	2019

Conferences

WUR Rheology workshop (WUR, NL) ^p	2017
Iberian meeting on rheology (Spanish Rheology Group, SP) ^{p*}	2017
Dutch Soft Matter Meeting (Leiden University, NL) ^o	2017
CHAINS (NWO, NL)	2017
Dutch Polymer Days (DPI, NL) ^o	2018
Food Colloids Conference (Leeds, UK) ^p	2018
Gordon Research Seminar Tribology (GRS, US) ^{p,o*}	2018
Gordon Research Conference Tribology (GRC, US) ^{p,o}	2018
WUR Rheology workshop (WUR, NL)	2018
CHAINS (NWO, NL) ^p	2018
Physics at Veldhoven (NWO, NL) ^p	2019
WUR Rheology workshop (WUR, NL)	2019
European Conference on Tribology (Austrian Tribology society, AT) ^{p,o}	2019
International symposium on food rheology and structure (ETH, CH) ^{p,o}	2019
Young EFFoST (IUFoST, NL) ^{o*}	2019
Wageningen PhD Symposium (Wageningen PhD council, NL) ^{o*}	2019
CHAINS (NWO, NL) ^o	2019
Physics at Veldhoven (NWO, NL) ^o	2020
Hydrocolloids conference (Elsevier, AU) ^o	2020
American Physical Society March Meeting (APS, virtual) ^o	2021
International Conference on Biotribology (Elsevier, virtual) ^{p,o}	2021

Other activities

Internship at <i>The University of Queensland</i> (AU)	2020
--	------

(Poster presentation: ^p, Oral presentation: ^o, Presentation award:*)

General courses

VLAG PhD week, (VLAG, NL)	2017
Posters and Pitching (WGS, NL)	2017
Efficient Writing Strategies (WGS, NL)	2017
Supervising BSc and MSc students (WGS,NL)	2019
PhD Carousel (WGS, NL)	2017
Scientific Publishing (WGS, NL)	2017
Journal Club (PCC, NL)	2017-2020

Other activities

Preparation of the research proposal (FPH/PCC)	2017
Organising PhD study tour to Singapore & Indonesia (FPH)	2018
Participating in PhD study tour to Singapore & Indonesia (FPH)	2018
PhD Council membership (VLAG)	2017-2019
Colloquia group meetings (FPH/PCC,NL)	2017-2020

*It's our problem-free philosophy:
Hakuna Matata!*

Colofon

The research described in this thesis was financially supported by the Graduate School VLAG, and was a collaboration between the Laboratory of Physics and Physical Chemistry of Foods the Laboratory of Physical Chemistry and Soft Matter at Wageningen University Research, The Netherlands.

Printed by Proefschriftmaken.nl.

Cover design by R.E.D. Rudge and Shu Wei Chin (TeapotOccamy).

